Development of feedback algorithms for future linear colliders

Rebecca Ramjiawan
St Edmund Hall

Thesis submitted in fulfilment of the requirements for the degree of Doctor of Philosophy at the University of Oxford

Hilary Term, 2019

Abstract

The Feedback On Nanosecond Timescales (FONT) intra-train feedback system has been designed to provide beam stabilisation at the interaction point (IP) of a future linear collider, such as the International Linear Collider (ILC). A prototype system based around cavity Beam Position Monitors (BPMs) is installed in the final focus system at the Accelerator Test Facility (ATF2) at KEK, and is designed to demonstrate nanometre-level stabilisation using low-latency beam-based feedback. One focus of this thesis is the development of this prototype system, including the optimisation of the BPM resolution and the improvement of the beam stabilisation performance. The feedback system was tested on trains of two bunches with a separation of 280 ns, for which the position of the first bunch was measured and the subsequent bunch was stabilised. The correction was implemented using a stripline kicker, with a custom power amplifier, and the feedback calculations were performed on a FONT5A digital board built around a Field Programmable Gate Array (FPGA).

Studies of the BPM resolution are presented, highlighting the importance of sample integration of the BPM waveforms in improving the resolution from ~ 40 nm to ~ 20 nm. Recent improvements to the FPGA firmware allow for the use of waveform integration during feedback operation. The feedback loop can be configured to include either input from a single BPM to provide local beam stabilisation, or to use signals from two BPMs to stabilise the beam at an intermediate location. Stabilisation to 50 nm and 41 nm have been demonstrated for 1-BPM and 2-BPM feedback respectively.

The ATF2 extraction-line feedback system has demonstrated the latency, resolution and correction range required for an ILC IP feedback system. Simulations were performed to show that a similar feedback system could be used to provide the required level of luminosity recovery and stabilisation for the ILC. The beam transport was modelled using PLACET and the beam-beam interactions were simulated in GUINEA-PIG. A bunch-by-bunch IP feedback system was modelled in Octave, for which various feedback algorithms were investigated. Ground motion, the jitter of the damping-ring extraction kicker and wakefields were modelled and preliminary studies suggested that the proposed feedback system could help achieve $\sim 95\%$ of the design luminosity.

Acknowledgements

My thanks goes first and foremost to my supervisor, Phil Burrows, for providing me with the opportunity and support to work on such an interesting project. I also owe a great deal of thanks to Colin Perry and Glenn Christian, whose expertise and patience are greatly appreciated.

Thanks also go to the other members of the FONT group, past and present. To Neven Blaskovic Kraljevic and Talitha Bromwich for their help and enthusiasm when I was a new student, and to Ryan Bodenstein and Luke Dyks for many interesting conversations. I am also grateful to Douglas Bett, whose extensive knowledge of the FONT system was invaluable. Thank you to Chetan Gohil and Pierre Korysko for all of their help with the simulations.

I would like to thank all of our colleagues at the ATF2 for their assistance during our time there. Thank you as well to my fellow students for making my time at KEK so enjoyable. I am grateful also to TMD Technologies for sponsoring this research.

I am thankful to everyone at Teddy Hall who have helped to make my time in Oxford so memorable, Floreat Aula! Finally, thank you to my friends and family for your continuous support throughout my many years at Oxford, I couldn't have done this without you all.

Contents

List of Figures

List of Tables

Chapter 1

Introduction

1.1 The Standard Model

1.1.1 Fermions and bosons

The Standard Model of particle physics describes the universe in terms of fundamental fermions and the force-mediating gauge bosons through which they interact [1]. By studying high-energy interactions, the predictions of the Standard Model have been corroborated to a high degree of accuracy [2].

In the Standard Model, fermions form the building blocks of matter and their behaviour and interaction are determined by the exchange of bosons [2]. The fundamental fermions, which have half-integer spin, comprise six leptons and six quarks; these are listed in Table 1.1. The charged leptons, along with their antiparticle counterparts, each have associated neutrinos. The leptons interact via both the electromagnetic and weak forces, with neutrinos confined solely to weak interactions. The quarks are fermions with charges of either $+\frac{2}{3}e$ or $-\frac{1}{3}e$. Energy exchange between quarks happens with the strong, weak and electromagnetic forces, with the strong force occurring through the exchange of gluons. The strong force binds the quarks into pairs and triplets in a phenomenon called 'confinement' and as a result quarks have never been observed to exist alone as 'free' quarks [3].

Three of the fundamental forces are transmitted via the exchange of the gauge bosons shown in Table 1.1 [4], with the classical theory of gravity currently not incorporated into the quantum theory of the Standard Model. The electromagnetic force has an infinite range and a massless boson, the photon (γ). The weak force, by virtue of its massive $W^{\pm}$ and Z gauge bosons, has a short range of $\sim 1 \times 10^{-18}$ m, as specified by the Heisenberg uncertainty

Table 1.1: Fundamental fermions and gauge bosons of the Standard Model.

Leptons		Quarks		Gauge bosons	
Type	Electric charge	Type	Electric charge	Type	Electric charge
Electron (e)	$-1e$	Up (u)	$+\frac{2}{3}e$	Photon (γ)	0
Muon (μ)	$-1e$	Charm (c)	$+\frac{2}{3}e$	W^+	$+1e$
Tau (τ)	$-1e$	Top (t)	$+\frac{2}{3}e$	W^-	$-1e$
Electron neutrino (ν_e)	0	Down (d)	$-\frac{1}{3}e$	Z^0	0
Muon neutrino (ν_μ)	0	Strange (s)	$-\frac{1}{3}e$	Gluon (g)	0
Tau neutrino (ν_τ)	0	Bottom (b)	$-\frac{1}{3}e$	Higgs (H^0)	0

principle [5]. The strong force is propagated by the exchange of massless gluons, which carry a property called 'colour charge' and have the ability to self-interact. Gluons bind quarks into structures of three quarks or quark-antiquark pairs, called baryons and mesons respectively.

Despite the success of the Standard Model in experiments across a broad energy range, with all fermions and bosons having been observed, the framework is known to be insufficient to describe all phenomena [6]. For example, further work is required to seamlessly unite general relativistic theories, which model spacetime as a continuum, with the Standard Model, in which energy and time are quantised [7]. Furthermore, in the Big Bang, matter and antimatter are expected to have been created in approximately equal quantities and there is no mechanism within the model for the matter-antimatter asymmetry observed in the universe. The Standard Model is also unable to account for the presence of dark matter and dark energy in the universe [8], and assumes that the neutrino has zero mass, which is disproved by neutrino oscillations [9]. Physics Beyond the Standard Model (BSM) must be further explored by pushing accelerators to higher energies and intensities, and detectors to increased precision.

1.1.2 The Higgs mechanism

The announcement of the discovery of the Higgs boson in July 2012 fuelled new plans to build colliders for the production and study of this particle [10]. The Higgs mechanism provides a way for the gauge bosons to acquire mass through electroweak spontaneous symmetry breaking and for the fermions to acquire mass through interaction with the Higgs field. The Higgs field is a uniform field, permeating all space, and the associated Higgs boson has zero spin and zero electric and colour charges [11].

The Higgs field is a complex scalar field with four components which form an isospin doublet with SU(2) symmetry [12]. It has degenerate minima with infinite ground states, each with an identical vacuum state energy [13]. Below a critical temperature, spontaneous symmetry breaking occurs, selecting a single vacuum state. During this process, three components of the complex doublet become longitudinal components of the $W^{\pm}$ and Z^0 bosons and they acquire mass. The other remaining component couples to fermion states, as described by the Yukawa interaction [13].

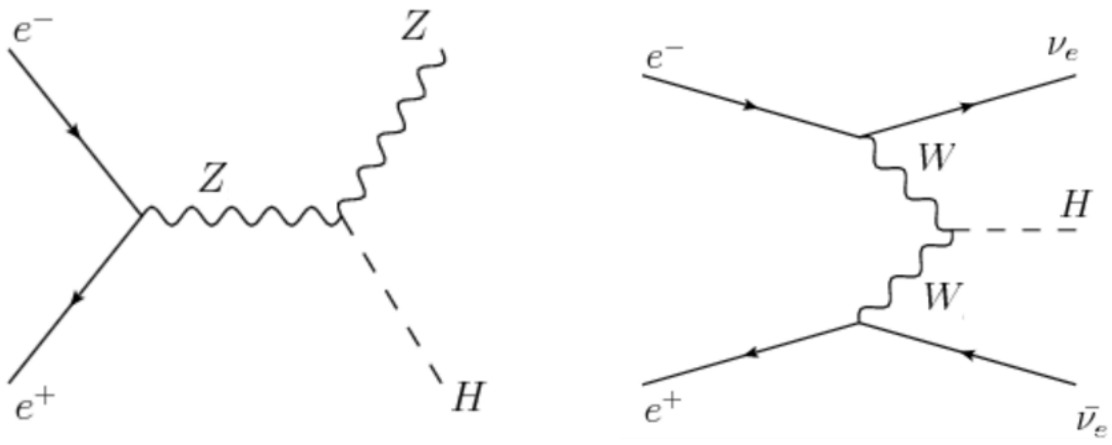

(a) (b)

Figure 1.1: Feynman diagrams showing the dominant mechanisms for the production of Standard Model Higgs bosons in e^+e^- interactions through (a) Higgs-strahlung and (b) WW fusion [14].

Further investigation into the coupling strengths and branching ratios of the Higgs boson are required to confirm whether the observed boson is the Standard Model Higgs boson or is part of an alternative model. Figure 1.1 shows two of the dominant mechanisms for the production of the Higgs boson through e^+e^- collisions that may be exploited to produce a large quantity of Higgs bosons in a future e^+e^- collider. By studying the coupling strengths and branching ratios of a large sample of Higgs bosons it may be possible to determine which model provides the best interpretation.

1.1.3 Top quark pair production

Top quark pair production can be used to probe for BSM contributions as manifested via anomalous couplings, which could be important to our understanding of electroweak symmetry breaking [15]. Precision measurements of the threshold for top quark pair production

can be used to determine the top quark mass. This is of interest as the top quark has a mass close to the electroweak scale and may therefore be involved in electroweak symmetry breaking [16]. The top quark electroweak couplings are predicted by the Standard Model and comparisons with experimental measurements could be used to search for deviations from the model. The dominant mechanisms for top quark pair production in e^+e^- collisions are shown in Fig. 1.2. By using polarised electron and positron beams, the left-right asymmetry can also be measured, which represents the variation of cross-section with changing beam polarisation. This asymmetry depends on the top quark and Higgs masses and can be used as a probe for BSM physics [17]. Similarly, the forward-backward asymmetry can also be determined by counting the number of events in the detector as a function of the polar angle [18].

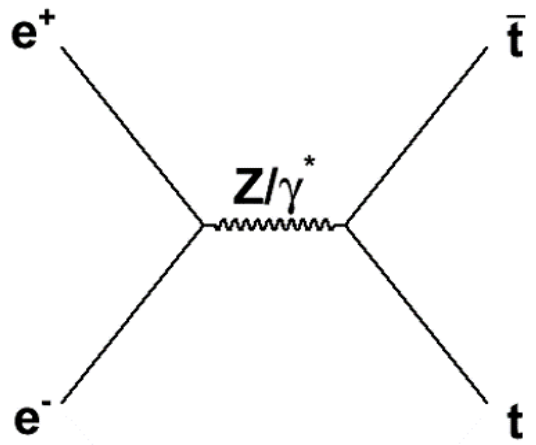

Figure 1.2: Feynman diagrams showing the dominant mechanisms for the production of a pair of top quarks in e^+e^- interactions [19].

1.2 Particle accelerators

1.2.1 Beam dynamics

To enable the study of the Standard Model, high-energy collisions are used to produce a wide range of fundamental particles. By using collisions with a stationary centre-of-mass, higher energy scales can be probed than with fixed-target colliders, with the LHC reaching collision energies of 13 TeV (2015-2016) [20]. Particle colliders comprise opposing high-energy particle beams which are focussed and brought to a collision at an Interaction Point (IP).

During the collision, the nature of the particles produced depends on the energy of the interaction, and the rate of production depends on a quantity called the luminosity, $\mathcal{L}$.

The luminosity is the proportionality constant relating the rate, $R(X)$, at which particle interaction X may occur and the cross-section, $\sigma(X)$, for that interaction [21],

$$R(X) = \mathcal{L}\sigma(X). \tag{1.1}$$

The interactions probed by colliders often have very small cross-sections, requiring a high luminosity to achieve the desired rate of production of particles.

Within the collider, radiofrequency (RF) cavities are used to accelerate bunches of charged particles. The cavities are shaped such that they have a resonant eigenmode with a longitudinal electric field component, E_z [21]. By oscillating the direction of the RF field synchronously with the bunches, a bunch can be made always to see acceleration in the direction of motion as it passes through a cavity. In this way, a particle that is exactly synchronous with the cavities' RF fields would receive the same acceleration at every cavity, as it would always arrive at the same phase. For particles before the peak of the RF wave, those which arrive earlier than the synchronous particle will see a lower accelerating gradient and those arriving late will see a higher accelerating gradient. Particles which receive more energy than the reference particle will arrive at the next cavity earlier than at the previous. In this way, the accelerated particles group into stable bunches of particles executing longitudinal oscillations about the reference particle, called synchrotron oscillations [22].

Magnetic components are used within the accelerator to bend and focus the beam of particles. One magnetic structure commonly used to provide beam focussing is the FODO lattice, consisting of alternating focussing and defocussing quadrupoles interspersed by drift space. The iterative focussing and defocussing causes the particles to execute transverse 'betatron' oscillations. The beta function, β, is related to the envelope of particle motion at a given longitudinal position along the beamline and characterises these oscillations. The oscillations reach a minimum at the defocussing quadrupoles and a maximum at the focussing quadrupoles [23]. Cartesian coordinates are used such that the x-y plane is transverse to the beam and the z axis is along the centre of the beampipe. The betatron oscillations are given by

$$y = \sqrt{\beta(z)\epsilon}\cos\left(\mu(z) + \mu_0\right), \tag{1.2}$$

where $\beta(z)$ is the beta function at longitudinal location z, ϵ is the beam emittance, and μ_0 is the phase of a particle at $z = 0$. The phase advance $\mu(z)$ represents the phase of the betatron oscillation at z relative to the phase at $z = 0$. The β function is one of the four 'Twiss parameters' (α, β, γ, ϵ), which parameterise the beam as it propagates through the beamline.

The emittance, ϵ, is a measure of the spread of particles in position-momentum phase-space, as shown in Fig. 1.3. The emittance is conserved, according to Liouville's theorem,

unless energy is gained or lost by the beam. If energy exchange occurs through processes such as RF acceleration or radiation damping [24], it is the normalised emittance $\gamma\epsilon$ which is conserved. The beam size at longitudinal position s can be defined in terms of the emittance, ϵ, and the beta function, $\beta(s)$, as $\sigma(s) = \sqrt{\beta(s)\epsilon}$.

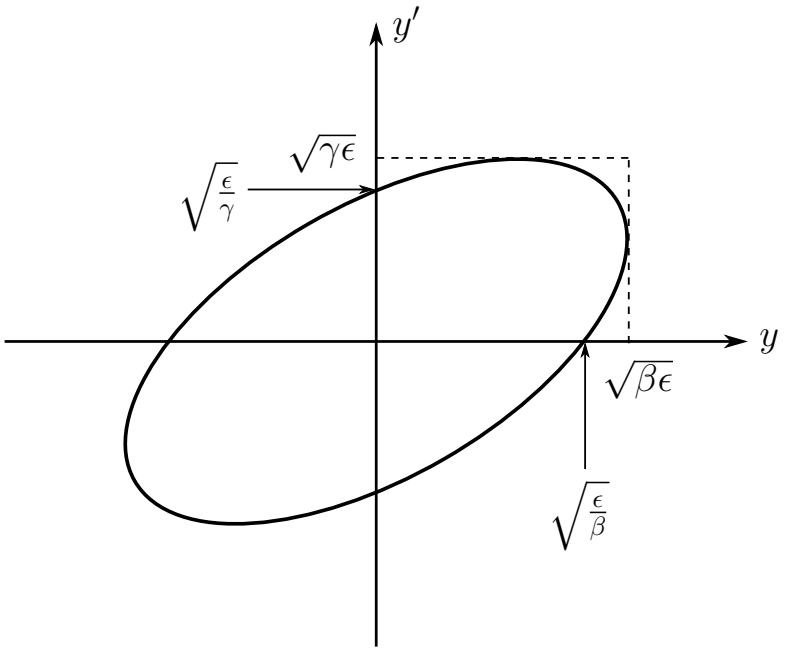

Figure 1.3: An ellipse representing the phase-space (y-y') which is occupied by a collection of particles; the beam emittance is defined as the area of phase-space occupied by the beam divided by π [23].

1.2.2 Linear and circular accelerators

Accelerators for use in high-energy physics experiments are typically either linear or circular. In a linear collider, particles are accelerated using separate, oppositely-directed linear accelerators, after which they are focussed and brought to collision. Circular colliders, on the other hand, accelerate particles incrementally by repeatedly traversing the same ring of accelerating cavities. Multiple interaction regions may be located around the ring. These two configurations provide different advantages and disadvantages depending on the type of particle being accelerated, among other factors. They also both come with a unique set of physics and engineering challenges, with respect to beam control, acceleration and stabilisation.

One key difficulty with a linear accelerator is that the accelerated particles have only a single opportunity to collide, so that beam stability at collision is critical. Conversely, although a circular collider offers the benefits of multiple opportunities for collision, it is

necessary to bend high-energy beams and maintain them over many rotations. This requires a high magnetic field strength, increasing the cost and difficulty of producing the magnets required [25]. Another consideration for circular colliders is the emission of energy through synchrotron radiation in the bending magnets. This is particularly problematic for electrons, as the power lost through synchrotron radiation scales as $\frac{E^4}{m^4\rho^2}$, where ρ is the bending radius [23]. For higher centre-of-mass energies, it becomes prohibitively expensive to replace the power lost through synchrotron radiation and, consequently, two of the primary designs for future e^+e^- collider are linear colliders, the Compact LInear Collider (CLIC) [26] and the International Linear Collider (ILC).

1.2.3 Electron-positron colliders

The study of the Higgs boson is one of the key motivators behind the construction of a next-generation high-energy collider, and consequently the proposals for CLIC and the ILC aim to maximise the rate of production of these bosons. When colliding hadrons, as in the LHC, it is the constituent quarks and gluons within the hadrons that interact. The energy of the interaction is then an unknown fraction of the full hadron energy, as particles interact whose precise mass is unknown. When colliding leptons, on the other hand, the energy of the collision is controllable and can be tuned, thus maximising the rate of production. Therefore, for the study of large samples of Higgs bosons, an e^+e^- collider is considered preferable [27].

Hadrons are composed of three quarks, gluons and quark-antiquark pairs. During collision, interactions between the constituent components lead to large background signals, with QCD jets being produced during the hadronisation of quarks. The dominant decay modes of the Higgs boson are $H \rightarrow b\bar{b}$ and $H \rightarrow WW^*$ [28] and these decay products must be distinguished from the background signal. This requires a good understanding of any background processes, as the background may be five to six orders of magnitude larger than the signal level. Interactions between leptons, on the other hand, produce a significantly lower background, providing a cleaner signal with which to study Higgs decays.

1.3 The International Linear Collider

One proposed design for a future linear e^+e^- collider is the ILC, which would have a nominal centre-of-mass energy of 250 GeV (with the possibility of future upgrade to 350 GeV or 500 GeV) [31]. A schematic of the ILC design is given in Fig. 1.4, with the machine design parameters given in Table 1.2. Such a collider could be tuned to produce up to 0.64 millions

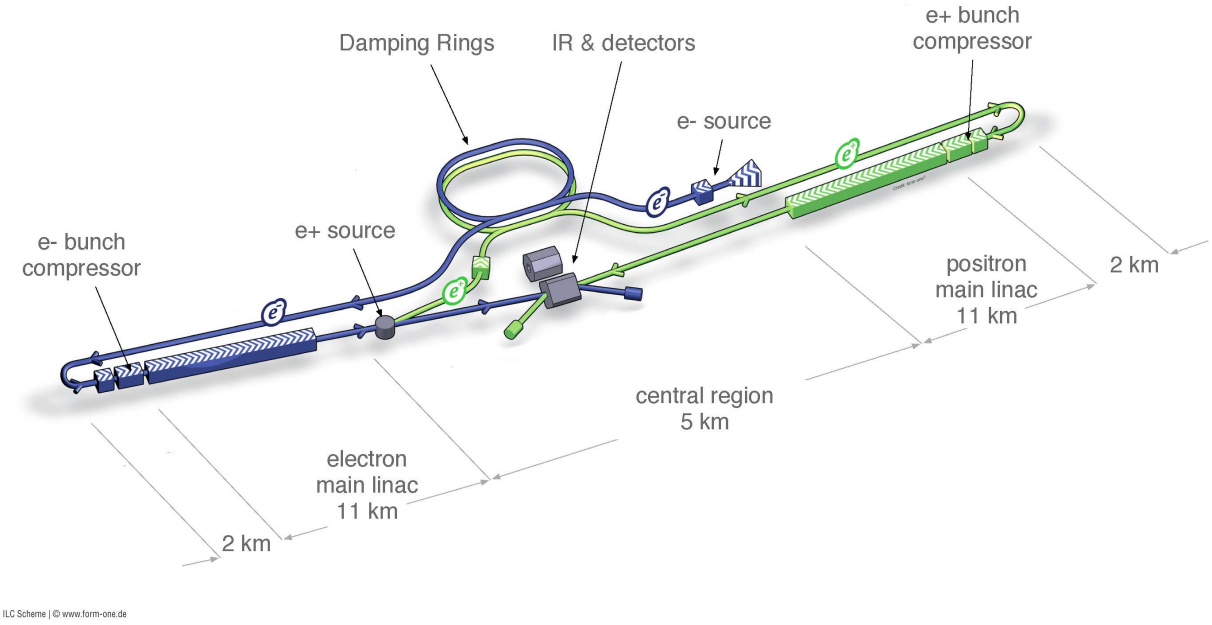

Figure 1.4: Schematic of the ILC layout for the 500 GeV baseline design [29].

Table 1.2: ILC design parameters for the 250 GeV, 350 GeV and 500 GeV baseline designs [29][30].

Centre-of-mass energy	250	350	500	GeV
Repetition rate	5	5	5	Hz
Bunches per train	1312	1312	1312	
Number of particles per bunch	2	2	2	$\times 10^{10}$
Bunch separation	554	554	554	ns
Bunch length at IP	300	300	300	µm
Peak luminosity ($\mathcal{L}$)	1.35	1	1.84	$\times 10^{34}\,\mathrm{cm}^{-2}\mathrm{s}^{-1}$
Horizontal r.m.s beam size at IP (σ_x^*)	729	684	474	nm
Vertical r.m.s beam size at IP (σ_y^*)	7.7	5.9	5.9	nm
Horizontal beta function at IP (β_x^*)	13	16	11	mm
Vertical beta function at IP (β_y^*)	0.41	0.34	0.48	mm
Normalised horizontal emittance at IP ($\gamma\epsilon_x$)	10	10	10	µm
Normalised vertical emittance at IP ($\gamma\epsilon_y$)	35	35	35	nm
Vertical disruption parameter (D_y)	24.5	24.3	24.6	

Higgs bosons in ten years through the leading production mode, Higgs-strahlung [32]. The 350 GeV upgrade could also be used to study top-top pair production (Section 1.1.3).

The 31 km collider would include an electron and positron source, two superconducting linear accelerators (linacs), damping rings (DRs) and a beam dump, as shown in Fig. 1.4. The electron source comprises a photocathode and laser system so that electrons can be produced with a minimum of 80% polarisation, with bunches of 2×10^{10} particles [33]. The electrons are accelerated to 5 GeV in a booster linac, after which a transfer line is used to pass the electrons to the DR. The repetition rate of the bunch trains would be 5 Hz, with 1312 bunches per train and a bunch-to-bunch separation of 554 ns [29].

Separate DRs, each 3.2 km in circumference, are utilised to reduce the beam emittance of the electron and positron beams. They are designed with a transverse damping time of 23.95 ms [34]. Both transverse and longitudinal damping occurs through the emission of synchrotron radiation and wigglers are included in the DR design to increase the rate of damping. RF cavities in the ring provide longitudinal acceleration to reintroduce the energy lost, so that the beam exits the damping ring at the same energy at which it was injected.

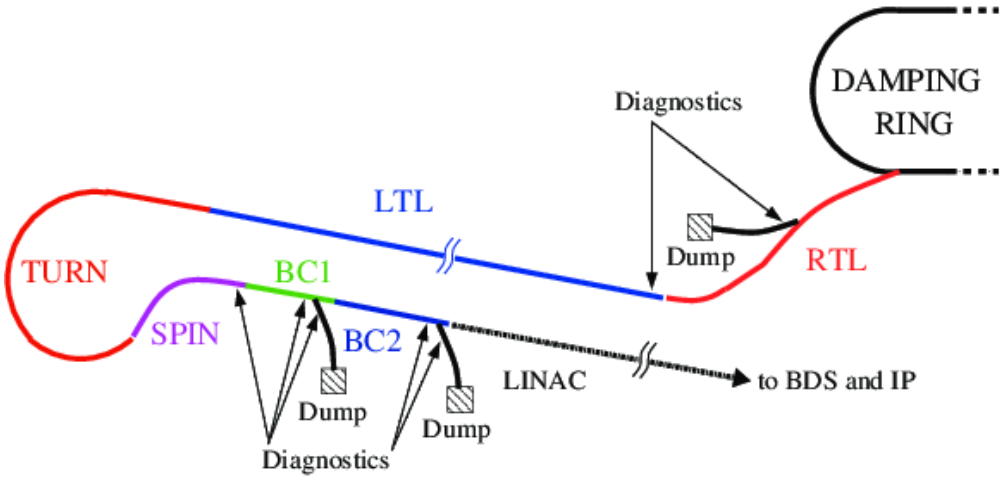

Figure 1.5: Schematic of the ILC RTML for the electron beam, showing the turnaround (TURN), Ring To Linac (RTL), Long Transfer Line (LTL) and Bunch Compressors (BC) [35].

The ultra-low emittance bunches are individually extracted from the DR to the Ring To Main Linac (RTML) system, shown in Fig. 1.5, using a fast extraction kicker. An RTML feedforward system, located at the turnaround, is used to reduce the beam jitter due to variations in the pulse from the damping ring extraction kicker [36]. In the RTML, the bunches are compressed from a bunch length of 6000 µm to 300 µm using a two-stage bunch compressor [37]. The bunch compressor operates by first introducing an energy-position (E-z) correlation to the bunches with an RF section, and then using a magnetic chicane, for which the beam path length is energy dependent.

RF cavities are used to increase the bunch energy from 5 GeV to 15 GeV and, at this energy, the beam is transferred to the Main Linac (ML). The ILC design has two MLs for the separate acceleration of the electron and positron beams. RF accelerating cavities with a gradient of 31.5 MV/m are used to increase the beam energy to the nominal collision energy. Each ML comprises 1.3 GHz superconducting, niobium accelerating cavities [34].

After the ML, the beam is transferred to the Beam Delivery System (BDS), shown in Fig. 1.6, the purpose of which is to match the Twiss parameters [38] into the final-focus, to focus the beam to a small spot size at the IP and, after collision, to safely dump the beams. Instrumentation in the BDS includes beam position monitors (BPMs), transverse and longitudinal emittance diagnostics and luminosity monitors.

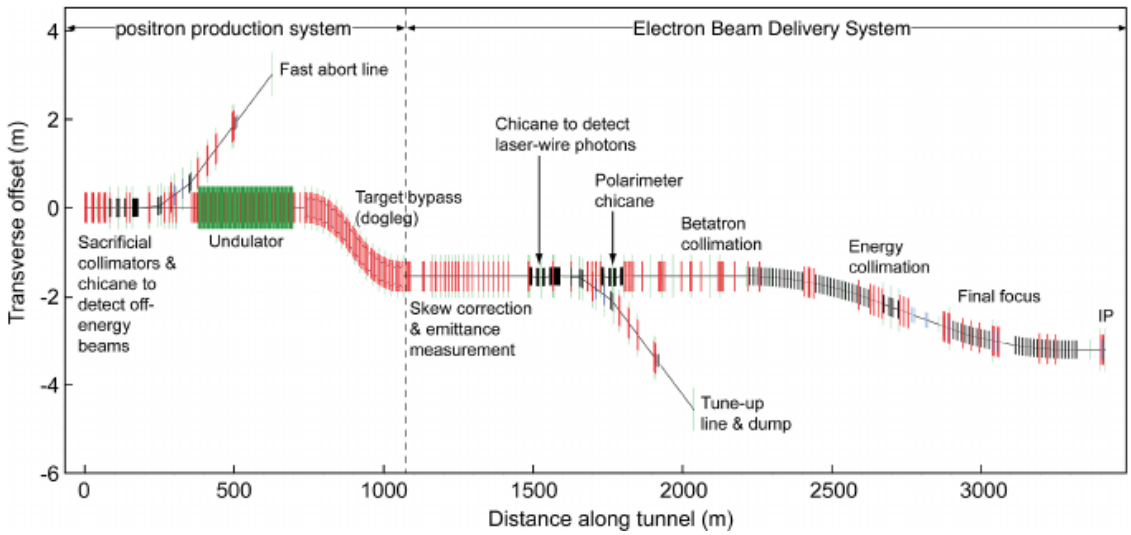

Figure 1.6: ILC BDS lattice layout for the electron beam, with the positron-production system shown upstream [34].

1.3.1 Ground motion

The alignment of the beamline components is critical in successfully transporting and focussing the beam, and is particularly important for the strong focussing region of the BDS. When considering the very small beam sizes in linear colliders, the offsets caused by ground motion become significant and, if not properly accounted for, could lead to significant luminosity loss.

Ground motion can be characterised in terms of 'slow' ground motion, at less than 1 Hz including sources such as coastal waves [39], and 'fast' ground motion, which is dominated by cultural noise. A feedback system acting between successive beam pulses could correct for ground motion at frequencies lower than 5 Hz but the mitigation of beam jitter above

this frequency requires a fast intra-train IP feedback system. It can be seen from Fig. 1.7 that ground motion above 5 Hz was measured for all of the sites. Vertical stabilisation of the beam at the IP is of particular importance due to the small vertical beam size of 5.9 nm compared with the horizontal beam size of 474 nm.

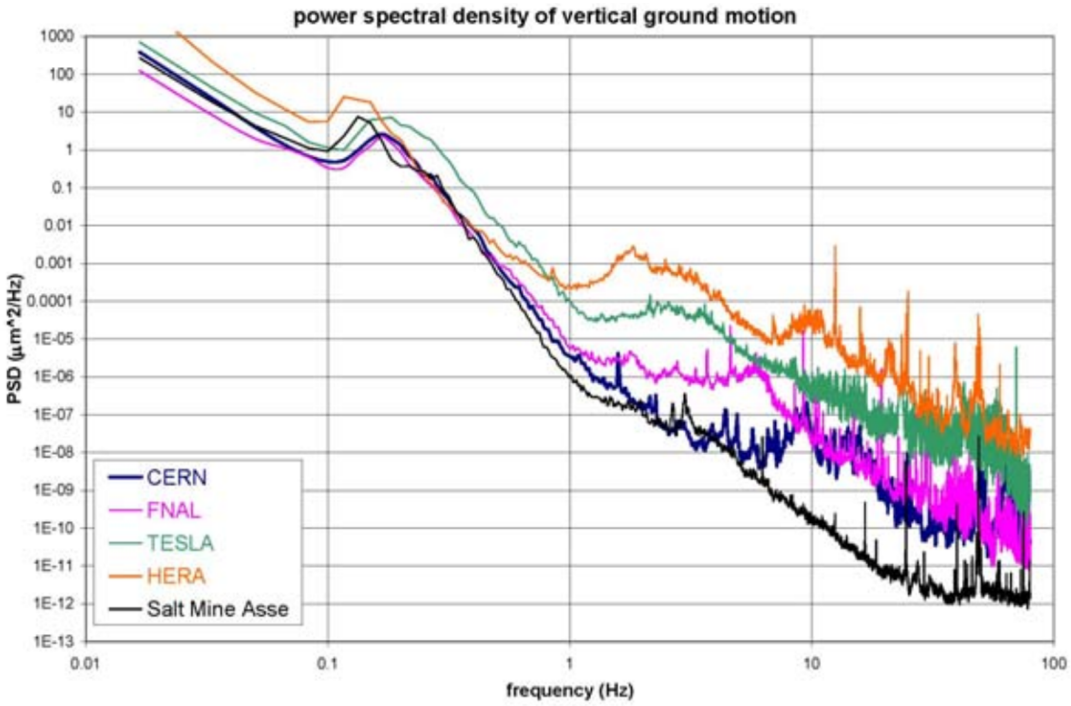

Figure 1.7: Power spectral density of ground motion versus frequency, as measured at various sites [39]. A particularly quiet site is shown in black. A proposed site for the TESLA accelerator is shown in green [40]; technology from the TESLA project was incorporated into the ILC design in 2004.

1.3.2 Bunch-by-bunch IP feedback

To achieve the ILC design luminosity, a beam-based, intra-train feedback system is required near the IP to provide stabilisation of the vertical beam position. For such a system, the bunch-bunch offset at the IP would be measured for a first 'pilot' bunch and used to calculate the correction required to remove the offset. The correction is then applied to the next bunch in the train and the remaining offset is determined. Feedback would then be repeated iteratively across the entire bunch train with a delay loop to maintain the preceding corrections [41]. This process requires a high correlation between the positions of consecutive bunches. For bunch-by-bunch feedback, the bunch separation sets a limit on the latency of the system of 554 ns. The schematic for a design proposed to meet the ILC resolution, kick and latency requirements is shown in Fig. 1.8.

The feedback system is based upon the principle that opposing bunches with a non-zero offset impart a strong transverse beam-beam kick to each other, causing both bunches to be deflected. The offsets of the deflected bunches are measured $\sim 4\,\text{m}$ downstream, at which point the offsets are larger and a downstream BPM with micron-level resolution would be sufficient for nanometre-level stabilisation at the IP. For example, an offset of 1 nm at the IP would translate to an offset at the BPM of $\sim 70\,\mu\text{m}$ (see Section 5.3.2). A stripline BPM has been proposed as a suitable candidate, as this has been demonstrated to meet the latency, resolution and dynamic-range requirements [42].

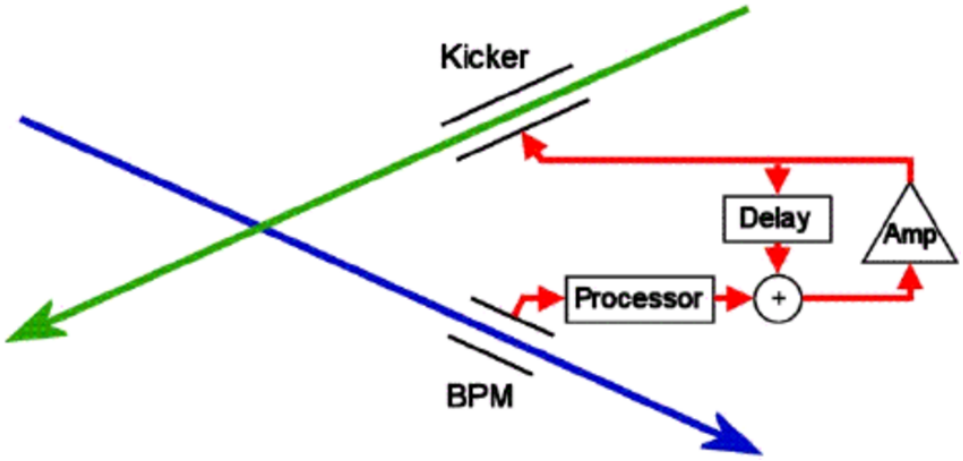

Figure 1.8: Schematic of the FONT IP intra-train feedback system [43].

The correction is implemented with the use of a stripline kicker located upstream of the final quadrupole and sextupole, as shown in Fig. 1.9. If the offsets of the deflected electron bunches are measured, it is the positron bunches which are corrected and vice versa; this is designed to reduce the latency from the signal propagation time. The stripline kicker is located ~ 8 m upstream of the IP and for a 250 GeV beam, is required to have a correction range of $\pm 60\,\text{nrad}$ [42]. The IP feedback system is designed with a capture range of $\pm 200\,\text{nm}$ at the IP, which propagates to an offset for the deflected bunch of $\pm 1400\,\mu\text{m}$ at the BPM [42]; this is discussed in Section 5.3.2. The capture range is defined as the range of beam-beam offsets which can be measured and corrected by the feedback system, without exceeding the linear operating region of the BPM or the feedback kicker. A $50\,\mu\text{m}$ offset of the deflected beam at the BPM corresponds to a 1% reduction in the luminosity, so that a micron-level resolution BPM would be sufficient to achieve close to nominal luminosity (see Section 5.6.1).

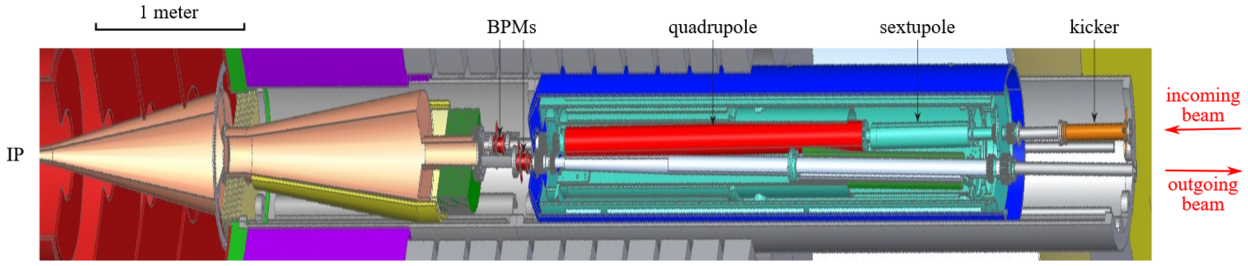

Figure 1.9: Schematic of the ILC IP region, showing the BPMs and kicker [42].

1.4 The Accelerator Test Facility

1.4.1 ATF2 beamline components

The Accelerator Test Facility (ATF) [44][45] at the High Energy Accelerator Research Organisation (KEK), consists of a 1.28 GeV electron accelerator [46]. The ATF was initially designed with the goal of demonstrating the ultra-low emittance beams necessary to meet the luminosity requirements for future linear colliders. The ATF facility was upgraded to the ATF2 project in 2008, for which the original linac and DR were used, and a new extraction-line and final-focus were installed [47]. A schematic of the ATF2 is shown in Fig. 1.10 and the main design parameters are given in Table 1.3.

One of the most important parameters to be considered during the design of a high-energy collider is the luminosity, and the two primary goals of the ATF2 reflect this. In order to demonstrate the feasibility of the ILC design luminosity, the ATF2 goals are to demonstrate a beam size of 37 nm and nanometre-level beam stability with the aid of a beam-based IP feedback system. The ATF2 final-focus system (FFS) is a scaled prototype of the Raimondi-Seryi Final-Focus System proposed for the ILC. The Raimondi-Seryi FFS is a compact design that uses a local chromaticity correction scheme [50]. The chromaticity correction is applied using sextupoles, with dipoles upstream to generate the necessary dispersion at the sextupoles. This FFS is also being considered for the CLIC project [26].

The electron bunches are generated with a laser-driven photocathode RF gun at a repetition frequency of 3.12 MHz. A bunch intensity of up to 1×10^{10} electrons is possible and can be adjusted by varying the laser pulse driving the photocathode [51]. The bunch is accelerated to 1.28 GeV by the linac before entering the 138.6 m DR. The bunch is stored in the DR for 100 ms, during which radiative damping reduces both the longitudinal and transverse emittances. Accelerating cavities are used in the DR to restore the longitudinal momentum lost and to preserve the beam energy at nominal.

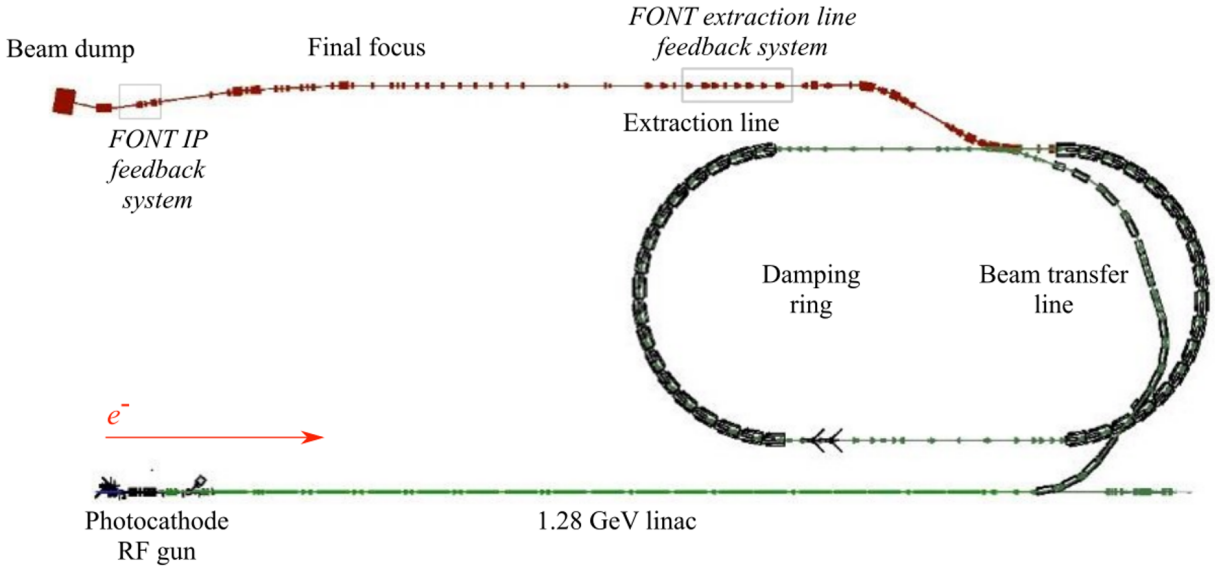

Figure 1.10: Schematic of the layout of the ATF2 beamline complex, with the FONT feedback systems highlighted [48].

Table 1.3: Design parameters for the ATF2 compared with the ILC 500 GeV baseline design [45][49].

Parameter	ATF2	ILC	Unit
Energy	1.3	500	GeV
Repetition rate	3.12	5	Hz
Electrons per bunch	1×10^{10}	2×10^{10}	
Bunch separation	280	554	ns
Normalised horizontal emittance at IP ($\gamma\epsilon_x$)	2	10,000	nm
Normalised vertical emittance at IP ($\gamma\epsilon_y$)	0.012	35	nm
Horizontal r.m.s beam size at IP (σ_x^*)	2.8	0.474	µm
Vertical r.m.s beam size at IP (σ_y^*)	37	5.9	nm
Horizontal beta function at IP (β_x^*)	4	11	mm
Vertical beta function at IP (β_y^*)	0.10	0.48	mm
Electron r.m.s energy spread	0.08	0.13	%

Trains of bunches are possible, with the bunch spacing determined by the timing of the bunch injection to the DR, as each bunch is injected separately. The full bunch train is extracted from the DR with a single pulse of a stripline extraction kicker [52]. The DR has 330 RF buckets each separated by 1.4 ns, allowing for a range of train configurations. The extraction kicker pulse has a flat top of approximately 300 ns so that bunch trains up to this length can be extracted with a single pulse. The extraction kicker timing can be adjusted so that bunch trains lie in the centre of this flat top, thus minimising any bunch-to-bunch offsets introduced during extraction. For the studies in this thesis, trains of two bunches were used with a separation of 280 ns, as this separation has been found to provide a high degree of correlation between the vertical positions of the two bunches.

After leaving the DR, the beam passes through the extraction line, in which the beam size and emittance are measured, phase-space and coupling correction are performed, and the beam is prepared for the FFS [44]. As there is only one beam, there can be no collision: the beam size is minimised at a virtual IP, where the beam size and beam stability can be measured, before the beam is dumped. A FONT feedback system is installed in the IP region to demonstrate stabilisation of the beam waist, with the goal of achieving nanometre-level beam stabilisation. Another FONT feedback system (shown in Fig. 1.10) is located in the extraction line and provides position and angle stabilisation of the ATF2 beam.

1.4.2 ATF2 extraction-line feedback system

A prototype fast feedback system is installed in the extraction line at the ATF2 to stabilise the vertical beam position and angle before it enters the FFS. A schematic of this system is presented in Fig. 1.11. Beam stabilisation is quantified in terms of reducing the bunch position jitter, defined as the standard deviation of positions measured over many successive bunches. The feedback system operates to stabilise the second and third bunches in a train, thus requiring a high correlation between the positions of the bunches.

The system comprises three stripline BPMs, P1, P2 and P3, and two stripline kickers, K1 and K2. The stripline BPMs P2 and P3 are used in the feedback loop and P1 is used as a witness. The BPMs and kickers are arranged into feedback loops P2-K1 and P3-K2, with the loops approximately separated by a betatron phase advance of $\frac{\pi}{2}$, allowing for correction of both position and angle. As the phase advance is not exactly $\frac{\pi}{2}$, the feedback loops are coupled. To increase the sensitivity of the BPMs to the K1 and K2 kicks, the BPMs are located at a phase advance approximately $\frac{\pi}{2}$ from their respective kickers.

The system has a latency of 148 ns, allowing for intra-train feedback, with a correction

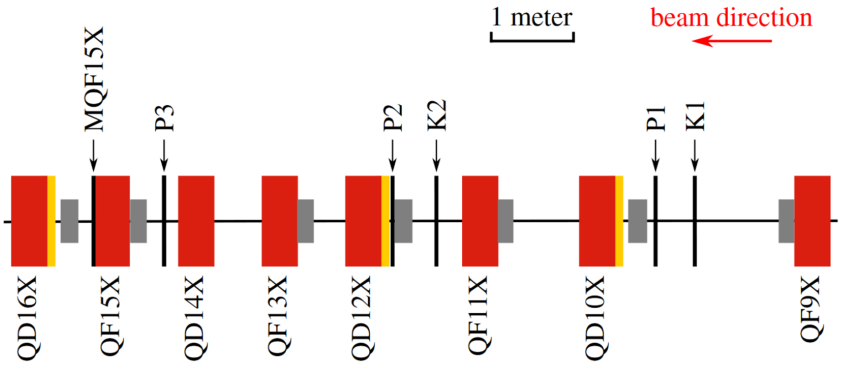

Figure 1.11: Layout of the stripline BPMs (P1, P2, P3) and kickers (K1 and K2) in the FONT extraction-line feedback system [42].

range of ±60 µm [42]. The kick range of K2 is ∼±35 µrad and by scaling this to the ILC energy, this would correspond to a correction range of ∼±180 nrad, satisfying the ILC kick requirements detailed in Section 1.3.2 [42]. The stripline BPMs have been demonstrated to have a resolution of 291 ± 10 nm for a bunch charge of ∼ 1 nC, and a linear working range of ±500 µm, thus meeting the ILC requirements [42].

1.4.3 ATF2 IP feedback system

A bunch-by-bunch feedback system, designed to demonstrate nanometre stabilisation of electron beams, is installed at the ATF2 IP. The beam orbit is measured using three cavity BPMs located around the IP, called IPA, IPB and IPC, as shown in Fig. 1.12. The bunch separation of 280 ns requires the system to operate with a low latency.

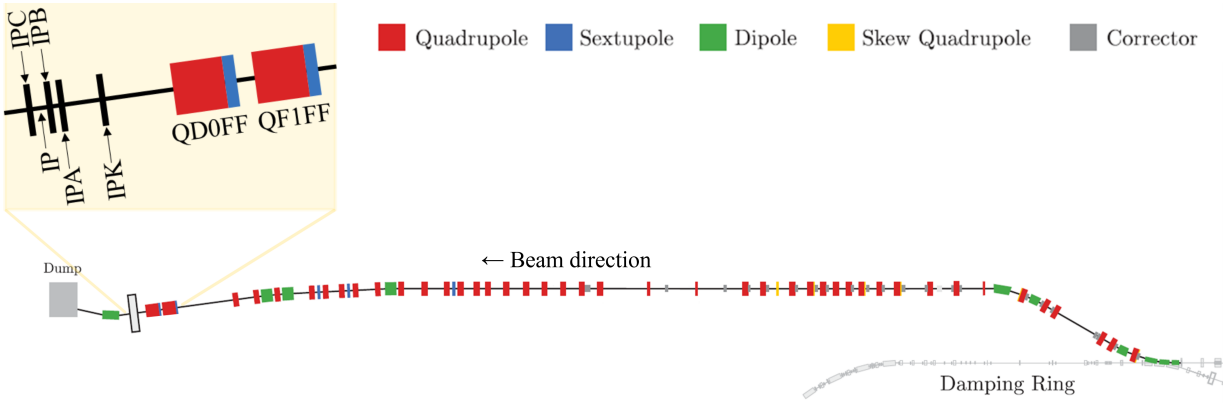

Figure 1.12: Schematic of the layout of the ATF2 extraction-line and final-focus [44], with the FONT IP region enlarged.

The BPMs are mounted on piezo-driven movers to facilitate the horizontal and vertical alignment of the BPMs with the beam, as well as the adjustment of the BPM pitch. The

longitudinal locations of the BPMs and submovers are shown in Fig. 1.13. The signals from the BPMs are digitised on a specialised FONT5A digital board and used to determine the feedback corrections required for beam stabilisation; this is further described in Chapter 4. The corrections are implemented with a stripline kicker, IPK, located upstream of the BPMs [53]. To stabilise the beam position at the IP, only a single corrector is required in the feedback loop.

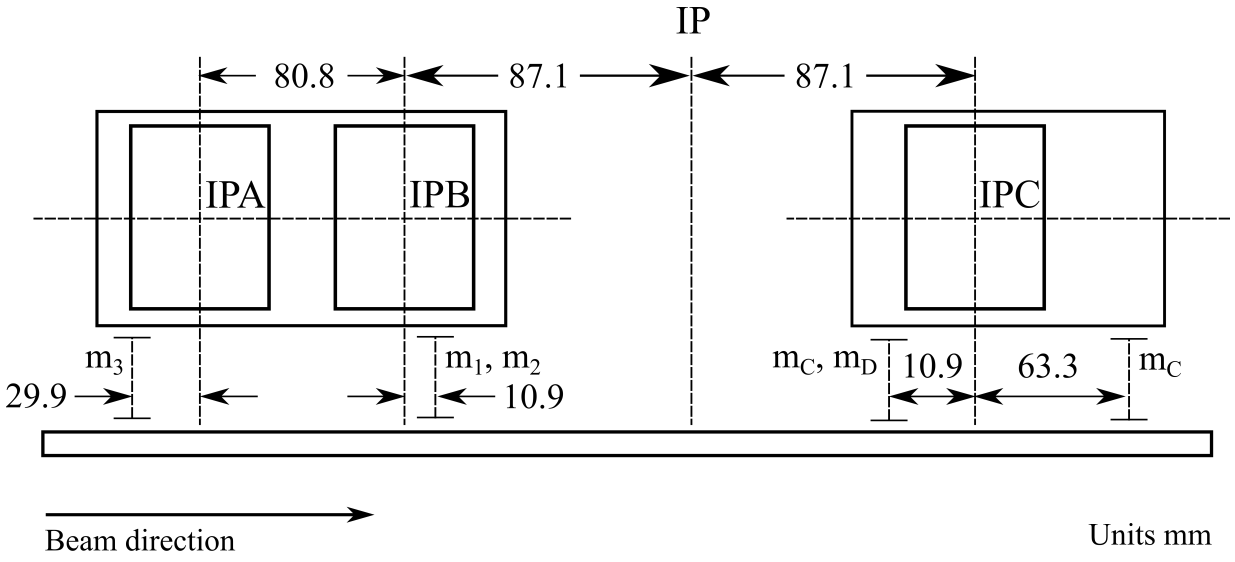

Figure 1.13: Schematic of the IP BPM configuration, with the IPAB mover block, on which IPA and IPB are mounted, with submovers m_1, m_2 and m_3, and the IPC mover block with submovers m_C, m_D and m_E, allowing for the adjustment of the BPM positions and tilts [49].

1.5 Thesis outline

The work described in this thesis is a contribution towards the design for a feedback system for beam stabilisation at the interaction point of a single-pass collider. The ATF2 IP feedback system which uses cavity BPMs is described, with work towards achieving nanometre-level BPM resolution and beam stabilisation detailed. Achievements using the extraction-line feedback system are also overviewed and the significance of these results on the proposed ILC IP feedback system are discussed.

In Chapter 2, the ATF2 feedback system is presented, with a focus on the development and operation of the three cavity BPMs. Chapter 3 reports studies of the BPM resolution and an analysis of the factors limiting their performance. In Chapter 4, the beam stabilisation results for two different feedback modes are presented, and recent improvements to the feedback calculation are discussed. In Chapter 5, simulations of the ILC and the proposed

IP feedback system are described, in order to demonstrate that a similar feedback system could help achieve the ILC design luminosity. Studies are presented on the effects of factors such as wakefields and ground motion on the performance of an IP feedback system. Various feedback algorithms were tested on the simulated bunch trains and the results are discussed. Conclusions and recommendations for further study are given in Chapter 6.

Chapter 2

Cavity IP BPMs

Three cavity BPMs, located in the IP region at the ATF2, are used to make beam orbit measurements that can be used as the input to an intra-train feedback system. As a charged bunch passes through the cavity-like structure, the cavity's electromagnetic eigenmodes are excited [54]; these modes can be used to determine the offset of the bunch from the cavity's electrical axis and also the charge of the bunch. Beam position measurements from one or two of these cavity BPMs can be used to drive the IP feedback system, for which the ATF2 goal is to demonstrate stabilisation to the nanometre level. Such stabilisation would require a BPM resolution of order a nanometre. Further information regarding the cavity BPMs can be found in [53]. A more detailed description of the cavity BPM signal processing can be found in [55].

In this chapter, the theory of the excitation of the cavities' eigenmodes is discussed, alongside the signal processing and digitisation required to extract a bunch position measurement from the BPM signals. The configuration of the ATF2 for various modes of BPM operation is described, with the benefits and drawbacks of each configuration. The process of calibrating the BPMs for position and angle measurements is detailed, and the dependence of the calibration on various parameters is considered. All analysis presented in this chapter is my own, including the BPM calibrations, studies of the BPM position and angle sensitivities and studies of the jitter on the BPM phase angle.

2.1 Operation of the cavity BPMs

2.1.1 Cavity eigenmodes

Of the resonant modes excited by a charged bunch passing through the cavity, the transverse magnetic (TM) resonant modes are of particular interest. These modes have a component of the electric (E) field along the cavity's longitudinal electrical axis and can therefore be excited by a bunch travelling in that direction. Separate cavities are designed for the extraction of the monopole and dipole TM modes, called 'reference' and 'dipole' cavities.

Stainless steel, cylindrical x and y reference cavities, shown in Fig. 2.1(a), are constructed such that the monopole mode is the dominant mode excited. The antennae are placed so as to couple to this mode [53]. The frequencies of the reference cavities are determined by the diameters of the cavities and can be tuned, within a range of ± 35 MHz, using tuning pins. The pins are used to adjust the frequency of the reference cavities to match that of their respective dipole cavities.

The three dipole cavities, IPA, IPB and IPC, are rectangular and use spatial filtering to suppress the dominant lower-frequency monopole mode so that the dipole mode can be extracted [56]. The cavities were designed with different vertical and horizontal dimensions so that the resonances of the horizontal and vertical dipole modes are uncoupled and can be separately extracted. The arrangement of coupling slots in the dipole cavities allows for the horizontal and vertical dipole modes to be extracted separately from the same BPM, each through a pair of waveguides. The outputs from these waveguides are then combined, thus doubling the signal from the antisymmetric dipole mode and cancelling the unwanted symmetric monopole mode. A 700 MHz bandwidth band-pass filter (BPF) after the hybrid then removes the remaining monopole signal. The BPM processing electronics are described in Section 2.1.5.

The electric field and resonant frequencies of the cavity depend on its dimensions, such that for a rectangular cavity, with dimensions given by $0 \leq x \leq a$ and $0 \leq y \leq b$, the electric field (E_z) along the longitudinal axis for the TM_{120} mode is

$$E_z(x, y) = E_z^{\max} \sin\left(\frac{\pi x}{a}\right) \sin\left(\frac{2\pi y}{b}\right). \tag{2.1}$$

The resonant frequency, f_{12}, is

$$f_{12} = \frac{c_0}{2}\sqrt{\left(\frac{1}{a}\right)^2 + \left(\frac{2}{b}\right)^2}, \tag{2.2}$$

where c_0 is the electromagnetic wave velocity [57]. For the dipole cavities, with dimensions of the order of centimetres, the resonant frequencies are of the order of GHz. The design

values of the resonant frequencies are given in Table 2.1. The cavity frequencies were chosen to be an integer multiple of the damping-ring frequency so that signals derived from the damping-ring master oscillator could be used to down-mix the cavity signals. Furthermore, C-band (4 to 8 GHz) frequency cavities were selected as these were found to reduce the sensitivity of the cavity output to the beam angle [55].

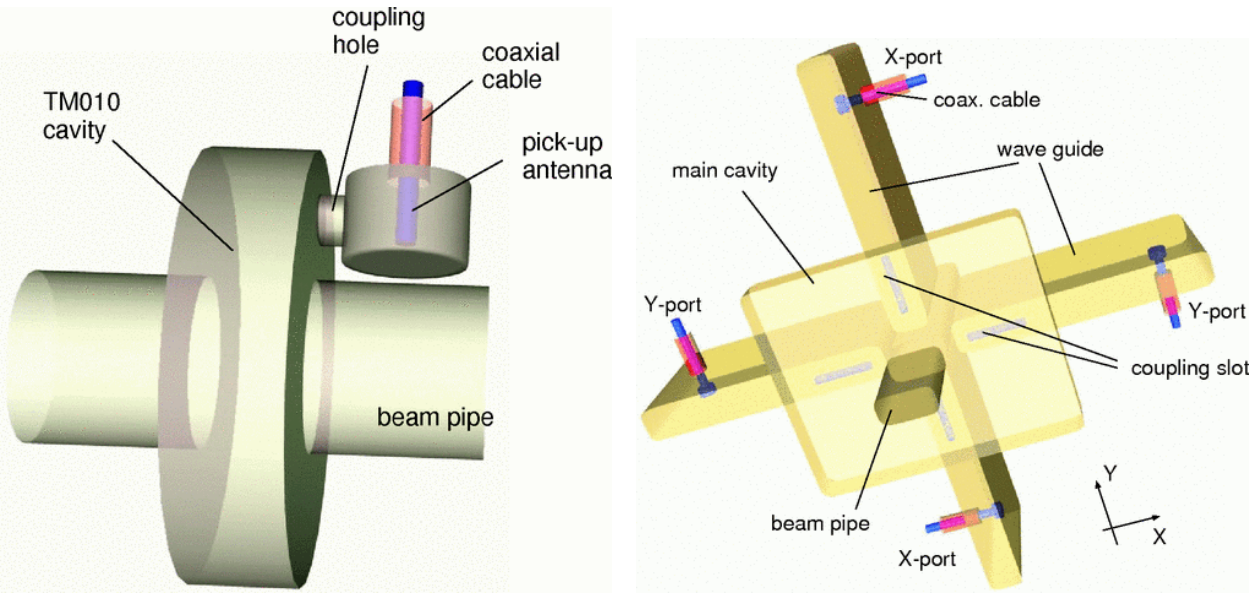

(a) (b)

Figure 2.1: Structure of the (a) cylindrical reference cavity BPMs and (b) rectangular dipole cavity BPMs, with coupling slots and waveguides highlighted [55].

Table 2.1: Measured values of the resonant frequencies and decay times of the dipole [58] and reference [59] cavity BPMs.

BPM		Resonant frequency (GHz)	Decay time (ns)
Dipole cavity	x-port	5.712	∼24
Dipole cavity	y-port	6.426	∼25
Reference cavity	x cavity	5.711	14
Reference cavity	y cavity	6.415	14

For the reference cavities, cylindrical polar coordinates (r, ϕ, z) are used, with z along the centre of the beampipe. For these BPMs, the $\mathrm{TM}_{r\phi z} = \mathrm{TM}_{010}$ monopole mode is the desired eigenmode, as it has an amplitude that is proportional to the bunch charge. For the dipole cavities, the rectangular structure means that Cartesian coordinates (x, y, z) are more convenient, and for these BPMs the $\mathrm{TM}_{xyz} = \mathrm{TM}_{210}$ and TM_{120} dipole modes are the useful

eigenmodes for x and y beam position measurements respectively. Example monopole and dipole TM modes are shown in Fig 2.2. The TM_{010} mode is symmetric about the cavity's electrical axis and has an amplitude which scales with the charge of the bunch. The mode is strongly excited for bunches close to the cavity's electrical axis and has, to first order, no dependence on the bunch position [54]. Conversely, the TM_{210} and TM_{120} modes are antisymmetric about the cavity's axis, leading to an amplitude that is dependent on both the bunch charge and the x and y offsets of the bunch, respectively.

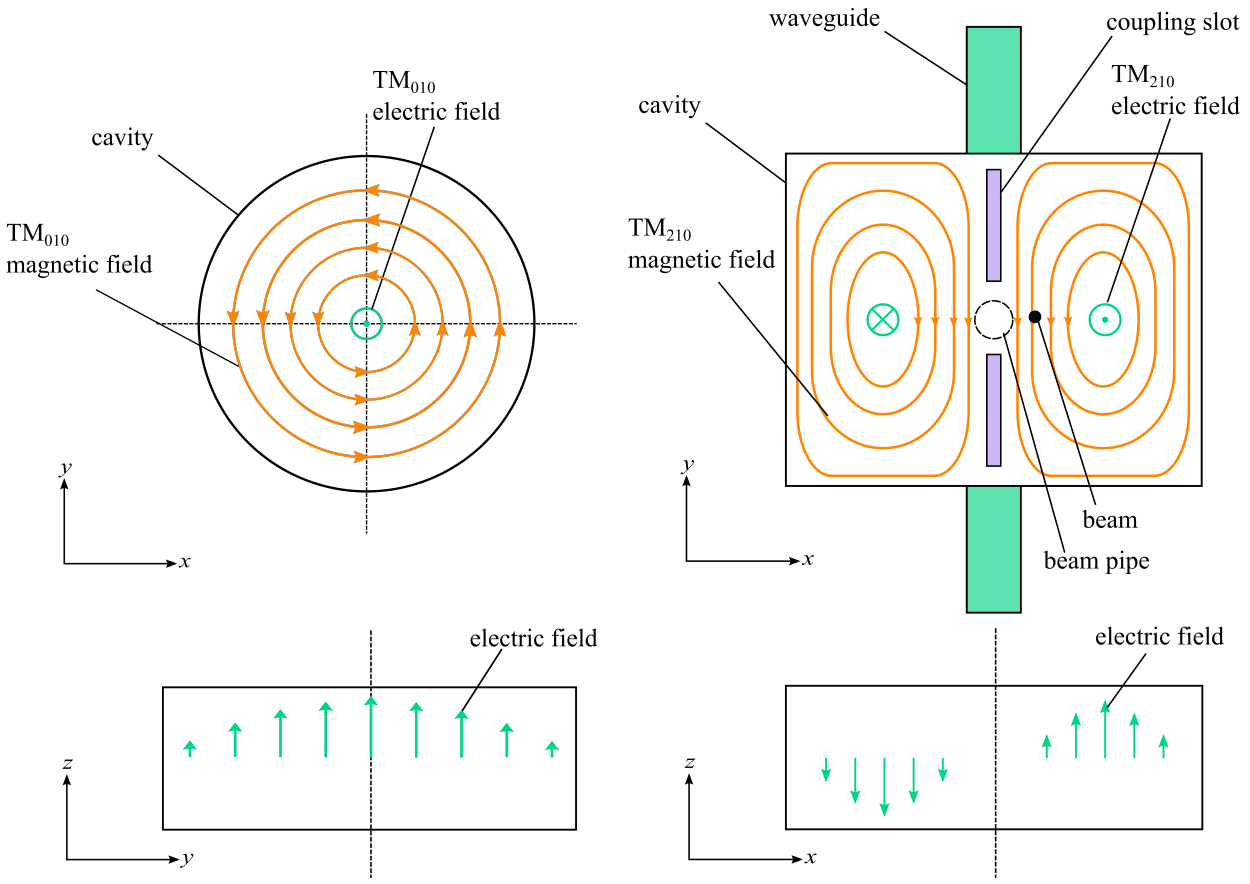

Figure 2.2: Schematic of the electric and magnetic fields lines of (a) the TM_{010} mode for a cylindrical cavity BPM and (b) the TM_{210} mode for a rectangular cavity BPM. The waveguides which couple to the TM_{210} mode are shown.

2.1.2 Cavity BPM configuration

There is a longitudinal separation of 80.8 mm between IPA and IPB, and 174.2 mm between IPB and IPC, with the nominal IP typically located half-way between IPB and IPC, as shown in Fig. 1.13. The x and y reference cavities are both located downstream of the three

dipole cavities. The three dipole cavities are mounted within a common vacuum chamber on piezo-mover systems to facilitate their horizontal, vertical and angular alignment with the beam. It should be noted that IPA and IPB are mounted on a single 'IPAB' mover block and are therefore unable to be moved independently from each other. The IPAB movers, manufactured by Cedrat Technologies, have a working range of 248 µm; the IPC mover, manufactured by PI, has a working range of 300 µm [49]. All submovers have feedback systems in place to ensure a position stability of better than ±2 nm [49].

The resolution of the BPM is limited by the signal-to-noise ratio. The signal level is partly determined by how much energy is transferred from the beam to the TM_{120} mode, and then how well this mode is coupled out of the BPM through the waveguides. There are multiple sources of noise in the system, including thermal and electronic noise, as well as signal contamination from the TM_{010} mode [54].

A variable attenuator on the dipole cavity signal offers the ability to increase the dynamic range of the BPMs at the expense of the system resolution. The dynamic range at 0 dB of ∼3 µm is increased by a factor of $\sqrt{10}$ per 10 dB of attenuation added. Similarly, as the signal level depends on the bunch charge, the dynamic range can be increased by reducing the bunch charge; although, this is also at the expense of the BPM resolution, which scales inversely with the bunch charge.

2.1.3 Cavity BPM decay time

The signal-to-noise ratio varies as a function of time as the excited modes decay. To achieve a good BPM resolution it is desirable to have as much of the waveform as possible with a high signal-to-noise ratio, meaning a longer decay time might be preferable. However, when performing intra-train feedback, it is important that the signal from the first bunch has decayed before the subsequent bunch arrives, to avoid signal contamination between consecutive bunches. The cavity decay time was optimised to satisfy both of these conditions.

The rate of energy dissipation of the resonant modes to the cavity walls and the waveguides depends on the quality factor Q, defined as [57]

$$Q_{mn} = 2\pi f_{mn} \frac{\text{average energy stored}}{\text{energy loss per second}}, \tag{2.3}$$

where f_{mn} is the frequency of the mode TM_{mn0}. From this equation, it can be seen that a lower Q corresponds to a shorter decay time. The dissipation of energy in the system creates a spectrum of frequencies at which excitations occur, around the frequencies of the nominal eigenmodes [54].

The cavities were designed with a low Q so as to have a short decay time. However, the Q values measured from the cavities after their production were significantly lower than their design values [60]. Consequently, the decay time was too short, thus reducing the time for which the BPM signals had a good signal-to-noise ratio. The addition of indium sealing to the cavities, to make a good-contact seal between the main cavity body and the cavity side cover plates (see Fig. 2.3), led to a higher Q and a decay time which was ∼2.5 times longer. Studies have demonstrated that the BPM resolutions were improved as a result of this indium sealing and that there was no signal contamination between consecutive bunches [60].

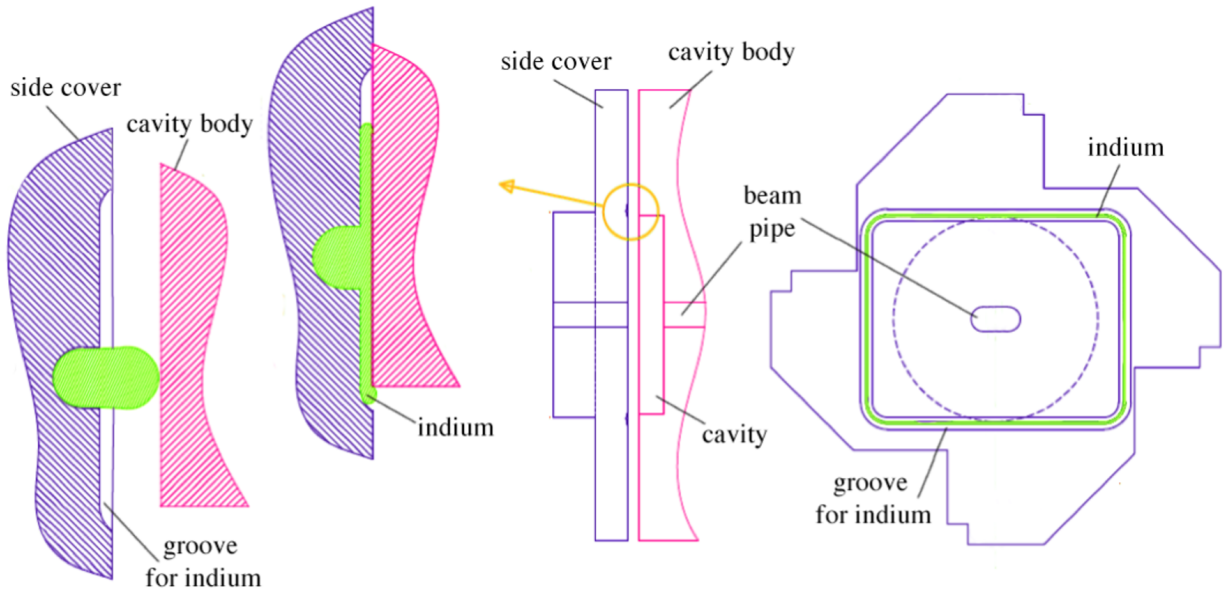

Figure 2.3: Schematic of the BPM side cover, main body and groove for indium sealing [61].

2.1.4 Cavity BPM signals

In addition to being excited by a position offset, the TM_{120} and TM_{210} modes can also be excited through other mechanisms. As well as the desired dependence on the offset (y) there is an unwanted dependence on the 'pitch' (y') and 'angle of attack' (α) of the bunch [53]. These parameters are measured with respect to the cavity's longitudinal electrical axis and are shown in Fig. 2.4. The dipole modes generated by the beam pitch and angle of attack are in quadrature to modes generated by a position offset and so can be decoupled [55].

The dipole signal, V, can be excited by an offset in y, y' or α, and will decay with time constant, τ. In the limit of $\alpha << 1$ and $y' << 1$ [54], the dipole signals can be written in the form

$$V_y \propto D_y q y e^{-\frac{t}{2\tau}} \sin(2\pi f_{\text{dip}} t + \phi_y), \tag{2.4a}$$

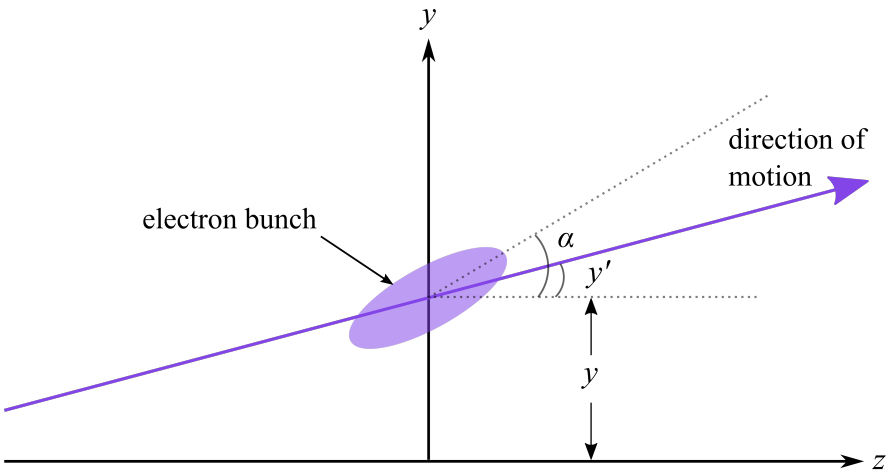

Figure 2.4: Schematic of an electron bunch showing the offset (y), angle of attack (α) and pitch (y').

$$V_{y'} \propto D_{y'} q y' e^{-\frac{t}{2\tau}} \cos(2\pi f_{\text{dip}} t + \phi_{y'}), \tag{2.4b}$$

$$V_{\alpha} \propto -D_{\alpha} q \alpha e^{-\frac{t}{2\tau}} \cos(2\pi f_{\text{dip}} t + \phi_{\alpha}), \tag{2.4c}$$

where D_y, $D_{y'}$ and D_α are the constant coefficients for the y-, y'- and α-dependent terms respectively. The total signal from the dipole cavity mode, V_{dip}, is the sum of these contributions:

$$V_{\text{dip}} = V_y + V_\alpha + V_{y'}. \tag{2.5}$$

For vertical bunch position measurements, the outputs extracted from the y-port of the dipole cavity and from the y reference cavity are $\sim 6.4\,\text{GHz}$ signals

$$V_{\text{dip}} \sim q(D_y y \sin(2\pi f_{\text{dip}} t)) + (D_{y'} y' - D_\alpha \alpha)\cos(2\pi f_{\text{dip}} t)), \tag{2.6a}$$

$$V_{\text{ref}} \sim qR(\sin(2\pi f_{\text{ref}} t + \Delta\phi)). \tag{2.6b}$$

where the terms f, q and $\Delta\phi$ represent the frequency, charge and phase with respect to the dipole signal, and R is a constant coefficient. It can be seen that the signals excited by a y' or α offset are 90° out of phase with the position component of the signal. The formula for the reference signal shows no dependence on position, which is valid for small bunch offsets.

2.1.5 Two-stage signal down-mixing

The high-frequency dipole and monopole modes must be down-mixed to produce signals that can be digitised. Two stages of down-mixing are used to produce a pair of signals, I and Q, at baseband; this is illustrated in Fig. 2.5 [53]. During the first stage of down-mixing a high-frequency local oscillator (LO) signal is used to down-mix to an intermediate frequency

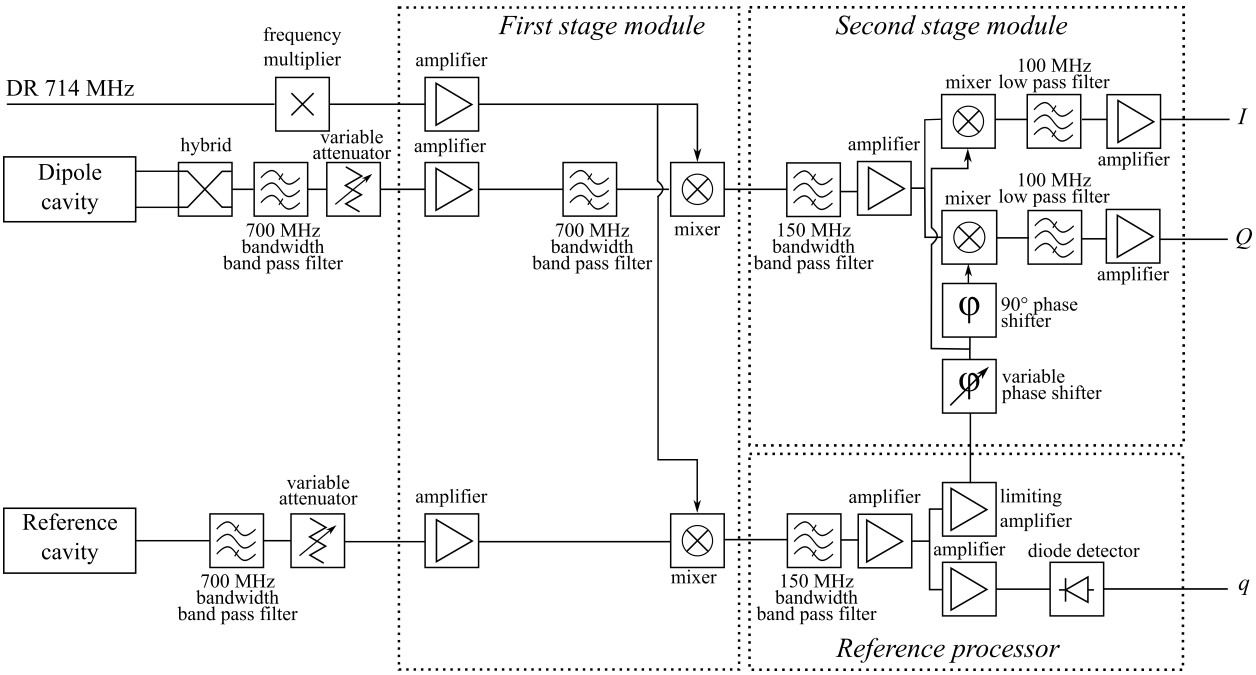

Figure 2.5: Simplified block diagram of the two-stage down-mixing process of the GHz-frequency dipole and reference cavity signals to baseband. Diagram adapted from [62].

(IF) of 714 MHz and this is then further down-mixed to baseband in the second stage. The baseband signals I and Q together contain all of the phase and amplitude information from the original high-frequency signals. I and Q both have a charge and position dependence and once they have been charge normalised, they can be combined to produce a signal whose amplitude is proportional to the bunch offset.

In the first stage of the signal processing, the monopole and dipole signals are frequency down-mixed using a common LO in order to retain the phase relation between the two modes. The first stage LO signal is obtained from the DR 714 MHz master oscillator using a frequency multiplier to produce a signal which is at the appropriate frequency and is phase-locked to the bunches [63]. The monopole and dipole cavity signals have frequencies which are integer multiples of the LO frequency, allowing for them to be down-mixed to baseband.

For the x dipole cavity outputs, the 5.712 GHz signals are down-mixed by a 6.426 GHz LO signal in the first stage processing module; for the y dipole cavity outputs the 6.426 GHz signals are down-mixed with a 5.712 GHz LO. The LO signal has the form

$$V_{LO} \sim L \sin(2\pi f_{\mathrm{LO}} t + \Delta\phi_{\mathrm{LO}}), \tag{2.7}$$

where f_{LO} is the frequency, and $\Delta\phi_{\mathrm{LO}}$ the phase of the LO signal relative to the dipole signal. The first stage of down-mixing the dipole and reference signals with this LO produces signals $V_{\mathrm{dip}} \otimes V_{\mathrm{LO}}$ and $V_{\mathrm{ref}} \otimes V_{\mathrm{LO}}$.

After the first stage of down-mixing, a 100 MHz low-pass filter (LPF), shown in Fig. 2.5, removes the high-frequency components dependent on $f_{\rm dip} + f_{\rm LO}$ or $f_{\rm ref} + f_{\rm LO}$, leaving only terms which are dependent on $f_{\rm dip} - f_{\rm LO}$ or $f_{\rm ref} - f_{\rm LO}$:

$$\begin{aligned} V_{\rm dip} \otimes V_{\rm LO} &= q\frac{L}{2}(D_y y \cos(2\pi(f_{\rm dip} - f_{\rm LO})t - \Delta\phi_{\rm LO}) \\ &\quad - (D_{y'}y' - D_\alpha\alpha) \times \sin(2\pi(f_{\rm dip} - f_{\rm LO})t - \Delta\phi_{\rm LO})), \end{aligned} \tag{2.8a}$$

$$V_{\rm ref} \otimes V_{\rm LO} = q\frac{LR}{2}(\cos(2\pi(f_{\rm ref} - f_{\rm LO})t + \Delta\phi - \Delta\phi_{\rm LO})). \tag{2.8b}$$

The down-mixed reference signal, $V_{\rm ref} \otimes V_{\rm LO}$, is then split. One of the outputs passes through a diode to produce a pulse whose magnitude can be used to determine the bunch charge. The other output passes through a limiting amplifier (limiter) to remove the charge dependence, in order to create a new LO signal. This LO is used during the second stage of the signal processing, to down-mix the dipole signal ($V_{\rm dip} \otimes V_{\rm LO}$) from 714 MHz to baseband.

After the limiter, the down-mixed reference signal has no charge dependence and would have the form

$$V_{\rm ref} \otimes V_{\rm LO} \propto \frac{L}{2}(\cos(2\pi(f_{\rm ref} - f_{\rm LO})t + \Delta\phi - \Delta\phi_{\rm LO})). \tag{2.9}$$

The second stage of the signal processing involves mixing the limited $V_{\rm ref} \otimes V_{\rm LO}$ signal and the $V_{\rm dip} \otimes V_{\rm LO}$ signal in-phase and in-quadrature to produce I and Q signals, respectively. The I and Q signals are orthogonal components, together representing the full amplitude and phase information of the amplitude modulated BPM waveform.

The I signal [64]

$$\begin{aligned} I &= (V_{\rm dip} \otimes V_{\rm LO}) \otimes (V_{\rm ref} \otimes V_{\rm LO}) \\ &\propto q(y\cos(\theta_{IQ}) - (D_{y'}y' - D_\alpha\alpha)\sin(\theta_{IQ})), \end{aligned} \tag{2.10}$$

and the Q signal

$$Q \propto q(y\sin(\theta_{IQ}) + (D_{y'}y' + D_\alpha\alpha)\cos(\theta_{IQ})), \tag{2.11}$$

can be written in terms of the the phase angle, θ_{IQ}, where

$$\theta_{IQ} = 2\pi(f_{\rm dip} - f_{\rm ref})t - \Delta\phi. \tag{2.12}$$

By using the same LO when down-mixing the dipole and reference signals, θ_{IQ} has no dependence on either $f_{\rm LO}$ or $\Delta\phi_{\rm LO}$. The I and Q signals will be at baseband if the reference cavity is tuned such that $f_{\rm dip} = f_{\rm ref}$.

2.1.6 Signal digitisation

The I, Q waveforms and the charge signal, q, are digitised at 357 MHz by a digital board called a FONT board, where the current iteration is the FONT5A board. The inputs and

outputs of this board are shown in Fig. 2.6. Examples of digitised I, Q and q waveforms are shown in Fig. 2.7 for two-bunch operation. When selecting the samples to use for position measurement, it should be noted that the samples significantly before the peak may contain transient effects from unwanted modes and also that samples late in the waveform have a poorer signal-to-noise ratio [65]. For the bunch position calculation, it is possible to use either a single sample of the waveforms or to integrate over a range of consecutive samples.

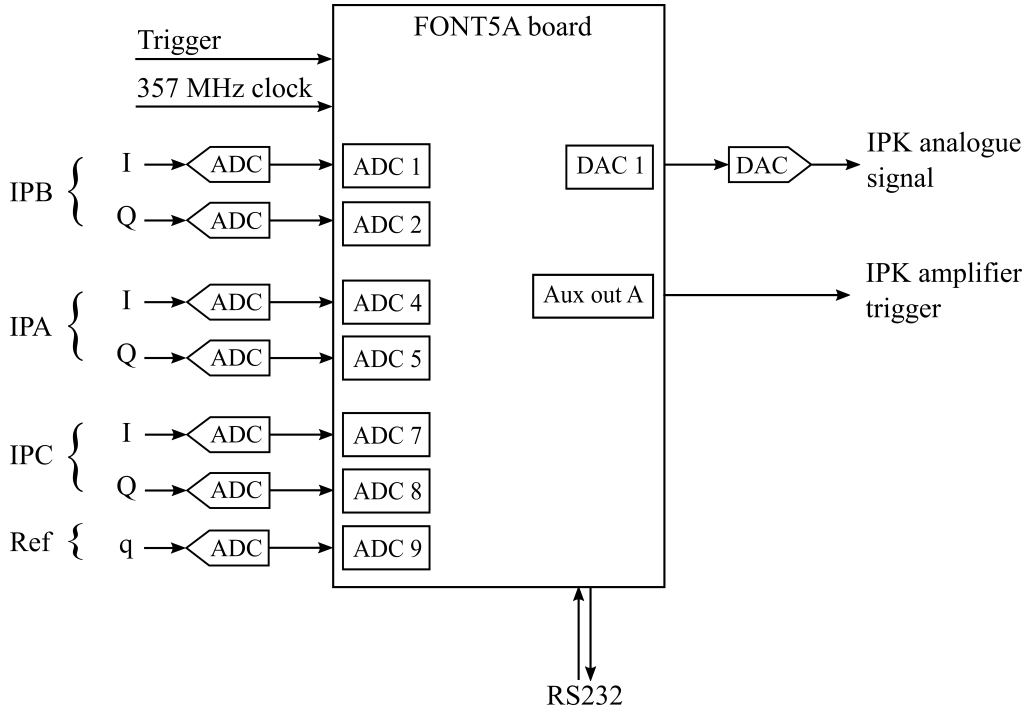

Figure 2.6: Block diagram of the FONT5A digital board, showing the main input and output signals used during feedback operation.

The I and Q signals are charge normalised to remove their dependence on q (Eqs. 2.10, 2.11). A single sample of the q waveform is used for the charge measurement, with the sample typically chosen to be at approximately 2000 ADC counts as the diode detector is known to perform well at this signal level. The accuracy of the diode detector has been verified by comparison with charge measurements from an Integrated Current Transformer (ICT) [53]. It should be noted that the diode detector has a non-linear response to lower voltages and, consequently, may not sufficiently remove the charge dependence at a very low bunch charge.

A linear combination of $\frac{I}{q}$ and $\frac{Q}{q}$ can be found to produce a signal, $\frac{I'}{q}$, with an amplitude proportional to the bunch offset. A signal orthogonal to $\frac{I'}{q}$ can also be generated, $\frac{Q'}{q}$, that is proportional to the beam pitch y' [55],

$$\frac{I'}{q} = \frac{I}{q}\cos(\theta_{IQ}) + \frac{Q}{q}\sin(\theta_{IQ}), \tag{2.13}$$

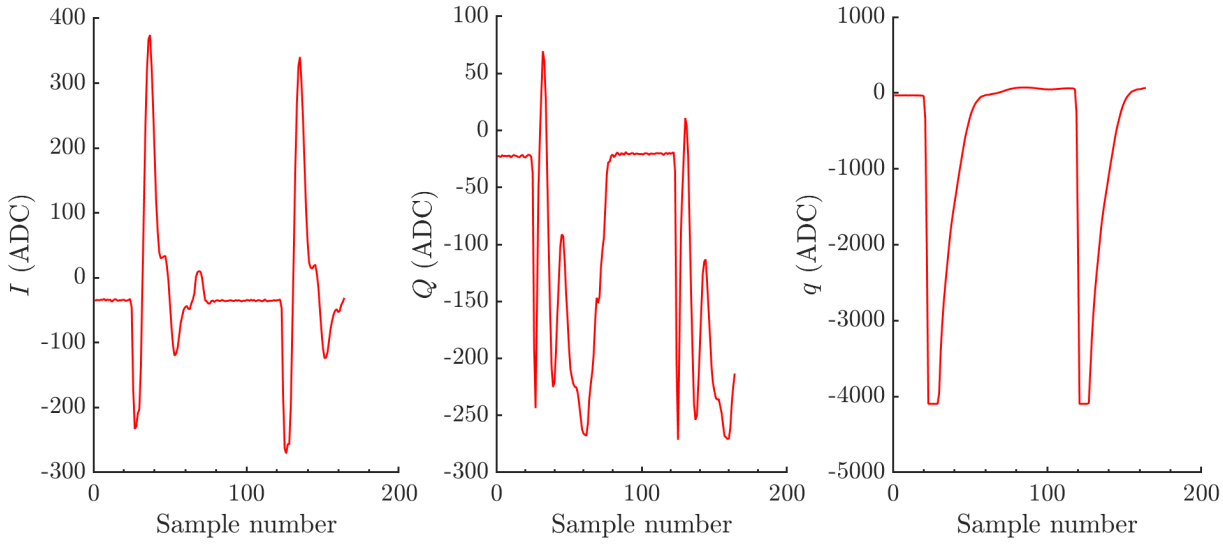

Figure 2.7: Digitised I, Q and q waveforms from IPC, showing two-bunch operation. The waveforms were sampled at intervals of 2.8 ns.

$$\frac{Q'}{q} = -\frac{I}{q}\sin(\theta_{IQ}) + \frac{Q}{q}\cos(\theta_{IQ}). \tag{2.14}$$

By substituting Eqs. 2.10 and 2.11 into Eq. 2.13, a proportionality between y and $\frac{I'}{q}$ can be found,

$$\begin{aligned} y &\propto \frac{I'}{q}, \\ y &= \frac{1}{k}\frac{I'}{q}, \end{aligned} \tag{2.15}$$

where k [μm^{-1}] is a constant, found through position calibration of the BPM.

2.2 ATF2 beam setup requirements

The limited dynamic ranges of the BPMs necessitate good alignment of the BPMs with the beam and also the minimisation of the beam jitter at any active BPMs. When operating with a single BPM, it is possible to improve results by locating the optical focal point of the beam, known as the beam waist, at this BPM [65]. The beam waists in x and y can be shifted longitudinally, largely independently of each other, by adjusting the focussing strength of the quadrupoles QD0FF and QF1FF respectively [66] [67]. This is achieved by varying the current in the magnets.

For an optics configuration with a nominal β_y^* value, the position jitter is seen to grow quickly with distance from the beam waist. As a result, to keep the beam within the dynamic

range of the BPM, operation close to the beam waist is essential. This requirement typically prohibits three-BPM operation with this 'nominal optics' configuration, as the jitter at the two BPMs furthest from the beam waist would exceed their dynamic ranges. For three-BPM operation it is useful to use an optics configuration with a reduced divergence at the IP, as this would reduce the jitter off-waist. This can be achieved with a vertical beta function β_y^* which is a factor of 1000 larger than the nominal value, in a configuration called 'high-beta optics'. The increase in β_y^* means a reduced beam jitter at the outer BPMs, at the expense of increasing the beam jitter at the beam waist.

To ensure the BPMs and the processing electronics are operating in a linear regime, the beam trajectory should be steered close to the electrical centres of the BPMs. It is possible to steer the trajectory of the beam by moving the quadrupoles in the final-focus region, as these are mounted on individual mover systems. In particular, moving the vertical or horizontal position of QD0FF will affect the beam position at the IP, while moving QF1FF or QF7FF will adjust the beam angle [66]. Off-axis quadrupoles will produce a dipole kick to the beam, and as the quadrupoles are located at a range of betatron phases, this allows for the adjustment of the beam waist in both position and angle. To aid in the BPM alignment process, the horizontal and vertical positions of the BPMs can be adjusted using the BPM piezo-mover system [49].

At the ATF2, studies were performed with bunch trains of either one or two bunches. During two-bunch operation, both bunches are extracted together from the DR by a pulsed magnetic kicker [52]. The extraction kicker pulse is a $\sim 300\,\text{ns}$ flat-topped pulse so that ideally extraction would occur without introducing an inherent transverse position offset between the two bunches. However, the kicker pulse is not a perfectly uniform signal and is known to introduce a small but measurable offset between the transverse position of two bunches. By varying the extraction-kicker timing, it is possible to locate the extraction of the two bunches at a region of the extraction-kicker pulse that minimises this offset. The two-bunch pulses are extracted at 3.12 Hz [44] with a separation of 280 ns, as this has been shown to offer a high correlation between the vertical positions of both bunches, which is critical for successful feedback operation [64].

2.3 IP BPM calibration

2.3.1 Position calibration

Calibrations are required at each BPM to determine the phase angle, θ_{IQ}, and the proportionality constant, k (Eq. 2.15). For the calibration process, the offset between the BPM and the beam is varied across a known range and the corresponding changes in I and Q are measured. Values for $\frac{I'}{q}$ are calculated for each trigger and plotted against the bunch offset, y; the gradient of this plot is the calibration constant k and is determined with a least-squares fit (Figs 2.8, 2.9 and 2.10). An 11-sample integration window was used, as this was found to optimise the BPM resolution for this configuration; further discussion on the BPM resolution is presented in Chapter 3.

A position offset of the beam relative to the BPM's electrical axis can be generated by either scanning the beam trajectory or by moving the BPM. The horizontal and vertical beam positions can be scanned using the mover for the final-focus quadrupole QD0FF, AQD0FF. QD0FF was chosen as the quadrupole for calibration because of its proximity to the BPMs, resulting in a simple transfer matrix between the two [60]. All calibrations included within this thesis were obtained using AQD0FF to vary the beam offset. Both methods of calibration have been compared and shown to be consistent [60].

In order to get an accurate measurement of the bunch position, care must be taken to sample the I and Q waveforms appropriately. This can be using either a single digitised sample or by integrating over a sample window. From these digitised samples, values for $\frac{I}{q}$ and $\frac{Q}{q}$ are calculated for every trigger and many triggers are recorded at each calibration setting; an example is shown in Fig. 2.8(a). If $\frac{Q}{q}$ is plotted against $\frac{I}{q}$, the measurements taken at a single calibration setting will group into clusters of points. A mean value of $\frac{I}{q}$ and $\frac{Q}{q}$ is found for each calibration setting; these points should lie along the $\frac{I'}{q}$ axis, due to the proportionality between $\frac{I'}{q}$ and the bunch offset. The $\frac{I'}{q}$ axis is calculated from the mean $\frac{I}{q}$ and $\frac{Q}{q}$ values using a perpendicular least-squares fit; this is illustrated in Fig. 2.8(b).

The angle between the $\frac{I'}{q}$ axis and the $\frac{I}{q}$ axis is θ_{IQ} and using Eq. 2.13, θ_{IQ} can be used to compute $\frac{I'}{q}$ for each trigger. $\frac{I'}{q}$ is plotted against the position offset, y, as shown in Fig. 2.8(c) and the gradient of a linear fit to the plot is k (Eq. 2.17). The orthogonal signal $\frac{Q'}{q}$ is proportional to the angular offset between the beam and the BPM. If the calibration is accurate, $\frac{Q'}{q}$ should not vary with changes in the beam position. From Fig. 2.8(d), it can be seen that there is a negligible dependence of the mean $\frac{Q'}{q}$ value with beam-position offset, suggesting the measurement of θ_{IQ} was accurate. Corresponding example calibration plots for IPB and IPC are presented in Figs. 2.9 and 2.10.

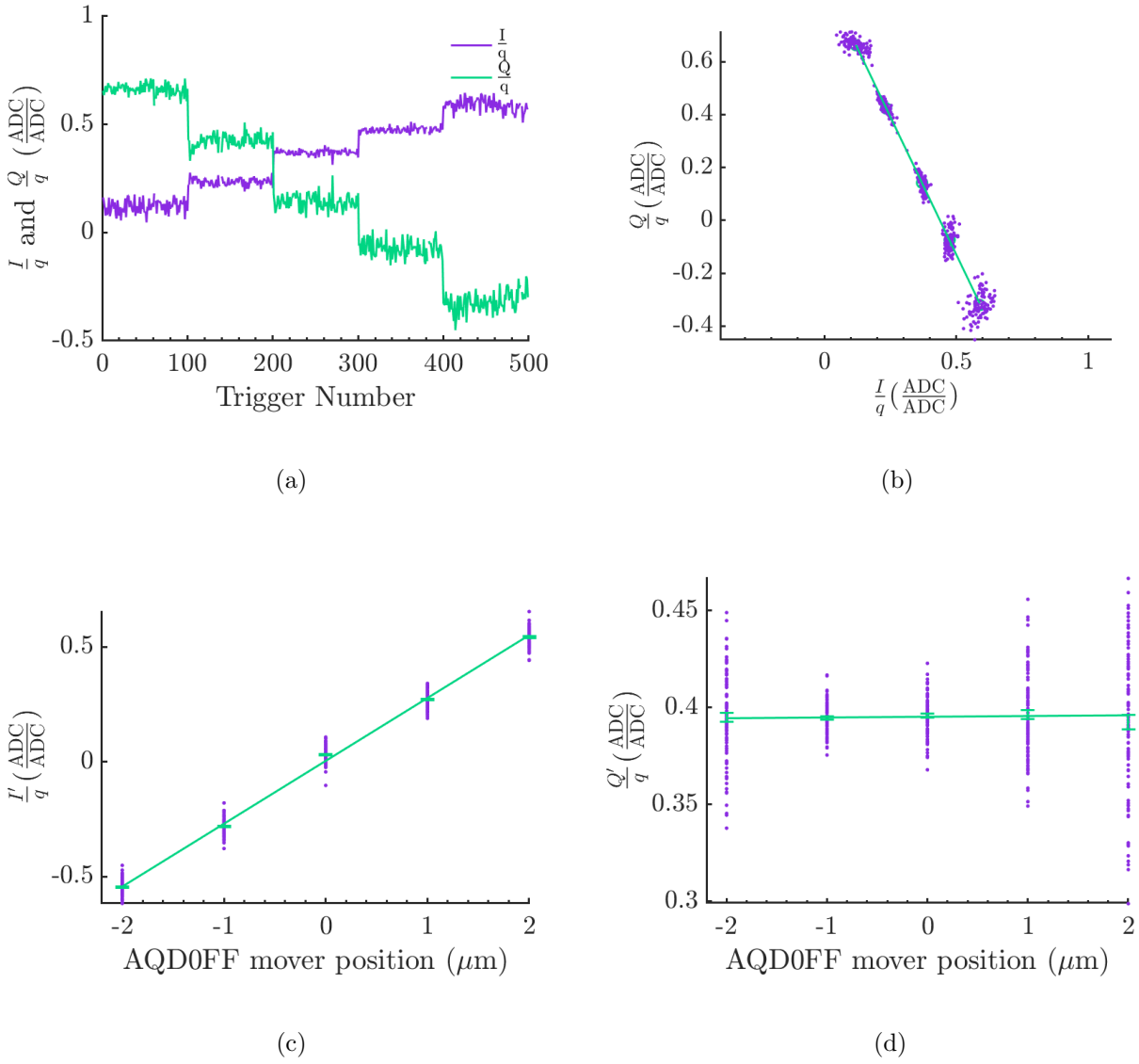

Figure 2.8: Normalised vertical position calibration of IPA, using an 11-sample integration range: (a) $\frac{I}{q}$ and $\frac{Q}{q}$ versus trigger number; (b) the data points show $\frac{Q}{q}$ versus $\frac{I}{q}$ and the line shows a least-squares fit to determine $\theta_{IQ} = -1.093 \pm 0.006$ radians; (c) the data points show $\frac{I'}{q}$ versus AQD0FF mover position, the error bars show the standard error on the mean values at each AQD0FF setting and the line shows a least-squares fit to determine $k = 0.184 \pm 0.002$ μm^{-1}; (d) the data points show $\frac{Q'}{q}$ versus AQD0FF mover position, the error bars show the standard error on the mean values at each AQD0FF setting and the line shows a least-squares fit.

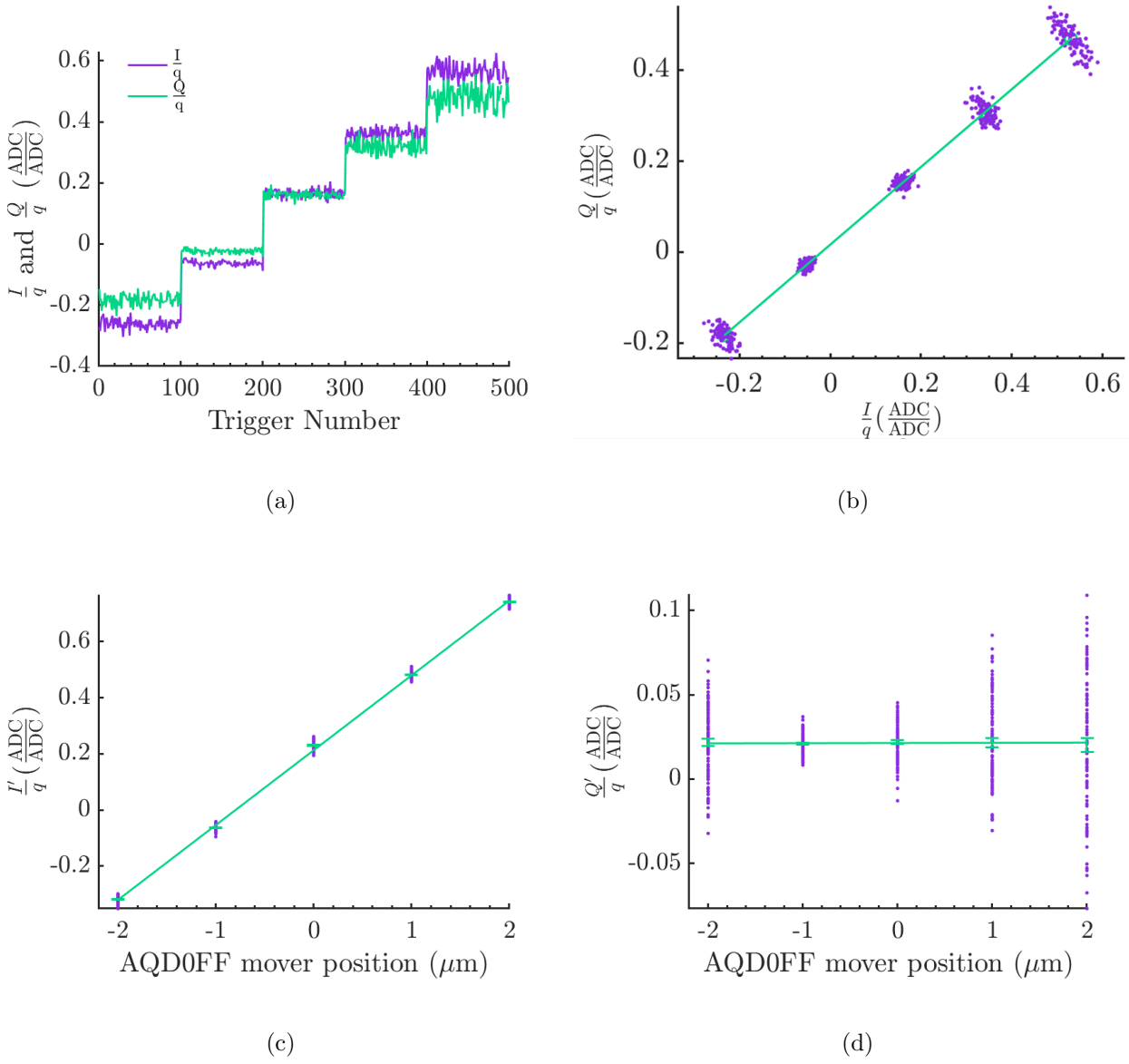

Figure 2.9: Normalised vertical position calibration of IPB, using an 11-sample integration range: (a) $\frac{I}{q}$ and $\frac{Q}{q}$ versus trigger number; (b) the data points show $\frac{Q}{q}$ versus $\frac{I}{q}$ and the line shows a least-squares fit to determine $\theta_{IQ} = 0.707 \pm 0.005$ radians; (c) the data points show $\frac{I'}{q}$ versus AQD0FF mover position, the error bars show the standard error on the mean values at each AQD0FF setting and the line shows a least-squares fit to determine $k = 0.168 \pm 0.002$ μm^{-1}; (d) the data points show $\frac{Q'}{q}$ versus AQD0FF mover position, the error bars show the standard error on the mean values at each AQD0FF setting and the line shows a least-squares fit.

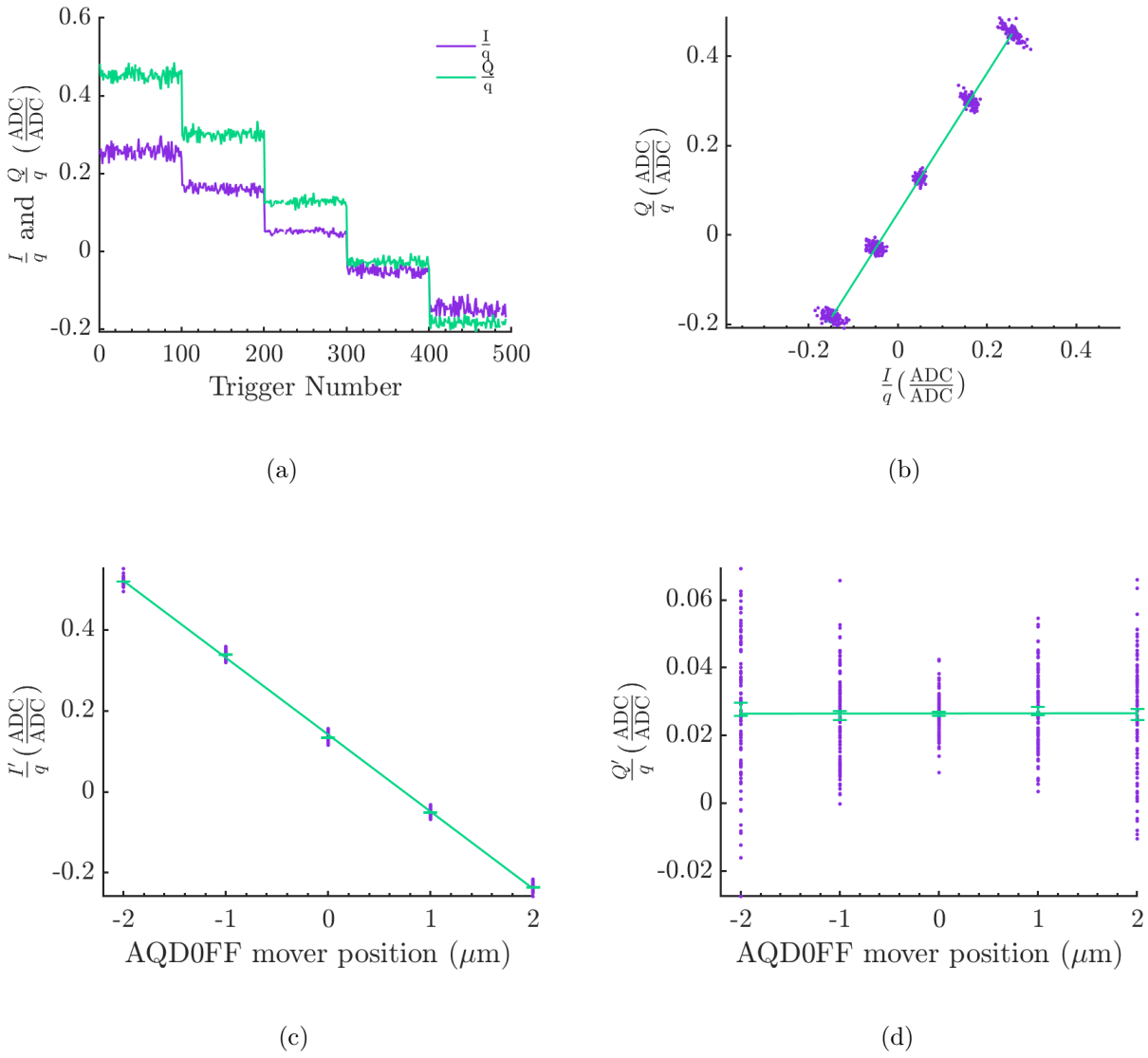

Figure 2.10: Normalised vertical position calibration of IPC, using an 11-sample integration range: (a) $\frac{I}{q}$ and $\frac{Q}{q}$ versus trigger number; (b) the data points show $\frac{Q}{q}$ versus $\frac{I}{q}$ and the line shows a least-squares fit to determine $\theta_{IQ} = 1.003 \pm 0.009$ radians; (c) the data points show $\frac{I'}{q}$ versus AQD0FF mover position, the error bars show the standard error on the mean values at each AQD0FF setting and the line shows a least-squares fit to determine $k = -0.110 \pm 0.001$ µm^{-1}; (d) the data points show $\frac{Q'}{q}$ versus AQD0FF mover position, the error bars show the standard error on the mean values at each AQD0FF setting and the line shows a least-squares fit.

2.3.2 Calibration constant as a function of dipole attenuation

The calibration constant, k, is expected to scale by $\sqrt{\frac{1}{10}}$ with every 10 dB attenuation added to the dipole signal. The dynamic range of the BPMs increases for higher dipole attenuation but at the expense of degrading the resolution. Consequently, for higher attenuations, the range over which the calibration was taken was extended. The calibration constants for the three BPMs versus the dipole attenuation are shown in Fig. 2.11; the corresponding values are listed in Table 2.2. The data were taken at a bunch charge of 0.7×10^{10} electrons, for which operation at 0 dB was not possible without the signal levels exceeding the linear working range of the first-stage processing electronics. The expected linear scaling from 50 dB is compared with the measured results in Fig. 2.11. The system showed good linearity from 50 dB down to 10 dB for all three BPMs.

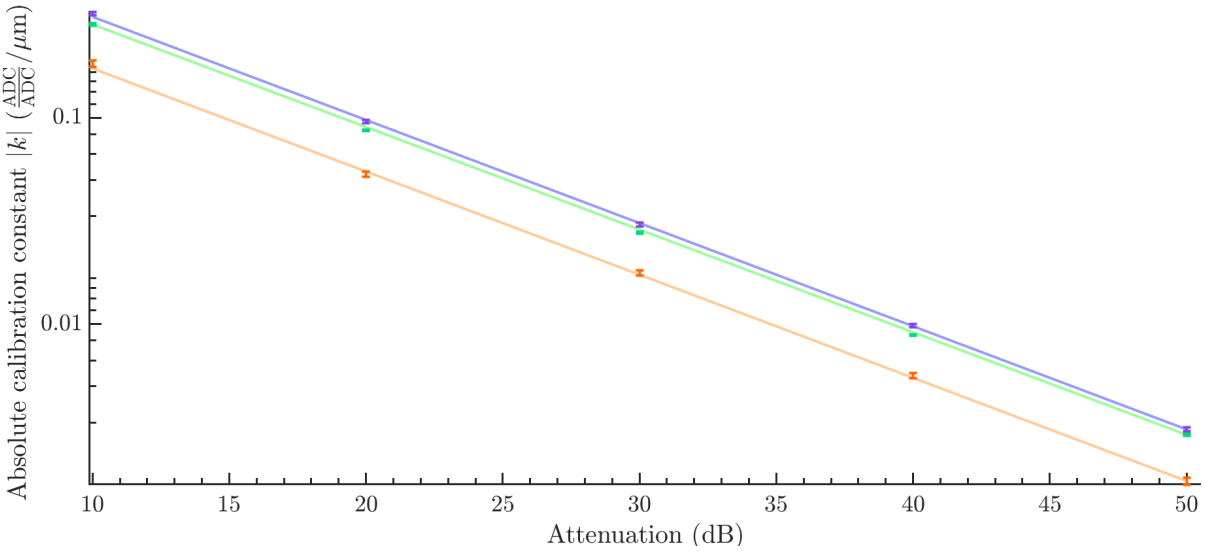

Figure 2.11: Absolute calibration constant $|k|$ versus dipole attenuation, for IPA (purple points), IPB (green points) and IPC (orange points). The expected scalings of the calibration constant with attenuation, calculated from the 50 dB measurement, are shown as coloured lines.

Table 2.2: Absolute calibration constant $|k|$ versus dipole attenuation.

Attenuation (dB)	Absolute calibration constant |k| ($\frac{\text{ADC}}{\text{ADC}}$/μm)		
	IPA	IPB	IPC
10	0.192 ± 0.004	0.170 ± 0.002	0.110 ± 0.004
20	0.0574 ± 0.001	0.052 ± 0.0004	0.032 ± 0.001
30	0.0182 ± 0.0004	0.0166 ± 0.0002	0.0106 ± 0.0003
40	0.00614 ± 0.0002	0.00550 ± 0.00004	0.00338 ± 0.0001
50	0.00185 ± 0.00005	0.00174 ± 0.00002	0.00104 ± 0.00004

2.3.3 Cavity output signal magnitude

The performance of the processing electronics depends on the magnitude of the input signal levels and so it is useful to derive a quantity representing this. The term $\sqrt{I^2+Q^2}$ can be used to represent the total signal level generated from both position and angle offsets. This parameter is independent of the phase θ_{IQ} and, consequently, provides a useful way of comparing results. The $\sqrt{I^2+Q^2}$ waveforms can also be used to estimate which samples have a good signal-to-noise ratio. The signal levels should vary linearly with bunch offset. It can be instructive to study $\sqrt{I^2+Q^2}$ for a range of offsets to verify this. As an illustration, the mean $\sqrt{I^2+Q^2}$ IPC waveforms have been plotted for a range of offsets from $-2\,\mu$m to

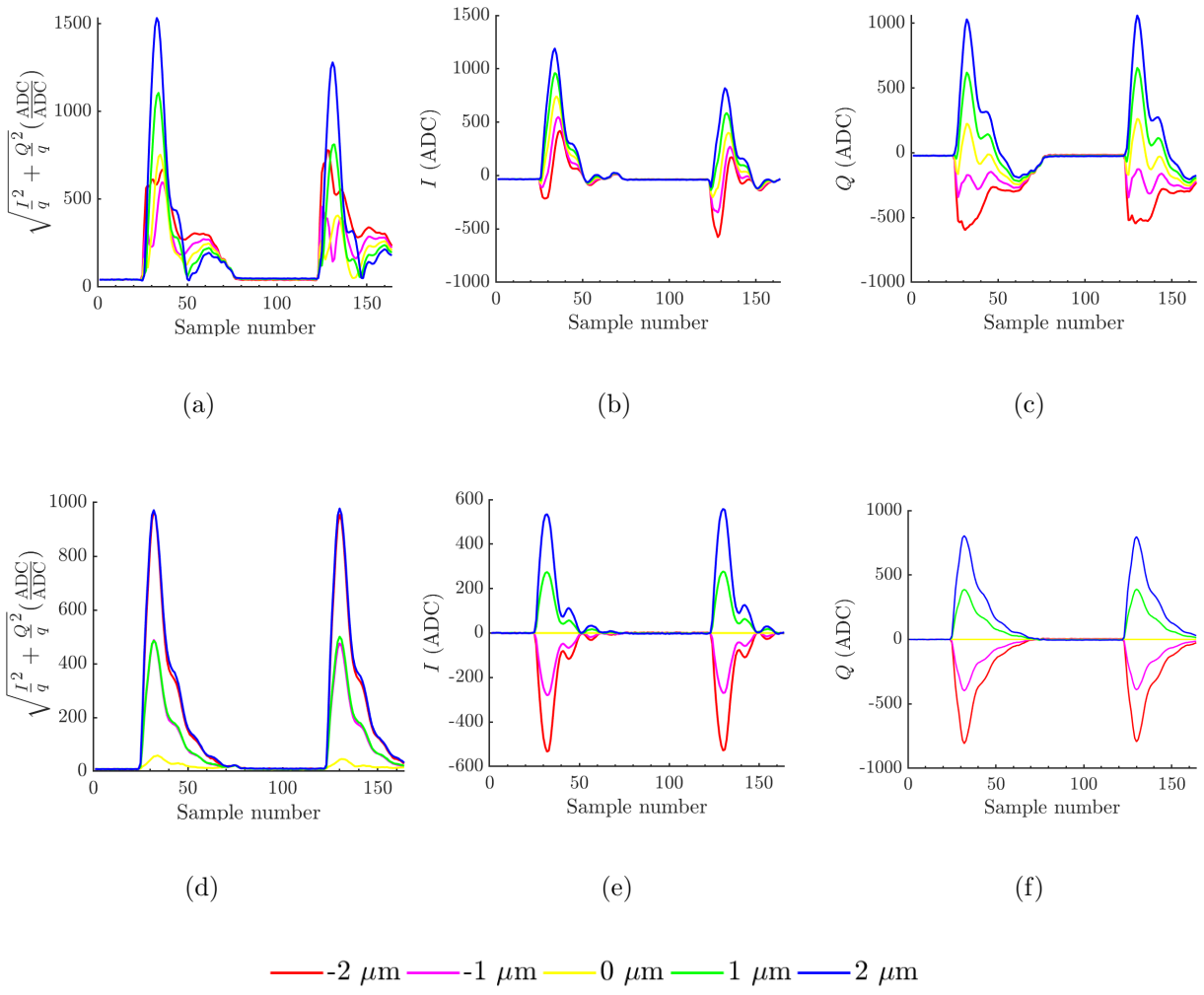

Figure 2.12: Mean IPC waveforms for a range of offsets between $\pm 2\,\mu$m: (a) signal magnitude $\sqrt{I^2+Q^2}$, (b) I signal, (c) Q signal; (d), (e) and (f) show the corresponding plots with the mean respective $0\,\mu$m offset waveform subtracted. The colour of the line denotes the offset. These data were taken with 6.4 GHz BPFs on the dipole signals.

2 µm in Fig. 2.12(a); the corresponding mean I and Q waveforms are shown in Fig. 2.12(b) and (c).

The BPM waveforms are a superposition of position-dependent signals generated by the beam, and position-independent signals. An example of a position-independent signal is the baseline produced when driving the second-stage mixer using the reference signal. To extract only the position-dependent signals, the difference between the waveforms recorded at a range of bunch offsets are considered. This was achieved by subtracting the mean $\sqrt{I^2+Q^2}$ waveform for a 0 µm offset from the other waveforms; the results are shown in Fig. 2.12(d).

As the dipole signal is antisymmetric, the magnitude of the signal should not depend on whether the position offset is positive or negative. Consequently, if the system were behaving linearly, the 1 µm setting should give the same signal magnitude as the −1 µm setting (see Fig. 2.12(d)). Any deviations from this typically indicate that the signal levels into the first-stage processing electronics are high enough to push the system into a non-linear regime.

The shape of the waveform is significantly changed by the addition of filtering on the BPM output signals. For the data presented in this thesis, 6.4 GHz BPFs were used on the dipole signals. Without these filters an unwanted 60 MHz oscillatory component is observed in the waveforms; examples of which are shown in Fig. 2.13(b) and (c). Fig. 2.13 shows the mean BPM waveforms for a range of offsets without the 6.4 GHz BPFs, both with and without the 0 µm offset waveform subtracted. For Fig. 2.13(d), (e) and (f), no 60 MHz component is visible, demonstrating that the signal is independent of position. Previous studies of the 60 MHz component have shown that it scales linearly with the bunch charge and consequently must derive from the beam [60].

2.3.4 Calibration constant as a function of waist position

In order to get a clean calibration, it is important to minimise the beam jitter at the BPM. This can be achieved by placing the beam waist on the BPM being calibrated (see Section 2.2). To get an accurate measurement of the calibration constant, k, the step size for the calibration should be significantly larger than the jitter. The calibration step size is restricted by the dynamic range of the BPM. For 10 dB, the dynamic range is a few microns and a step size of 1 µm is used, requiring the position jitter to be kept well below 1 µm.

When operating with nominal optics, the BPM must be close to the beam waist as the angle jitter leads to a high position jitter off-waist. To locate the beam waist, a scan of jitter versus QD0FF current is used, an example of which is presented in Fig. 2.14. The 123 A

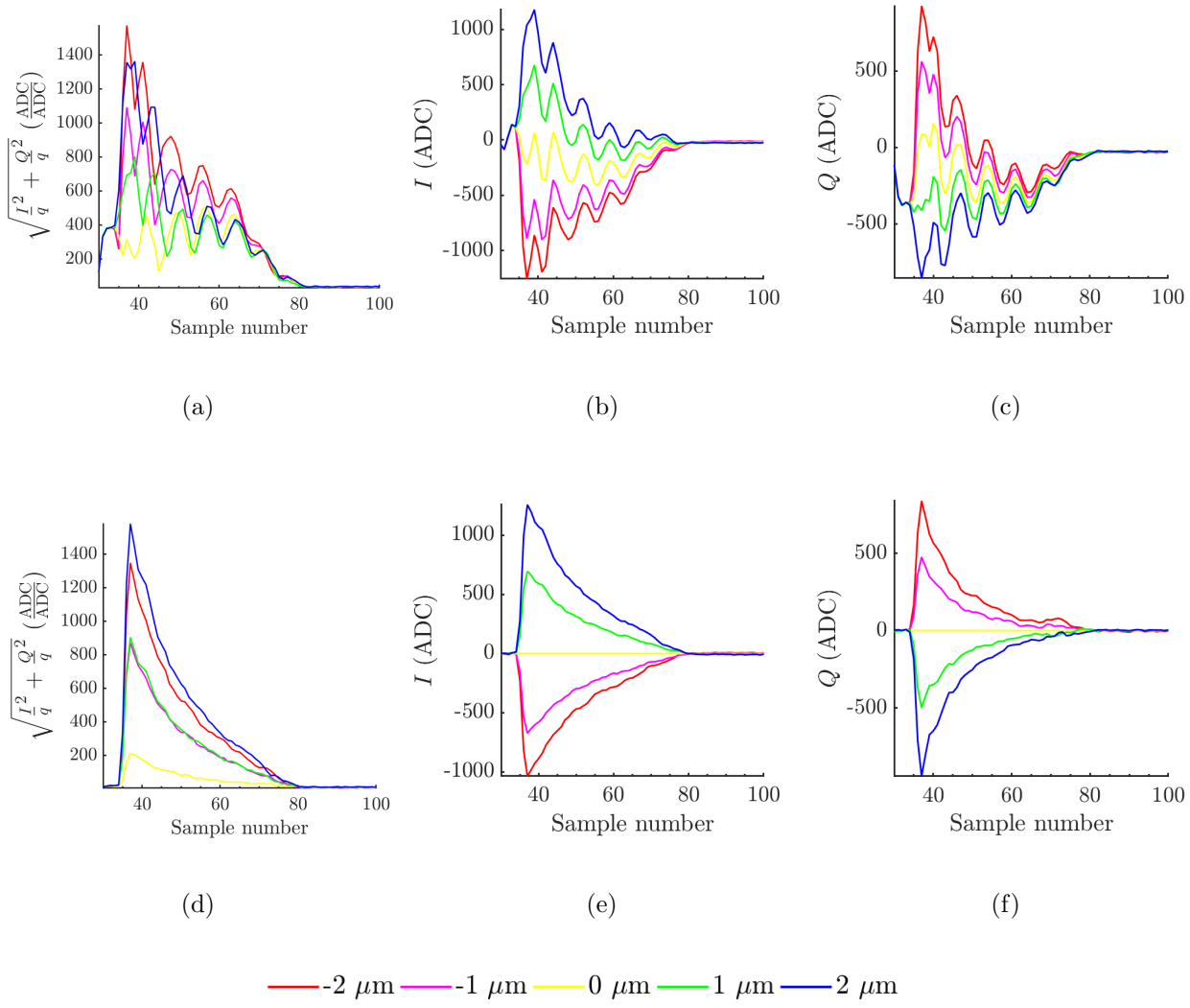

Figure 2.13: Mean IPC waveforms for a range of offsets between ±2 µm: (a) signal magnitude $\sqrt{I^2 + Q^2}$, (b) I signal, (c) Q signal; (d), (e) and (f) show the corresponding plots with the mean respective 0 µm offset waveform subtracted. The colour of the line denotes the offset. These data were taken with no 6.4 GHz BPFs on the dipole signals.

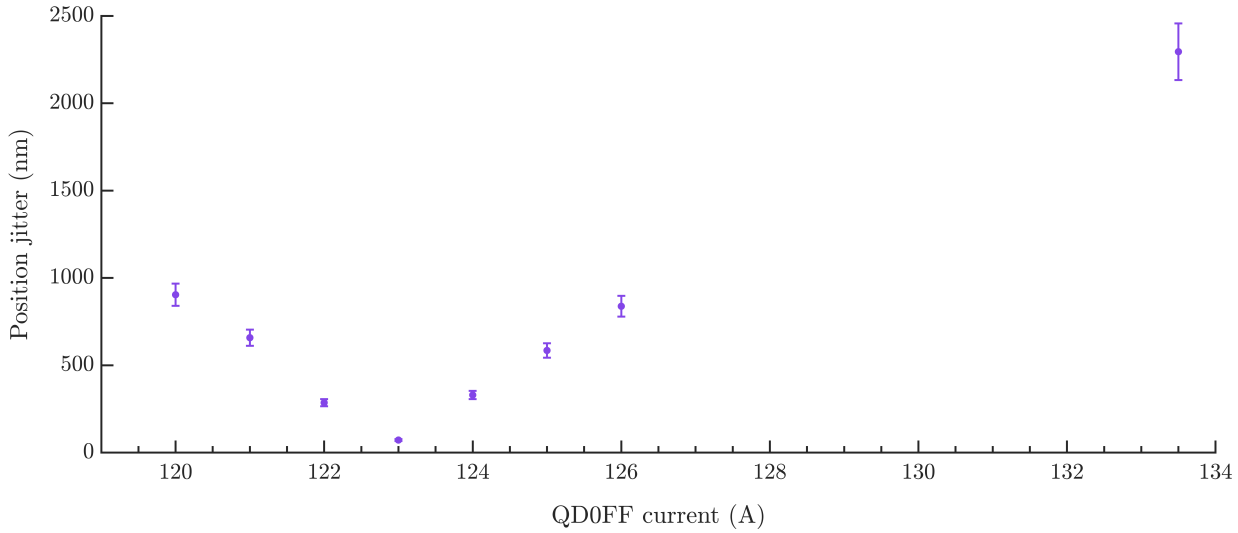

Figure 2.14: IPC position jitter versus QD0FF current setting; standard errors on the jitter are given. A current of 123 A puts the beam waist on IPC and a current of 133.4 A puts the beam waist half way between IPA and IPC, at a distance of 127.5 µm from IPC.

QD0FF setting has the smallest jitter and, consequently, this setting represents the beam waist closest to IPC.

IPC calibration plots of $\frac{I'}{q}$ versus AQD0FF setting are given for a range of QD0FF currents in Fig. 2.15. As the waist gets further from IPC (123 A), the position jitter increases, where for current settings of 120 A and 126 A, the $\frac{I'}{q}$ data points at each successive calibration step exhibit an overlap. As the calibration constant is determined from the mean $\frac{I'}{q}$ values at each mover setting, the high levels of jitter lead to a larger error on the calibration constant.

The calibration constant is not expected to vary with beam-waist location. The IPC calibration constants calculated for the various QD0FF current settings are shown in Fig. 2.16. It can be seen that the measurements are all consistent with the nominal setting (123 A), although the error on the calibration constant grows quickly with offset of the beam waist from IPC.

2.3.5 Angular calibration

The angular offset of the bunch from the BPM's electrical axis (shown in Fig. 2.4 as y') will generate a dipole signal 90° out of phase from the position signal [55]. The position and angle signals are decoupled during the calibration process; however, any error in the measurement of the phase angle, θ_{IQ}, would lead to the angle signal corrupting the position measurement. Ideally, the BPMs would be significantly more sensitive to position than angle, to reduce

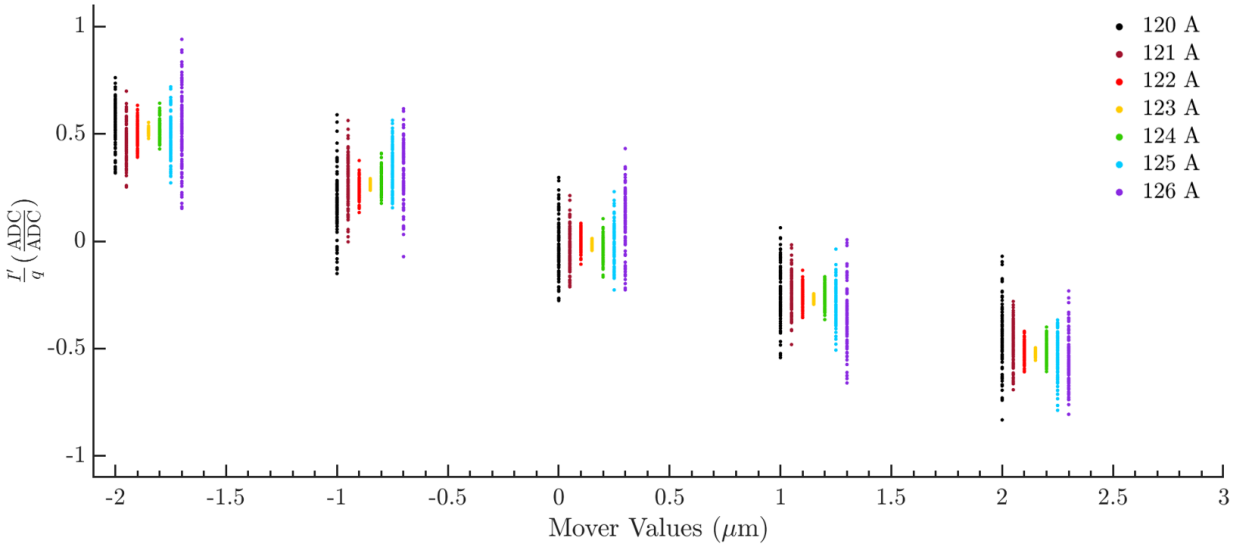

Figure 2.15: $\frac{I'}{q}$ versus AQD0FF mover setting for an IPC calibration. The QD0FF current for which the calibration was performed is denoted by the colour of the data point. For clarity, each tilt setting has been plotted with a small arbitrary offset in the x direction.

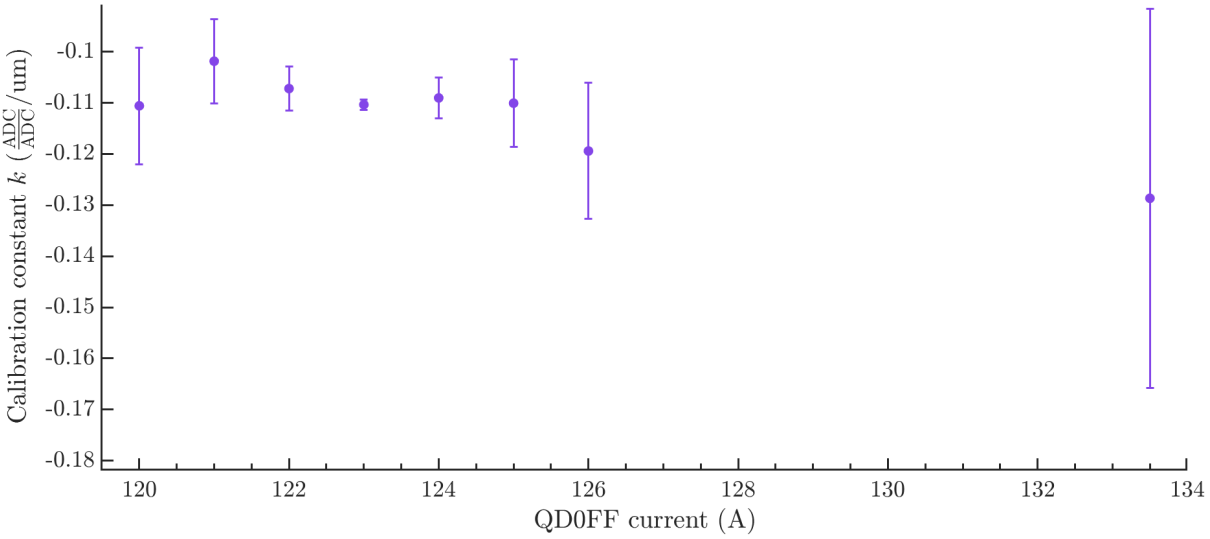

Figure 2.16: IPC calibration constant k versus QD0FF current. The error bars show the statistical error on k.

the impact of errors in the phase measurement. The comparative sensitivity of the BPM to position and angle offsets was estimated by comparing position and angle calibrations.

Angular calibrations were performed by tilting each BPM using the submovers (Fig. 1.13), while keeping the vertical offset of the BPM electrical centre stationary. The submovers allow for an angular range of ±1 mrad and ±2 mrad for the IPAB and IPC mover blocks, respectively [49]. The $\frac{Q'}{q}$ signal amplitude was measured at a range of angular offsets and a calibration constant extracted in a similar manner to the position calibration (Section 2.3.1); the results are presented in Fig. 2.17 and listed in Table 2.3.

As was the case for the position calibration, IPC has a lower calibration constant than IPA and IPB, with the calibration constants for IPA and IPB being similar. With a position-to-angle sensitivity of $\sim 0.003\ \frac{\mu\text{m}}{\mu\text{rad}}$ and typical angle jitter measurements of tens of microradians, it was concluded that for a well-aligned BPM the bunch position measurements are not overly corrupted by angular information.

2.4 Jitter on the local phase angle

2.4.1 Theory of phase jitter

During the down-mixing process, the limiting amplifier (limiter) introduces a phase delay on the reference signal. This delay has been observed to vary from trigger-to-trigger, thus introducing jitter on the local phase angle θ_{IQ} [68]. The jitter on θ_{IQ} can be seen in a calibration plot of $\frac{Q}{q}$ versus $\frac{I}{q}$ as a rotational smearing of the data, as exhibited in Fig. 2.18(a).

Phase jitter is distinct from jitter on the angle y' (Fig. 2.4) which manifests itself as a spread in the data along the $\frac{Q'}{q}$ axis (Fig. 2.18(b)). By measuring the distributions of θ_{IQ} at each of the calibration settings, it is possible to distinguish angular jitter from phase jitter. For angular jitter, the standard deviation of θ_{IQ} would be larger at calibration settings closer to the centre of rotation, whereas, for phase jitter it would be independent of calibration setting.

Position calibrations were taken at a range of y' offsets, examples of which are shown in Fig. 2.19. A distinct rotational smearing of the data points can be seen about a central location, showing the effect of phase jitter. The centre of rotation is demonstrably non-zero, and depends on the position-independent components of the I and Q signal; these are discussed further in Chapter 3.

Following from Eq. 2.13, we can separate out θ_{IQ} into the constant phase delay (θ^0_{IQ}) and

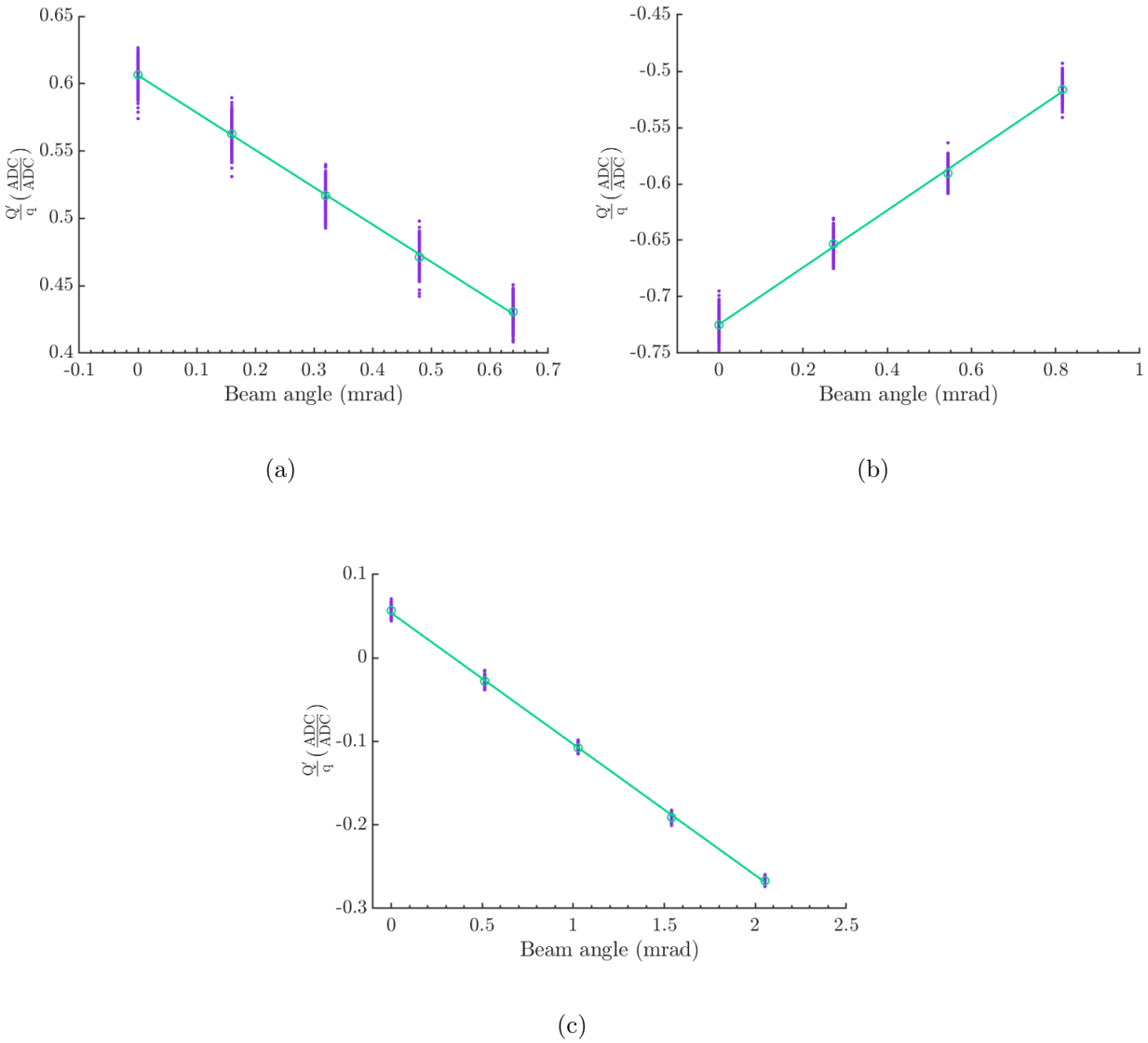

Figure 2.17: Angular calibrations of (a) IPA, (b) IPB and (c) IPC: the data points show $\frac{Q'}{q}$ versus tilt of the BPM, the circles show the mean values for each calibration setting, and the lines show the least-squares fit to the mean values.

Table 2.3: BPM angular calibration constants and position-to-angle sensitivities.

BPM	Abs. calibration const. (μrad^{-1})	Position-to-angle sensitivity ($\frac{\mu\text{m}}{\mu\text{rad}}$)
IPA	0.277	0.0034
IPB	0.253	0.0032
IPC	0.157	0.0028

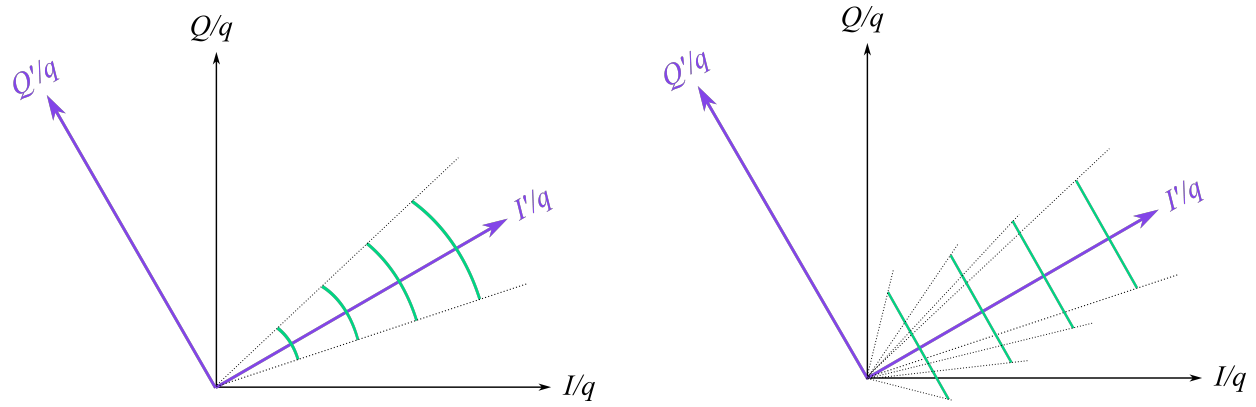

(a) (b)

Figure 2.18: Schematics of the distribution of data points at different calibration settings (green) plotted as $\frac{Q}{q}$ versus $\frac{I}{q}$, with (a) phase (θ_{IQ}) jitter and (b) angular (y') jitter. The $\frac{Q'}{q}$ and $\frac{I'}{q}$ axes are given in purple, and the phase distribution of points at each calibration setting is given as a dotted line.

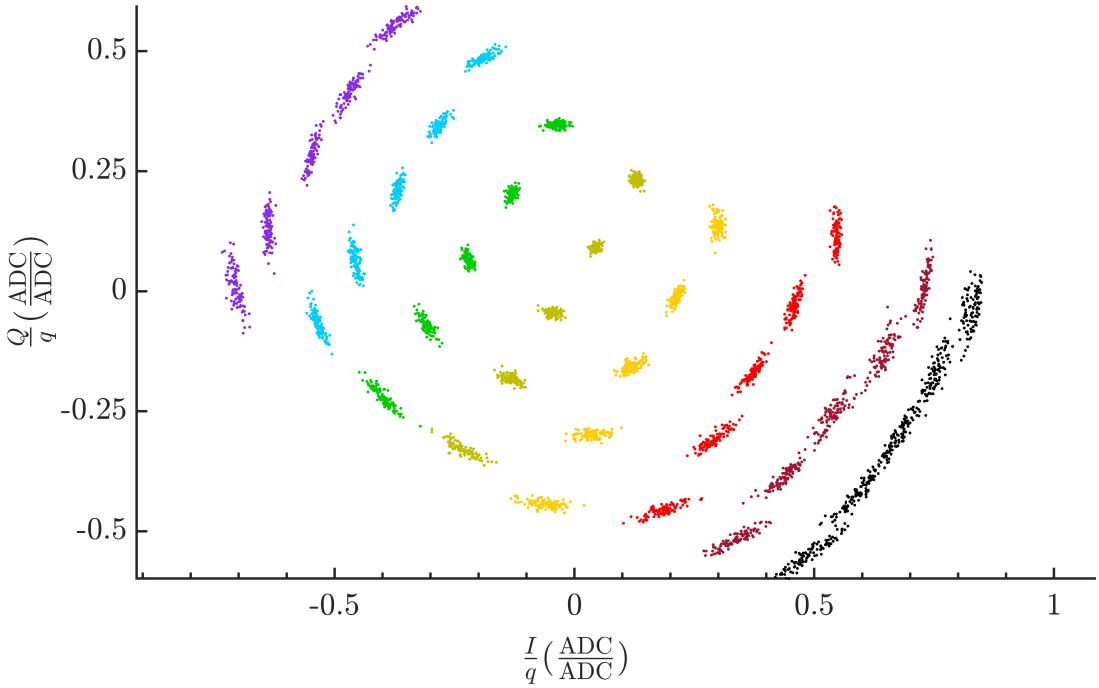

Figure 2.19: IPC calibration plots of $\frac{Q}{q}$ versus $\frac{I}{q}$ for a range of BPM tilt settings, from -2.5 mrad (black) to 1.5 mrad (purple). The colour of the data points denote triggers at a given BPM tilt setting.

the component which varies trigger-to-trigger ($\delta_{\theta_{IQ}}$),

$$y \propto \frac{I}{q}\cos(\theta^0_{IQ} + \delta_{\theta_{IQ}}) + \frac{Q}{q}\sin(\theta^0_{IQ} + \delta_{\theta_{IQ}}). \tag{2.16}$$

Utilising trigonometric expansions for $\cos(A+B)$ and $\sin(A+B)$, and small-angle approximations, $\cos\delta\theta \sim 1$ and $\sin\delta\theta \sim \delta\theta$, an approximation for y can be made:

$$\begin{aligned} y &\propto \frac{I'}{q}\cos(\delta_{\theta_{IQ}}) + \frac{Q'}{q}\sin(\delta_{\theta_{IQ}}), \\ &\propto \frac{I'}{q} + \frac{Q'}{q}\delta_{\theta_{IQ}}. \end{aligned} \tag{2.17}$$

Bench tests of the limiter have shown a dependence of the limiter phase delay on the input signal amplitude [68], in this case the reference signal. As the input signal level depends on the bunch charge and the reference-signal attenuation, the limiter phase jitter has previously been studied as a function of these parameters [60].

The phase jitter introduced by the limiter reduces the accuracy of the BPM calibrations, particularly for configurations where there is a larger angular offset between the BPM and the beam. This effect can be seen in Fig. 2.20, where for the settings with a larger IPC tilt, the $\frac{I'}{q}$ jitter is larger. The nominal calibration constant, calculated at a BPM tilt of ~ 0 mrad, was $-0.107 \pm 0.001\,\mu\text{m}^{-1}$ which can be compared with the calibration constants calculated for the extreme tilt settings, -2.4 mrad and 1.8 mrad, of $-0.098 \pm 0.006\,\mu\text{m}^{-1}$ and $-0.104 \pm 0.005\,\mu\text{m}^{-1}$ respectively. Therefore, for a -2.4 mrad tilt, the calibration constant was inconsistent with the nominal calibration constant.

2.4.2 Experimental setup to measure phase delay

The limiter (see Fig. 2.5) introduces a phase delay to the reference signal which can couple angular information into the position measurement (Eq. 2.17). To determine the effect this would have on a position measurement, the phase delay was measured trigger-by-trigger. A simplified block diagram of the setup used to measure the phase delay is depicted in Fig. 2.21.

The reference signal was split, with one copy of the signal passing through the limiter and one which does not. These two versions of the reference signal are then mixed using a spare second-stage processing module to extract $I_{\text{lim.}}$ and $Q_{\text{lim.}}$ signals

$$I_{\text{lim.}} \propto q\cos(\Delta\phi + \delta_{\theta_{IQ}}), \tag{2.18}$$

$$Q_{\text{lim.}} \propto q\sin(\Delta\phi + \delta_{\theta_{IQ}}), \tag{2.19}$$

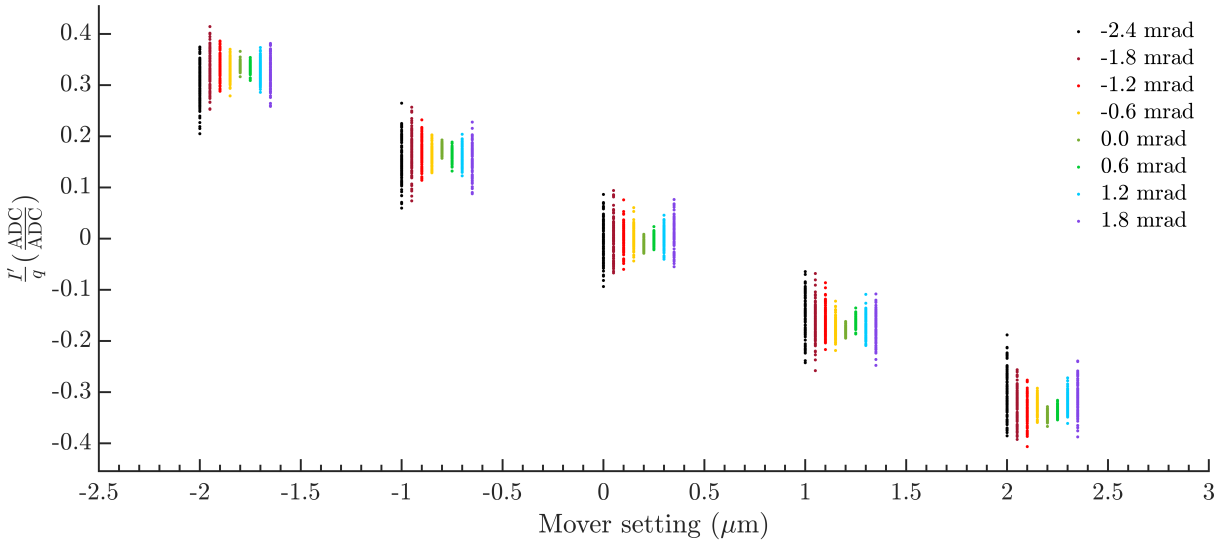

Figure 2.20: $\frac{I'}{q}$ versus AQD0FF mover setting; where the colour of the data points denote the IPC tilt at which the data were taken. For clarity, each tilt setting has been plotted with a small arbitrary offset in the x direction.

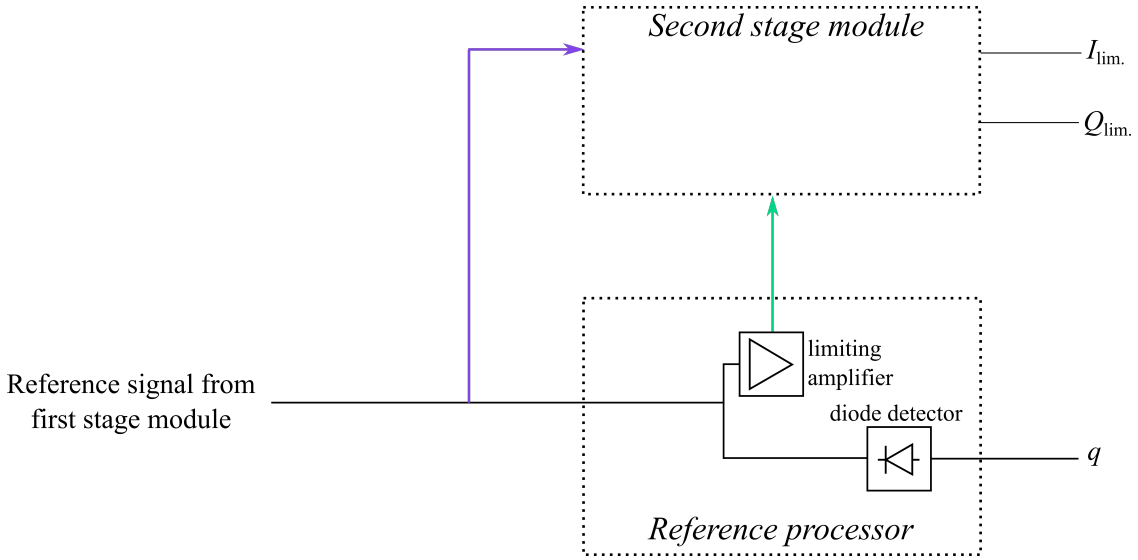

Figure 2.21: Block diagram of the setup used to measure the phase delay introduced by the limiting amplifier between the limited (green) and non-limited (purple) reference signals, using a second-stage processing module.

where $\Delta\phi$ is the mean phase delay between the two versions of the reference signal (shown in purple and green in Fig. 2.21), and $\delta_{\theta_{IQ}}$ is the variation in the phase delay trigger-by-trigger. By dividing Eq. 2.18 by Eq. 2.19

$$\frac{Q_{\text{lim.}}}{I_{\text{lim.}}} = \tan\left(\Delta\phi + \delta_{\theta_{IQ}}\right). \tag{2.20}$$

Therefore, by plotting the data on axes $Q_{\text{lim.}}$ versus $I_{\text{lim.}}$, it is possible to determine $\Delta_\phi + \delta_{\theta_{IQ}}$ for each trigger from the inverse tangent of the gradient of a line passing through the data point and the origin. The limiter phase jitter is defined as the standard deviation of $\Delta_\phi + \delta_{\theta_{IQ}}$ over many consecutive triggers.

2.4.3 Limiter phase jitter results

The BPMs were operated with 40 dB attenuation on the reference signal, as it was determined that this provides sufficient signal to drive the second-stage mixer but not so high that $I_{\text{lim.}}$ and $Q_{\text{lim.}}$ are saturated. Example $I_{\text{lim.}}$ and $Q_{\text{lim.}}$ waveforms are shown in Fig. 2.22(a). This study was performed at a charge of 0.6×10^{10} electrons per bunch.

Many consecutive triggers were recorded and the data were plotted as $Q_{\text{lim.}}$ versus $I_{\text{lim.}}$ for a range of sample numbers; this is shown in Fig. 2.22(b). At samples for which the values of $I_{\text{lim.}}$ and $Q_{\text{lim.}}$ are close to zero, the limiter phase jitter cannot be accurately measured. The limiter phase jitter as a function of sample number is shown in Fig. 2.22(c), from which it can be seen that the phase jitter is approximately constant at 0.037 radians from samples 57 to 65 but increases later in the waveform as the magnitude of the reference signal driving the limiter has decayed.

The limiter phase jitter was also analysed for integrated sample windows; an example is shown in Fig. 2.22(d) for integration windows starting at sample 59. The limiter phase jitter was observed to decrease when integrating up to sample 80, at which point the $I_{\text{lim.}}$ waveform crosses zero and the measurement of θ_{IQ} becomes inaccurate. The decrease of the phase jitter from 0.037 to 0.028 radians with sample integration suggests that some of the phase jitter is uncorrelated sample-to-sample. However, as integration over twenty samples has reduced the phase jitter by less than one quarter, it can be concluded that most of the phase jitter is correlated sample-to-sample.

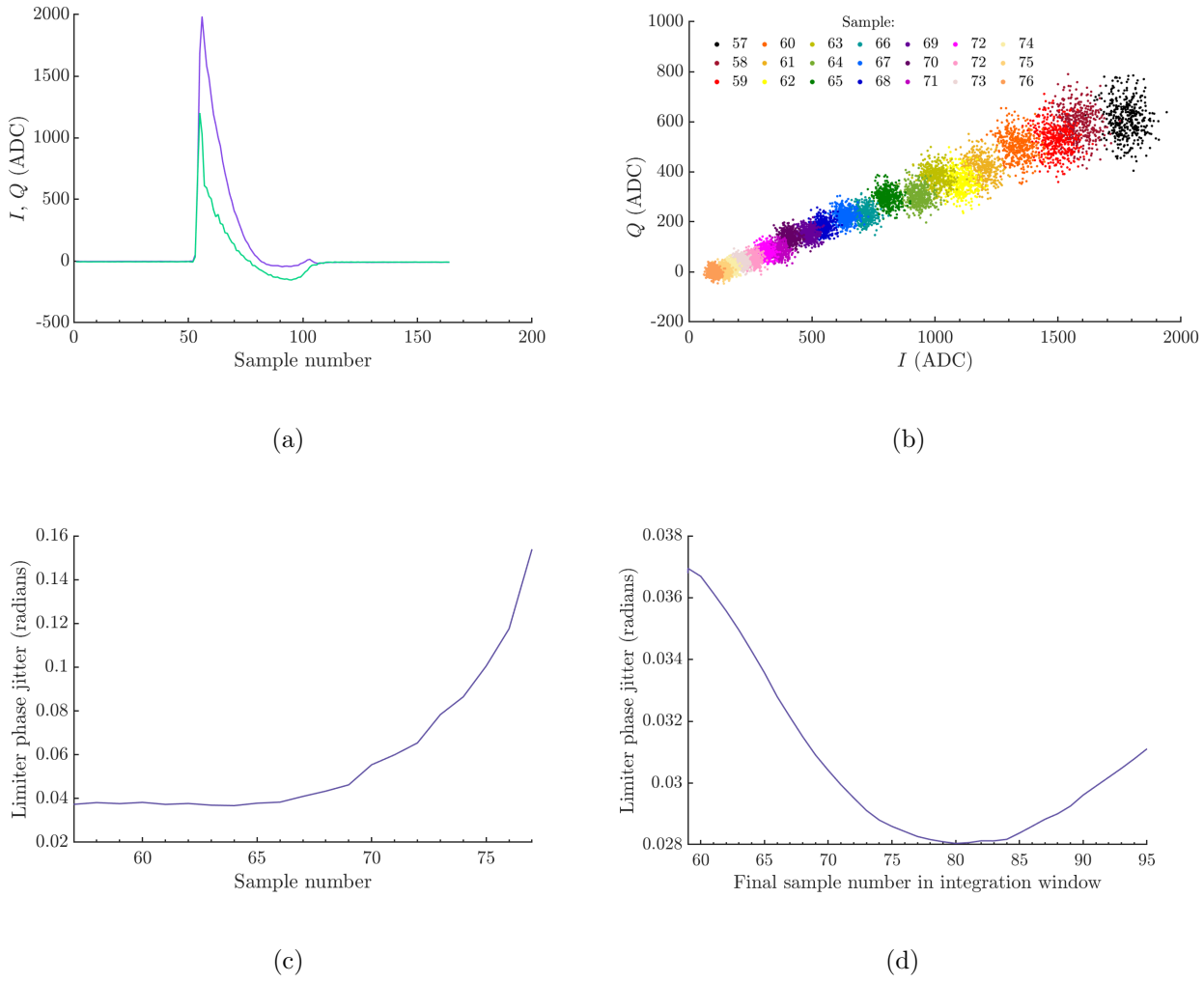

Figure 2.22: (a) Example $I_{\text{lim.}}$ (purple) and $Q_{\text{lim.}}$ (green) waveforms; (b) $Q_{\text{lim.}}$ versus $I_{\text{lim.}}$, with each colour representing the values for a single sample; (c) limiter phase jitter as a function of sample number; (d) limiter phase jitter as a function of sample integration window, starting from sample 59.

2.5 Summary

This chapter has introduced the cavity BPM system at the ATF2 and the process for extracting a position measurement from the high-frequency BPM signals. The properties of the eigenmodes of the reference and dipole cavities were discussed, as was the extraction and spatial filtering of these signals. The use of the FONT5A board to digitise the waveforms and extract a bunch position measurement was described. Also detailed were the requirements for configuring the ATF2 for BPM operation, including the alignment of the beam within the dynamic ranges of all active BPMs simultaneously.

The method for position calibration was presented and examples of calibrations were given. By performing calibrations over a range of longitudinal beam-waist locations, it was shown that, with a nominal optics configuration, it is important to place the BPM to be calibrated close to the beam waist. The system linearity was tested by calculating how the calibration constant scaled with the dipole attenuation. The results showed good agreement with the theory and the calibration constant was shown to scale as expected from 50 dB to 10 dB, for all three BPMs.

Angular calibrations were also performed, from which the position-to-angle sensitivities of the BPMs were measured to be $\sim 0.003\ \frac{\mu m}{\mu rad}$. For both the position and angle calibrations, IPC was shown to have a lower sensitivity to offsets and a smaller calibration constant.

The magnitude of the phase jitter introduced by the limiting amplifier was studied, along with its effect on the accuracy of the calibrations. As discussed in Section 2.4.1, the angular offset of the beam with respect to the cavity's electrical axis should be minimised so as not to couple angular information into the position measurement. The impact of the phase jitter was studied by performing calibrations at a range of BPM tilts and it was shown that the error on the calibration constant increases with larger angular offsets as a result of the phase jitter. Finally, a direct measurement of the magnitude of the limiter phase jitter was made, as a function of both sample number and sample integration window. The single-sample limiter phase jitter was measured to be 0.037 radians which was reduced to 0.028 radians with the use of a twenty-sample integration window.

Chapter 3

IP BPM resolution

For the ATF2 IP feedback system, cavity BPM measurements form the input to the beam-position feedback loop and, consequently, it is crucial to improve the resolution of these measurements to get the best beam-stabilisation performance.

The resolution of the BPM system can be estimated by making measurements of the bunch trajectory with all three BPMs. The bunch follows a straight-line trajectory, so that only two BPMs are required to characterise the bunch path; the third BPM can then be used to estimate the resolution of the measurement. In order to do this, the bunch position at one BPM is predicted using the measured bunch positions at the other two BPMs, together with a knowledge of the beam transport. The difference between the measured and predicted positions is calculated, and the process is repeated for many triggers, forming a distribution. The standard deviation of this Gaussian distribution is the resolution.

Two methods of calculating the resolution are presented in this chapter, called the 'geometric' and 'fitted' resolutions. The geometric method uses the known longitudinal separations of the BPMs, together with the straight-line trajectory of the bunch, to make the bunch-position prediction. The fitting method uses instead a linear fit to the measured positions at one BPM as a function of the positions at the other two. The fitting method may separately be applied to each of the three BPMs, giving three correlated estimates of the resolution.

In this chapter, for the fitting method, the dependence of the resolution on various parameters is considered. Studies of the dependence of the resolution on the alignment of the BPM, in both position and angle, are presented. The variation in resolution with different waveform-sampling methods is studied and the importance of sample integration is discussed. The degradation of the resolution as a result of the limiter phase jitter is analysed

and techniques for the mitigation of this effect are given. Finally, studies of the resolution as a function of dipole attenuation and charge are presented, in order to estimate the system linearity.

3.1 BPM resolution calculation

Due to the lack of intermediate magnetic components, the beam is expected to follow a straight-line trajectory through the three BPMs. Consequently, the beam position, y_i, at BPM i, can be represented as a linear combination of the positions of the beam at the other two BPMs, y_j and y_k,

$$y_i = A_{ij}y_j + A_{ik}y_k, \tag{3.1}$$

where A_{ij} and A_{ik} are coefficients, so that the prediction for the beam position, $y_i^{\text{pred.}}$, at BPM i can be written in terms of the measured positions $y_i^{\text{meas.}}$, as

$$y_i^{\text{pred.}} = A_{ij}y_j^{\text{meas.}} + A_{ik}y_k^{\text{meas.}}. \tag{3.2}$$

The difference between the geometric and fitted resolution methods is in how the coefficients A_{ij} and A_{ik} are determined.

Measurement errors will always be present and alongside the true beam position, y^{true}, a measured position will have an associated error, ϵ_i, where

$$\epsilon_i = y_i^{\text{meas.}} - y_i^{\text{true}}. \tag{3.3}$$

The distributions of these errors are assumed Gaussian with a standard deviation defined to be the BPM resolution, σ_i [53].

The residual, R, is defined as the difference between $y^{\text{meas.}}$ and $y^{\text{pred.}}$,

$$R_i = y_i^{\text{meas.}} - y_i^{\text{pred.}}; \tag{3.4}$$

hence

$$R_i = y_i^{\text{meas.}} - A_{ij}y_j^{\text{meas.}} + A_{ik}y_k^{\text{meas.}}, \tag{3.5}$$

and

$$R_i = \epsilon_i - A_{ij}\epsilon_j - A_{ik}\epsilon_k. \tag{3.6}$$

The errors ϵ_i, ϵ_j and ϵ_k are assumed to be uncorrelated random variables and therefore

$$(\text{std}(R_i))^2 = \sigma_i^2 + A_{ij}^2\sigma_j^2 + A_{ik}^2\sigma_k^2. \tag{3.7}$$

To calculate the resolutions of the BPMs, it is assumed that all three BPMs have the same resolution: $\sigma = \sigma_i = \sigma_j = \sigma_k$. With this condition, Eq. 3.7 can be rearranged to give the resolution

$$\sigma = \frac{\mathrm{std}(R_i)}{\sqrt{1 + A_{ij}^2 + A_{ik}^2}}. \tag{3.8}$$

The denominator, $\sqrt{1 + A_{ij}^2 + A_{ik}^2}$, is referred to as the 'geometric factor', which takes into account how the separations between the BPMs determine the precision of $y^{\mathrm{pred.}}$ at each of the BPMs. This factor is used for both the geometric and fitting methods.

In order to measure the resolution, typically hundreds of triggers were recorded. A small number of these triggers might be outliers, which are considered not representative of the beam in general. Several cuts were performed to remove the outliers; these are listed in Table 3.1. For example, triggers are discarded if any of the bunches in a train do not meet a charge threshold value, as this may indicate a missing bunch. Triggers are also cut if they exceed the FONT5A board ADC digitisation window of ±4095 ADC counts, as this would lead to incorrect charge normalisation. Two consecutive cuts are also performed on the bunch positions and charges, removing those lying more than 3σ away from the mean, where the mean and standard deviation are recalculated after the first cut. Typically, for a given data set less than 5% of the triggers are removed as outliers.

Table 3.1: Data are considered outliers if they fail to meet any of these requirements.

Variable	Requirement
Charge	$500\,\mathrm{ADC\,counts} < \lvert q \rvert < 4095\,\mathrm{ADC\,counts}$
Charge	$\mu + 3\,\sigma < q < \mu + 3\,\sigma$
Position	$\mu - 3\,\sigma < \frac{I'}{q} < \mu + 3\,\sigma$

3.1.1 Geometric method

The bunch positions in the three BPMs are denoted by y_1, y_2 and y_3. Figure 3.1 shows the bunch trajectory through the three BPMs, which have longitudinal locations l_1, l_2 and l_3.

From the linear trajectory of the beam through the three BPMs, the beam positions and the longitudinal centres of the BPMs can be related using the beam angle θ, so that

$$\tan\theta = \frac{y_2 - y_1}{l_2 - l_1} = \frac{y_3 - y_2}{l_3 - l_2} = \frac{y_3 - y_1}{l_3 - l_1}. \tag{3.9}$$

This can be rearranged and written in a more general form as

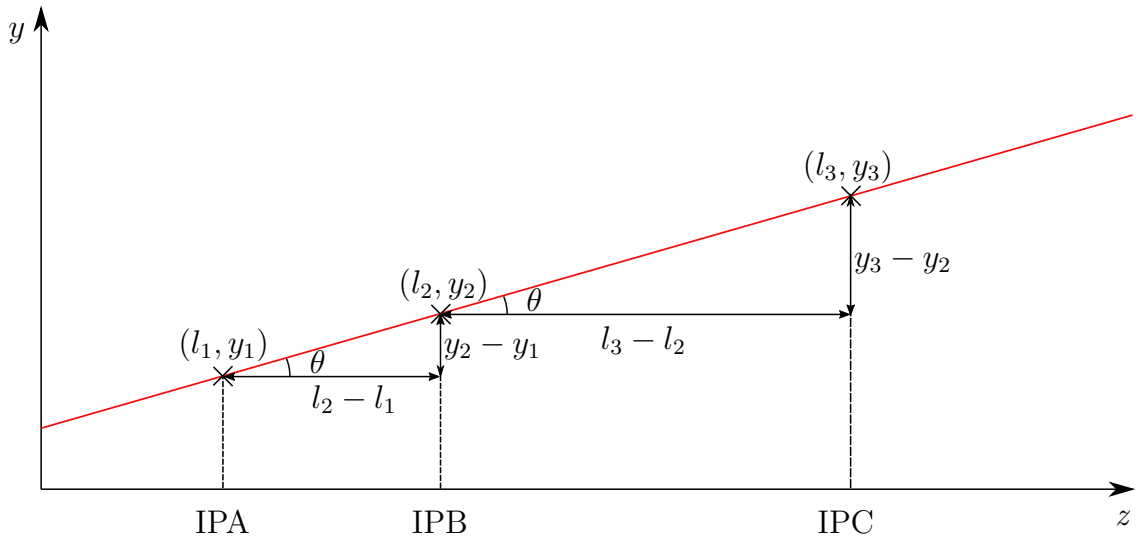

Figure 3.1: The red line shows the bunch trajectory through the three IP BPMs. The bunch positions in the three BPMs are denoted by y_1, y_2 and y_3, the longitudinal locations of the centres of the three BPMs are given by l_1, l_2 and l_3, and the angle of the beam is given by θ.

$$y_i = y_j - \frac{y_k - y_j}{l_k - l_j}(l_j - l_i), \tag{3.10}$$

so that the predicted position, $y_i^{\text{pred.}}$, can be estimated using

$$y_i^{\text{pred.}} = y_j^{\text{meas.}} - \frac{y_k^{\text{meas.}} - y_j^{\text{meas.}}}{l_k - l_j}(l_j - l_i), \tag{3.11}$$

where i, j and k represent the three BPMs in any permutation. The longitudinal separations of the BPM centres are given in Table 3.2.

Table 3.2: Longitudinal separation of the IP BPMs' centres [49].

	Longitudinal distance (mm)
IPA to IPB	80.8 ± 0.1
IPB to IPC	174.2 ± 0.1

The process of bunch-position prediction is repeated for hundreds of consecutive triggers, forming distributions of $y^{\text{meas.}}$ and $y^{\text{pred.}}$ for each BPM. As beam-position measurements are taken with respect to the BPMs' electrical centres, the mean offset at each BPM is arbitrarily determined by the settings of the BPM movers. A Gaussian fit is performed to the distribution of the residuals, R_i, to determine std(R_i). The resolution of the BPM system

can be found using Eq. 3.8. The geometric resolution is independent of the BPM at which the beam-position prediction was made, as the set of simultaneous equations represented by Eq. 3.11 are fully constrained.

3.1.2 Fitting method

A second method of estimating the BPM resolution can be used to corroborate the geometric estimation. To calculate the BPM resolution using the fitting method, a linear least-squares fit to the bunch positions measured for many consecutive triggers is performed for

$$y_i^{\text{meas.}} = A_{ij} y_j^{\text{meas.}} + A_{ik} y_k^{\text{meas.}} + C_i \tag{3.12}$$

in order to estimate the constants A_{ij}, A_{ik} and C_i. Equation 3.12 follows from Eq. 3.2 with the addition of a constant term, C_i, to account for the arbitrary offset to beam-position measurements generated by the BPM movers.

As the coefficients of the terms y_j and y_k are found through fitting, the calibration constants for these BPMs are effectively fitted-out. While the longitudinal separation of the BPMs is unchanging and known to a high degree of accuracy, the calibration constants depend on a range of parameters and consequently, might vary over time. Both of these parameters are grouped together under the terms A_{ij} and A_{ik}. Differences between the geometric and fitted resolution methods can therefore highlight that the BPM calibrations are inaccurate.

Multi-parameter fitting method

It is also possible to include other parameters into the least-squares fit. For example, by including $\frac{Q'}{q}$ terms into the fit, the phase angle θ_{IQ} is absorbed into the fitting coefficient, which can correct for any errors in the phase measurement. It is possible for $\frac{Q'}{q}$ to couple into the position measurement via the phase jitter, $\delta_{\theta IQ}$ (Eq. 2.17); fitting to $\frac{Q'}{q}$ and $\delta_{\theta_{IQ}}$ can highlight this. While, $\frac{Q'}{q}$ terms cannot be included in the feedback calculation due to latency constraints (Section 1.4.3) it is useful to determine whether the resolution is significantly worse as a result of phase jitter. Other parameters may also be included in the fit to determine any unwanted residual position dependence. For example, including the bunch charge might highlight imperfect charge normalisation. With this method, the bunch positions are fitted as

$$y_i = B_1 \frac{I'_j}{q} + B_2 \frac{Q'_j}{q} + B_3 \frac{I'_k}{q} + B_4 \frac{Q'_k}{q} + B_5 q + B_6 \delta_{\theta_{IQ}} + C_i, \tag{3.13}$$

where B_i and C_i are the fitting coefficients.

3.2 Resolution dependence on dipole attenuation

The BPM resolution depends on the signal-to-noise ratio of the digitised BPM waveforms and varies as a function of a number of parameters. Increasing the bunch charge and decreasing the attenuation on the dipole signal increases the signal level, but care must be taken not to exceed the linear operating region of the processing electronics. Similarly, if the BPMs are poorly aligned and the beam is outside the dynamic range, this will degrade the measurement. It was also shown, in Chapter 2, that the limiter phase jitter could introduce an error into the position measurement, which would also affect the resolution.

The bunch positions used in determining the resolution can be calculated using either a single sample of the BPM waveforms or a sample integration window. As sample integration can improve the signal-to-noise ratio, it can improve the BPM resolution.

The resolution is expected to scale with the signal-to-noise ratio of the measurements and, consequently, would depend directly on the input signal level to the processing electronics. This signal level can be varied by adjusting the attenuation on the dipole cavity signal located after the hybrid, shown in Fig. 2.5. If the charge is kept constant, the resolution should scale by a factor of $\frac{1}{\sqrt{10}}$ for every 10 dB added to the dipole attenuation, as the power scales with the square of the signal amplitude [53].

Table. 3.3 shows the geometric resolution measured with dipole attenuations from 10 dB to 50 dB: the results are plotted in Fig. 3.2. The system was recalibrated for each different attenuation setting, with the calibration range extended for higher attenuations to reflect increase in the dynamic range of the BPMs with added attenuation (Fig. 2.11). Operating with 0 dB attenuation was not possible for this data set, which was taken with a bunch charge of $\sim 0.7 \times 10^{10}$ electrons, as the signal levels would have exceeded the linear operating region of the first-stage processing electronics.

Table 3.3: Single-sample and six-sample integrated geometric resolution versus dipole attenuation. The errors represent the statistical uncertainty on the resolution.

Attenuation (dB)	Single-sample resolution (nm)	Integrated-sample resolution (nm)
10	55 ± 3	24 ± 1
20	97 ± 5	54 ± 4
30	285 ± 15	165 ± 8
40	894 ± 44	457 ± 24
50	2890 ± 145	1619 ± 79

The results show a good scaling of the resolution with dipole attenuation from 50 dB to

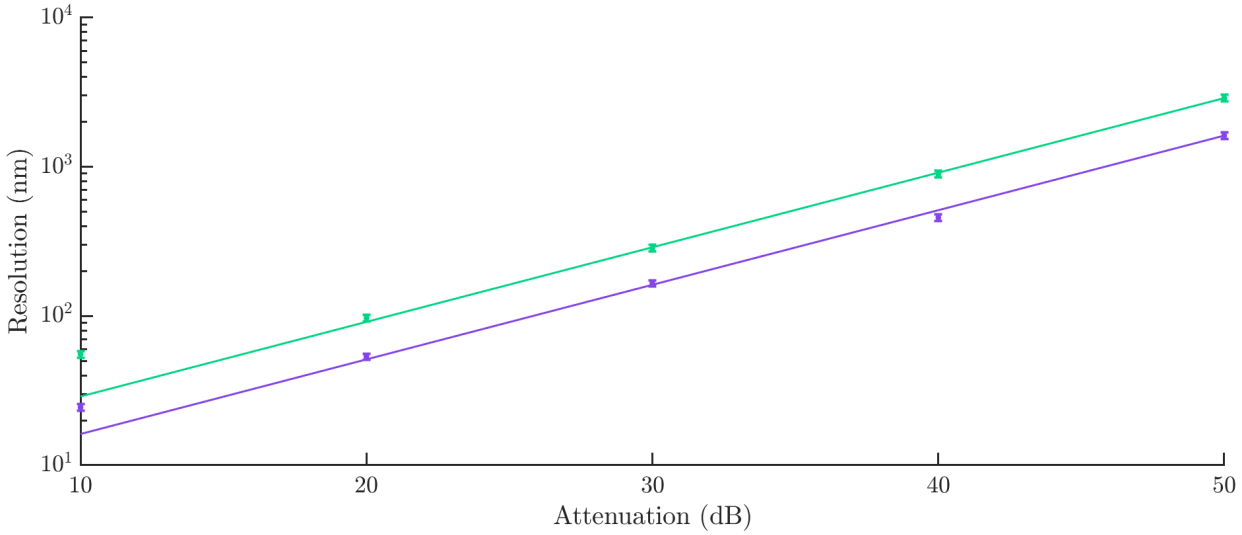

Figure 3.2: Single-sample (green) and integrated-sample (purple) geometric resolution versus dipole attenuation. The data points show the measured resolutions, the lines show the expected scaling from 50 dB and the error bars show the statistical uncertainty on the resolution

20 dB, but a deviation at 10 dB. Both the single-sample and integrated-sample resolutions show a poorer resolution at 10 dB, compared with the values derived from scaling the 50 dB results, which were 29 nm and 16 nm respectively.

Although the resolution does not scale as expected to 10 dB, the calibration constant was shown in Fig. 2.11 to scale well with attenuation, even down to 10 dB. This may mean that at a charge of $\sim 0.7 \times 10^{10}$ electrons per bunch, saturation effects are starting to appear, with the resolution being more sensitive to these effects than the calibration constant. While the resolution is the standard deviation over many consecutive triggers, the calibration constant is calculated using the mean and so may be less sensitive to saturation effects. In an attempt to minimise BPM saturation, operating bunch charges are typically kept below 0.7×10^{10} electrons.

3.3 BPM resolution results

Figure 3.3 shows a measurement of the geometric resolution as a function of the number of samples integrated. The analysis was performed on data taken in June 2017, at a bunch charge of 0.5×10^{10} and with a dipole attenuation of 10 dB, in order to avoid the saturation effects observed in Section 3.2. This data set gives the current best geometric resolution result for the BPM system. The resolution shows an improvement of more than a factor

of two by integrating over an extended sample window when compared with single-sample analysis.

The best single-sample and integrated-sample resolution results for this data set are listed in Table 3.4. Sample integration is shown to improve both the geometric and the fitted resolution. It can also be seen to bring the resolutions estimated by fitting to each of the three BPMs into better agreement. This suggests that the calibrations are more accurate and there is less coupling of $\frac{Q'}{q}$ into the position signal. The single-sample fitted resolution for IPC was systematically higher than for IPA and IPB, suggesting that either the IPC calibration was inaccurate or a larger IPC tilt led to more $\frac{Q'}{q}$ coupling. The fitted resolution of IPC particularly benefitted from sample integration. From Fig. 2.10, IPC was shown to have a lower sensitivity to position than IPA or IPB; this may contribute to some of the differences in the resolution estimates between the BPMs. Eq. 3.12 assumed that the BPMs have the same resolution, whereas this may not be the case if IPC has a lower sensitivity to position.

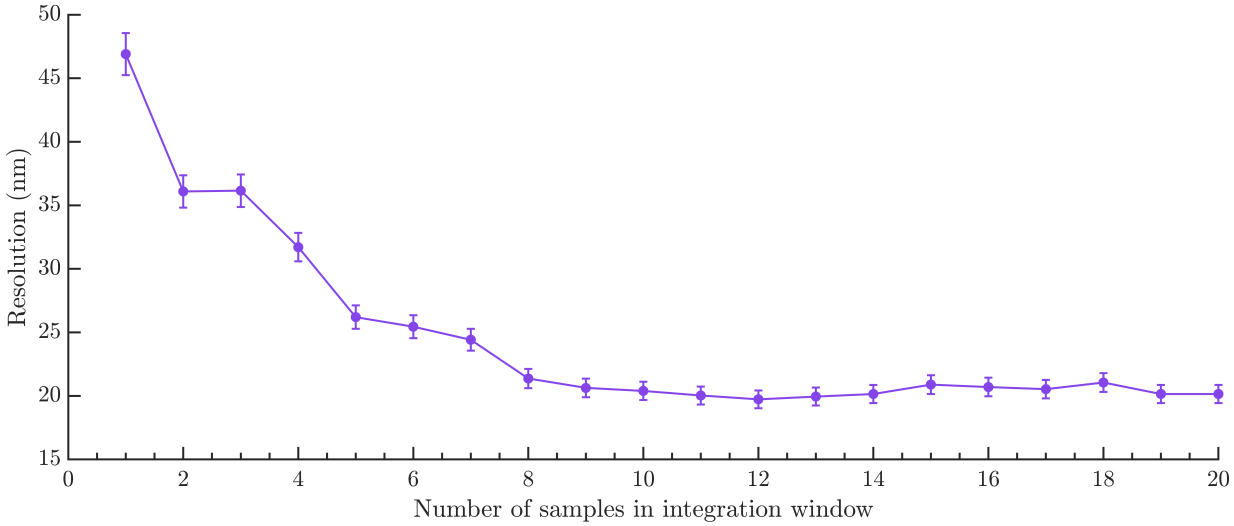

Figure 3.3: Resolution versus number of samples integrated. The data points show the geometric resolution, the lines connect the data points and the error bars show the statistical uncertainty on the resolution. The location of each integration window was chosen so as to optimise the geometric resolution.

3.4 Dependence on sample number

The magnitude of the calibration constant k gives an indication of the signal-to-noise ratio, from which it is possible to estimate which samples are likely to have a good resolution.

Table 3.4: The best single-sample and integrated-sample resolution measurements for the geometric method and resolution with fitting to $\frac{I'}{q}$, $\frac{Q'}{q}$ and q.

Number of samples analysed	Geo. (nm)	IPA fit (nm)	IPB fit (nm)	IPC fit (nm)
1	40.6 ± 1.0	40.6 ± 1.0	40.8 ± 1.0	62.8 ± 1.3
11	19.0 ± 0.4	19.2 ± 0.6	19.4 ± 0.6	17.6 ± 0.4

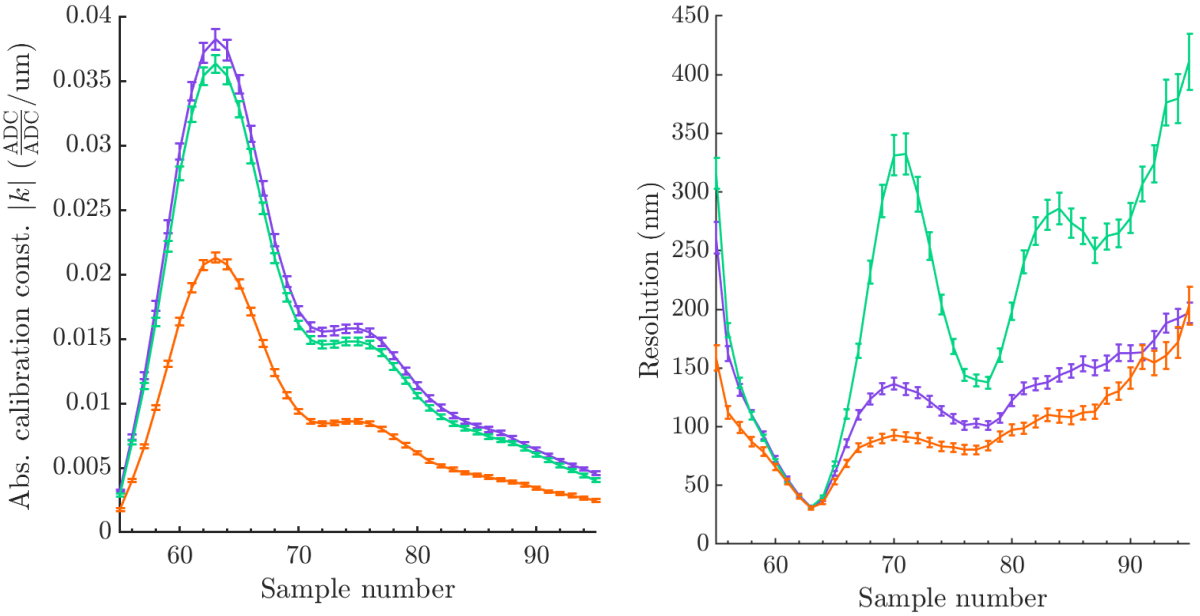

(a) (b)

Figure 3.4: (a) Absolute calibration constant |k| versus sample number and (b) resolution calculated by fitting to bunch positions versus sample number, for IPA (purple), IPB (green) and IPC (orange). The lines join the data points and the error bars show the statistical uncertainty.

The calibration constants as a function of sample number are shown in Fig. 3.4(a) for the three BPMs. Samples are typically chosen which correspond to the peaks of the curves of k. The calibration constants for IPA and IPB are similar, with the calibration constant for IPC being a factor of two smaller. All three BPMs were designed to have the same sensitivity to position offset, and so ideally should have similar calibration constants. However, IPC is consistently measured to have a lower calibration constant, the cause of which is currently unknown.

The fitted resolutions as a function of sample number for the three BPMs are shown in Fig. 3.4(b). The samples from 59 to 64 offer the best fitted resolution for all three BPMs,

with the resolution estimates from the three BPMs in good agreement, which suggests the calibrations were accurate. The resolution for all three BPMs decreases for later sample numbers as the BPM signal decays away, with this effect being most noticeable for IPB. IPB was the BPM closest to the beam waist for this scan and, consequently, has the smallest signal levels.

The sample window (59 to 64) which optimised the resolution corresponds to the peak of Fig. 3.4(a). Consequently, an estimation of the optimum sample window can be obtained from the calibration constant, using measurements from only one BPM, as opposed to measuring the resolution directly, which requires all three BPMs.

3.5 Resolution dependence on BPM position

Ideally, the resolution should not vary with bunch offset within the dynamic range of the BPM. Outside of the dynamic range, non-linearities are expected to manifest themselves as a degradation in the resolution.

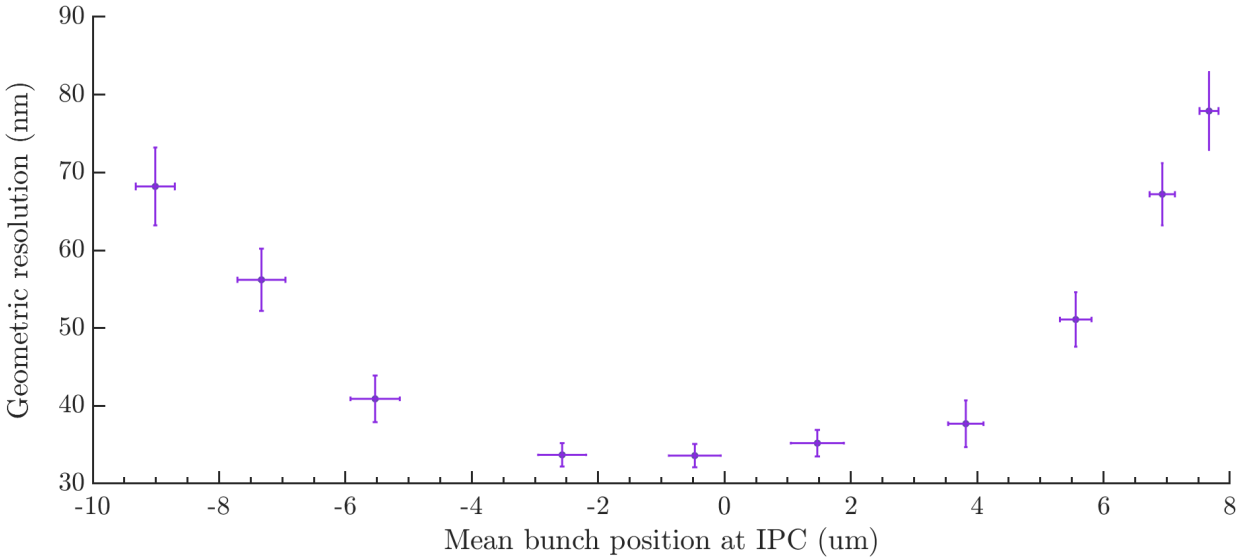

Figure 3.5: Geometric resolution versus mean IPC offset, where IPA and IPB were unchanged. Analysis was performed with a five-sample integration window.

The geometric resolution was measured while scanning the IPC offset from $-9\,\mu m$ to $8\,\mu m$ using the BPM movers; this is shown in Fig. 3.5. The study was performed at a bunch charge of 0.7×10^{10} electrons per bunch, with 10 dB attenuation on the dipole signal. The dynamic range of the system in this configuration was expected to be a few microns, and the geometric resolution was measured to be consistent across this range. The resolution had

started to degrade by $\sim 4\,\mu m$ offset and continued to deteriorate until $-10\,\mu m$ and $9\,\mu m$, at which point the BPM signals exceeded the digitisation window and were saturated.

The measurements of the resolutions are seen to be asymmetric about a $0\,\mu m$ offset which suggests that there is an offset between the *measured* and *true* offsets. Further evidence for this is discussed in Section 3.6.

3.6 Resolution dependence on angular offset

If the beam is within the dynamic range of the BPM system, the resolution should not vary with beam position or angular offset. To test the stability of the resolution across the dynamic range, measurements were taken for a range of position offsets and BPM tilts of $\pm 3\,\mu m$ and $\pm 2\,mrad$ respectively. For this study, IPA and IPB were kept stationary and IPC was offset and tilted using the IPC submovers. When varying the tilt of IPC, the BPM submovers were scanned using increments calculated such that the transverse position of the electrical centre remained unchanged. Throughout the study, the I and Q waveforms were kept within ± 2000 ADC counts as this was estimated to be the linear working region for the first-stage processing electronics.

Example waveforms from each of the settings of the scan are shown in Fig. 3.6. The integration window used in analysis (samples 59 to 64) was chosen to optimise the resolution when IPC was well-aligned. High-beta optics were used so as to be able to align all three BPMs with the beam, with 10 dB attenuation on the dipole signal. The scan was started with a charge of 0.7×10^{10} electrons per bunch but this was observed to decrease during the scan; this is discussed further in Section 3.6.3. In order to reduce the position jitters at IPA and IPC simultaneously, the beam waist was placed half-way between them. Throughout the study, measurements at the nominal position and angle settings were taken periodically to be used as reference measurements. The whole scan was repeated for comparison.

The geometric resolutions measured for the different IPC position and angular offsets are shown in Fig. 3.7. The angular offset specifies the offset between the BPM electrical axis and the beam angle; this was determined using the process detailed in Section 2.3.5. The resolution shows a noticeable dependence on angular offset which is asymmetric about the nominal setting, despite the nominal setting being measured to be close to 0 mrad. This is a consequence of the down-mixed BPM waveforms having position-independent components which mean a zero beam offset does not correspond to zero BPM signal. One such example is the baseline generated by driving the second-stage mixer, which introduces a constant offset to all I and Q measurements while the reference signal is present. Operationally, this makes

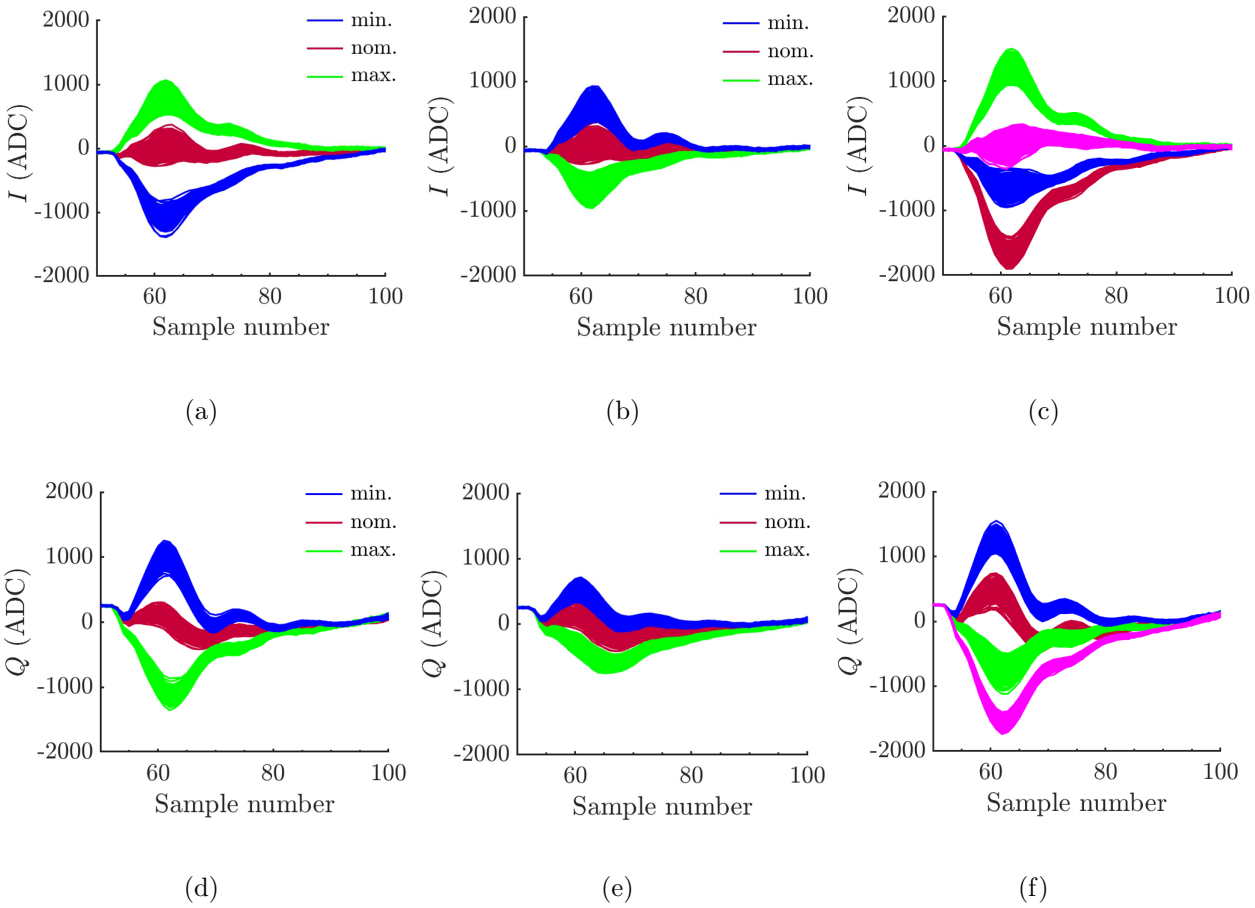

Figure 3.6: IPC (a) I and (d) Q waveforms for an IPC angle scan; (b) I and (e) Q waveforms for an IPC position scan; (c) I and (f) Q waveforms for an IPC position and angle scan. The lines show the triggers recorded; the position and tilt settings are denoted by the colour of the line, with the settings for (c) and (f) given in Table 3.5.

Table 3.5: Position and tilt settings for Fig. 3.6(c) and (f).

	Min. position	Max. position
Min. tilt	blue	green
Max. tilt	red	magenta

alignment more complicated, as this constant offset can only be estimated by processing and analysing the data.

In order to determine which parameters were responsible for the dependence of the resolution on the angular offset, the multi-parameter fitted resolution was studied. As there is a mechanism for angular information to couple into the position measurement through the limiter phase jitter, both the angular signal, $\frac{Q'}{q}$, and the limiter phase delay were investigated as fitting parameters.

3.6.1 Resolution dependence on the limiter phase delay

As shown in Eq. 2.17, the measured bunch position has a dependence on the limiter phase delay, which for typical operation is assumed negligible. The error introduced by this assumption can be estimated by comparing the resolution determined by fitting to the bunch position, σ_1, and the resolution determined by fitting to both the bunch position and limiter

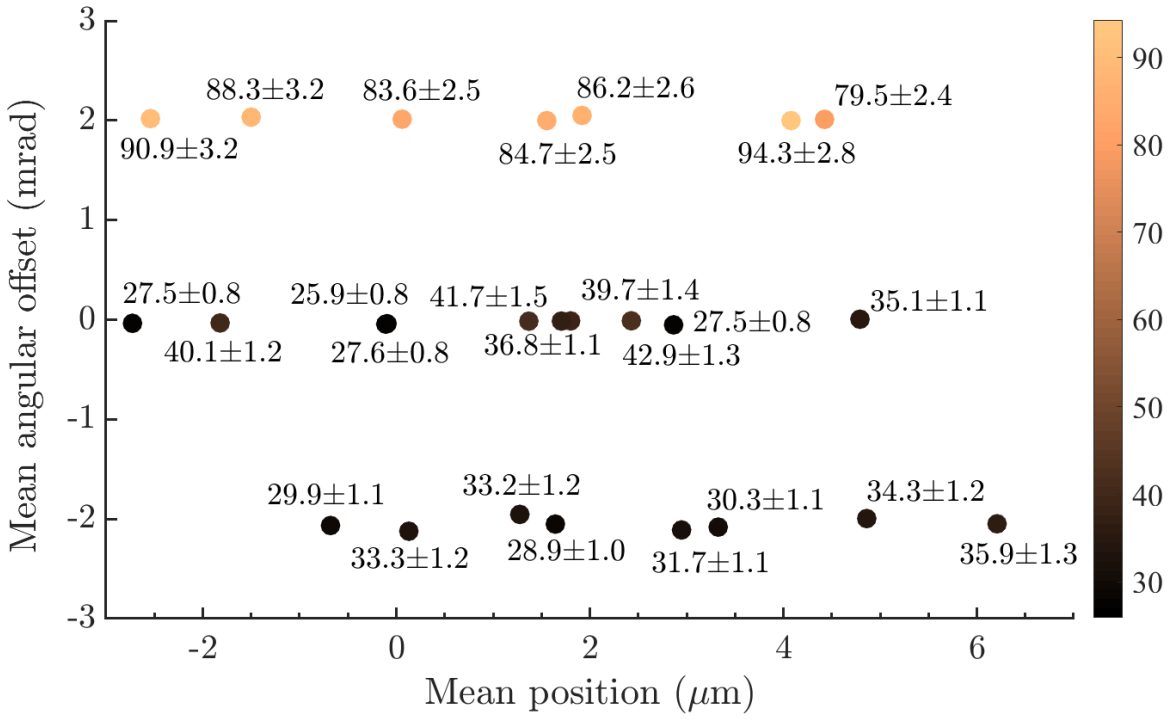

(a)

Figure 3.7: Geometric resolution versus IPC position (x-axis) and angular offset (y-axis). The resolution is given by the colour of the data point (right-hand scale in nm). All data were analysed with an integration window of samples 59 to 64. The errors show the statistical uncertainty on the resolution measurement.

phase-delay, σ_2. These fitted resolutions were calculated for all of the data sets taken during the position and angle scan, described in Section 3.6. By comparing σ_1 and σ_2, the effect of the limiter phase jitter on the resolution can be characterised as a function of the angular offset. As the resolution is defined as the standard deviation over residuals, resolution terms should be added in quadrature. The improvement to the resolution by adding an extra fitting parameter is then defined to be $\sqrt{{\sigma_1}^2 - \sigma_2^2}$.

The limiter phase delay was determined using the setup shown in Fig. 2.21, which produces $I_{\text{lim.}}$ and $Q_{\text{lim.}}$ waveforms. The waveforms must be sampled in order to extract a value of the local phase angle, θ_{IQ}, for each trigger. Either single-sample or integrated-sample calculations are possible and $\sqrt{\sigma_1^2 - \sigma_2^2}$ was studied as a function of different samples and sampling windows; this is shown in Fig. 3.8. An improvement to the resolution by additionally fitting to the limiter phase delay highlights this as a key parameter that is degrading the resolution. These data were from the maximum tilt setting of the scan, where there was maximal coupling of the limiter phase delay into the position signal.

For samples 50 to 54, there was little improvement to the resolution as the reference signal had not yet arrived. For samples 57 to 59, the $I_{\text{lim.}}$ and $Q_{\text{lim.}}$ waveforms were saturated to a constant value, thus offering no improvement to the resolution. Additionally fitting to the limiter phase delay was seen to make a significant improvement to the resolution for samples 62 to 65, where $I_{\text{lim.}}$ and $Q_{\text{lim.}}$ were high enough to get an accurate measurement of θ_{IQ}. At sample 70, the sampled values of $I_{\text{lim.}}$ and $Q_{\text{lim.}}$ cross zero and an accurate measurement of θ_{IQ} cannot be made. After sample 70, $I_{\text{lim.}}$ and $Q_{\text{lim.}}$ were both negative and non-zero and θ_{IQ} could again be calculated. After sample 80, the signal-to-noise ratio was low and the performance decreased.

The improvement to the resolution, $\sqrt{\sigma_1^2 - \sigma_2^2}$, was then measured as a function of sample integration window for the $I_{\text{lim.}}$ and $Q_{\text{lim.}}$ waveforms; this is shown in Fig. 3.8(b). $\sqrt{\sigma_1^2 - \sigma_2^2}$ increased by using sample integration compared with single-sample analysis, with the highest value of 44.3 nm seen for a five-sample integration window. This indicates that a more accurate value of θ_{IQ} can be obtained with sample integration. However, after sample 64, $\sqrt{\sigma_1^2 - \sigma_2^2}$ decreases as the signals $I_{\text{lim.}}$ and $Q_{\text{lim.}}$ have decayed and the signal-to-noise ratio is poorer. This can also be seen in Fig. 3.8(a) with a decrease in $\sqrt{\sigma_1^2 - \sigma_2^2}$ after sample 64.

Measurements of $\sqrt{\sigma_1^2 - \sigma_2^2}$ were repeated for all of the position and angle settings in the resolution scan. For the limiter phase delay measurement, samples 60 to 64 of the $I_{\text{lim.}}$ and $Q_{\text{lim.}}$ waveforms were used, as this was shown in Fig. 3.8(b) to give the biggest improvement. Figure 3.9 gives $\sqrt{\sigma_1^2 - \sigma_2^2}$ as a function of the IPC angular offset, demonstrating the importance of minimising the angular offset in reducing the degradation of the resolution from

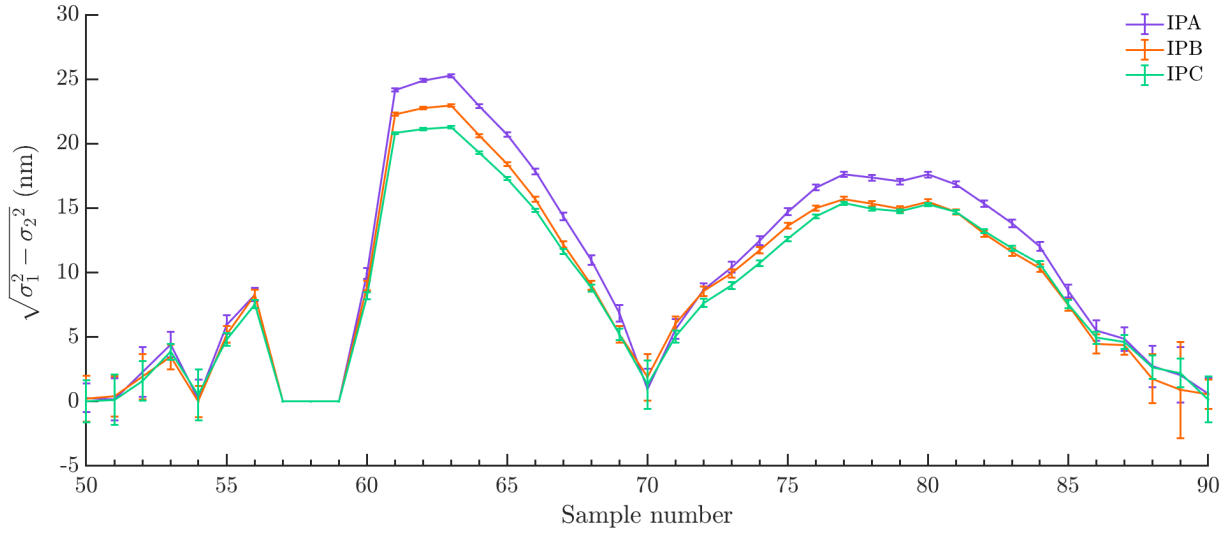

(a)

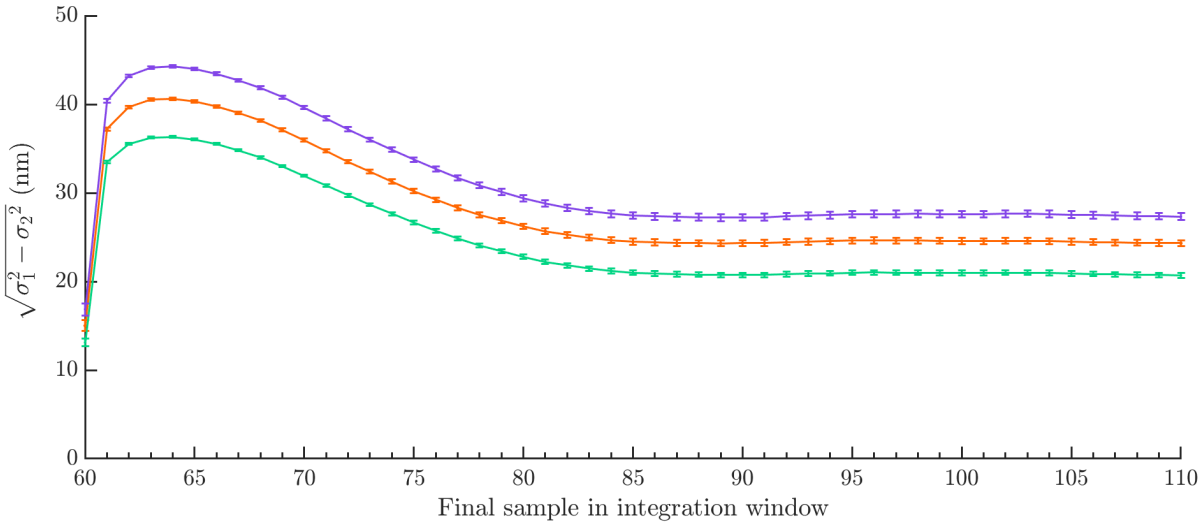

(b)

Figure 3.8: The improvement to the fitted resolution by adding the limiter phase delay as a fitting parameter versus (a) sample number and (b) final sample in the integration window (starting at sample 60) for signals $I_{\text{lim.}}$ and $Q_{\text{lim.}}$. The term σ_1 corresponds to the resolution from fitting to position and σ_2 to fitting to both position and limiter phase delay. The data points show the improvement to the resolution for IPA, IPB and IPC, the lines connect the data points and the error bars show the statistical uncertainty.

the limiter phase jitter. Although it is possible to fit out the effect of the limiter phase jitter in offline analysis, this calculation is not possible within the latency constraints imposed by intra-train feedback.

The data are asymmetric about 0 mrad, providing further evidence that $\frac{Q'}{q} = 0$ does not correspond to zero angular offset and that there is a constant baseline offset. From a least-squares fit to the data, a minimum of 2.8 nm is obtained for an angular offset of -0.52 mrad.

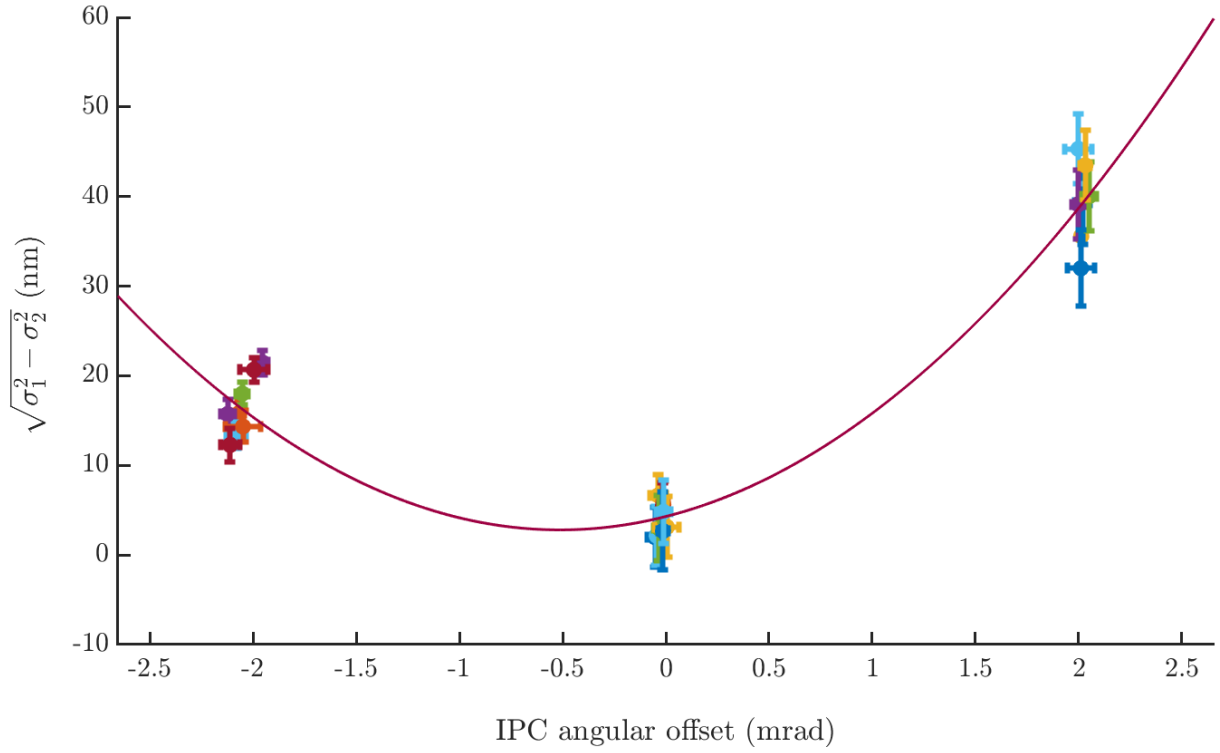

Figure 3.9: The improvement to the IPC resolution by fitting to position and limiter phase delay compared with the resolution by fitting to just position versus angular offset. The term σ_1 corresponds to the resolution from fitting to position and σ_2 to fitting to both position and limiter phase delay. The error bars represent the statistical uncertainty and the line shows a quadratic fit to the data. The colours of the data points are used for clarity, to distinguish separate points.

3.6.2 Improvement to the resolution by fitting to $\frac{Q'}{q}$

The dependence of the resolution on IPC angular offset was considered further by calculating the fitted resolution with $\frac{Q'}{q}$ as an additional fitting parameter. This analysis was performed on the data sets from the position and angle scan, described in Section 3.6.

Figure 3.10 shows the geometric and fitted resolutions versus the IPC angular offset, for three different sets of fitting parameters. Fig. 3.10(a) shows the geometric resolution and the resolution calculated by fitting to only the BPM positions; Fig. 3.10(b) shows the resolution calculated by fitting to position ($\frac{I'}{q}$) and angle ($\frac{Q'}{q}$); Fig. 3.10(c) shows the resolution calculated by fitting to position ($\frac{I'}{q}$), angle ($\frac{Q'}{q}$) and the limiter phase delay.

It can be seen from Fig. 3.10(a) and (b) that by adding the fitting parameter $\frac{Q'}{q}$, the dependence of the resolution on the BPM pitch is reduced. Further, by also fitting to the limiter phase delay, as shown in Fig. 3.10(c), the resolution estimates determined from IPA, IPB and IPC are brought into better agreement. By fitting to position only, the resolution estimates at the maximum tilt setting range from 70 to 90 nm. With the addition of $\frac{Q'}{q}$ as a fitting parameter these estimates are improved to 30 to 40 nm. Finally, by adding the limiter phase delay to the calculation, resolution estimates for all three BPMs are reduced to 25 to 35 nm, which is consistent with measurements at the nominal tilt setting.

A quadratic fit to the resolutions displayed in Fig. 3.10 was used to estimate that the geometric resolution would have a minimum value of 27 nm, at an offset of -1.1 mrad. As the resolution is expected to be optimised when the angular offset is removed, this may suggest that there is a zero-offset of the $\frac{Q'}{q}$ measurements of -1.1 mrad. The quadratic fits to the fitted resolutions also show similar locations for the minima, with values for the three BPMs in good agreement, particularly for Fig. 3.10(c).

Even when adding $\frac{Q'}{q}$ and the limiter phase delay as fit parameters, a spread in the resolutions was observed at each BPM tilt setting. For the nominal tilt setting, fitted resolutions were measured between 20.7 nm and 29.9 nm. As the resolution is known to depend on the bunch charge, which was observed to decrease across the course of the scan, this was considered to be a possible mechanism for the variation observed.

3.6.3 Resolution dependence on the bunch charge

The initial bunch charge of 0.7×10^{10} electrons was observed to decrease by a factor of 1.5 during the scan. As the resolution is expected to scale inversely with the bunch charge, the decrease in charge would be expected to lead to a poorer resolution towards the end of the scan.

The nominal position and tilt resolution measurements were plotted as a function of the bunch charge to observe any dependences; this is presented in Fig. 3.11. It can be seen that some of the variation can indeed be attributed to the bunch charge. The expected inverse scaling of the resolution with charge is shown. The geometric resolution, although showing

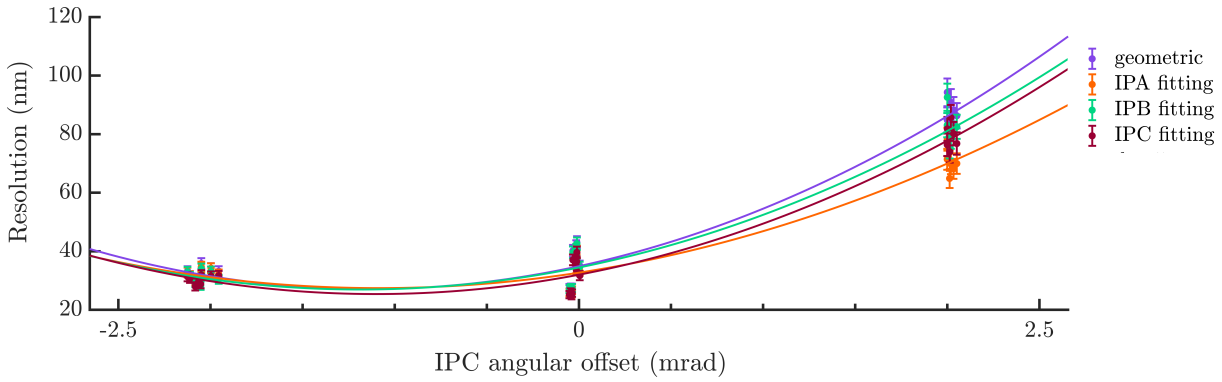

(a)

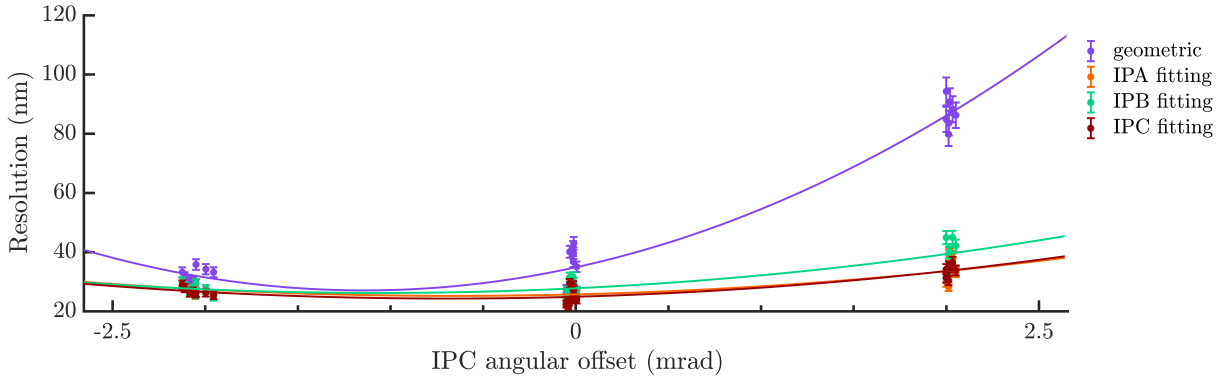

(b)

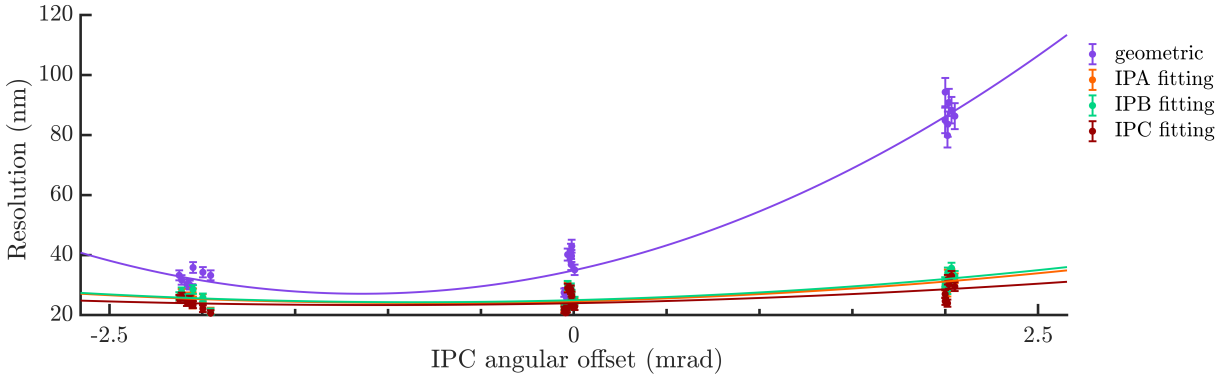

(c)

Figure 3.10: Resolution versus IPC angular offset. Data points show the geometric resolution and resolutions determined by fitting to (a) $\frac{I'}{q}$, (b) $\frac{I'}{q}$ and $\frac{Q'}{q}$ and (c) $\frac{I'}{q}$, $\frac{Q'}{q}$ and the limiter phase delay. The colour of the data show the resolution method; the error bars show the statistical uncertainty; least-squares quadratic fits to the data are given as lines of the respective colour.

an improved resolution with increased bunch charge, does not follow the expected $\frac{1}{q}$ scaling. Measurements at a higher bunch charge were seen to outperform the predicted scaling, which may be an indication of non-linear charge effects.

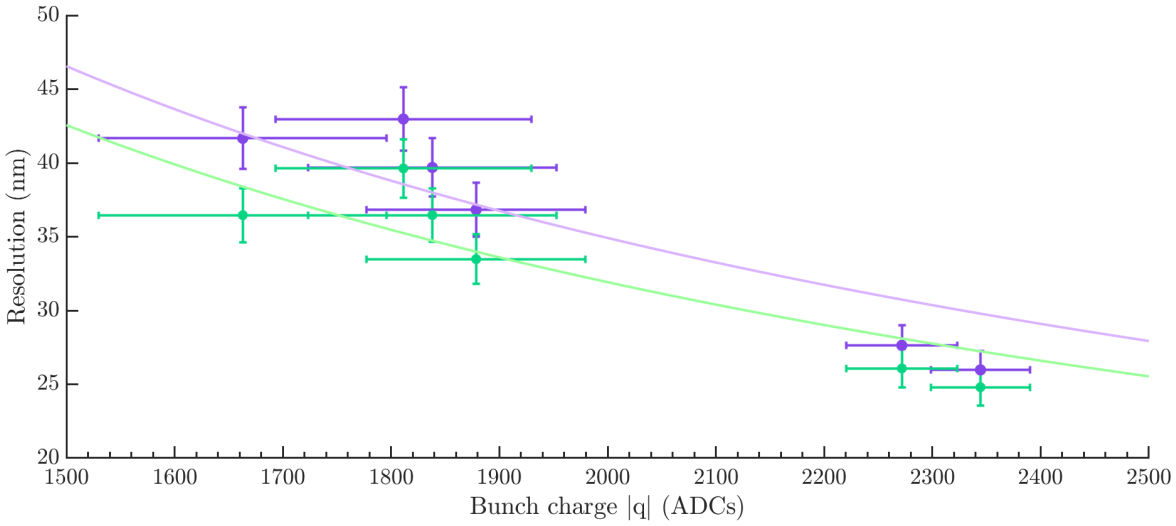

Figure 3.11: Geometric (purple) and IPC (green) fitted resolutions versus mean bunch charge. These data were analysed using a sample integration window of 59 to 64. Horizontal error bars show the standard deviation over 384 triggers and vertical error bars show the statistical uncertainty on the resolution. The expected inverse scalings of resolution with charge are shown as lines of respective colour.

3.6.4 Analysis of the IPC calibration constant

The calibration constant was calculated for the IPC position and tilt scan to investigate the dependence of the BPMs' position sensitivity on the angular offset. As the formulation for bunch offset (Eq. 2.17) contains a second-order term dependent on the beam angle, there is a mechanism for the beam angle to affect the calibration constant. This second-order dependence is assumed negligible so that, ideally, the calibration constant would not vary significantly as a function of angular offset.

The fitted calibration constants were determined for the data sets taken during the IPC scan, using Eq. 3.12. The results of the fitted calibration constants for IPA and IPC are shown in Fig. 3.12 as a function of the angular offset. The measured calibration constants are also given for comparison, where the calibrations were performed at a setting with good BPM alignment in both position and angle. For this study, it was assumed that the IPB calibration constant remained the same, as IPB was not moved during the scan.

The fitted calibration constant for IPA remains largely consistent with the measured value

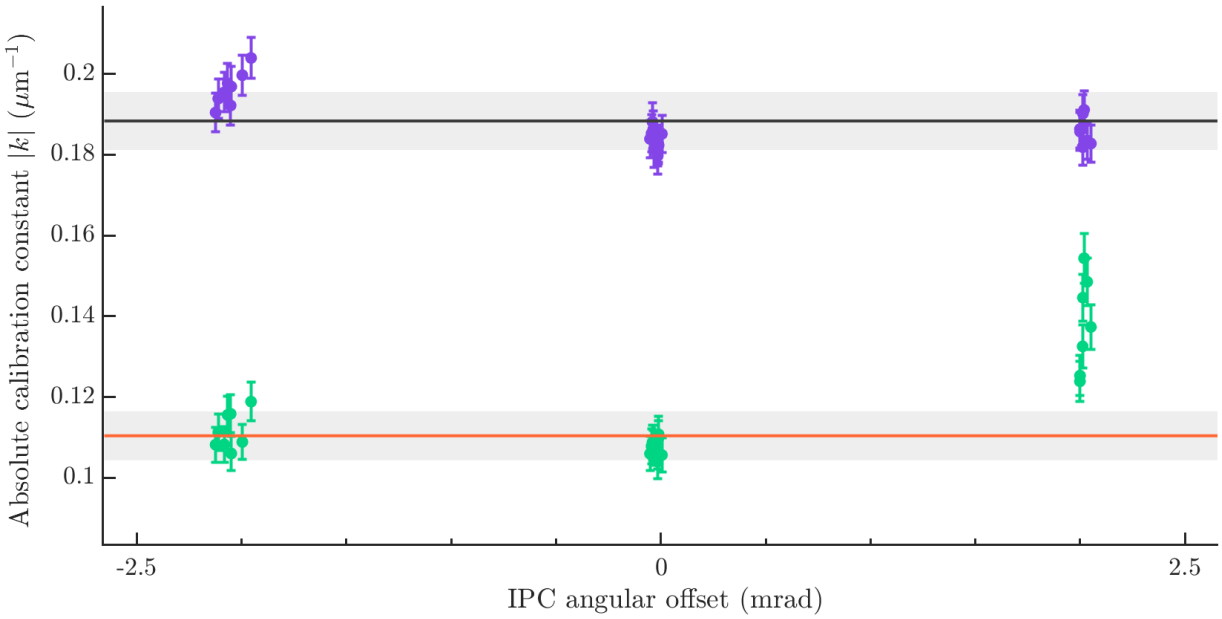

Figure 3.12: Absolute fitted calibration constants for IPA (purple) and IPC (green) versus IPC angular offset. The measured calibration constants are shown as black (IPA) and orange (IPC) lines, and the errors on the measurements shown as grey rectangles. Error bars show the statistical uncertainty on the fitted values of k.

throughout the scan, which was as expected as this BPM was not moved. The agreement between the data is a confirmation of the accuracy of the IPA calibration. On the other hand, the fitted calibration constant for IPC with a 2.1 mrad angular offset shows a significant deviation from the measured value. The fitted IPC calibration constants for the -2.1 mrad and 0 mrad settings are consistent with the measured values, suggesting the calibration was accurate and unchanged between these settings.

From Fig. 3.10, the minimum resolution was predicted to occur at a -1.1 mrad angular offset, suggesting that there was a -1.1 mrad offset between the measured and true positions. Taking this constant offset into account, the minimum, nominal and maximum tilt settings would correspond to angular offsets of -1 mrad, 1.1 mrad and 3.2 mrad, respectively. As the calibration constants are consistent for the minimum and nominal tilt settings. this would suggest that the calibration constant is stable for angular offsets of up to ± 1 mrad, which typical BPM operation would not exceed.

3.6.5 Analysis of the position jitter

It is also of interest to consider the measured bunch position jitter as a function of angular offset. As the feedback system is designed to reduce the beam jitter, it is crucial that an

accurate measurement of this can be made.

From Eq. 2.17, $y \propto \frac{I'}{q} + \frac{Q'}{q} \times \delta_{\theta_{IQ}}$, but for typical operation the second term is considered negligible and the approximation $y \propto \frac{I'}{q}$ is made. For the IPC scan, the $\frac{I'}{q}$ jitter was compared with the $\frac{I'}{q} + \frac{Q'}{q} \times \delta_{\theta_{IQ}}$ jitter to test the validity of this approximation for different angular offsets. If the $\frac{I'}{q} + \frac{Q'}{q} \times \delta_{\theta_{IQ}}$ jitter is significantly different to the jitter on $\frac{I'}{q}$, it would suggest that the term $\frac{Q'}{q} \times \delta_{\theta_{IQ}}$ cannot be considered negligible. Fig 3.13 shows $\frac{I'}{q} + \frac{Q'}{q} \times \delta_{\theta_{IQ}}$ versus $\frac{I'}{q}$ for the minimum, nominal and maximum BPM tilt settings. It can be seen that for the nominal setting, the assumption that $\frac{Q'}{q} \times \delta_{\theta_{IQ}}$ is negligible remains valid but that this is not the case for the minimum and maximum tilt settings. Care must be taken to ensure good angular alignment during BPM operation as the $\frac{Q'}{q} \times \delta_{\theta_{IQ}}$ term cannot be included in the position measurement within the latency constraints imposed by intra-train feedback.

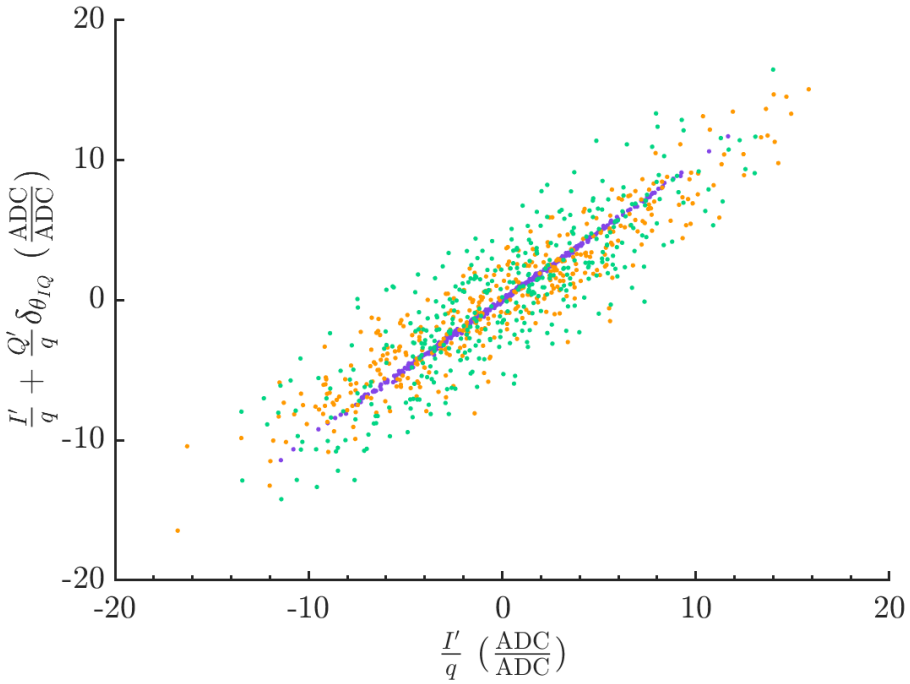

Figure 3.13: $\frac{I'}{q} + \frac{Q'}{q} \times \delta_{\theta_{IQ}}$ versus $\frac{I'}{q}$, for IPC angular offsets of -2.1 mrad (orange), 0 mrad (purple) and 2.1 mrad (green). All data were taken while minimising the position offset at all three BPMs.

The standard deviations of $\frac{I'}{q}$ and $\frac{I'}{q} + \frac{Q'}{q} \times \delta_{\theta_{IQ}}$ are given in Table 3.6 alongside the IPC position and tilt setting for which the data were collected. The standard deviations of the two terms are similar for the data at nominal tilt settings, even if the IPC position is not minimised. This is as expected, as it was shown that the resolution has little dependence on the bunch position offset while within the BPM's dynamic range (Section 3.5). For data sets with an IPC angular offset of ± 2.1 mrad, the standard deviations of the two parameters are different by approximately 10%, with the standard deviation of $\frac{I'}{q}$ always being the larger

term. From this it was concluded that the position measurement had been corrupted by angle information and consequently, angular offsets should always be kept much less than $\pm\,2$ mrad.

Table 3.6: Jitter on $\frac{I'}{q}$ and $\frac{I'}{q} + \frac{Q'}{q} \times \delta_{\theta_{IQ}}$ as a function of IPC position and tilt, where minimum and maximum position settings represent a $\pm 3\,\mu$m offset from nominal, and minimum and maximum tilt settings represent a ± 2.1 mrad angular offset. The errors represent the standard error on the jitter.

Pos. setting	Tilt setting	Scan	std($\frac{I'}{q}$) ($\frac{\text{ADC}}{\text{ADC}}$)	std($\frac{I'}{q} + \frac{Q'}{q} \times \delta_{\theta_{IQ}}$) ($\frac{\text{ADC}}{\text{ADC}}$)
Nom.	Max.	1	6.8 ± 0.2	6.2 ± 0.2
Nom.	Max.	2	5.6 ± 0.2	4.8 ± 0.2
Nom.	Min.	1	5.6 ± 0.2	5.1 ± 0.2
Nom.	Min.	2	7.9 ± 0.3	7.2 ± 0.3
Nom.	Nom.	1	4.0 ± 0.1	4.0 ± 0.1
Nom.	Nom.	2	4.6 ± 0.2	4.5 ± 0.2
Min.	Nom.	1	3.9 ± 0.1	3.8 ± 0.1
Min.	Nom.	2	5.8 ± 0.2	5.8 ± 0.2

3.6.6 Multi-parameter fitted resolution

It has been determined that the resolution most strongly depended on the angular offset $\frac{Q'}{q}$, the limiter phase delay and the bunch charge. The resolution was calculated while fitting to all of these variables, in order to get an estimation of how much of the decrease in resolution could be attributed to them. The multi-parameter fitted resolutions for the IPC position and angle scan are presented in Fig. 3.14, in a format analogous to Fig. 3.7. It can be seen that by adding these fitting parameters, the resolutions measured throughout the scan are brought into better agreement. The resolution measurements at the maximum BPM tilt setting were particularly improved, from a geometric resolution of 90.9 nm to a multi-parameter fitted resolution of 30.5 nm.

There remains a noticeable decrease in the resolution for the minimum position, maximum angle setting with resolutions of ~ 35 nm. This may indicate the signal levels were high enough that the processing electronics were in a non-linear operating regime. From Fig. 3.6, it can be seen that the Q waveforms for this setting were approaching the edge of the expected linear operating region of ± 2000 ADC. These results suggest that the linear operating region is smaller than expected and care should be taken to minimise the magnitude

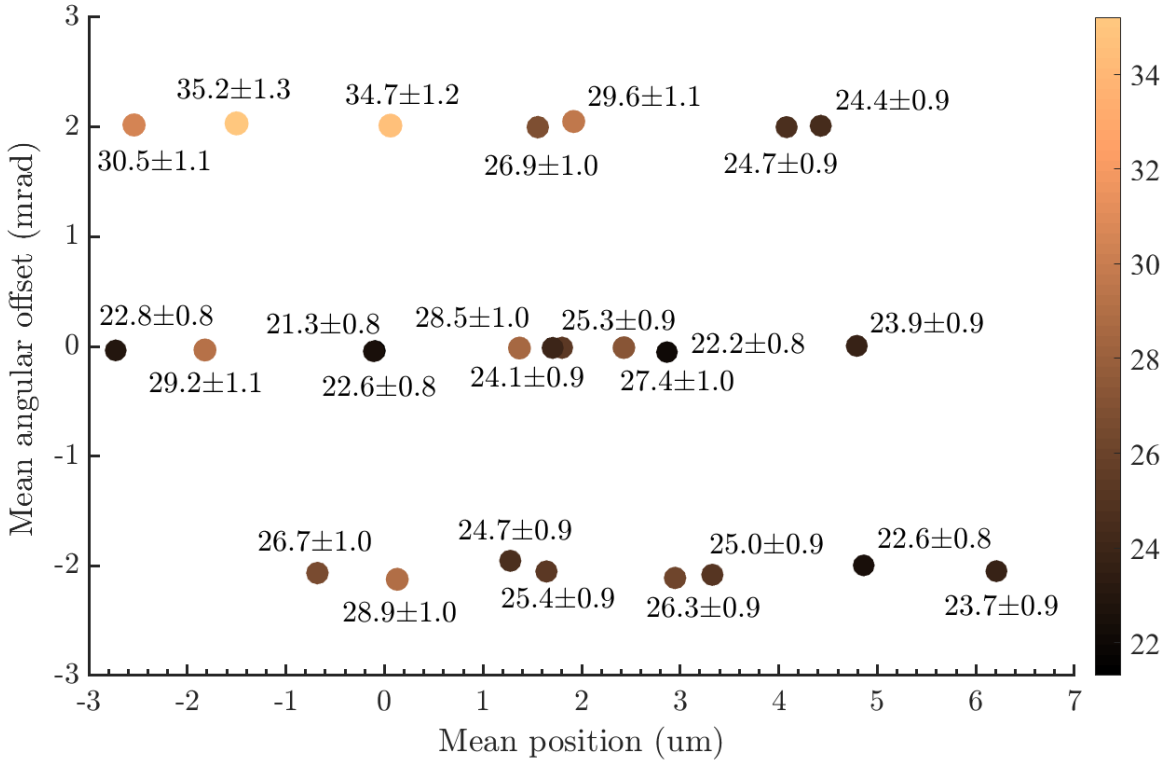

(a)

Figure 3.14: IPC resolution determined by fitting to $\frac{I'}{q}$, $\frac{Q'}{q}$, the limiter phase and the charge versus IPC position (x-axis) and angle (y-axis). The resolution is given by the colour of the data point (right-hand scale in nm). All data were analysed with an integration window of 59 to 64.

of the signals with careful BPM alignment.

3.7 Summary

This chapter has presented studies of the resolution of the cavity BPM system. Two methods of estimating the resolution were compared; the geometric method showed good agreement with the fitting method. Both estimates of the resolution were shown to improve with the use of sample integration; with the single-sample geometric resolution of 40 nm brought to 20 nm by integrating 11 samples. Sample integration is also seen to bring the three resolution estimates generated using the fitting method into better agreement, with fitted resolutions of ~ 19 nm agreeing well with the geometric estimate.

The BPM resolution was studied as a function of signal attenuation and was expected to scale linearly with the signal level. The resolution was shown to scale as expected from 50 dB to 20 dB but underperformed at 10 dB, with an integrated-sample geometric resolution of 24 ± 1 nm compared with the predicted performance of 16 nm. This may indicate non-linearities in the system, as a result of the higher signal levels present when the attenuation is reduced. Consequently, further studies of the dependence of the resolution on the dipole attenuation are recommended, at a range of bunch charges. The resolution was shown to have little dependence on the BPM position offset while within the expected dynamic range of the BPMs. The calibration constant was also shown to be consistent throughout this range.

The resolution was analysed as a function of the angular offset with respect to the beam, as studies in Chapter 2 suggested a BPM angular offset might degrade the performance. The geometric resolution was shown to decrease to ~ 80 nm for a 2.1 mrad BPM angular offset. The degradation of the resolution was explained by the limiter phase jitter coupling angular information into the position measurements. To test this, the resolution was calculated while fitting out the effect of the limiter phase jitter, which was shown to improve the geometric resolution from ~ 80 nm to ~ 30 nm.

The analysis of the fitted calibration constant at IPC as a function of the IPC angular offset offered further evidence of the non-linearities introduced from poor angular alignment. For a 2.1 mrad offset, the fitted calibration constant was inconsistent with the calibration constant for a 0 mrad offset, demonstrating the need for good angular alignment when operating the BPMs. Measurements of both the resolution and the calibration constant show asymmetric behaviour for positive and negative angular offsets, suggesting that the angular offset is minimised for a non-zero value of $\frac{Q'}{q}$. In this case, it would be advisable to

minimise the angular offset by performing a BPM tilt scan and measuring the resolution.

Chapter 4

ATF2 IP feedback

This chapter details the progress towards achieving the ATF2 goal of nanometre vertical stabilisation of the beam waist, with an intra-train IP feedback system. The system uses vertical position measurements of the first bunch in a two-bunch train to predict and correct the position of the second bunch. This process requires a high bunch-to-bunch position correlation; any reduction in the correlation will degrade the feedback performance. Each train consists of two bunches separated by 280 ns, a separation that was found to optimise the bunch-to-bunch correlation. This separation sets an upper limit for the latency of the feedback system. Recent work towards improving the resolution that is achievable in real-time with the feedback system is presented, along with the subsequent improvement to the beam stabilisation performance.

My contributions to this work include improvements to the feedback firmware to incorporate some new, useful features. The features (further described in Section 4.1.2) allow for sample integration of the BPM waveforms, the option for constant offsets to be added to the I and Q signals, and the ability to easily switch which BPMs contribute to the feedback loop.

Two different feedback modes are described, which are differentiated by the number of BPMs used to calculate the bunch position; these are shown in Figs. 4.1(a) and 4.1(b). The first mode, 1-BPM feedback, uses measurements taken at a single BPM for local stabilisation. The second mode is 2-BPM feedback, which uses measurements from two BPMs, to stabilise the beam at an intermediate location. Both modes of feedback are single-loop, such that only one corrector is used in the feedback loop (see Fig. 2.6). All analysis concerning the operation of the feedback system is my own.

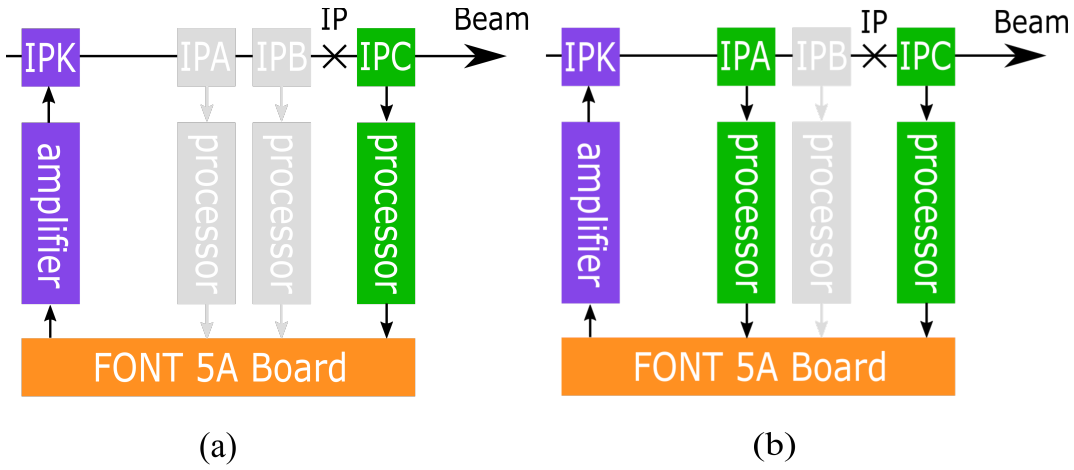

Figure 4.1: Diagrams of feedback loops with cavity BPMs (IPA, IPB and IPC) and a stripline kicker (IPK) for (a) 1-BPM feedback, with position measurements and beam stabilisation at IPC and (b) 2-BPM feedback, with position measurements at IPA and IPC, for beam stabilisation at an intermediate location.

4.1 Components of the IP feedback system

The intra-train feedback system takes inputs from either one or two of the BPMs. The bunch corrections are implemented using a stripline kicker, IPK, located upstream of the BPMs (Fig. 4.1). The digitisation of the BPM signals and the feedback calculations are performed on a FONT5A digital board. The board produces an analogue feedback signal which is amplified and used to drive IPK.

4.1.1 FONT5A digital board

The computations for IP feedback are performed on a FONT5A board. The board consists of a Printed Circuit Board (PCB) constructed around a Xilinx Virtex-5 XC5VLX50T FPGA [69], a chip whose functionality can be reprogrammed with the use of configurable logic blocks (CLBs). The PCB is mounted within a case with BNC connectors, allowing for signals to be input and output from the board [70]. The FONT5A board is shown in Fig. 4.2 with the case removed.

The FONT5A board is used to digitise the BPM signals, perform digital signal processing and to generate the feedback signal used to drive IPK. The firmware, written in the hardware description language Verilog, is typically stored on a non-volatile Xilinx XCF32P Programmable Read-Only Memory (PROM) chip and transferred to the FPGA upon powering the board [70].

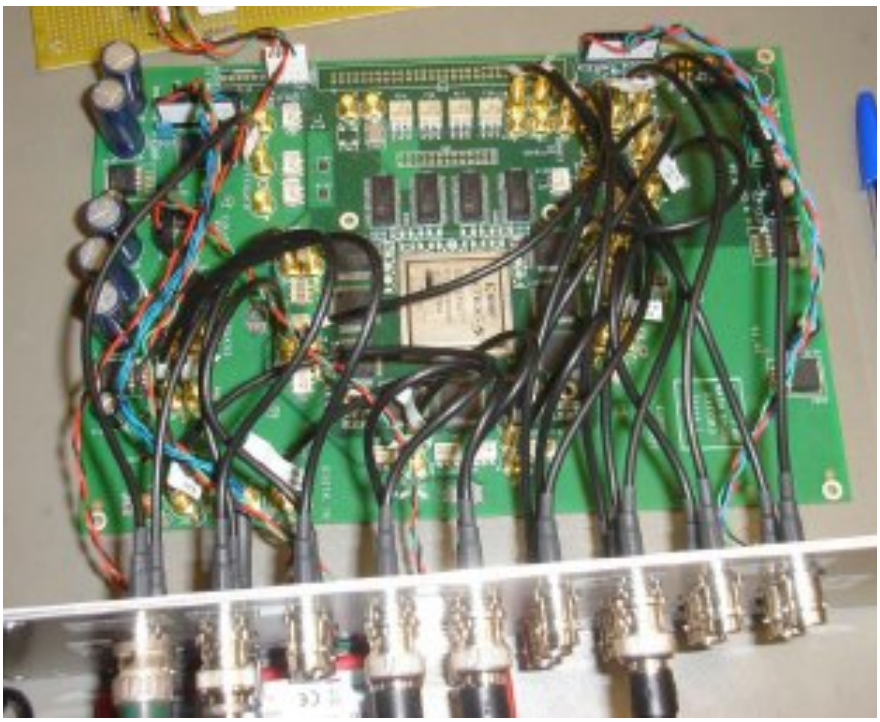

Figure 4.2: Photograph of the FONT digital board with the case removed [70][71].

The board contains nine 14-bit analogue-to-digital converters (ADCs) grouped into banks of three, with each bank separately clocked. The ADCs are used to digitise the I, Q and q waveforms coming from the two-stage processing electronics (see Section 2.1.5). During digitisation, the least significant bit is removed as it corresponds to the noise level of the signals [70]. The signals are amplified before digitisation, so as to reduce the effect of the quantisation noise from the ADCs. The nine ADC channels each contain an inherent offset on their baseline signal. This baseline can be brought to zero by coupling each analogue input signal with the output of a 16-bit digital-to-analogue converter (DAC), referred to as a trim DAC. The values used as input to the trim DAC can be set using the associated FONT LabVIEW DAQ [72]. The DAQ is used to transmit values to the board through an RS-232 Universal Asynchronous Receiver/Transmitter (UART) [70] via an Ethernet serial device server [72].

The ouptut from the FONT5A board is through a DAC which is used to pass the feedback signal to the stripline kicker, IPK. The board has the capability to output up to four of these signals but only one is required when operating single-loop feedback. The 14-bit output corresponds to a $\pm 2\,\mathrm{V}$ DAC range and so the board's output passes through a specially designed kicker amplifier to generate the high current signal needed to drive the kicker.

The board has a Joint Test Action Group (JTAG) connector, enabling a computer to load firmware directly to either the FPGA or the PROM. The inputs and outputs to the

PCB which are used for operating feedback are through Micro Coaxial connectors. These outputs are patched to the front panel BNC connectors [70].

Two clocks are used for the FPGA logic, a slow-clock at 40 MHz and a fast-clock at 357 MHz. The slow-clock is internally generated and used to clock the FPGA logic which is not time critical. For the time-critical logic, a 357 MHz clock is derived from the 714 MHz DR master oscillator, meaning it is phase locked to the bunches. The frequency of the fast-clock determines the sampling frequency of the ADCs. The start of the sampling window is set with respect to the trigger, which is internally delayed on the board. The sampling window for a single beam pulse consists of 164 samples, each separated by 2.8 ns, allowing for both bunches in a train to be digitised within the same window.

The digital signal processing (DSP) is implemented on specifically designed elements within the FPGA called DSP48E slices, so named because there are 48 of them available [73]. Many arithmetic operations are possible using the DSP48E slices and logic can be assembled from pre-existing elements within the slices, including a 25×18 two's-complement multiplier and a 48-bit accumulator [73]. The logic within a slice can be clocked at up to 550 MHz, which is critical in reducing the latency of calculations [69].

4.1.2 FONT5A firmware

In Chapter 3, it was demonstrated that the resolution could be improved by integrating over multiple digitised samples. Previously, sample integration was only possible in offline analysis and not in real-time while operating intra-train feedback. Previous studies have demonstrated a best single-sample feedback performance of 74 ± 5 nm stabilisation for 1-BPM feedback [74], and 57 ± 4 nm stabilisation for 2-BPM feedback [60]. These results were collected in 2015 and 2017 respectively, and are consistent with a single-sample BPM resolution of $\sim$ 45 nm.

One of the new features within the firmware mean it is now possible to use sample integration while performing feedback, thus improving the resolution achievable by the BPMs within the intra-train feedback loop. The integration within the firmware is performed on the I and Q signals, such that on every rising fast-clock edge within the integration window the most recent value is summed with the previous total. To allow for manual control over the parameters that govern the operation of the feedback system, they are stored in 7-bit registers, called 'control registers'. It is possible to amend the values which are preloaded to these control registers using the FONT LabVIEW DAQ [72]. The use of the control registers which are inherited from previous iterations of FONT5A firmware are detailed

in [70] and [72]. The control registers specific to the sample integration mechanism are listed in Table 4.1.

Table 4.1: Control registers used during the implementation of feedback using an integrated sample window. All control registers in this table are clocked at 40 MHz.

Register Name	Size	Function
`bpm_sel`	2 bits	Select which BPMs to use as input to feedback.
`no_bunches`	2 bits	Number of bunches in a bunch train.
`no_samples`	4 bits	Width of sample integration window.
`sample_spacing`	8 bits	Number of samples between successive bunches.
`b1_strobe`	8 bits	First sample in I and Q integration window (bunch-1).
`b2_strobe`	8 bits	Sample number to use for q (bunch-1).

The requirements for low-latency feedback preclude the direct implementation of division within the firmware and, instead, a method of lookup tables (LUTs) is employed. The charge, q, is used as an address to the LUTs, for which the elements are preloaded with the reciprocal of q scaled by the appropriate feedback coefficient G,

$$q \xrightarrow{LUT_i} \frac{G_i}{q}. \tag{4.1}$$

There are four instances of the LUT logic, each loaded with a different value of G, allowing for up to two BPMs to be used as input to the feedback system. The LUTs have 13-bit address widths and 28-bit elements.

The signal sent to the kicker is a 14-bit binary number expressed in 'two's-complement' representation, thus describing a range of values between -4096 to +4095. Any DAC values lying outside this range saturate at either -4096 or +4095 to avoid positive values wrapping around to negative ones and vice versa. This correspondingly maps to a linear operating range for the kicker of $\pm 10\,\mu$m.

The timing of the signal sent to the kicker is fixed in the firmware to match the time required to integrate over 15 samples, regardless of how many samples are actually integrated. If fewer than 15 samples are integrated, the output is delayed so that the latency of the system is independent of the integration window. This is designed so that the decay of the kicker pulse signal at the arrival of the second bunch is independent of the number of samples integrated. This means that IPK does not need recalibrating when extending the integration window. If lower latency is required the firmware may be trivially changed to reduce the maximum integration window.

The feedback system can be configured to provide a constant DAC output to the kicker,

IPK, with the same timing structure as a feedback pulse; this is used for the kicker calibration. It is also possible to add a constant DAC value to the feedback output, and this can be used to adjust the transverse location at which the bunches are stabilised. The longitudinal location of stabilisation can be adjusted by scaling the feedback coefficients; this is described further in Section 4.2.2.

Multiplexers have been added so that it is straightforward to change which BPMs are used as input to the feedback calculation. Four multiplexers allow for any of the three BPMs to be used either individually or as a pair of BPMs. These are controlled through the `bpm_sel` register and changed through the LabVIEW DAQ.

Another new feature in the feedback firmware is the ability to provide a constant offset to the I, Q and q signals before they are used to calculate the bunch position. This feature affords more flexibility when handling the inherent voltage offset individual to each ADC channel. It can also be used for the removal of the position-independent baseline signals that are generated on each I and Q waveform at the second stage of the signal processing. The baseline component can be found by heavily attenuating the position signal and measuring the remaining I and Q signals. Once the baseline waveforms are characterised, the constant offset functionality can be used to minimise the signal amplitude of the samples to be used for the bunch position measurement. Example baseline waveforms, with a constant offset applied, are displayed in Fig. 4.3.

The baseline waveforms are expected to be flat DC signals, present whenever the reference signal has a sufficient magnitude to drive the second-stage mixer; this region is shown in Fig. 4.3 in blue. Consequently, the signal should resemble a step function. The Q waveforms for IPA and IPC show the expected shape with little variation in the signal amplitude from samples 25 to 65. For IPB, the Q waveform shows proportionally more variation in amplitude, as this signal is smaller. On the other hand, the I signal baselines show much more variation with sample number and do not exhibit the ideal step function behaviour. The cause of the variation in signal amplitude between samples 25 and 65 in the I signals is currently unknown but it is typically small compared with the size of the position signal (see Fig. 2.7).

4.1.3 Latency measurements

In order to determine the feedback latency, the system was exercised in constant DAC mode, while interleaving triggers with kick 'off' and 'on'. A delay was added to the kicker pulse fire-time and was incremented until the kick arrived too late to disturb the second bunch in

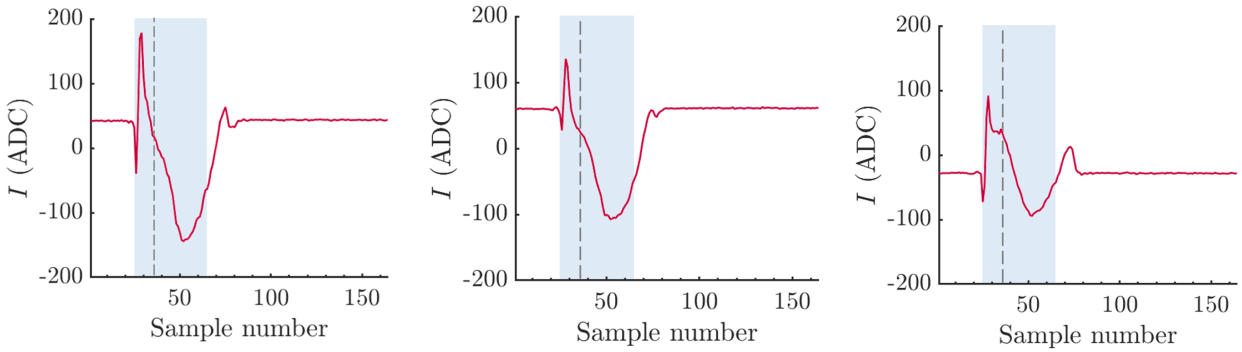

(a) IPA(I)

(b) IPB(I)

(c) IPC(I)

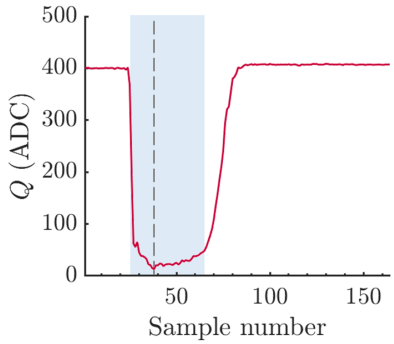

(d) IPA(Q)

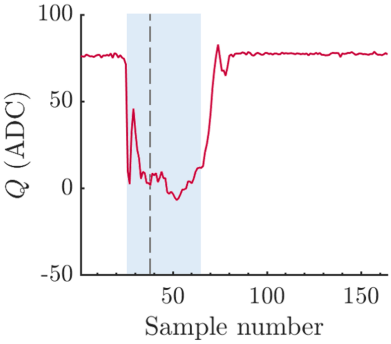

(e) IPB(Q)

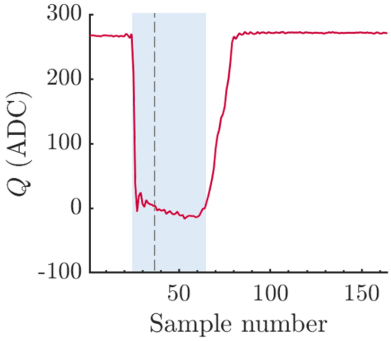

(f) IPC(Q)

Figure 4.3: Mean I and Q waveforms with 70 dB dipole signal attenuation. A constant value has been added to the I and Q waveforms to minimise the signal amplitude for sample 37 (marked by a dotted line). Without the constant offset, samples 1 to 20 have I and Q values of approximately zero. The blue rectangle shows the samples for which the signal amplitude should be similar.

the train. The deflection of bunch-2 was then measured as a function of the delay introduced. The latency is defined as the time between the first bunch entering the feedback system and the kicker pulse reaching 90% of its output value, where a kick of 2000 DAC counts was applied. The latency is therefore equal to the bunch spacing minus the delay required to reduce the kick by 10%.

Fig. 4.4, shows the deflection between the kicked and unkicked bunches as a function of the delay introduced to the signal sent to the kicker. The latency was determined with a sigmoid fit to the data of the form:

$$f(x) = p_1 + \frac{p_2 - p_1}{1 + 10^{p_3 - p_4 x}}, \tag{4.2}$$

where the coefficients from this fit are given in Table 4.2.

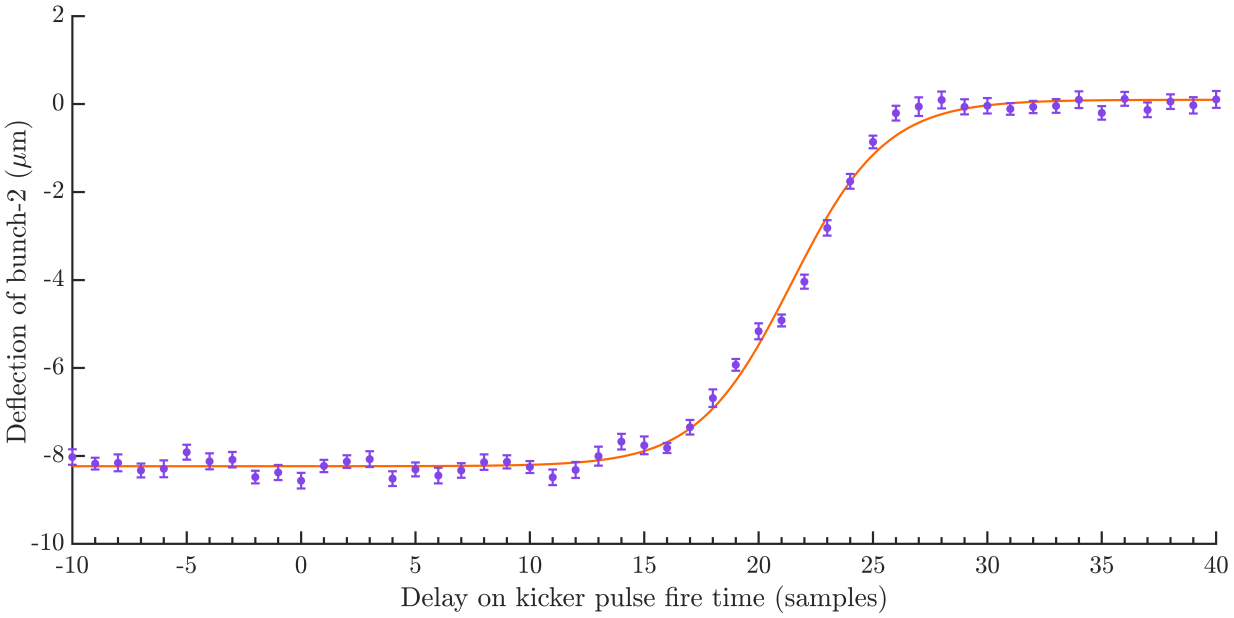

Figure 4.4: The deflection between the kicked and unkicked pulses as a function of the delay introduced to the signal sent to the kicker. The parameters of the sigmoid fit are given in Table 4.2.

From the sigmoid fit it was estimated that it would take a delay of 48 ns to reduce the kick to 90% of the nominal output value. The latency is therefore

$$280\,\text{ns} - 48\,\text{ns} = 232\,\text{ns}. \tag{4.3}$$

It should be noted that this latency includes the 15 sample delay introduced by integrating over the maximum number of samples allowed by the firmware. If reduced latency is required, the firmware may be trivially changed to reduce the maximum integration window.

A small sinusoidal variation can be seen in Fig. 4.4 even for regions where the deflection is expected to be constant, such as for delays of between -10 and $+10$ samples. This is thought

Table 4.2: Coefficients of the sigmoid fit from Eq. 4.2 to the data in Fig. 4.1.3. The χ^2 per degree of freedom for this fit is 1.9.

Coefficient	Value
p_1	-8.233
p_2	0.097
p_3	21.44
p_4	0.211

to be a result of the cooling water cycle at ATF2, which has a cycle length of approximately five minutes [75].

4.1.4 Kicker and kicker amplifier

Beam corrections were applied with a stripline kicker, IPK, that was designed in Oxford and manufactured at KEK. The signal from the FONT5A board requires amplifying before it can be used to drive the kicker; this is performed with custom-made kicker amplifiers, manufactured by TMD Technologies Ltd [76]. The stripline kicker, shown in Fig. 4.5, consists of two conducting strips, approximately 30 cm in length and separated by 24 mm, located at the top and bottom of the inside of the beampipe [42].

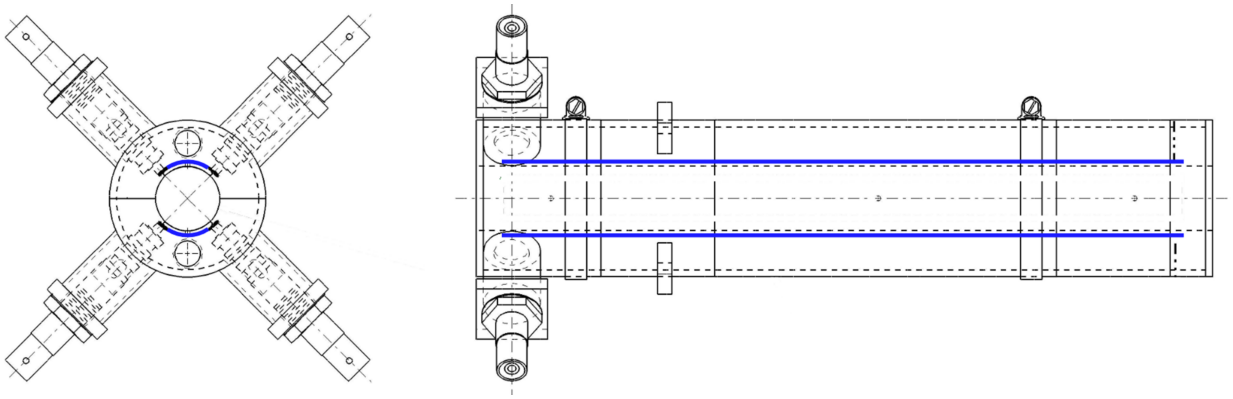

Figure 4.5: Transverse (left) and longitudinal (right) schematics of the stripline kicker [77]. The conducting strips are shown in blue.

The electrodes at the upstream end of the strips are both grounded and the electrodes at the downstream end are driven by opposite polarity signals from the FONT5A board. The conducting strips and the beampipe walls form two coupled transmission lines, so that when a current flows in opposite directions in the two strips, a traveling electromagnetic wave is induced between them, moving upstream. This electromagnetic wave will provide a

transverse kick to charged particles traveling in the opposite direction to the wave [78][79].

The amplifiers were designed with a fast rise time of 35 ns to reach 90% of the peak output, so as to meet latency requirements. The amplifiers are capable of a drive current of ±30 A [42].

4.2 Theory of feedback performance

To obtain the best feedback performance, the bunch-to-bunch position correlation must be maximised. With 100% correlation, the limit to the beam stabilisation is then set by the BPM resolution, $\sigma_{\text{res.}}$: this limit has been determined for both 1-BPM and 2-BPM feedback.

4.2.1 1-BPM feedback

To calculate the expected beam stabilisation, first consider the corrected bunch-2 positions, Y_2, in terms of the uncorrected bunch-1 and bunch-2 positions, y_1 and y_2,

$$Y_2 = y_2 - gy_1 + c, \tag{4.4}$$

where g is the feedback gain, and c is a constant offset which may be applied to the second bunch. Taking the variance of Eq. 4.4 gives

$$\sigma_{Y_2}^2 = g^2\sigma_{y_1}^2 + \sigma_{y_2}^2 - 2g\sigma_{y_1}\sigma_{y_2}\rho_{12}, \tag{4.5}$$

where ρ_{12} is the bunch-to-bunch position correlation, and σ_{Y_2}, σ_{y_1} and σ_{y_2} represent the jitters on positions Y_2, y_1, y_2 respectively.

The optimum gain setting, g^*, is defined as the gain which minimises the jitter σ_{Y_2}. This can be found by partial differentiation of Eq. 4.5 with respect to g,

$$2\sigma_{Y_2}\frac{\partial\sigma_{Y_2}}{\partial g} = 2g\sigma_{y_1}^2 - 2\sigma_{y_1}\sigma_{y_2}\rho_{12}, \tag{4.6}$$

and then by setting $\frac{\partial\sigma_{Y_2}}{\partial g}$ equal to zero,

$$0 = 2g^*\sigma_{y_1}^2 - 2\sigma_{y_1}\sigma_{y_2}\rho_{12}. \tag{4.7}$$

This can be rearranged to give

$$g^* = \frac{\sigma_{y_2}}{\sigma_{y_1}}\rho_{12}. \tag{4.8}$$

Consequently, when there is an imperfect bunch-to-bunch correlation, the gain should be scaled accordingly, so as to avoid overcorrecting bunch-2. Equally, if the jitters of the two bunches are different the gain must be adjusted to account for this.

In the resolution-limited case, for which $\sigma_{\text{res.}} \gg \sigma_{y_1}$ and $\sigma_{\text{res.}} \gg \sigma_{y_2}$, the measured correlation $\rho_{12} \to 0$, and the measured beam jitters $\sigma_{y_{1,2}} \to \sigma_{\text{res.}}$, as the resolution component dominates the measurement. These terms can be substituted into Eq. 4.5 to give

$$\sigma_{Y_2}^2 = \sigma_{y_1}^2 + \sigma_{y_2}^2 = 2\sigma_{\text{res.}}^2, \tag{4.9}$$

$$\sigma_{Y_2} = \sqrt{2}\sigma_{\text{res.}}. \tag{4.10}$$

For 1-BPM feedback, the resolution in this equation is the resolution of the feedback BPM.

4.2.2 2-BPM feedback

In order to predict the feedback performance for two BPMs, the positions in Eq. 4.4 would refer to the interpolated position measurements, $y_{\text{interp.}}$. Eq. 4.4 would then become

$$Y_{2_{\text{interp.}}} = y_{2_{\text{interp.}}} - y_{1_{\text{interp.}}} + c, \tag{4.11}$$

which after taking the variance gives

$$\sigma_{Y_{2_{\text{interp.}}}}^2 = \sigma_{y_{1_{\text{interp.}}}}^2 + \sigma_{y_{2_{\text{interp.}}}}^2 - 2\sigma_{y_{1_{\text{interp.}}}}\sigma_{y_{2_{\text{interp.}}}}\rho_{12_{\text{interp.}}}. \tag{4.12}$$

In the limit for which the resolution dominates the position measurement

$$\sigma_{Y_{2_{\text{interp.}}}}^2 = 2\sigma_{\text{res. interp.}}^2. \tag{4.13}$$

For the 2-BPM feedback studies presented in this report, measurements from IPA and IPC were used to stabilise the beam at IPB. The interpolated measurement at IPB, $y_{\text{B}_{\text{interp.}}}$, can be written in terms of the measured positions at IPA and IPC, scaled appropriately by the proportional longitudinal displacements of both BPMs from IPB [53]. The longitudinal offsets between the BPMs are given in Tab. 3.2.

$$\begin{aligned} y_{\text{B}_{\text{interp.}}} &= \frac{174.2}{174.2 + 80.8} y_{\text{A}} + \frac{80.8}{174.2 + 80.8} y_{\text{C}}, \\ &= 0.683 y_{\text{A}} + 0.317 y_{\text{C}}. \end{aligned} \tag{4.14}$$

Equation 4.14 can be used to determine a relationship for the interpolated jitter at IPB, $\sigma_{Y_{\text{B}_{\text{interp.}}}}$, in terms of the jitters at IPA and IPC. As for the 1-BPM case, if it is assumed that the jitters are significantly less than the resolution, the resolution-limit to the feedback performance is

$$\sigma_{Y_{\text{B}_{\text{interp.}}}}^2 = 0.683^2 \sigma_{\text{Y}_\text{A}}^2 + 0.317^2 \sigma_{\text{Y}_\text{C}}^2 = 0.567 \times 2\sigma_{\text{res.}}^2. \tag{4.15}$$

It is possible to write the measured jitter in terms of the true jitter, $\sigma^2_{\mathrm{Y_{B_{true}}}}$, and the resolution; this is done for both the measured IPB jitter ($\sigma^2_{\mathrm{Y_B}}$) and the jitter interpolated to IPB ($\sigma^2_{\mathrm{Y_{B_{interp.}}}}$),

$$\sigma^2_{\mathrm{Y_B}} = \sigma^2_{\mathrm{Y_{B_{true}}}} + \sigma^2_{\mathrm{res.}}, \tag{4.16a}$$

$$\sigma^2_{\mathrm{Y_{B_{interp.}}}} = \sigma^2_{\mathrm{Y_{B_{true}}}} + \sigma^2_{\mathrm{res.\ interp.}}. \tag{4.16b}$$

The true jitter for both cases is the same as this is a property of the beam and not of the measurement.

A substitution of $\sigma^2_{\mathrm{Y_{B_{true}}}}$ can be made from Eq. 4.16a to Eq. 4.16b, to give

$$\sigma^2_{\mathrm{Y_{B_{interp.}}}} = \sigma^2_{\mathrm{Y_B}} - \sigma^2_{\mathrm{res.}} + \sigma^2_{\mathrm{res.\ interp.}}. \tag{4.17}$$

$\sigma^2_{\mathrm{Y_B}}$ and $\sigma^2_{\mathrm{res.\ interp.}}$ are substituted from Eqs. 4.10 and 4.15 and the limit to stabilisation at IPB using 2-BPM feedback is

$$\begin{aligned} \sigma^2_{\mathrm{Y_{B_{interp.}}}} &= (2 - 1 + 0.567)\sigma^2_{\mathrm{res.}} \approx 1.6\sigma^2_{\mathrm{res.}}, \\ \sigma_{\mathrm{Y_{B_{interp.}}}} &\approx \sqrt{1.6}\sigma_{\mathrm{res.}}. \end{aligned} \tag{4.18}$$

This can be compared with the resolution-limit of 1-BPM feedback of $\sqrt{2}\sigma_{\mathrm{res.}}$, over which it offers a $\sim 12\%$ improvement.

The best feedback performance using two BPMs would be stabilisation of the beam waist half-way between IPA and IPC, with both BPMs contributing equally. In this configuration the resolution limit to stabilisation would be $\sqrt{1.5}\sigma_{\mathrm{res.}}$.

4.3 Derivation of feedback coefficients

For 1-BPM feedback, the beam position measurement, y, for bunch-1 is constructed from the sampled I, Q and charge, q, signals as

$$y = \frac{1}{k}\frac{I'}{q} = \frac{I}{q}\cos\theta_{IQ} + \frac{Q}{q}\sin\theta_{IQ}, \tag{4.19}$$

where k refers to the bunch-1 position calibration constant, and θ_{IQ} to the IQ phase angle [53]. Positions are calibrated by vertically scanning the beam through a known range of offsets relative to the BPM, and measuring the corresponding change in BPM signals, as described in Section 2.3. The beam was steered vertically by moving the final quadrupole, QD0FF [66].

The correction to be applied to bunch-2 is then $-y$, where an arbitrary constant value, c, may be added to change the transverse stabilisation location. The signal sent to the

kicker, V, is measured in DAC counts, thus requiring a calibration constant M (µm/DAC) to convert between V and the position offset induced, y,

$$V = \frac{-gy}{M} + c. \tag{4.20}$$

The feedback gain, g, is set to 1 for a beam with 100% bunch-to-bunch correlation and equal bunch-1 and bunch-2 jitters. If the bunch positions are not fully correlated, the gain should be scaled accordingly as in Eq. 4.8.

4.3.1 1-BPM feedback coefficients

For 1-BPM feedback with local beam stabilisation, the firmware determines a value for the kick, $V_{\text{1-BPM}}$, using a linear combination of the $\frac{I}{q}$ and $\frac{Q}{q}$ signals scaled by appropriate coefficients A_1 and A_2,

$$V_{\text{1-BPM}} = A_1\frac{I}{q} + A_2\frac{Q}{q}. \tag{4.21}$$

After substituting Eq. 4.19 into Eq. 4.20, the resulting equation is in the form of Eq. 4.21 and A_1 and A_2 can be extracted:

$$A_1 = \frac{-g\cos\theta_{IQ}}{Mk},\ A_2 = \frac{-g\sin\theta_{IQ}}{Mk}. \tag{4.22}$$

The firmware automatically assumes input from two BPMs and four feedback parameters, so that for 1-BPM operation, the appropriate two feedback parameters should be set to zero.

4.3.2 2-BPM feedback coefficients

For 2-BPM feedback, there is a linear interpolation of signals from IPA and IPC, so there are twice the number of feedback coefficients, denoted by B_i $(i = 1, 2, 3, 4)$,

$$V_{\text{2-BPM}} = B_1\frac{I_{\text{A}}}{q} + B_2\frac{Q_{\text{A}}}{q} + B_3\frac{I_{\text{C}}}{q} + B_4\frac{Q_{\text{C}}}{q}. \tag{4.23}$$

When operating the feedback system in this manner, IPB becomes a witness BPM at which the feedback performance can be independently verified.

As was the case for 1-BPM feedback, the signal sent to the kicker is proportional to the bunch-1 beam position, which, for 2-BPM feedback, is the interpolated position, $y_{\text{B}_{\text{interp.}}}$, from Eq. 4.14,

$$\begin{aligned} V_{\text{2-BPM}} &= \frac{-gy_{\text{B}_{\text{interp.}}}}{M_{\text{B}_{\text{interp.}}}}, \\ &= \frac{-0.683gy_{\text{A}} - 0.317gy_{\text{C}}}{M_{\text{B}_{\text{interp.}}}}. \end{aligned} \tag{4.24}$$

When determining the kicker calibration factor, $M_{\mathrm{B}_{\mathrm{interp.}}}$, the interpolated beam position is plotted against the DAC value sent to the kicker and the gradient ascertained. Eq. 4.19 is used to rewrite y_A and y_C to create an equation of the form of Eq. 4.23, from which the feedback parameters are extracted as coefficients of the $\frac{I}{q}$ and $\frac{Q}{q}$ terms,

$$\begin{aligned} B_1 &= \frac{-g \times 0.683 \cos\theta_{IQ}}{M_{\mathrm{B}_{\mathrm{interp.}}} k}, \; B_2 = \frac{-g \times 0.683 \sin\theta_{IQ}}{M_{\mathrm{B}_{\mathrm{interp.}}} k}, \\ B_3 &= \frac{-g \times 0.317 \cos\theta_{IQ}}{M_{\mathrm{B}_{\mathrm{interp.}}} k}, \; B_4 = \frac{-g \times 0.317 \sin\theta_{IQ}}{M_{\mathrm{B}_{\mathrm{interp.}}} k}. \end{aligned} \tag{4.25}$$

The LUT mechanism used within the firmware requires the feedback coefficients to be preloaded. For both modes of feedback, from Eqs. 4.22 and 4.25, these depend on the phase angle θ_{IQ}, the position calibration constant k and the kicker calibration factor, M. The values for k and θ_{IQ} can be calculated through position calibration of the BPMs, as described in Section 2.3.

4.3.3 Kicker calibration

A similar process of kicker calibration is required for both 1-BPM and 2-BPM feedback: the kicker is scanned through a range of constant DAC values and the corresponding shift in position at the desired location of stabilisation is determined. The difference between the two modes is that for 1-BPM feedback, the kicker scan is performed as a function of measured beam position, whereas for 2-BPM feedback it is as a function of an interpolated beam position.

The kicker calibration plots are given in Fig. 4.6, where Fig. 4.6(a) shows the kicker calibration for 1-BPM feedback using IPC, and Fig. 4.6(b) shows the kicker calibration for 2-BPM feedback, using measurements from IPA and IPC interpolated for beam stabilisation at IPB. The range of the scan of constant DAC values was determined by the dynamic range of the BPMs.

4.4 1-BPM IP feedback operation

The use of sample integration for 1-BPM feedback was tested with beam stabilisation at IPC. To determine the effect of the feedback, it was switched on and off for alternative bunches.

The longitudinal position of the beam waist can be shifted in the x and y plane by varying the strengths of the quadrupoles in the final doublet [66]. For 1-BPM feedback operation, the

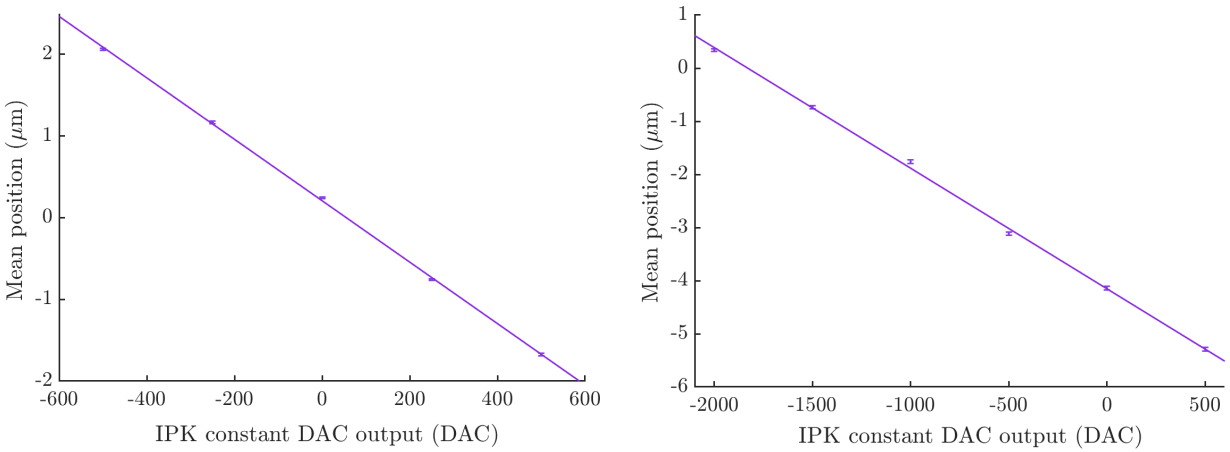

(a) (b)

Figure 4.6: Mean position of bunch-2 while operating IPK in constant DAC mode: (a) position measured at IPC and (b) position interpolated to IPB. A least-squares fit has been applied to both with gradients (a) $-0.0038 \pm 0.0002\,\mu\text{m/DAC}$ and (b) $-0.0022 \pm 0.0001\,\mu\text{m/DAC}$, and χ^2/d.o.f values (a) 0.34 and (b) 0.36.

data were collected with the waist close to IPC. The mean waveforms for the two bunches, with feedback off, are presented in Fig. 4.7.

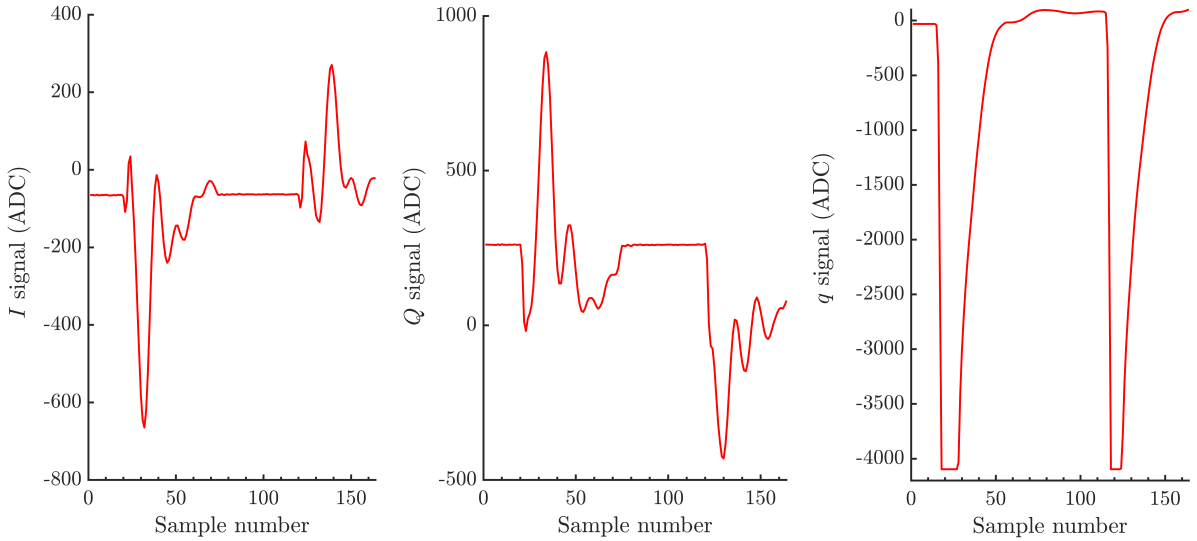

Figure 4.7: Digitised IPC waveforms versus sample number; (a) I signal, (b) Q signal and (c) q signal.

4.4.1 Bunch-to-bunch position correlation

The bunch-to-bunch position correlation can be measured using either a single sample or from an integrated sample window. The single-sample and integrated sample correlation measurements are presented in Figs. 4.8(a) and (b) respectively. The measured correlation depends on both the true correlation and the BPM resolution for the sample window. The resolution introduces a random component to the measured positions, which will reduce the measured correlation. By improving the resolution through sample integration, the measured correlation will be brought closer to the true correlation.

As shown in Fig. 4.8(b), sample integration increases the measured bunch-to-bunch position correlation, suggesting an improved resolution. From Fig. 4.8(a), it can be seen that there are single-sample correlation values which almost equal the performance of the integrated correlation values. The correlation measured from sample 33 had a value of 84.1%, close to the best integrated correlation of 85.1%. Selecting the single sample for feedback which gives the best correlation is not always possible. This sample may vary between data sets and is particularly susceptible to the random fluctuations that occur during digitisation. Sample integration averages over much of the thermal and electronic noise so that the correlation has less dependence on the exact sample numbers used and is more consistent between data sets.

4.4.2 Optimising the gain

The IP feedback algorithm stabilises the beam by removing the jitter that is correlated between consecutive bunches. In practice, the bunches are not fully correlated and the gain, g, accounts for this. Measurements of the bunch-2 jitter were made while operating feedback with a range of gains in a 'gain scan'. The optimal gain determined by this scan was $g = 0.95$, and the feedback coefficients used were: $A_1 = -101$ and $A_2 = -46$.

The optimum gain setting was further corroborated in offline analysis, where the feedback performance with different gain settings was simulated using the triggers with feedback off. The performance of the simulated feedback is shown in Fig. 4.9 as a function of the feedback gain, with the optimum gain found to be 0.93. This is consistent with Eq. 4.8, for bunch jitter and correlation values $\sigma_{y_1} = 109$, $\sigma_{y_2} = 119$ and $\rho_{12} = 0.85$:

$$\frac{119}{109} \times 0.85 = 0.93. \tag{4.26}$$

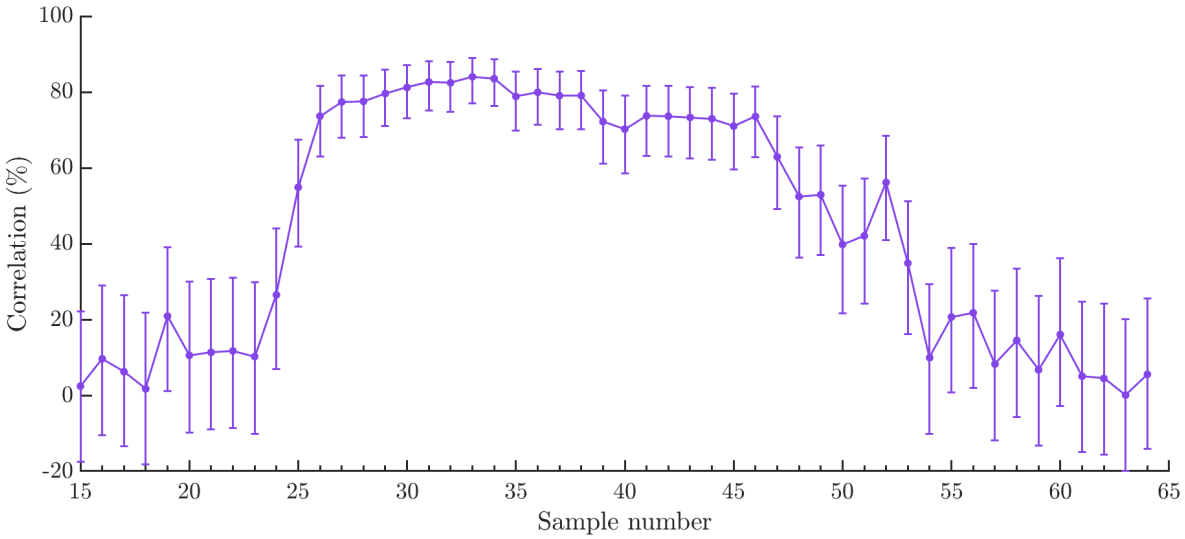

(a)

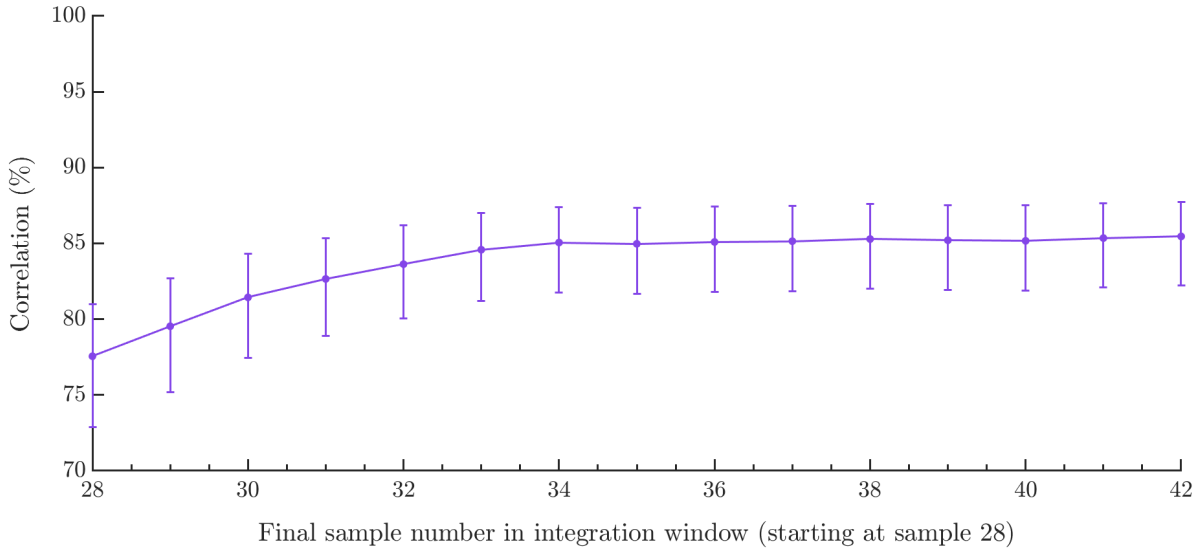

(b)

Figure 4.8: Bunch position correlation versus (a) sample number and (b) sample integration window. The error bars indicate the one-sigma confidence interval.

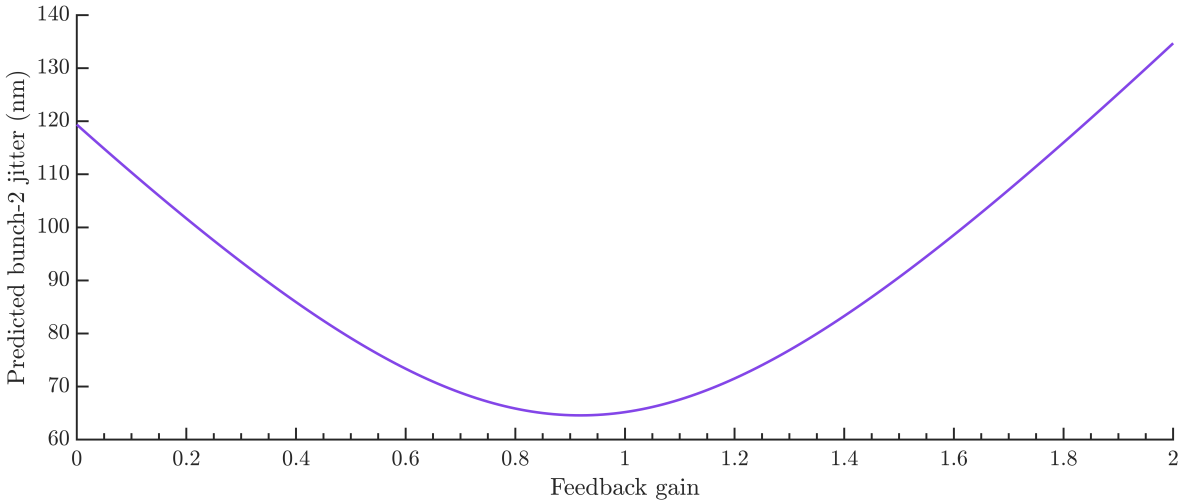

Figure 4.9: Simulation of the optimum gain setting for 1-BPM feedback using position measurements for triggers with feedback off: the line shows predicted bunch jitter versus simulated gain. The optimum gain is the one which minimises the bunch-2 jitter; this was found to be 0.93 with a corrected bunch-2 jitter of 65 nm.

4.4.3 Feedback results

The best results measured for 1-BPM feedback with sample integration are shown in Fig. 4.10 and Table 4.3. The feedback was operated and the data were analysed with an integration range of samples 28 to 37. The data were collected on the 12th of December 2017.

The position jitter of the first bunch was unchanged with feedback as this bunch was only measured and not corrected. The second bunch showed both a reduction in jitter and in mean position offset. The remaining mean bunch-2 offset stems from the initial offset between bunch-1 and bunch-2 and can be trivially adjusted by including a constant offset, c (Eq. 4.20).

Table 4.3: Position jitter and bunch-to-bunch position correlation with feedback off and on, for 1-BPM feedback.

Feedback	**Position jitter (nm)**		**Correlation (%)**
	Bunch-1	**Bunch-2**	
Off	109 ± 11	119 ± 12	$85.1^{+2.5}_{-3.5}$
On	118 ± 12	50 ± 5	$-26.0^{+9.8}_{-8.8}$

The feedback performance was reduced by having an imperfect bunch-to-bunch position correlation. The correlation with feedback off was reasonably poor at $85.1^{+2.5}_{-3.5}\%$. The effect

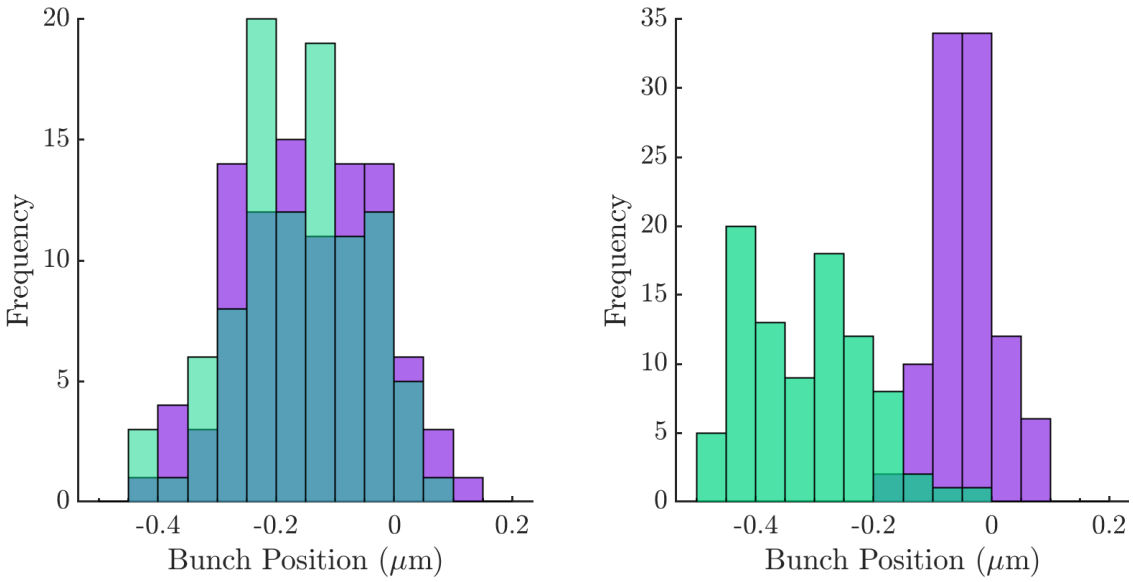

Figure 4.10: Distribution of bunch positions measured at IPC, for bunch-1 (left) and bunch-2 (right) with feedback off (green) and feedback on (purple).

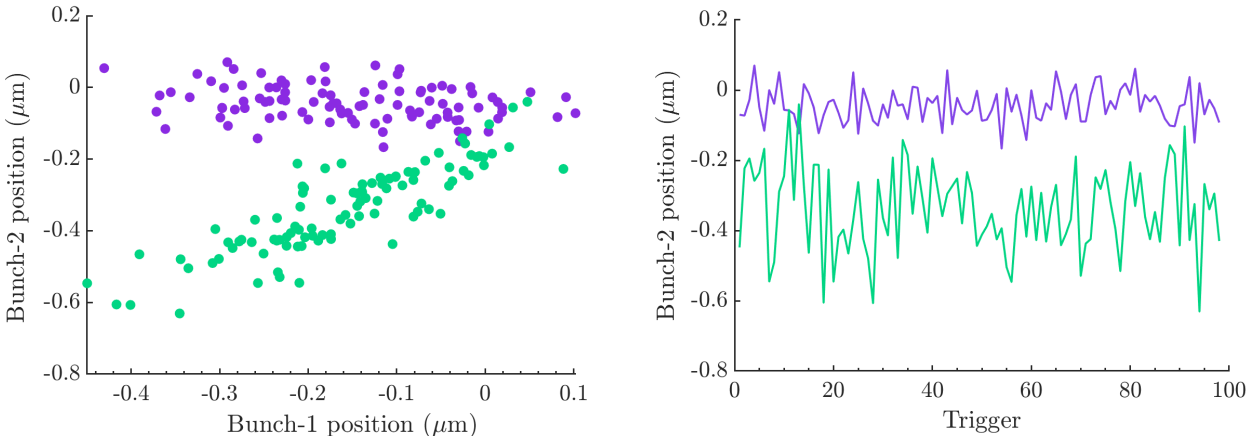

(a) (b)

Figure 4.11: (a) IPC bunch-2 position versus bunch-1 position and (b) bunch-2 position versus trigger number; for feedback off (green) and feedback on (purple).

of the feedback on the bunch-2 positions is shown in Fig. 4.11, as a function of the bunch-1 position and the trigger number. The effect of the feedback can be seen in Fig. 4.11(a) as a rotation of the distribution of data points, to minimise the spread of bunch-2 positions. The slight overcorrection to $-26.0^{+9.8}_{-8.8}$ correlation can be seen in the negative slope of the data points with feedback on. This suggests an improved performance may be possible with a lower feedback gain. Fig. 4.11(b) shows that there are no slow position drifts corrupting the jitter measurement and the feedback performance is consistent throughout the dataset.

The feedback system stabilised bunch-2 to 50 ± 5 nm. However, from Eq. 4.5, given the jitter and correlation of the uncorrected bunches, the feedback was predicted to stabilise the beam to 65 nm (see Fig. 4.9). The actual performance exceeded the predicted level of stabilisation, suggesting the measured incoming bunch-to-bunch correlation was considerably lower than the true correlation, where the results are consistent with a correlation of 91%. This is probably as a result of the BPM resolution introducing an error to the position measurements which would reduce the measured correlations.

4.5 2-BPM IP feedback operation

4.5.1 High-beta optics

When performing 2-BPM feedback, high-beta optics were used with a β^*_y value 1000 times the nominal value. In this configuration, there is a reduced divergence at the IP so that the beam jitters at IPA and IPC are smaller, making alignment of the beam within the BPMs' dynamic range easier. The amplitudes of the BPM waveforms were minimised by reducing the position and angle offset of the BPMs with respect to the beam. The process of BPM alignment was complicated by IPA and IPB being mounted on a common mover block so that they could not be moved independently. There was also an offset of ~ 100 nm between the positions of the two bunches in a train at IPB, so that aligning both bunches simultaneously was not possible. The I, Q and q waveforms for the three BPMs with feedback off are presented in Fig. 4.12.

The bunch trajectories for bunch-1 and bunch-2 are displayed in Figs. 4.13(a) and (b) respectively, for many consecutive triggers. For the bunch-1 trajectories, the jitters were approximately 270 nm, 110 nm and 360 nm at IPA, IPB and IPC, respectively. The corresponding jitters for bunch-2 were approximately 220 nm, 100 nm and 290 nm, respectively. The jitters for bunch-1 and bunch-2 were similar which was beneficial for the feedback performance. However, having different trajectories for bunch-1 and bunch-2 made alignment

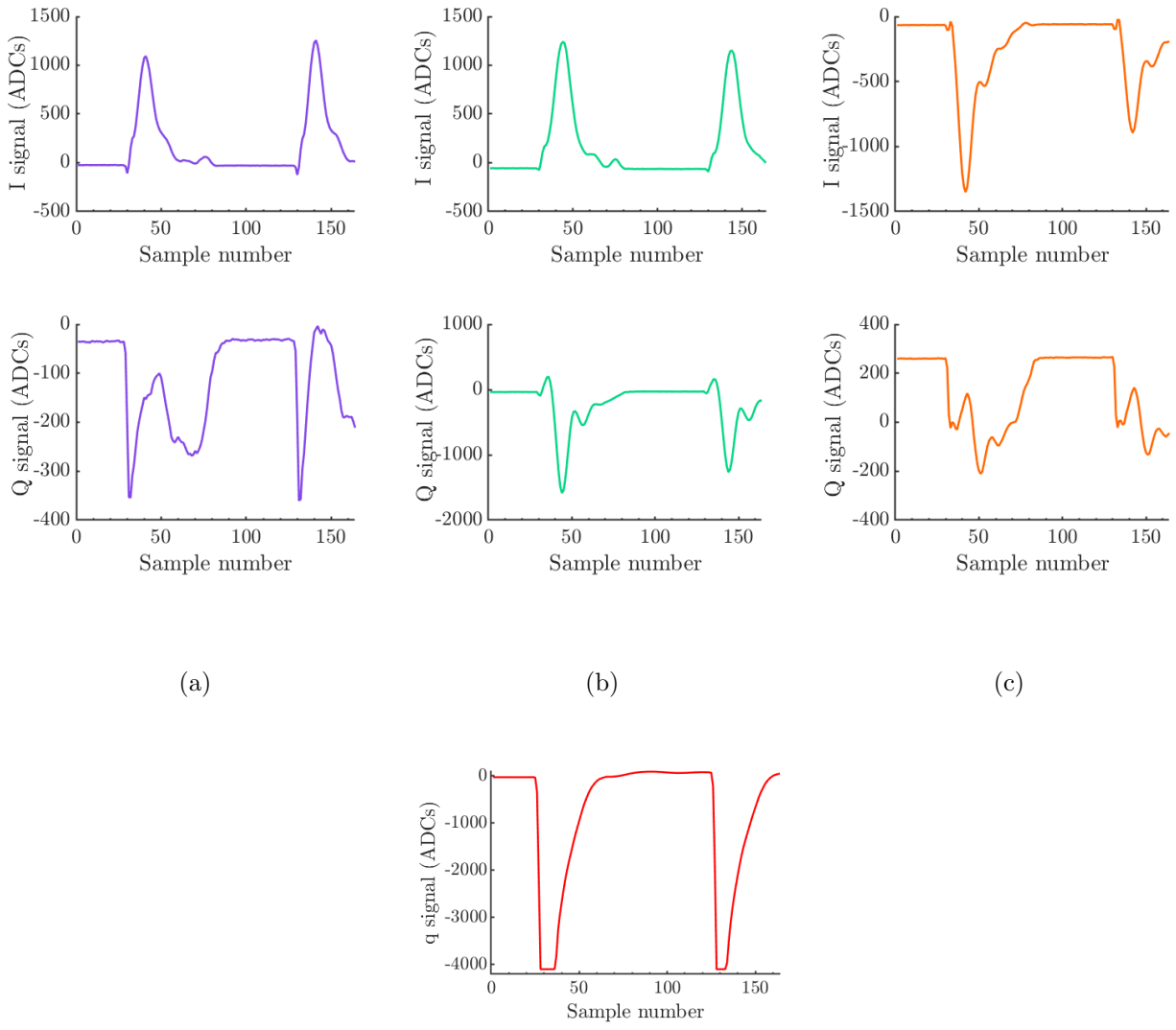

Figure 4.12: I and Q signal waveforms for (a) IPA, (b) IPB and (c) IPC and (d) the reference q signal.

of the bunches within the BPMs' dynamic ranges more difficult.

The interpolated jitter for bunch-1 is shown in Fig. 4.13(c), from which the estimated jitter on waist was ~ 95 nm at a distance of 16 mm from IPB. The interpolated jitters are in close agreement for the three different configurations shown in Fig. 4.13(c), suggesting the calibration constants for the three BPMs are accurate.

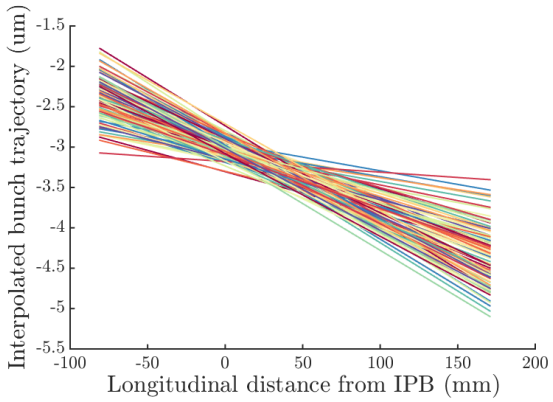

(a)

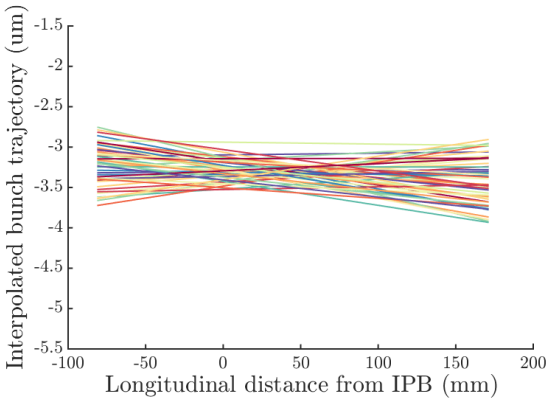

(b)

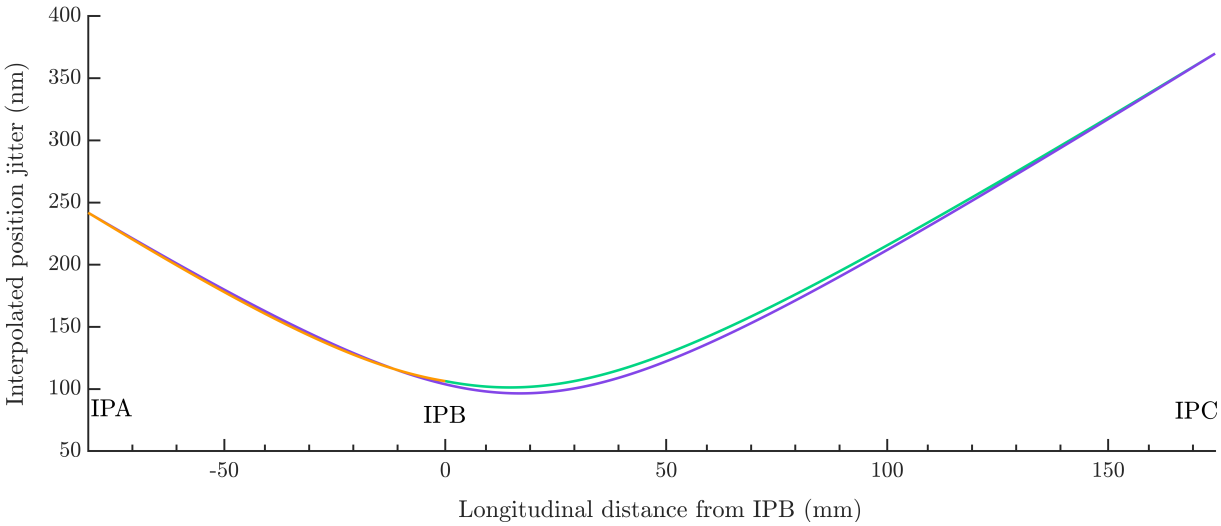

(c)

Figure 4.13: The trajectories of (a) bunch-1 and (b) bunch-2, interpolated from bunch position measurements at IPA and IPC; (c) the interpolated bunch-1 position jitter as a function of longitudinal position, with interpolation between IPA and IPC (purple), IPA and IPB (orange) and IPB and IPC (green).

4.5.2 Optimising the resolution

The single-sample resolution was used to analyse which sample numbers have a good signal-to-noise ratio, and how the resolution degrades with the decaying signal level across the waveform. The resolution is predicted to scale inversely with the bunch charge [53][60] and as the charge of bunch-2 was $\sim 75\%$ of the bunch-1 charge, the resolution was correspondingly poorer. The single-sample geometric resolution versus sample number is shown in Fig. 4.14. It can be seen that the resolution becomes worse as the signal decays and that the resolution for bunch-2 is systematically worse than for bunch-1. The oscillatory shape is caused by variations in the signal-to-noise ratio and can also be observed in the calibration constant versus sample number (Fig. 3.4(a)).

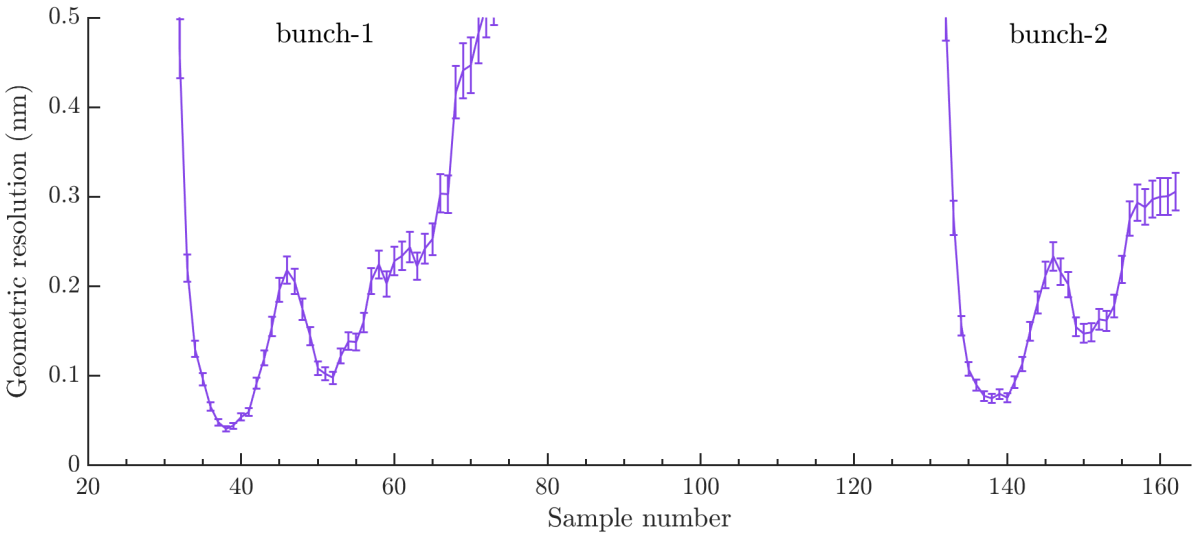

Figure 4.14: Single-sample geometric resolution versus sample number. The data points show the resolution, the lines join the data points and the error bars show the statistical uncertainty on the resolution. Samples with resolutions worse than 500 nm have been cut for data display purposes as these represent samples with little to no bunch information.

For the best feedback performance, it is critical to optimise the BPM resolution (Eq. 4.15). By considering the resolution for a range of sample integration windows, the one which optimises the resolution can be determined; this is shown in Fig. 4.15. The best geometric and fitted resolutions were found to be for sample windows located before the peaks of the I and Q waveforms (Fig. 4.12). This suggests that there were saturation effects degrading the resolution for the peak I and Q samples. It also explains why the resolution improves for some of the sample windows when including later samples, for which the signal levels are lower. The optimum sample window is 36 to 40, for which the geometric resolution is 31.2 nm. From Eq. 4.15, with this resolution the best possible 2-BPM feedback performance

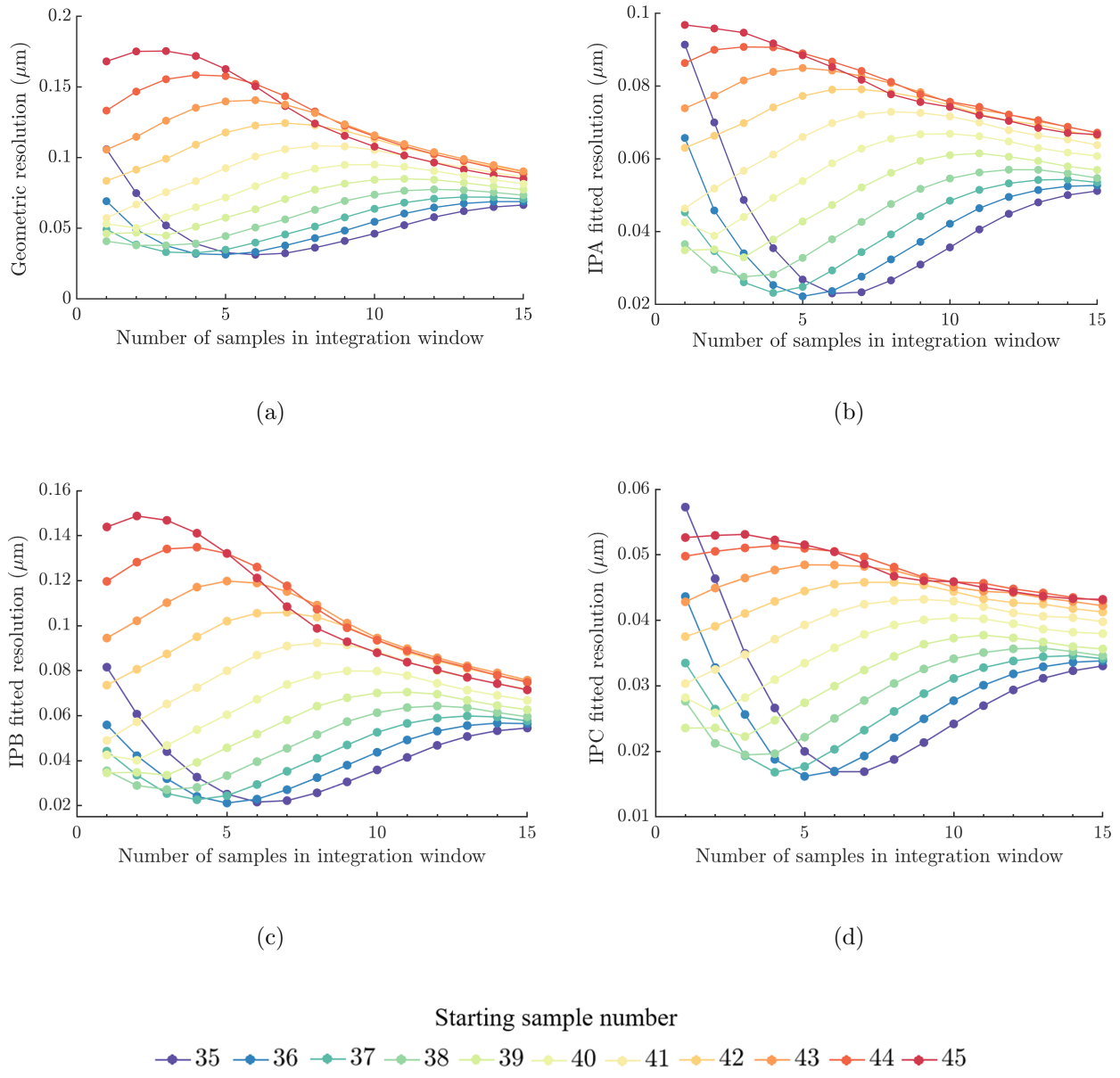

Figure 4.15: (a) Geometric, (b) IPA fitted, (c) IPB fitted, (d) IPC fitted resolution estimates for a range of integration windows. The width of the integration window is given by the x-coordinate and the sample number at which the window starts is denoted by the colour of the data points, for which the corresponding legend is shown below the plots. The fitted resolution was calculated by fitting to bunch positions for bunch-1.

would be $\sqrt{1.6} \times \sigma_{\text{res.}} \approx 39\,\text{nm}$ stabilisation.

The fitted resolution as a function of sample window shows a similar pattern as the geometric resolution; although there is a slight disagreement between the geometric and fitted resolution estimates. This is symptomatic of higher signal levels leading to non-linearities in the system which would degrade the feedback performance.

4.5.3 Bunch-to-bunch position correlation

The bunch positions at IPB can be determined by either direct measurement or by interpolation. Similarly, the bunch-to-bunch position correlation can either be measured at IPB directly or interpolated. The measured correlation will tend towards the actual correlation as bunch position measurements become more precise.

Figs. 4.16 shows the measured bunch-to-bunch correlation as a function of sample number for both the directly measured and interpolated cases. As expected, the correlation is low before the bunch arrives and after the position signal has decayed away. Fig. 4.17 shows the equivalent plot but as a function of integration window. The correlation calculated using interpolation is higher than the correlation directly measured at IPB, with a longer period of high correlation before it decays away. The highest single-sample correlations were $71.8^{+5.7}_{-8.6}\%$ and $89.7^{+2.2}_{-3.7}\%$, for the measured and interpolated cases respectively, which increased to $91.6^{+1.8}_{-3.1}\%$ and $96.1^{+1.0}_{-1.7}\%$ when sample integration was used.

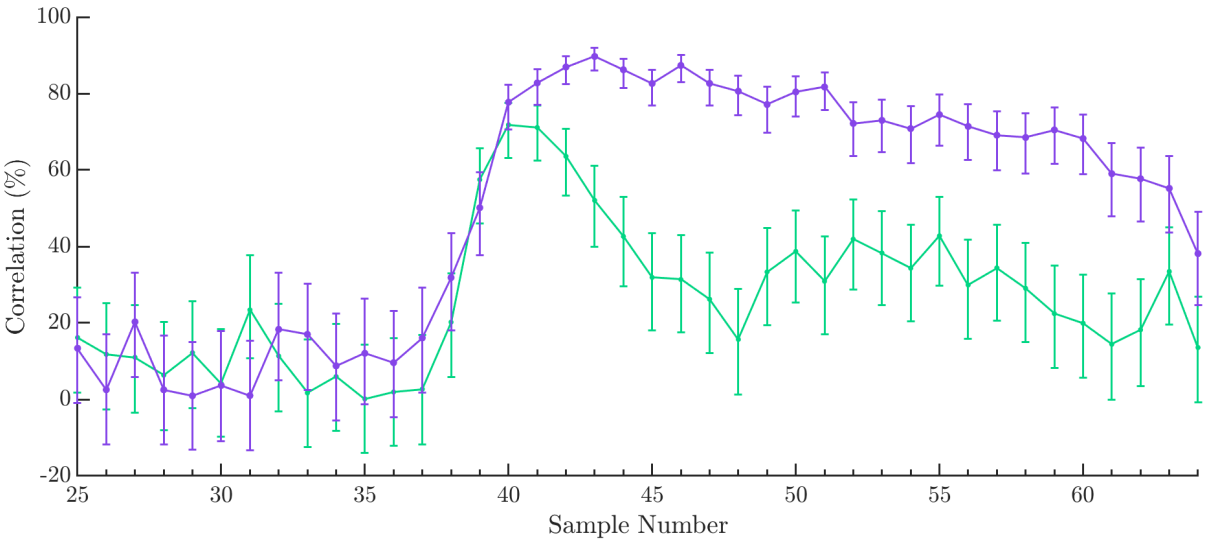

Figure 4.16: Single-sample measurements of bunch-to-bunch position correlation for measured IPB bunch positions (green) and measurements interpolated to IPB (purple). The error bars indicate the one-sigma confidence interval.

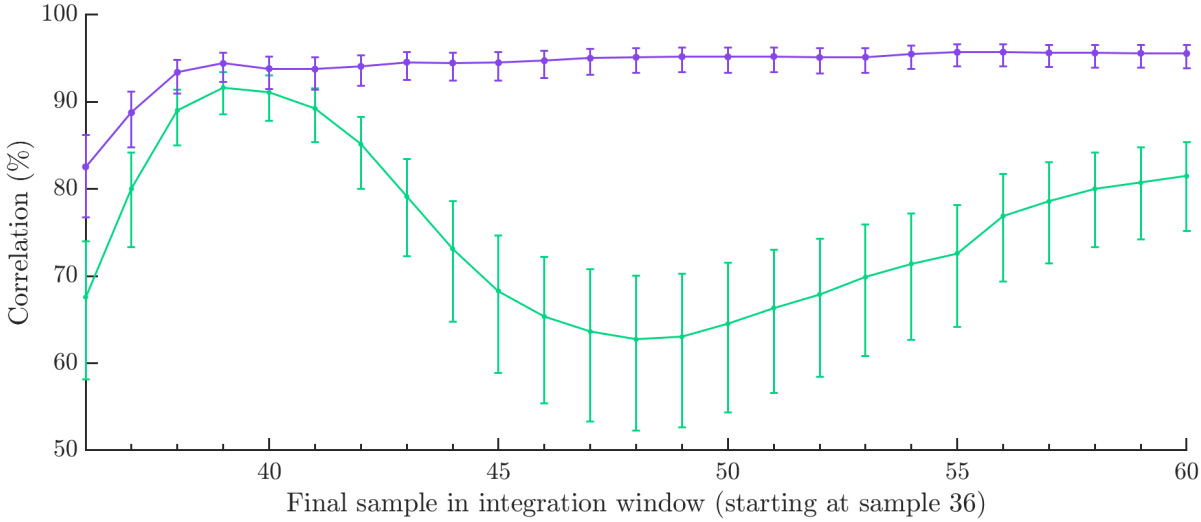

Figure 4.17: Integrated-sample measurements of bunch-to-bunch position correlation for measured IPB bunch positions (green) and measurements interpolated to IPB (purple). The x-axis shows the final sample in an integration window beginning at sample 36. The error bars indicate the one-sigma confidence interval.

For the interpolated case, the correlation using sample integration continues increasing, even to a 25-sample integration window. The measured IPB correlation, on the other hand, started to decrease for sample windows extending beyond sample 39. Although, after sample 45, the interpolated single-sample correlation decreases, the weighting given to these values in integration also decreases because the position signal is lower at these sample numbers. This implicit weighting of different sample numbers during integration can offer an improvement to the measured correlation even when including sample numbers with sub-optimal correlation.

4.5.4 Predicted feedback performance

The feedback performance can be predicted while taking into account the imperfect correlation and the differences in bunch-1 and bunch-2 jitters. The expected performance was calculated using Eq. 4.5 for a range of sample integration windows. For each width of integration window, the window location giving the best resolution was used (as calculated in Section 4.5.2); the results are presented in Table 4.4. Both the resolution and the predicted feedback performance are seen to benefit from sample integration when compared with single-sample mode. The best predicted single-sample performance was stabilisation to 62.4 nm, whereas the best predicted performance overall was for a five-sample integration window and was stabilisation to 40.1 nm. The predicted performance is consistent for windows of four to six samples but degrades for longer sample windows when the samples at

the peak of the I and Q waveforms are included. The five-sample resolution of 31.2 nm is poorer than the best achieved resolution of 19 nm (Table 3.4); with a 19 nm resolution the predicted feedback performance would be stabilisation of up to ~ 25 nm.

Table 4.4: Predicted feedback performance for a range of widths of integration window, with the window located so as to optimise the geometric resolution.

Window width	Res. (nm)	Pred. performance (nm)	Sample window
1	40.8 ± 2.9	62.4 ± 5.2	38
2	37.9 ± 2.7	58.0 ± 5.4	38 to 39
3	33.1 ± 2.3	48.2 ± 5.2	37 to 39
4	31.9 ± 2.3	40.4 ± 5.3	36 to 39
5	31.2 ± 2.2	40.1 ± 5.5	36 to 40
6	31.2 ± 2.2	40.4 ± 5.2	35 to 40
7	32.3 ± 2.3	42.4 ± 5.3	35 to 41
8	36.2 ± 2.6	53.4 ± 5.1	35 to 42
9	41.0 ± 2.9	67.9 ± 8.7	35 to 43
10	46.1 ± 3.3	82.5 ± 9.0	35 to 44

4.5.5 Feedback results

Feedback was performed using the five-sample integration window which optimised the resolution, 36 to 40 (Table 4.4). The feedback results achieved in this configuration are shown in Fig. 4.18 and Table 4.5. The feedback has reduced the bunch jitter to 41 ± 4 nm, in excellent agreement with the predicted stabilisation of 40.1 nm (Table 4.4). The mean bunch-2 position has been shifted by 2 µm, which is an artifact of the relative offsets between the three BPMs and can be removed by using the constant offset, c from Eq. 4.20. For future operations, this constant offset is recommended to bring the corrected bunch-2 mean position in line with the bunch-1 mean position, so that both bunches can be well-aligned with the BPMs simultaneously.

From Table 4.5, it can be seen that the correlation was not fully removed with feedback. The feedback gain was $g = 0.8$ which was optimised experimentally. The feedback-on correlation of $41.3^{+9.1}_{-12.3}$% suggests that with a higher gain, the feedback performance could be improved and further analysis determined that the optimum gain would be ~ 0.83. The feedback system was tested on bunch trains with a correlation of $91.6^{+1.9}_{-3.2}$ but, ideally, the

system would be tested on trains with a higher bunch-to-bunch correlation to demonstrate the best stabilisation.

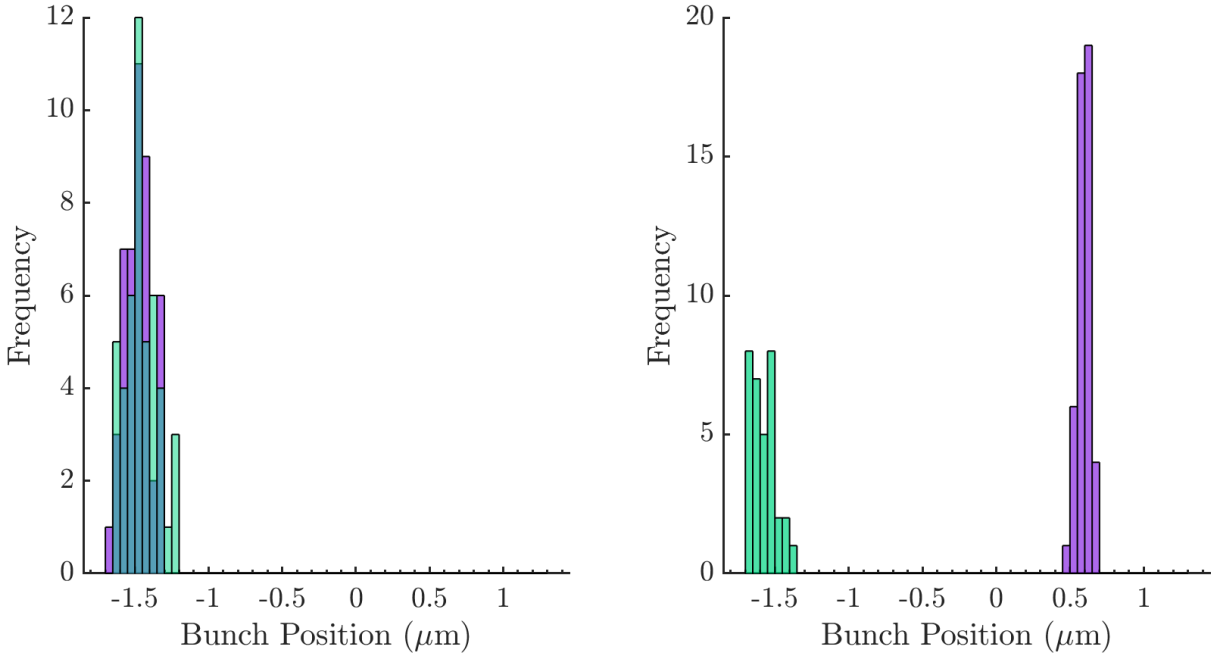

Figure 4.18: Distribution of bunch-1 (left) and bunch-2 (right) positions measured at IPB, with feedback off (green) and feedback on (purple). Feedback was performed in 2-BPM mode, stabilising at IPB using beam position measurements from IPA and IPC.

Table 4.5: Position jitters and bunch-to-bunch correlation with feedback off and on, for 2-BPM feedback.

Feedback	**Position jitter (nm)**		**Correlation (%)**
	Bunch-1	**Bunch-2**	
Off	106 ± 11	96 ± 10	$91.6^{+1.8}_{-3.1}$
On	100 ± 10	41 ± 4	$41.3^{+9.1}_{-12.3}$

4.6 Summary

This chapter introduced the FONT ATF2 IP feedback system and presented the latest results for two different feedback modes. The FONT5A digital board used for signal digitisation and the feedback calculation was presented, with a description of the components on the board, including the ADCs, DACs and a Virtex-5 FPGA. The feedback firmware was introduced and recent improvements made to the firmware discussed. It was demonstrated in Chapter

3 that the resolution could be improved with the use of sample integration. Previously, however, it was only possible to perform feedback using single-sample calculations because of restrictions in the feedback firmware. Improvements were made to the firmware to allow for the use of an integrated sample window during the bunch position calculation. The firmware was measured to operate with a system latency of 232 ns, when integrating up to 15 samples. The stripline kicker used to implement the feedback correction was introduced and the kicker calibrations were presented for two different feedback configurations.

The new firmware was tested with two different feedback modes, using either one or two BPMs as the input to the feedback system. For 1-BPM feedback, the best result achieved was stabilisation to 50 $\pm$ 5 nm, which was performed with a nominal optics configuration. The best result for 2-BPM feedback was stabilisation to 41 $\pm$ 4 nm, which was achieved with a high-beta optics configuration so that the beam could be aligned within the dynamic range of the two feedback BPMs simultaneously.

The 1-BPM feedback performance exceeded predictions, suggesting the bunch-to-bunch correlation measurement of 85.1% was an underestimation. The 2-BPM feedback performance, on the other hand, showed very good agreement with the predicted performance of 40.1 nm stabilisation. Both of these results show an improvement over the single-sample feedback performance. For the best demonstrated resolution of 19 nm and with 100% bunch-to-bunch correlation it would be predicted that stabilisation to 25 nm should be possible with the current feedback system and firmware. For the best feedback performance, it is important to have a good alignment of both bunches with any active BPMs. For future studies, any inherent offset between the two bunches in a train could be removed with a constant kick from an upstream feedback system.

Chapter 5

Feedback algorithms for the ILC

Results from the FONT ATF2 extraction-line feedback system have demonstrated that the latency, resolution and kick requirements for the ILC can be met [42]. In this chapter, simulations are detailed in order to confirm that such a feedback system could operate to help achieve the design value for the luminosity of the 500 GeV ILC baseline design. Variations in the beam parameters, such as the bunch length, emittance and intensity would affect the performance of the feedback system and, as such, must all be studied with simulations.

A model of the beam transport through the Main Linac (ML) and Beam Delivery System (BDS) was used to investigate the importance of various beam effects. In particular, the position jitter introduced by the damping ring (DR) extraction kicker was considered, alongside short-range and long-range wakefield effects and various models of ground motion.

Studies are also presented towards the development of suitable feedback algorithms for the ILC. When simulating the performance of feedback algorithms, important considerations included the magnitude of the offset at the IP and the bunch-to-bunch position correlation. The limits to the feedback system were probed using bunch trains with a range of internal structures and recommendations on appropriate feedback algorithms are given.

5.1 Beam effects in the ILC

In order to achieve the ILC design luminosity, the beam must be transported from the DR to the IP without excessive emittance growth. This requires tight tolerances on the alignment and stability of the beamline components. Mechanisms which particularly contribute to jitter at the IP are described here; these must be considered when optimising the luminosity.

5.1.1 DR extraction kicker

Bunch trains are compressed so an entire train can fit within the DR without it having an unreasonably large circumference, as the un-compressed trains are 300 km [34]. The bunch trains must then be decompressed before they enter the ML so the average current in the ML stays below acceptable limits. To achieve this decompression, bunches are extracted individually from the DR with individual pulses of a fast extraction kicker, at a frequency corresponding to the desired bunch spacing. As a result of the individual extraction, any shot-to-shot instability in the kicker-pulse magnitude will introduce transverse bunch jitter [80].

The DR extraction is performed horizontally as the tolerance for stability is lower in this plane due to the larger horizontal bunch size. Spurious vertical components of the kick, along with x-y coupling, might also be expected. As well as bunch-to-bunch variations being introduced, slow drifts across the bunch train could also occur [36]. To mitigate these effects, both horizontal and vertical feed-forward loops are proposed and would operate in the turnaround of the RTML (see Fig. 1.5) [36]. Any jitter introduced by the extraction kicker which is uncorrelated between consecutive bunches cannot be corrected with intra-train feedback, which would instead amplify it.

The intra-train feed-forward system would utilise a pair of BPMs at the end of the return line (shown as LTL in Fig. 1.5) and a fast kicker downstream of the turnaround [34][52]. The turnaround time of 0.5 µs is sufficient for the bunch position measurement, signal processing, and the implementation of a feed-forward correction on the same bunch [36]. This is intended to stabilise the beam so that the effect on the beam jitter when propagated to the IP is within 10% of the beam size [81] .

5.1.2 Wakefield effects

The low emittance achieved within the DR must be conserved during transport through the RTML, ML and BDS and consequently the effect of wakefields must be considered. Short-range wakefields would distort the bunch shape, thus degrading the luminosity, and long-range wakefields would introduce bunch-to-bunch offsets within the train. After extraction from the DR, the design values for the horizontal and vertical normalised emittances are 8 µm and 24 nm respectively. The tolerances on the emittance growth permit maximum horizontal and vertical emittances at the IP of 10 µm and 35 nm respectively.

In the BDS, resistive-wall wakefields are excited behind each charged bunch as it interacts

with the beam pipe and they provide a transverse kick to the tail of the bunch [82][83]. Short-range wakefields are also generated in the ML accelerating cavities by the heads of the bunches that reduce the accelerating gradients seen by the tails. This spectrum of gradients produces a spread in energy which varies longitudinally across the bunch, causing E-z coupling. Wakefields could also cause a transverse kick to the tail of the bunch, creating offsets which vary longitudinally, i.e. so-called 'banana-bunches'. Wakefields are induced at transitions between beam pipes which, when combined with transverse beam jitter, will act to increase the emittance. Consequently, in order to meet the design values for the emittance, wakefields must be minimised by considering the beam-pipe material, aperture and any transitions between beam pipes [82].

For the ILC, scans of luminosity as a function of beam position and angle can be used to help maximise luminosity, even in the presence of banana-bunch effects. During operation, the luminosity can be estimated by the ILC beam calorimeter which performs measurements of the integrated energy of the electron-positron pairs produced during collision [84]. The beam calorimeter forms part of the fast beam-diagnostics, with measurements taken after every bunch crossing.

Long-range wakefields refer to the disruption of a train by the leading bunches. The wakefields created by the first bunches impart a transverse kick to subsequent bunches and increase the emittance of the train by deflecting bunches off-axis [85]. The effect of long-range wakefields can be written as a sum of individual modes, such that the wake potential $W(t)$ is

$$W(t) = 2\sum_{\mathrm{p}} K_{\mathrm{p}} \sin(\omega_{\mathrm{p}} t) e^{-\frac{\omega t}{2Q_{\mathrm{p}}}}, \tag{5.1}$$

where the modes are denoted by p, $\frac{\omega_{\mathrm{p}}}{2\pi}$ is the frequency of mode p, K_{p} is the kick factor and Q_{p} is the damping Q factor [86].

The beam disruption from long-range wakefields is to be mitigated by a 'train straightener' at the entrance to the BDS, comprising a double-loop kicker and BPM system for bunch-by-bunch correction of the vertical position and angle [87]. This is designed to reduce wakefield effects to below 10% of the jitter of the beam position and angle [88].

5.1.3 5 Hz cascaded feedback system

Previous studies have determined that throughout the ML and BDS the beam jitter should be kept less than the beam size [89]. This tolerance is required to minimise the emittance growth from wakefield effects and to minimise the effect of the position jitter on Dispersion Free Steering (DFS) [89]. In particular, the beam jitter at the end of the ML was specified to

be less than 50% of the beam size. To help maintain the beam jitter within acceptable limits, a 5 Hz cascaded feedback system is proposed to stabilise pulse-by-pulse orbit variations.

The cascaded feedback system for the ML consists of 5 feedback loops, each with 8 BPMs and 4 correctors in both the x and y planes. A single feedback loop is proposed for the BDS, with 9 BPMs and 9 dipole correctors [89]. They are configured such that each loop transfers information to the nearest downstream loop, so as to avoid overcorrection of orbit perturbations.

Simulations were performed to test 5 Hz feedback with the use of a Kalman filter [90]. A Kalman filter describes an algorithm used to extract more accurate estimates of state variables from a series of noisy measurements [91]. Estimations of state variables are constructed from predictions and measurements combined as a weighted average. The lower the uncertainty of an estimate, the higher the weighting given to it. By applying a Kalman filter to the data during feedback, a more accurate estimation of the bunch position can be made, thus improving stabilisation. It was determined that 5 Hz feedback could be used to increase the luminosity from 17% to 84%, with the main loss to luminosity stemming from ground motion effects in the BDS [89].

Vibrations at frequencies above 5 Hz cannot be stabilised with pulse-by-pulse feedback and require the use of a fast intra-train feedback system. Similarly, due to its location, any beam offset introduced by Final Doublet vibrations can only be removed with IP feedback. The tolerance on the relative stability of the quadrupoles in the Final Doublet is ~ 100 nm, with jitter which would correspond one-to-one to jitter at the IP.

Stabilisation of the beam angle at the IP is vital, as the offset at the feedback BPM depends on the incoming beam angle as well as the desired beam-beam deflection. If the incoming beam angle was large or varied significantly this would confuse the feedback system. An IP angle feedback system has been designed to correct the beam orbit through the FF [92] and to stabilise the beam angle at the IP. The corrector would be placed at the same phase as the IP to provide angle correction only.

5.2 Beam-beam effects

5.2.1 Luminosity

The luminosity, $\mathcal{L}$, of a linear collider can be expressed as [38]

$$\mathcal{L} = H_D \frac{N^2}{4\pi\sigma_x\sigma_y} n_b f, \tag{5.2}$$

where N is the number of particles per bunch, $\sigma_{x,y}$ are the horizontal and vertical transverse r.m.s bunch sizes at the IP, n_b is the number of bunches per train, f_r is the train repetition frequency and H_D is the luminosity enhancement factor from the self-focussing between the oppositely charged e^+ and e^- bunches. Equation 5.2 demonstrates that to maximise $\mathcal{L}$, $\sigma_x\sigma_y$ should be minimised.

When colliding small beams at the IP, the charge density is very high, generating strong electromagnetic fields [93]. For oppositely charged e^+e^- pairs, during collision the electromagnetic fields focus the bunches with a mechanism called the 'pinch effect'. This reduces the beam sizes thus increasing the luminosity. As the charged bunches are deflected by the electromagnetic fields they emit synchrotron radiation called 'beamstrahlung'. The emission of beamstrahlung creates a spread in the particles' energies, forming a luminosity spectrum [93]. The energy spectrum caused by beamstrahlung is characterised by the beamstrahlung parameter, Υ, with

$$\langle\Upsilon\rangle \propto \frac{1}{\sigma_x + \sigma_y}. \tag{5.3}$$

To reduce the energy lost through beamstrahlung, $\sigma_x + \sigma_y$ should be increased. To simultaneously maximise the luminosity and reduce beamstrahlung, a flat beam is recommended with $\sigma_x >> \sigma_y$ [94].

The 'hourglass effect' describes the loss in luminosity that occurs when the bunch length, σ_z, becomes comparable to β_y^*. β_y grows parabolically with longitudinal distance from the IP, meaning a larger transverse bunch size and, consequently, lower luminosity [95]. For the ILC, the nominal β_y^* value of 480 µm is larger than the nominal bunch length of 300 µm, but if the bunch length were to increase, the hourglass effect would become more significant.

5.2.2 Disruption parameters

The electromagnetic field between opposing bunches acts to focus the beams; the disruption parameter, D, quantifies this effect. If the fields of the charged bunches are represented by lenses, D represents the focal length of the lens.

The horizontal and vertical disruption parameters D_x and D_y can be written as

$$D_{x,y} = \frac{2Nr_e\sigma_z}{\gamma\sigma_{x,y}(\sigma_x + \sigma_y)} \tag{5.4}$$

where σ_z is the bunch length, N is the number of particles per bunch, γ is the Lorentz factor and r_e is the classical electron radius ($r_e \approx 2.8\,\text{fm}$). As $\sigma_x >> \sigma_y$, the vertical disruption parameter would be much larger than the horizontal parameter.

The design values for the ILC disruption parameters are $D_x = 0.3$ and $D_y = 24.6$ [34]. A large value of D_y can lead to a process called 'kink instability', for which any existing beam distortions are amplified, causing the beams to oscillate in the vertical plane. The instability can be generated by a bunch-bunch offset and can lead to large losses in luminosity. As D_x is considerably smaller than D_y, kink instability is most likely to occur in the vertical plane only. The dependence of D_x and D_y on the transverse bunch dimensions are shown in Fig. 5.1, from which it can be seen that they increase quickly with decreasing transverse bunch size.

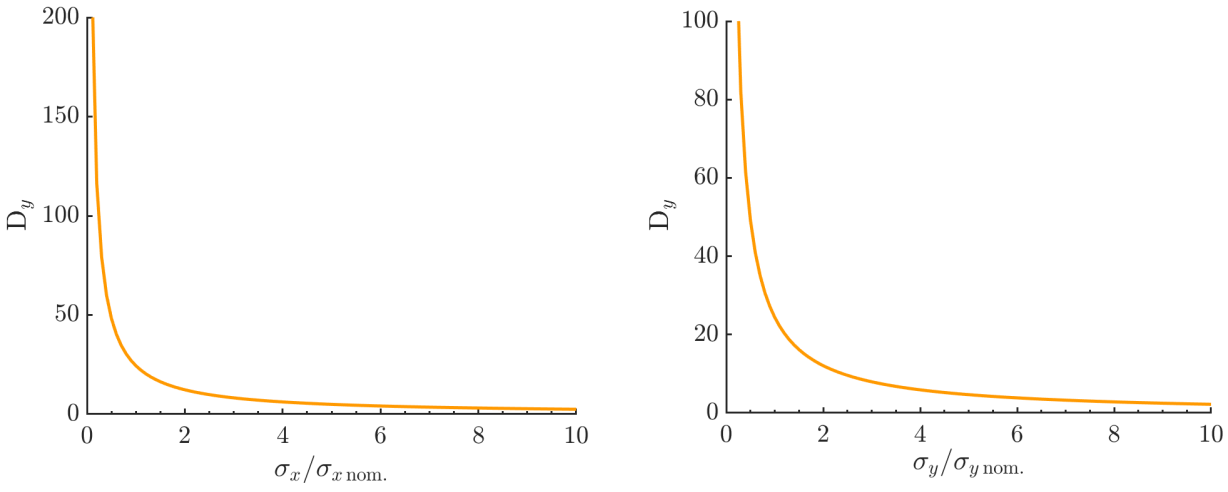

(a) (b)

Figure 5.1: The disruption parameter D_y versus normalised (a) horizontal and (b) vertical transverse bunch sizes.

Previous studies determined that if the IP offset Δ_y satisfies $\frac{\Delta_y}{\sigma_y} \leq D_y$ then there should be no significant reduction in the luminosity from the kink instability [96]. For very small offsets, the kink instability can actually increase the luminosity by bringing the heads of the bunches closer [97]; however, by increasing the offset, instability occurs and the luminosity falls. The number of sinusoidal oscillations, n, caused by kink instability is approximately [98][99]

$$n = \sqrt{D_y}\frac{\sqrt{2\sqrt{3}}}{2\pi\beta}, \tag{5.5}$$

where $\beta = \frac{v}{c}$. For the ILC, with $D_y = 24.6$, $n \sim 1.5$.

The enhancement of the luminosity from beam-beam effects, including the pinch effect, can be characterised in terms of $D_{x,y}$ [98],

$$\begin{aligned}\mathcal{L} &= \mathcal{L}_0(1 + {D_{x,y}}^{\frac{1}{4}} \times (\frac{{D_{x,y}}^3}{1 + {D_{x,y}}^3}) \times (\ln(\sqrt{D_{x,y}} + 1) + 2\ln(\frac{0.8{\beta_{x,y}}^*}{\sigma_z}))) \\ &= H_D\mathcal{L}_0.\end{aligned} \tag{5.6}$$

where H_D is the luminosity enhancement factor, $\mathcal{L}$ is the luminosity including beam-beam effects and $\mathcal{L}_0$ is the luminosity without. The term $2\ln(\frac{0.8\beta_{x,y}{}^*}{\sigma_z})$ derives from the hourglass effect. The equations for the disruption parameter $D_{x,y}$ (Eq. 5.4) and the luminosity enhancement factor H_D (Eq. 5.6) are only valid when the hourglass effect is sufficiently small, such that $\sigma_z/\beta_y^* < 1$ [100].

5.2.3 Beam-beam deflection

The deflection angle, Θ_y, can be written in terms of D_y as

$$\Theta_y = \frac{1}{2} D_y F \frac{\Delta_y}{\sigma_z}, \tag{5.7}$$

where F is a function determined through simulations, for which the larger the value of D_y, the larger the region of linearity between Θ_y and the beam-beam offset Δ_y [88]. An IP feedback system measuring the deflected beam is therefore dependent on D_y. Consequently, before operating feedback, the deflection angle as a function of the offset at the IP should be determined for the actual bunch parameters, as opposed to assuming nominal values.

5.3 ILC simulation overview

To model the performance of intra-train IP feedback, a simulation of the ML, BDS and IP feedback system was constructed. The beam transport was simulated with tracking code PLACET (version 1.0.3) [101], the beam-beam interaction was simulated in GUINEA-PIG (version 1.2.0) and the feedback system was modelled in Octave [102]. An overview of the structure of the simulation is presented in Fig. 5.2; the input and output files (`acc.dat` and `beam.dat`) are described further in Section 5.3.2. PLACET was used to model the beam transport for ILC-like trains of 1312 bunches. These bunches were tracked to the IP, where PLACET was interfaced with GUINEA-PIG to simulate the beam-beam interaction. PLACET also has the facility to interface with Octave, allowing for the simulation of a feedback system which interacts with the beamline components in PLACET.

5.3.1 PLACET

PLACET (Program for Linear Accelerator Correction Efficiency Tests) is a tool for the simulation of beam transport in a linear accelerator. Effects such as the misalignment of beamline components, ground motion and short-range and long-range wakefields can be

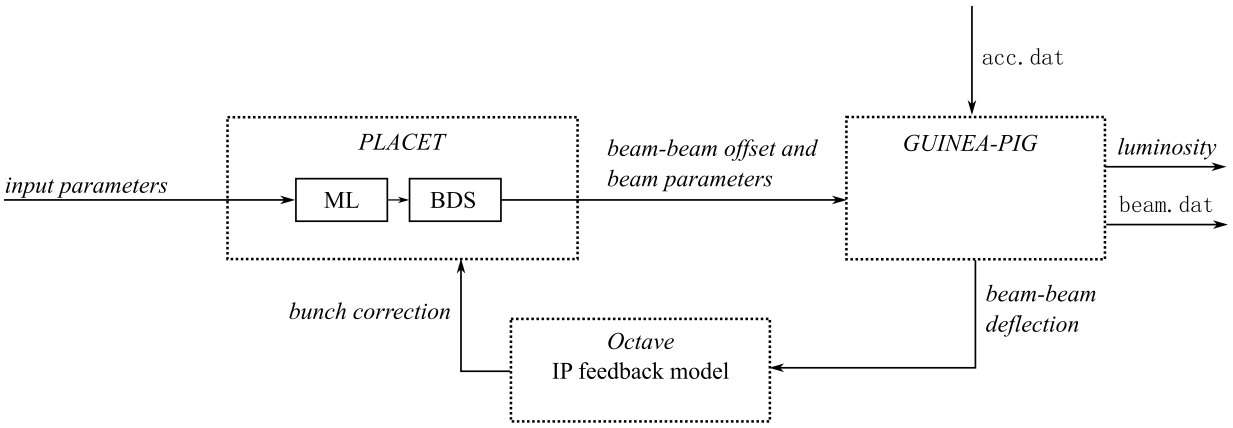

Figure 5.2: Block diagram of a combined simulation of the ILC ML and BDS in PLACET, the beam-beam interaction in GUINEA-PIG and an IP intra-train feedback system in Octave.

included. Bunches can either be modelled as slices of macroparticles, all at the same longitudinal position, or as many single particles, each defined in phase-space by six dimensions (x, x', y, y', z, E); with x and y, the horizontal and vertical positions, x' and y', the horizontal and vertical angles and, E, the energy [101]. This phase-space vector is evolved along the beamline, with each accelerator component being represented by a 6D transfer matrix.

PLACET, which is written in the scripting language Tcl/Tk [103], can be interfaced with Octave [102] and Python. This allows for more flexibility when handling variables, with the addition of tools from the Octave and Python libraries [104].

To run a simulation in PLACET, the beamline must first be defined using a lattice file, along with the parameters of the beam to be tracked. If required, pre-alignment and beam-based correction are then specified [101]. For theses studies the `TestNoCorrection` command was used, for which no beam-based correction is implemented. The beam is tracked through the lattice and a file '`emitt.dat`' is produced, which can be configured to contain [101]:

- **ex** (horizontal emittance [10^{-7} m])
- **ey** (vertical emittance [10^{-7} m])
- **x** (mean horizontal bunch position [µm])
- **y** (mean vertical bunch position [µm])
- ***σ*_x** (horizontal transverse r.m.s bunch size [µm])
- ***σ*_y** (vertical transverse r.m.s bunch size [µm])
- **E** (mean energy [GeV])

- **dE** (energy spread [GeV])
- **s** (longitudinal element position [m]).

For these simulations, the 2016 ILC lattice (RC2016X) [105] was used with beam parameters as specified in [34] for a 500 GeV collision energy. The Twiss parameters used at the start of the ML are stated in Table 5.1. The beam was tracked from the start of the ML to the IP where the bunch offset and luminosity were determined. Beam effects which were considered include short-range and long-range wakefields, ground motion and bunch jitter from the DR extraction.

Table 5.1: Parameters of the ILC beam at the start of the ML [105].

Parameter	Value	Unit
β_x	64.07	mm
β_y	75.30	mm
α_x	1.16	
α_y	-1.22	

The design parameters for the normalised emittance ($\gamma\epsilon_x$), energy (E) and bunch length (σ_z) are specified in Table 5.2. The bunches are extracted from the DR with a length of 6000 µm and two stages of bunch compression within the RTML (BC1 and BC2) compress the bunches to 300 µm. In the RTML, RF cavities are used to increase the beam energy from 5 GeV to 15 GeV; the energy is further increased to the collision energy of 250 GeV in the ML. Example profiles for a bunch tracked through an ideal lattice to the IP are shown in Fig. 5.3, for which $\sigma_y = 5.8$ nm, $\sigma_x = 472$ nm and $\sigma_z = 295$ µm.

Table 5.2: Design parameters of the ILC beam from the RTML to the IP [34].

Location	$\gamma\epsilon_x$ (um)	$\gamma\epsilon_y$ (nm)	E	σ_z (um)
Start of the RTML	5.5	20	5	6000
Start of the ML	8.4	24	15	300
Start of the BDS	9.4	30	250	300
IP	10	35	250	300

Long-range wakefields were modelled using wake potentials for the fourteen most destructive modes, based on wake potentials measured at the ATF2 [106], which are summarised at [108]. The wake potential of an ILC dipole cavity is presented in Fig. 5.4 and the frequencies and wake potentials of the cavity modes are specified in Table 5.3. With all cavities tuned to the same frequency, the long-range wakefields would be amplified and the beam quickly blows up. To suppress this effect, each of the cavities were detuned by 0.1%, after which the beam becomes stable [85].

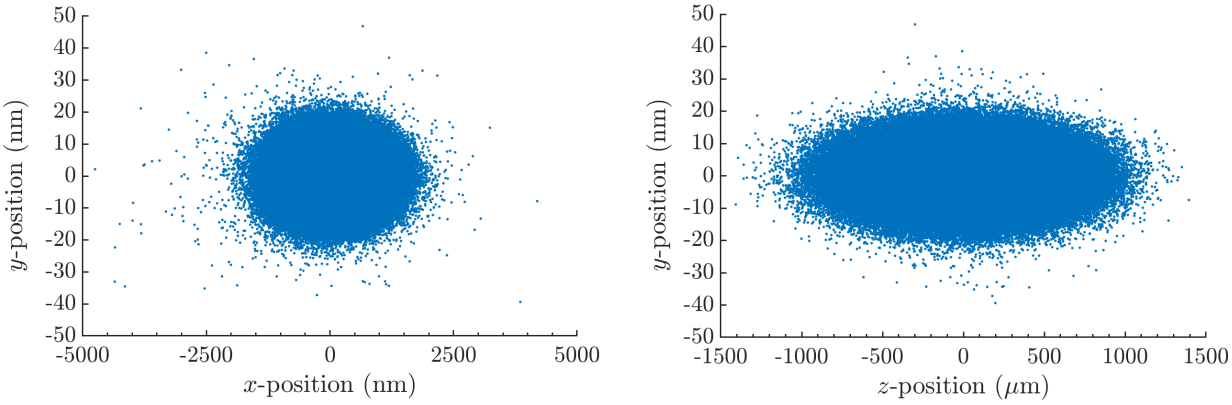

(a) (b)

Figure 5.3: IP bunch profiles in the (a) x-y and (b) z-y planes. Bunches were simulated with 50,000 macroparticles and 31 slices; data points represent the positions of the macroparticles.

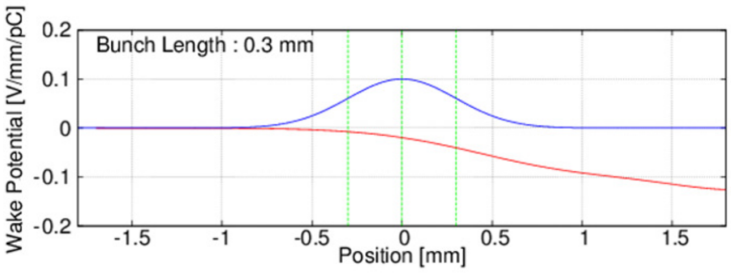

Figure 5.4: Wake potential for an ILC dipole cavity [106]. The bunch charge distribution is shown in blue and the wake potential in red.

Table 5.3: Wake potentials k and quality factors Q of long-range wakefield modes with frequency f, for TESLA-like ILC cavities; the accelerating cavity fundamental frequency is 1.3 GHz [107].

f [GHz]	k [$\frac{\text{V}}{\text{pCm}^2}$]	Q	f [GHz]	k [$\frac{\text{V}}{\text{pCm}^2}$]	Q
1.6506	19.98	7e4	1.8509	11.26	2.5e4
1.6991	301.86	5e4	1.8643	191.56	5e4
1.7252	423.41	2e4	1.8731	255.71	7e4
1.7545	59.86	2e4	1.8795	50.8	1e5
1.7831	49.2	7.5e3	2.5630	42.41	1e5
1.7949	21.70	1e4	2.5704	20.05	1e5
1.8342	13.28	5e4	2.5751	961.28	5e4

5.3.2 GUINEA-PIG

GUINEA-PIG (Generator of Unwanted Interactions for Numerical Experiment Analysis - Programme Interfaced to GEANT) [109] is a simulation tool for modelling e^+e^- beam-beam interactions, allowing for the calculation of luminosity and beam-beam deflection. Beam-beam effects are simulated including the pinch effect and the emission of beamstrahlung, among others [110].

GUINEA-PIG uses an input file '`acc.dat`' which defines the accelerator and beam parameters at collision and the dimensions of the 3D mesh with which to study the collision. The bunches are split into cells, as defined by the mesh, and the forces are evaluated at the intersections of the mesh by solving the Poisson equation.

The beam was split into slices, where a slice represented all macroparticles with the same longitudinal position. The interaction between colliding bunches was modelled as the interaction between slices at the same longitudinal location. The forces were simulated to act solely in a transverse plane, an assumption based on the Lorentz contraction of the EM fields of the ultra-relativistic bunches [93]. The slices were then advanced longitudinally with a velocity equal to the speed of light, using time-symmetric differential equations, and the calculation was performed again [111]. At each step the transverse kicks were applied and the charge distribution was re-evaluated.

Bunch parameters defined in '`acc.dat`' include the transverse bunch sizes ('`sigma_x`' and '`sigma_y`'), horizontal and vertical emittances ('`emitt_x`' and '`emitt_y`'), bunch length ('`sigma_z`') and charge ('`particles`'). The outputs from GUINEA-PIG include the luminosity and mean horizontal and vertical deflection angles. Other outputs files include '`beam1.dat`' and '`beam2.dat`' for the electron and positron beams, respectively, which contain the 6D vector (x, x', y, y', z, E) for each of the macroparticles at the IP after collision. This vector is determined by extrapolating the bunch positions back to the interaction plane from their positions and angles after interaction [112]. The nominal parameters used for these GUINEA-PIG simulations were [110]

- **E** = 250 (energy [GeV])
- **particles** = 2 (number of particles per bunch [10^{10}])
- **cut_x** = $1500 + \Delta x$ (horizontal size of the grid [nm])
- **cut_y** = $100 + \Delta y$ (vertical size of the grid [nm])
- **cut_z** = 900 (longitudinal size of the grid [µm])

- **n_x** = 64 (number of cells in the horizontal direction)
- **n_y** = 512 (number of cells in the vertical direction)
- **n_z** = 64 (number of cells in the longitudinal direction)
- **n_t** = 5 (number of time-steps to move one slice to the next slice of the opposing bunch)

where Δx and Δy represent the beam-beam horizontal and vertical offsets at the IP respectively.

Interactions were simulated with a range of bunch-bunch offsets and the deflection angle and luminosity were calculated; results of the simulation are presented in Fig. 5.5. The peak luminosity was simulated to be $1.79 \times 10^{34}\,\mathrm{cm}^{-2}\mathrm{s}^{-1}$, which was obtained for a vertical offset of approximately zero, suggesting there is very little effect from banana-bunch effects. The luminosity drops to 99% of the peak value with an offset of $\sim 0.3\,\mathrm{nm}$ and continues to fall quickly to below 10% of the peak value by a 100 nm offset.

The deflection-angle curve has a steep linear region up to 1 nm offset, after which the gradient drops and the curve can be approximated as linear again. The deflection-angle curve has extrema at $\pm 230\,\mathrm{nm}$ outside which IP intra-train feedback would erroneously estimate the bunch offset from the deflection angle. This is consistent with the design value for the system's capture range of $\pm 200\,\mathrm{nm}$ [42]. The maximum deflection angle of $\sim \pm 360$ µrad would propagate to an offset at the BPM 4 m downstream of the IP of $\pm\,1400\,\mu\mathrm{m}$, requiring the BPM to have a linear working range larger than this.

5.3.3 IP feedback system

For collisions with disruption parameters $D \ll 1$, the incoming beam can be modelled as a thin lens and the beam-beam interaction solved analytically [94]. However, when $D \gg 1$, as is the case for the ILC, simulations are required as analytic models become prohibitively complicated. GUINEA-PIG was used to determine the deflection angle of the bunches after collision, from which the offset of the bunch at the BPM 4 m downstream of the IP could be determined (see Fig. 1.9). The simulated IP feedback system would then 'measure' the bunch offset of the deflected beam, with the BPM modelled to have a measurement error which was sampled from a Gaussian distribution with a standard deviation equal to the resolution. The process for the feedback simulation is illustrated in Fig. 5.6.

A bunch offset at the IP could then be estimated from the offset measured at the BPM

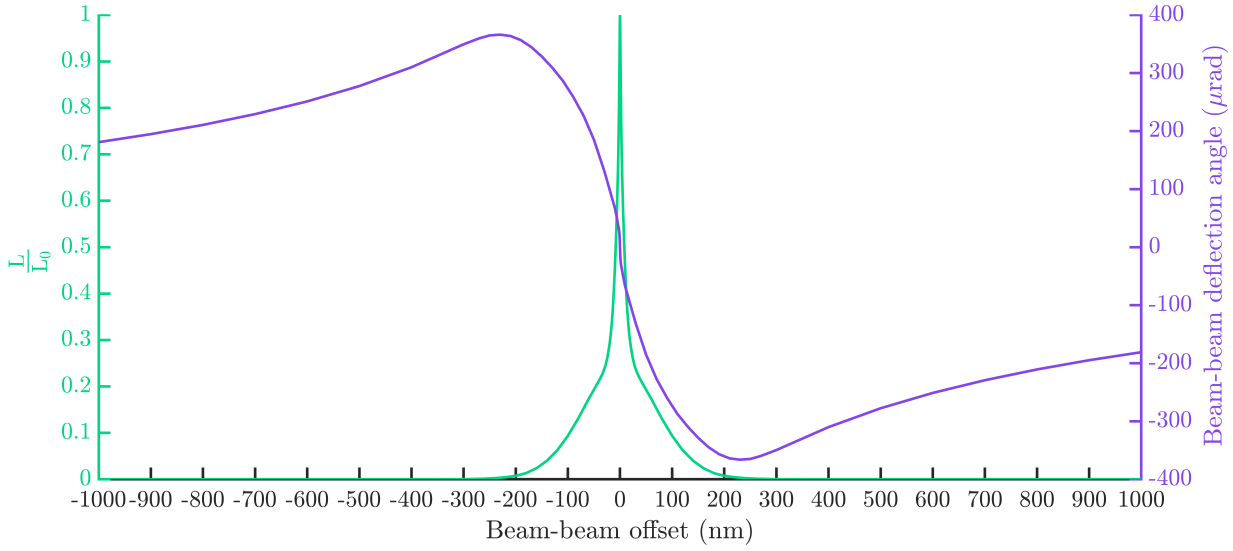

(a)

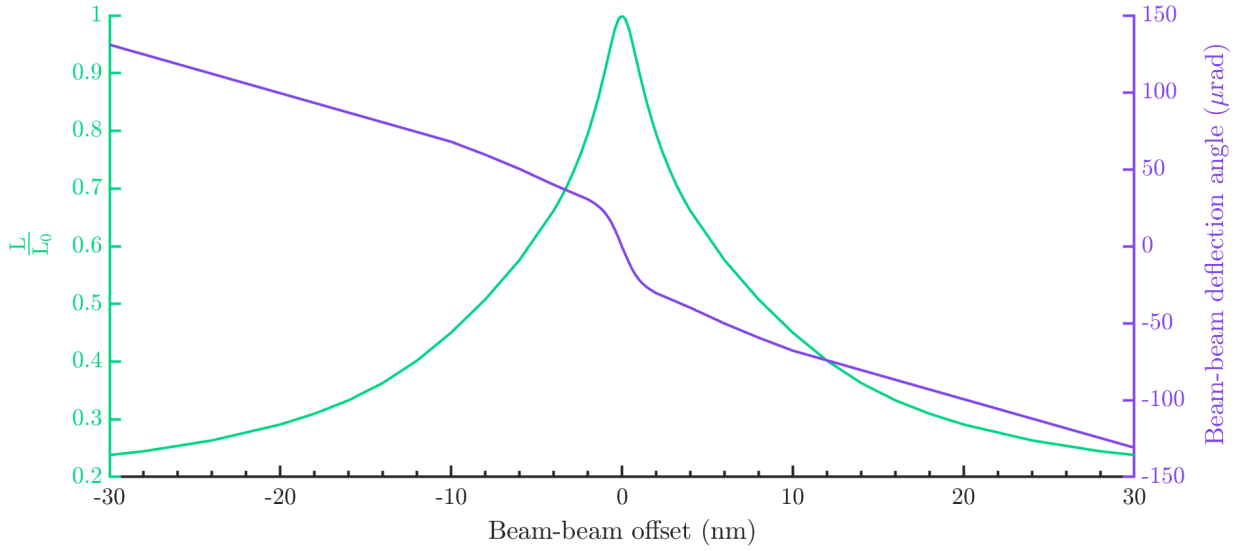

(b)

Figure 5.5: ILC luminosity (green) and deflection angle (purple) versus vertical IP offsets over a (a) ±1000 nm offset and (b) ±30 nm offset.

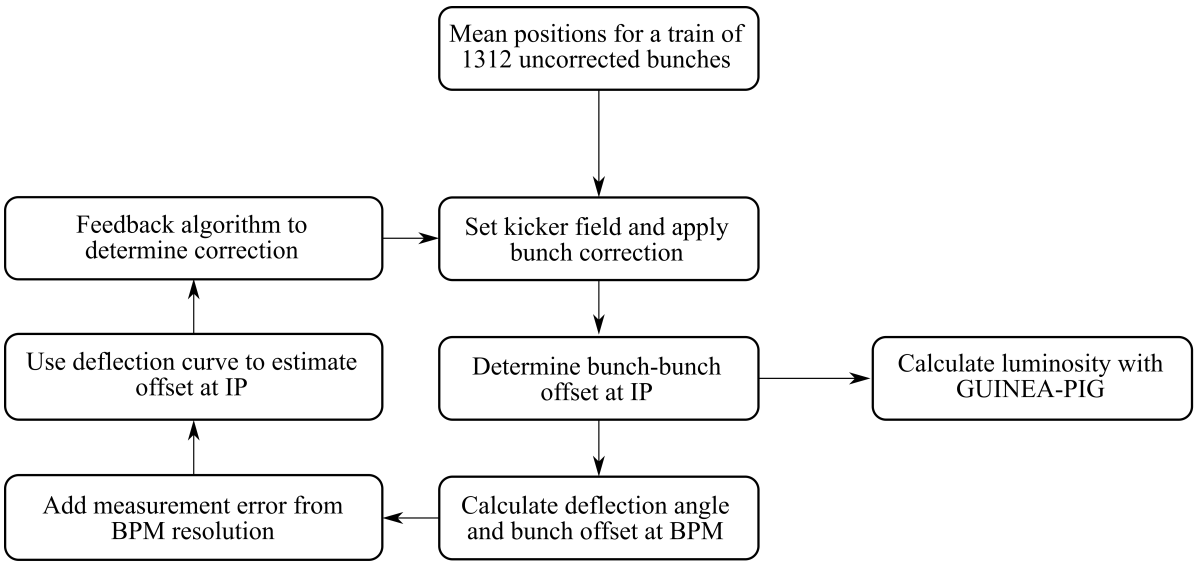

Figure 5.6: Block diagram for a simulation of an intra-train feedback system acting on ILC-like bunch trains.

using a predetermined mapping. In order to meet latency requirements, a lookup table (LUT) approach would be recommended, where the addresses of the LUT correspond to the measured bunch offsets at the BPM and the LUT elements are the respective offsets at the IP. The accuracy of this approach depends almost entirely on the accuracy with which the deflection angle curve is estimated. As this curve depends on the bunch parameters, the LUT should be reloaded whenever they are known to change.

Within PLACET, the stripline kicker (see Fig. 1.9) was calibrated so that the offset at the IP was converted to a kicker voltage. For these simulations, a Gaussian distributed kicker error of 0.1% was modelled [41]. The correction signal, determined in Octave, was then passed to PLACET and the kicker voltage set, in time for the correction to be applied to the next bunch in the train. After correction, the bunch interaction was simulated in GUINEA-PIG and the process was applied iteratively for the whole bunch train.

Two methods for determining the luminosity were used. The simulation could be interfaced with GUINEA-PIG to output a luminosity measurement for every bunch, although this was a very time-consuming process. Another possibility was to use a predetermined curve of luminosity versus bunch-bunch offset. Similarly to the beam-beam deflection curve, the luminosity curve must be recalculated using GUINEA-PIG each time the bunch parameters change.

Different inputs to the Octave-based feedback system were considered. Initially, bunch train structures were generated in Octave to test the limits of the system and then, once the limits were understood, simulated bunch trains tracked through the ML and BDS were

used. Bunch trains generated in Octave include trains with a constant offset of the whole train, a slow drift, and also higher-order harmonics within the bunch train. Factors affecting the performance of the feedback system were considered, such as a reduced bunch-to-bunch correlation and BPM resolution effects.

5.3.4 Feedback algorithms

Feedback algorithms which were modelled were based on Proportional-Only and Proportional-Integral control. For Proportional-Only feedback, the correction $u(t)$ implemented at time t is proportional to the error $e(t)$, defined as the difference between the reference set point and the measured value, so that

$$u(t) = G_{\mathrm{p}} e(t), \tag{5.8}$$

where G_{p} is the feedback gain. As Proportional-Only control requires a measured error in order to generate an output, in a real system with a non-zero resolution and measurement errors, $e(t)$ would never fully be removed. Instead the system would stabilise to a value which is offset from the set point, creating what is known as an 'offset error' or 'steady-state error'. To remove this offset an integral term can be introduced, which increases the correction as a function of both the error and the amount of time the error has been present. With an integral term, if the correction is insufficient to fully remove the error, the correction would be increased over time. For Proportional-Integral control the correction can be written as

$$u(t) = G_{\mathrm{p}} e(t) + G_{\mathrm{i}} \int_0^t e(\tau) d\tau, \tag{5.9}$$

where G_{p} and G_{i} are the gains for the proportional and integral terms respectively.

The use of Proportional-Integral control means that the system reacts quickly to any initial errors because of the proportional term, but also stabilises the error to zero as a result of the integral term. The gains of the proportional and integral components must be optimised for the system, so as to remove the initial error as quickly as possibly without introducing instability into the system.

5.4 Beam-beam interactions

The offsets of all simulated macroparticles are output by GUINEA-PIG and can be used to plot the bunch profiles at interaction. The angular trajectories of the macroparticles can be used to propagate the bunch downstream. An example bunch profile of a nominal ILC electron bunch at collision is shown in Fig. 5.7(a); profiles of the bunch propagated

600 µm and 1200 µm downstream are given in Figs. 5.7(b) and (c) respectively. Although no beam-beam offset was included in the simulation of the interaction, small asymmetries in the bunch profile were amplified during the interaction. The pinch effect is visible in Fig. 5.7(a) with the centre of the beam focussed by the field of the opposing bunch. After collision, the distribution of angular trajectories increases the vertical bunch size further from collision, although as the centroid remains approximately constant this should have little effect on the IP feedback performance.

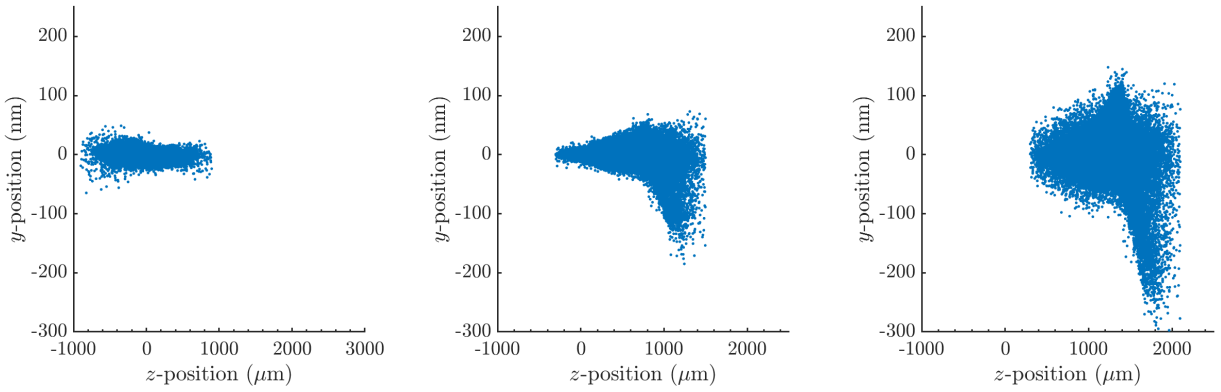

Figure 5.7: z-y profiles of the bunches after interaction at longitudinal positions (a) 0 µm, (b) 600 µm and (c) 1200 µm for an e^-e^+ interaction with a 0 nm IP offset.

The kink instability, described in Section 5.2.2, is expected to be generated by vertical bunch offsets due to the large disruption parameter, D_y. Plots of the bunch profiles are shown in Fig. 5.8 for an interaction with a bunch-bunch offset of 25 nm. It can be seen that the bunch shape has developed a kinked structure with a larger vertical distribution of macroparticles than seen in Fig. 5.7(a).

To measure the oscillations introduced by the kink instability, the mean vertical offset for the bunch was calculated as a function of longitudinal position. This was achieved by binning the data into subsets of 500 macroparticles based on their longitudinal positions, and then calculating the mean vertical offset of each bin. The results are presented in Fig. 5.9(a) for a 0 nm initial bunch offset and in Fig. 5.9(b) for a 25 nm offset. From Eq. 5.5, 1.5 periods of oscillation are predicted to be generated by the kink instability, which is consistent with the results presented in Fig 5.9. For a 25 nm offset, corresponding to $\sim 4\sigma_y$, the effect of the kink instability on the bunch trains is more significant and is particularly visible when propagated downstream.

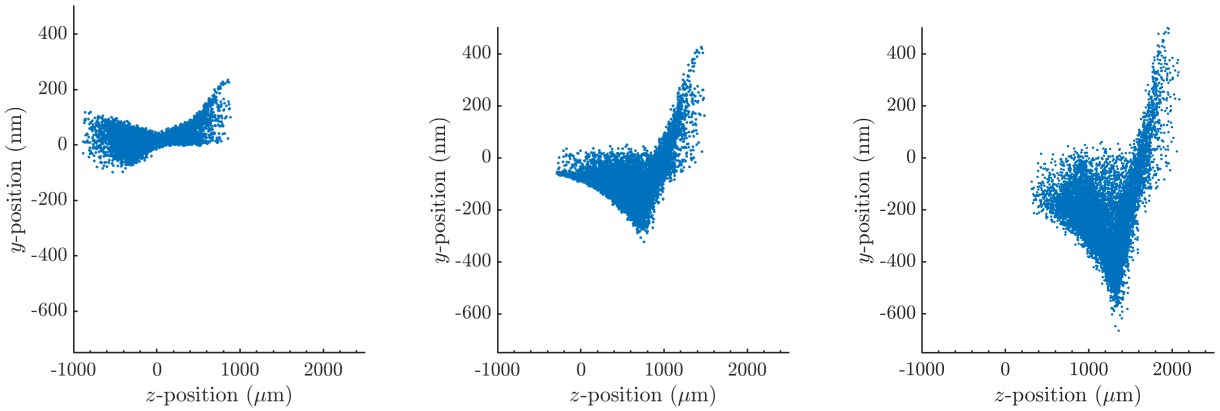

(a) (b) (c)

Figure 5.8: z-y bunch profiles after interaction at longitudinal positions (a) 0 µm, (b) 600 µm and (c) 1200 µm for an e^-e^+ interaction with bunch-bunch offset of 25 nm .

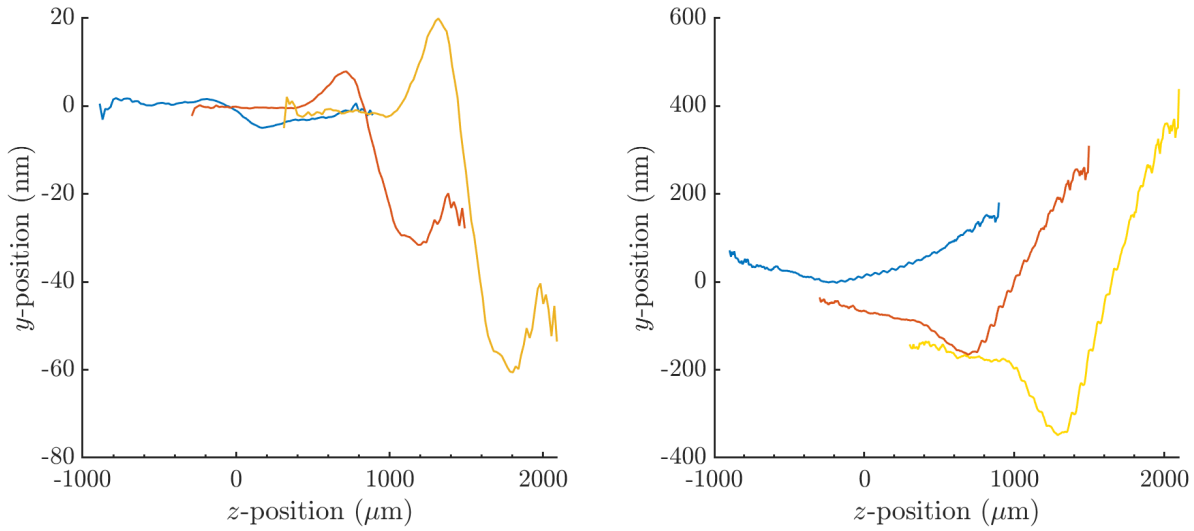

(a) (b)

Figure 5.9: z-y mean bunch profiles after interaction at longitudinal positions 0 µm (blue), 600 µm (red) and 1200 µm (yellow) for an e^+e^- interaction with an IP bunch-bunch offset of (a) 0 nm and (b) 25 nm.

5.5 Beam-beam deflection angle

For the feedback calculation, the offset of the deflected beam at the BPM is assumed to be directly proportional to the deflection angle. For interactions with disruption parameters $D_x \ll 1$ and $D_y \ll 1$, the deflection-angle curve can be modelled analytically. For the ILC, with a large vertical disruption parameter, analytic calculations break down and simulations are required to correctly model the beam-beam interaction.

5.5.1 Dependence on charge

The disruption parameter is proportional to the bunch charge, N, so that the deflection angle would also scale with N. This was studied with simulations of bunches with a range of charges between 10% and 110% of the nominal value. The resulting deflection angle curves are presented in Fig. 5.10. It can be seen that for higher bunch charges, there is a larger range of vertical beam-beam offsets with a linear relationship between the deflection angle and the offset. For lower bunch charges, the maximum deflection angle is reduced and so is the offset at which the maximum occurs. This leads to a reduced resolution of the estimation of the beam-beam offset at the IP. It also means a reduced feedback capture range, as the system works best when there is a one-to-one mapping between the offset at the BPM and the offset at the IP.

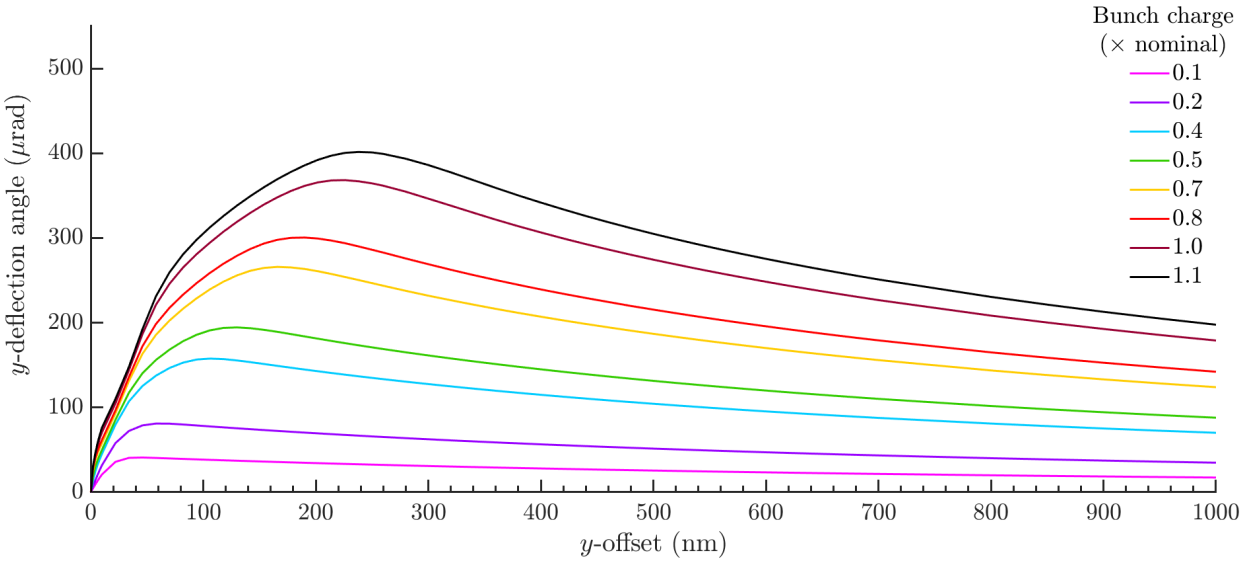

Figure 5.10: Beam deflection angle versus vertical beam-beam offset at the IP, where the colour of the line denotes the bunch charge.

The luminosity was also considered, where analytically it was expected to scale quadratically with the bunch charge. The luminosity versus bunch offset at the IP is presented in

Fig. 5.11(a) for five charge settings, with the luminosity seen to fall quickly with decreasing bunch charge. The normalised luminosity versus bunch charge for a 0 nm offset is shown in Fig. 5.11(b), showing very good agreement with the expected scaling of $\mathcal{L} \propto N^2$.

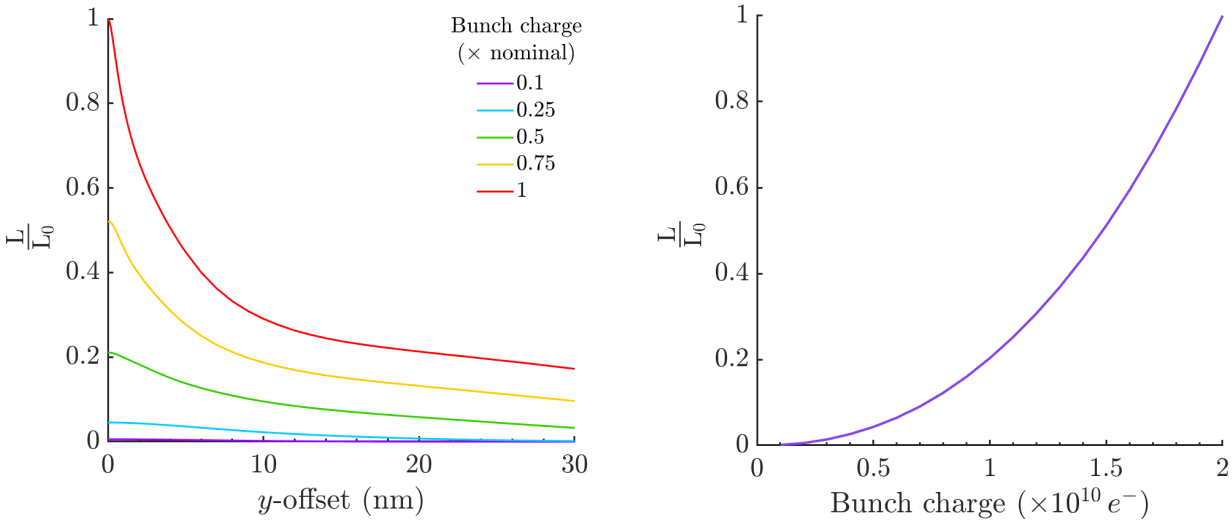

Figure 5.11: (a) Normalised luminosity versus vertical beam-beam offset at the IP, the bunch charge is denoted by the colour of the line; (b) normalised luminosity versus bunch charge for an interaction with 0 nm offset.

5.5.2 Dependence on bunch length σ_z

There are multiple effects contributing to the dependence of the deflection angle and luminosity on σ_z. These effects are not taken into account in the analytic calculation of the deflection angle, which predicts no dependence on σ_z [113]. Simulations include the hourglass effect and kink instability, which both become more prominent with increasing bunch length. The disruption parameters (D_x, D_y) scale with the bunch length, so that the characteristic number of oscillations generated in the bunch train scales with $\sqrt{\sigma_z}$ (Eq. 5.5).

Figure 5.12 shows the post-interaction bunch profiles in the z-y plane for three different bunch lengths. The bunch profile for the nominal ILC bunch length is shown in 5.12(a); interactions with longer bunches, and consequently higher disruption parameters, are given in Figs. 5.12(b) and (c), with D_y = 24, 81 and 122 respectively. Figure 5.13 shows the equivalent set of plots for interactions with a 25 nm offset at the IP for which the effect of the kink instability is more pronounced. The oscillations in the bunch structure are particularly visible for the central region of the bunches, especially for the σ_z = 1500 µm case.

The beam-beam deflection angle versus vertical bunch-bunch offset at the IP is presented

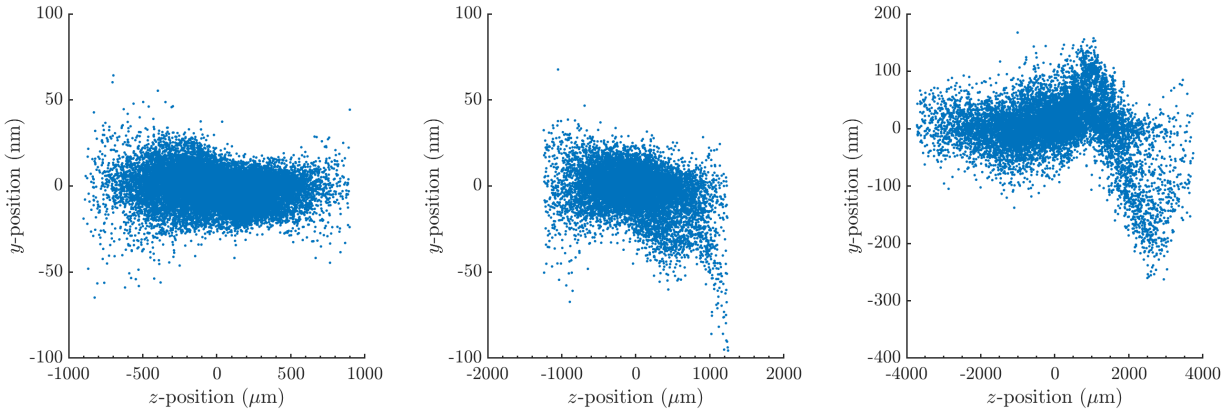

(a) (b) (c)

Figure 5.12: Bunch profiles in the z-y plane for 0 nm IP offset with bunch lengths (a) 300 µm (b) 500 µm (c) 1500 µm; the bunch has been simulated as a Gaussian distribution cut at 3σ and the data points represent the 20,000 macroparticles.

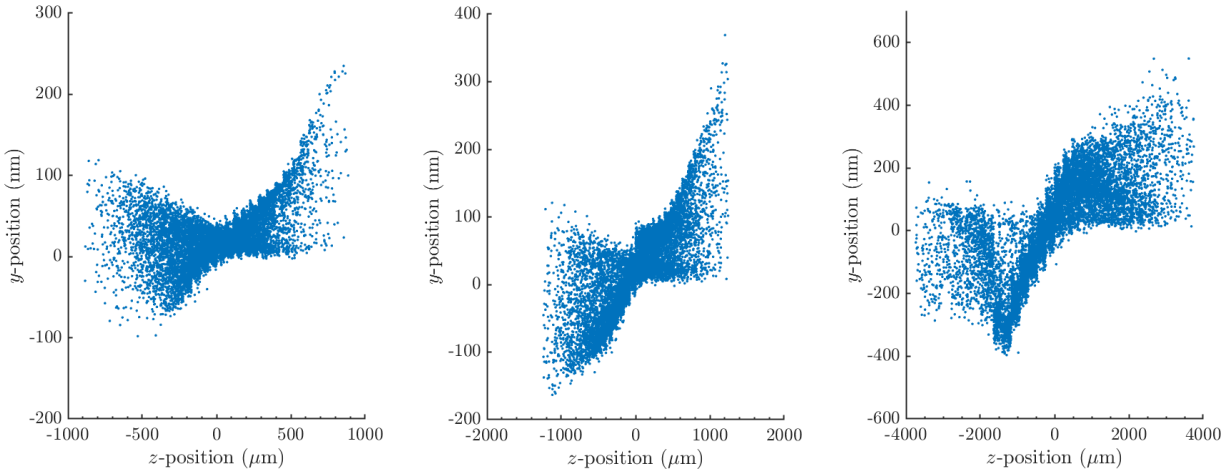

(a) (b) (c)

Figure 5.13: Bunch profiles in the z-y plane for 25 nm IP offset with bunch lengths (a) 300 µm, (b) 500 µm and (c) 1500 µm; the bunch has been simulated as a Gaussian distribution cut at 3σ and the data points represent the 20,000 macroparticles.

in Fig. 5.14 for a range of bunch lengths from 300 µm to 600 µm. For bunch offsets of up to 20 nm, there is little difference between the curves as the offsets are small enough not to generate kink instability and the analytic approximation holds. With larger bunch offsets, this approximation begins to break down and kink instability becomes an important factor. From Fig. 5.13, with a 25 nm offset, significant variation is observed in the transverse position longitudinally and so, for larger offsets, the beam-beam deflection will also vary during collision. Beam-beam effects are less significant for larger vertical offsets at the IP as the electromagnetic forces are lower and, consequently, the deflection angle curves for different bunch lengths become similar again.

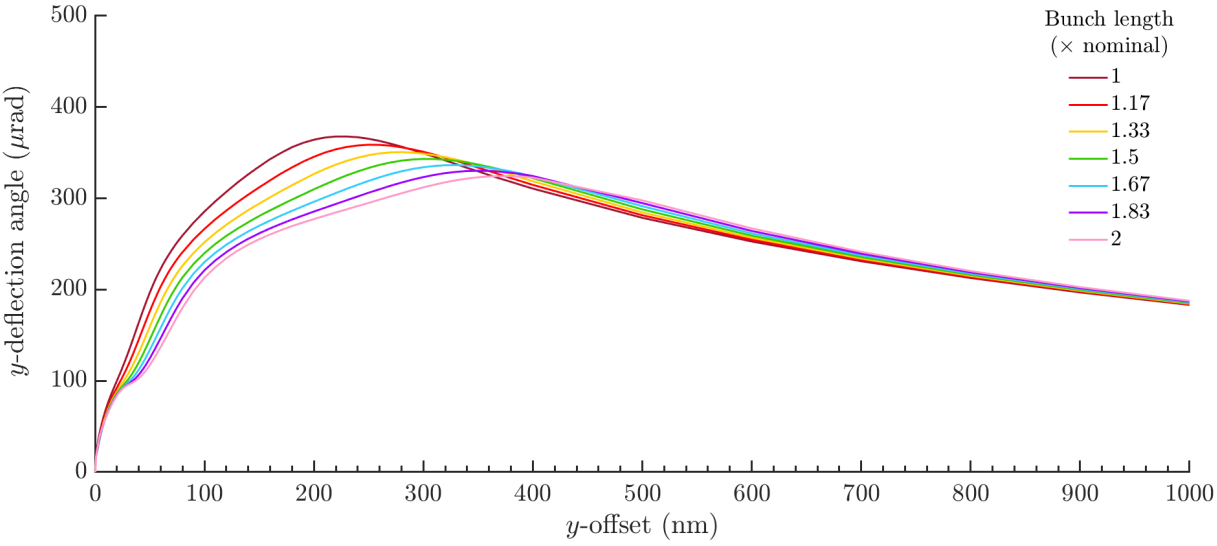

Figure 5.14: Beam-beam deflection angle versus vertical beam-beam offset at the IP, where the colour of the line denotes the bunch length.

5.5.3 Dependence on vertical bunch size σ_y

As shown in Fig. 5.1, the disruption parameter D_y, and consequently the deflection angle, depend on both σ_x and σ_y. Simulations were performed to determine the beam-beam deflection for a range of vertical bunch sizes between 1 and 10 times the nominal values; the results are presented in Fig. 5.15.

A significant dependence of the gradient of the curve with σ_y can be seen for offsets up to $\sim$ 400 nm. For larger offsets the curves converge, as when compared with the y-offset, the change in the bunch distributions are negligible. The difference between the curves is particularly significant for offsets of up to 1 nm with the curves becoming shallower as σ_y increases.

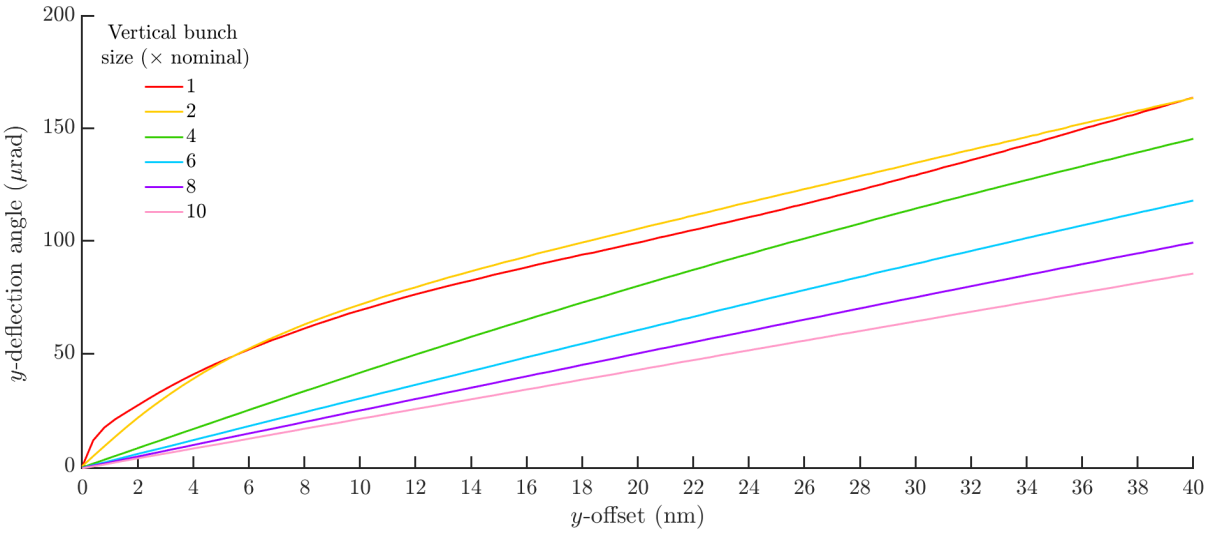

(a)

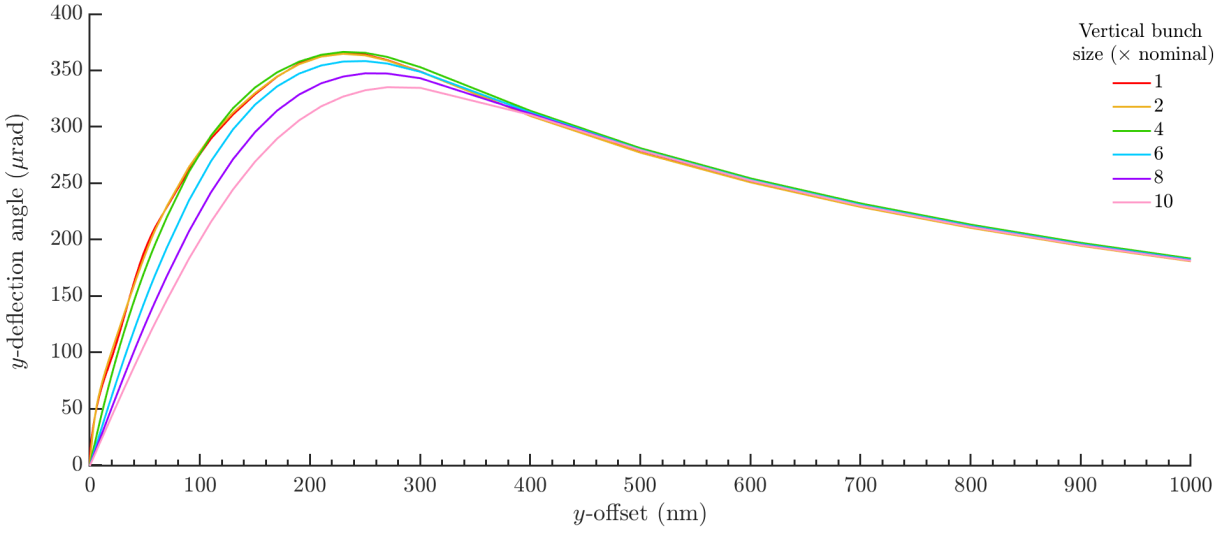

(b)

Figure 5.15: Beam-beam deflection angle versus vertical beam-beam offset at the IP, where the colour of the line denotes the vertical bunch size at the IP: (a) offsets up to 40 nm and (b) offsets up to 1000 nm.

Comparing the different curves is complicated by the fact the bunch size is being varied in the same plane as the offset is measured. This is particularly significant for smaller offsets, as the bunch-bunch overlap depends on the value of σ_y. The curves for bunch sizes $1 \times \sigma_y^{\text{nominal}}$ and $2 \times \sigma_y^{\text{nominal}}$ are similar in magnitude but with slightly different shapes. As a result, the IP feedback system should be relatively robust with respect to minor variations in σ_y.

5.5.4 Dependence on horizontal bunch size σ_x

The vertical deflection angle is proportional to $\frac{F}{\sigma_x+\sigma_y}$ (Eq. 5.7) and so will decrease with increasing σ_x. Results of simulating the beam deflection angle versus offset at the IP for various horizontal bunch sizes, are presented in Fig. 5.16. The maximum deflection angle occurs at a smaller offset for larger σ_x, as the electromagnetic forces between bunches is reduced by the lower charge density.

For bunch offsets less than 2 nm, the gradients of the curves vary approximately inversely proportional to σ_x. For offsets of more than 2 nm, the gradients of the curves for smaller σ_x decrease quicker than for larger σ_x and the inverse proportionality breaks down. The maximum deflection angle gets closer to the origin with increasing bunch size, where for $\sigma_x^{\text{nominal}}$ the maximum deflection angle occurs at 230 nm offset and deflection angle of 360 μrad but with $2 \times \sigma_x^{\text{nominal}}$, the maximum deflection angle occurs at 140 nm and 200 μrad.

As the feedback system operates best at offsets inside the extrema of the deflection angle curve, for larger σ_x values, the capture range of the feedback system is significantly reduced.

5.5.5 Feedback with non-nominal beam parameters

In order to reduce the latency of the system, a LUT is employed to map between the bunch offset at the BPM and the bunch-bunch offset at the IP. As this mapping depends on bunch parameters which may vary over time, errors could be introduced; simulations were performed to estimate the significance of these errors. A range of bunch parameters was modelled but the mapping used by the simulated feedback system assumed nominal ILC bunch parameters. For these simulations, Proportional-Only feedback was tested on bunch trains with an initial 200 nm offset; the results with feedback gain $G_{\text{p}} = 1$ are shown in Fig. 5.17.

The results for different bunch charges are presented in Fig. 5.17(a). If the bunch charge is higher than nominal, the system will overestimate the offset at the IP and overcorrect.

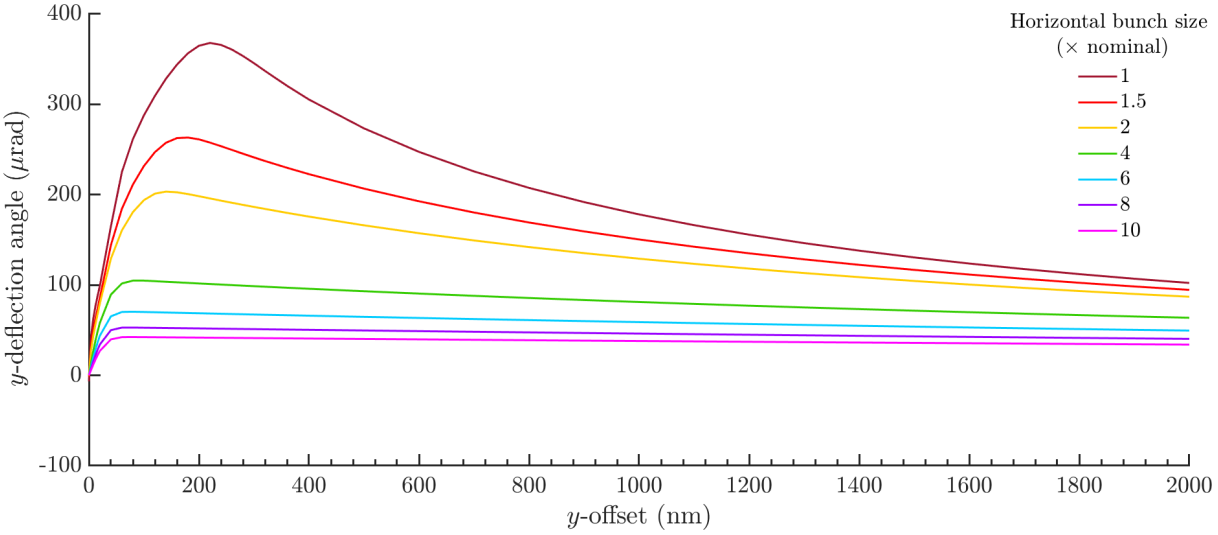

Figure 5.16: Beam-beam deflection angle versus vertical bunch-bunch offset at the IP, where the colour of the line denotes the horizontal bunch size at the IP.

The further the true beam parameters are from the nominal parameters, the longer the system will take to stabilise. As the deflection angle varies considerably as a function of bunch charge, this is a key parameter requiring accurate measurement prior to operating feedback. The performance for the lowest bunch charges are especially poor because of the reduced maximum deflection angle for the respective deflection angle curves. Nevertheless, the bunches will still eventually stabilise, as the correction is always applied in the right direction. A system of several LUTs could be used to make it quicker and easier to load the appropriate mapping for a given bunch charge. However, it should be noted that there is a limit to the number of LUTs which can be implemented within an FPGA and so careful selection of suitable parameters is essential.

Results of simulations with a range of bunch lengths are presented in Fig. 5.17(b). As the deflection angle curves up to 20 nm show little dependence on the bunch length, the system quickly stabilises smaller offsets, regardless of bunch length. The offset of the maximum deflection angle increases with bunch length so that there are no issues with exceeding the capture range.

The feedback system was also simulated for a range of σ_y values and the results are presented in Fig. 5.17(c). As the deflection angle curves between ± 200 nm have qualitatively similar shapes, but with different gradients, the changes in the feedback performance with σ_y are equivalent to scaling the feedback gain. Consequently, errors in the measurement of σ_y could be largely mitigated by adjusting the gain.

When simulating different σ_x values, as in Fig. 5.17(d), similar issues arise as with the

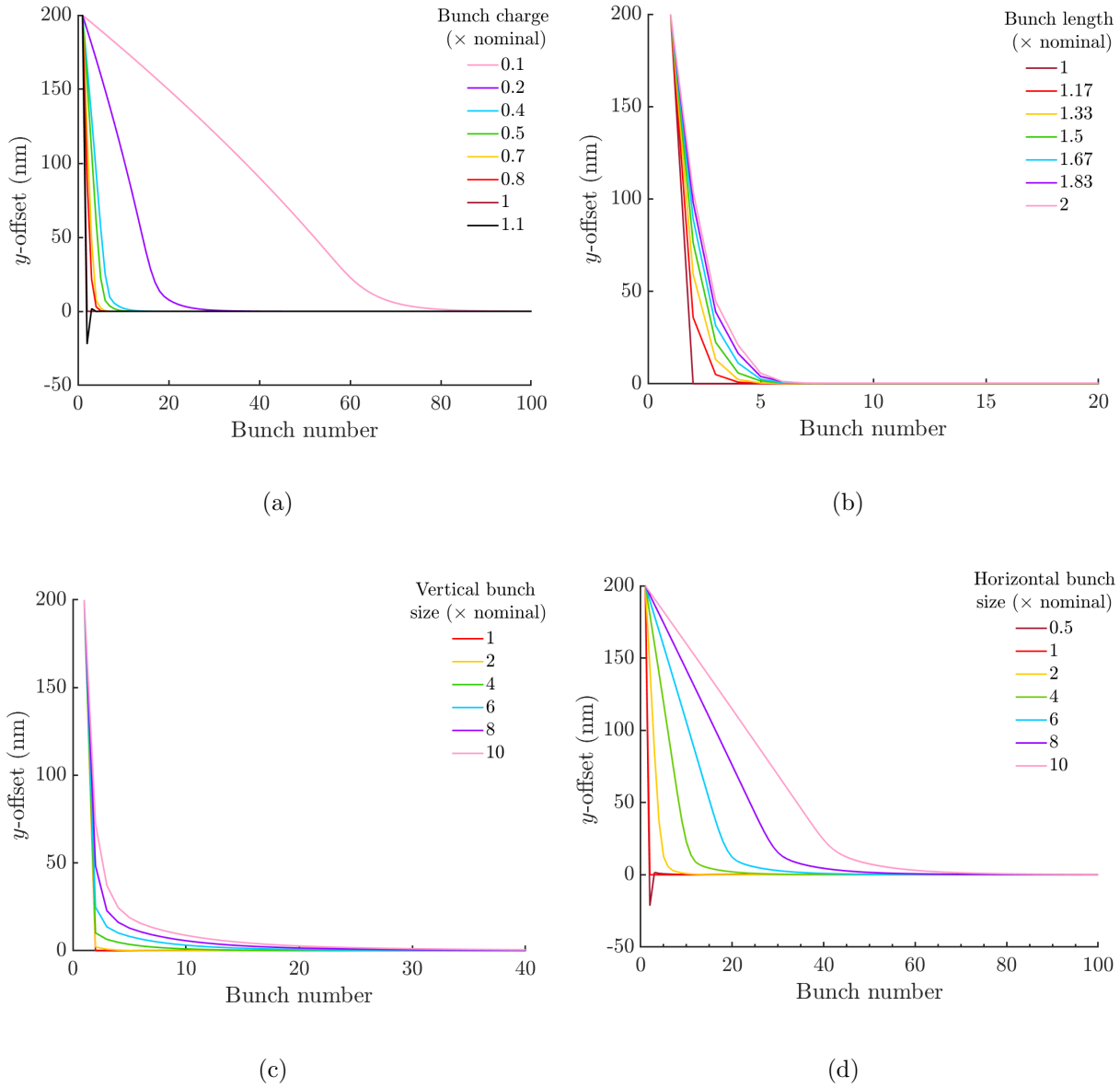

Figure 5.17: Vertical bunch-bunch offsets at the IP versus bunch number, with Proportional-Only feedback implemented. Bunches are modelled with a range of (a) charges, (b) σ_z values, (c) σ_y values and (d) σ_x values, denoted by the colour of the line. The uncorrected train has an offset of 200 nm. While simulating feedback, the LUT mapping between bunch position at the BPM and bunch position at the IP assumes nominal bunch parameters.

study of varying the bunch charge: the changes in location of the maximum deflection angle reduce the good working region. As the gradients of the curves are particularly sensitive to changes in σ_x for small offsets, this leads to slow correction of nanometre-level offsets.

It would be expected that if the bunch parameters were to vary, the charge would likely be lower than nominal and the transverse bunch sizes would be larger than nominal, which would all lead to under-correction. The correction should never be over-estimated, as this would lead to over-correction and 'ringing'; this can be avoided by reducing the feedback gain, which is discussed further in Section 5.6.2.

5.6 Development of feedback algorithms

Preliminary IP feedback studies were performed for bunch trains with a range of train shapes. While ground motion and wakefield effects have previously been studied for the ILC, much of the higher-frequency facilities noise that could be expected remains unknown and, consequently, understanding the limits of the system is vital [89].

Examples of bunch-train structures which were considered are shown in Fig. 5.18, where

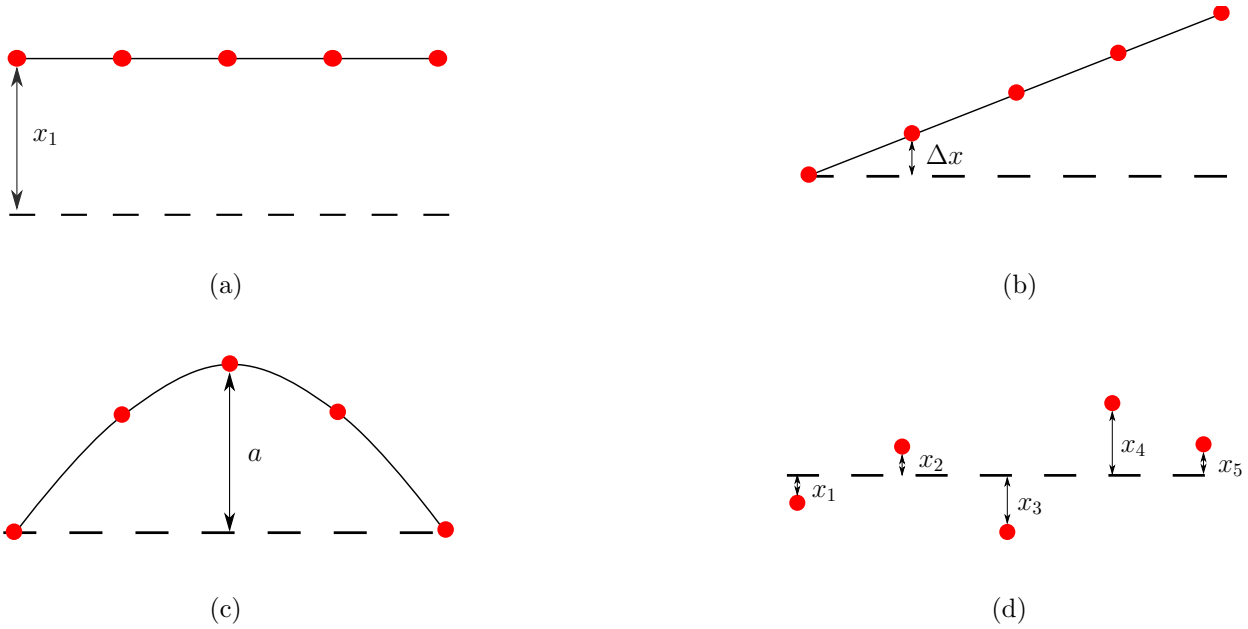

Figure 5.18: Schematic of a train with the bunches shown in red, for (a) a constant offset x_1, (b) a slow drift across a bunch train, with an offset of Δx between consecutive bunches, (c) a harmonic structure with amplitude a and (d) bunch-to-bunch jitter. The dashed line represents the ideal position of the bunches.

there are mechanisms within the accelerator which could generate them all. A constant offset across the entire bunch train could be caused by low-frequency ground motion (see Section 1.3.1), or by static component misalignments. A slow drift across the bunch train and bunch-to-bunch jitter could both be caused by variations in the DR extraction kicker pulses. Bunch-to-bunch jitter could also be introduced by high-frequency facilities noise. Finally, harmonic components in the bunch train could occur as a result of long-range wakefields and higher-order modes within the accelerating cavities.

5.6.1 BPM resolution

A study of the luminosity achievable as a function of BPM resolution was performed, with resolutions up to 100 µm modelled. Because of the changing gradient of the deflection angle curve, the resolution of the estimation of the offset at the IP varies as a function of the offset itself. For small offsets, a change in position offset at the IP corresponds to a deflection angle with a sensitivity of approximately 4 µrad/nm. As the bunch-bunch offset approaches the maximum of the curve, the gradient tends towards zero and a change in offset at the IP corresponds to a much smaller change in position at the BPM.

Proportional-Only feedback was tested on a rigid bunch train with zero IP offset. Various BPM resolutions were modelled and the results are presented in Fig. 5.19. The bunch trains were initially perfectly aligned so the reduction in the luminosity derives entirely from the resolution. A BPM resolution of 1 µm was found to reduce the luminosity by less than 0.1% and a resolution of 20 µm reduced the luminosity by 1.5%. Therefore, if the luminosity is required to be maintained within 0.1% of the design value, a BPM resolution of better than 1 µm is needed.

5.6.2 Rigid bunch trains

Proportional-Only feedback was tested on rigid bunch trains, for which every bunch has an equal offset at the IP. The feedback performance was studied for a range of initial offsets, with a feedback gain $G_{\mathrm{p}} = 1$; this is shown in Fig. 5.20. In an ideal system, for offsets within the capture range, the feedback system should be able to bring the bunches close to alignment by the second bunch. If the bunch offset lies outside the maximum of the curve, the one-to-one mapping between offset at the IP and offset at the BPM breaks down and the system under-corrects. For larger offsets it can take several iterations of feedback to bring the bunches into alignment, with a 1000 nm offset the system takes 11 iterations.

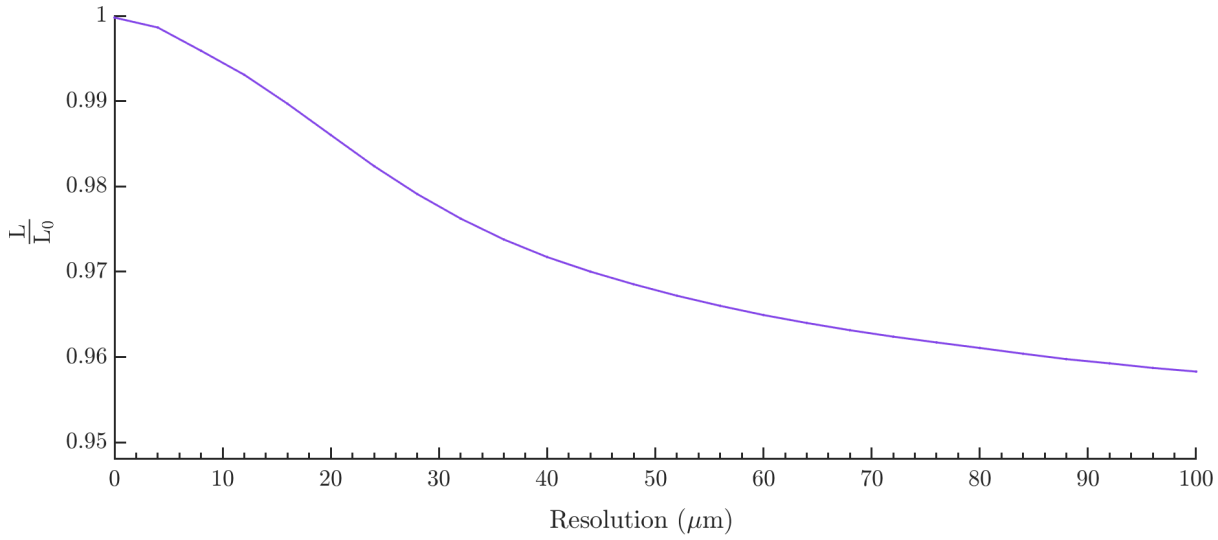

Figure 5.19: Normalised luminosity versus BPM resolution, with Proportional-Only feedback for a bunch train with zero initial offset.

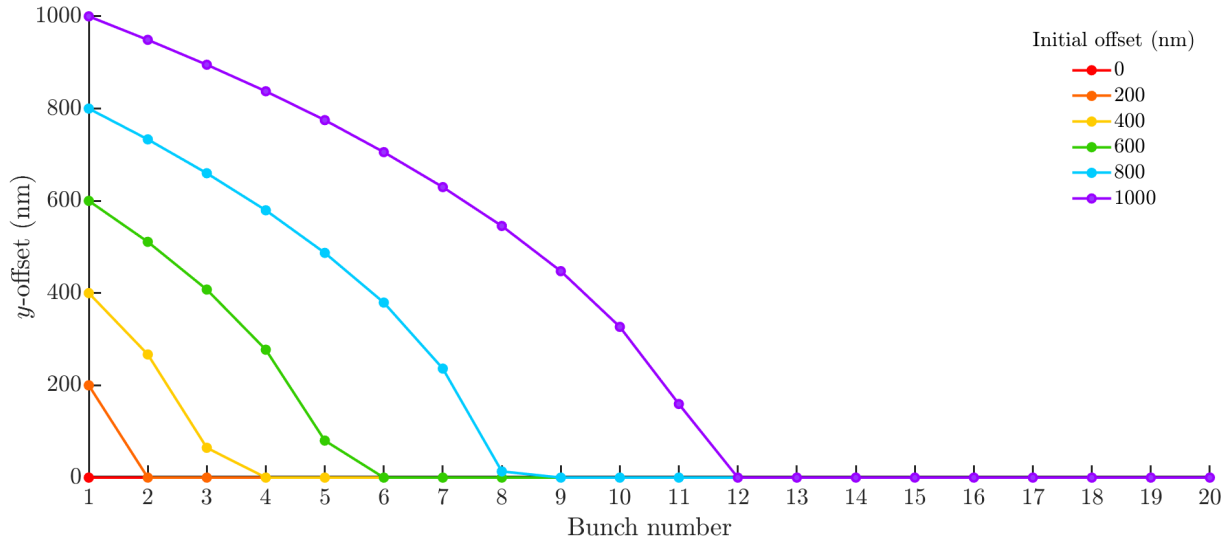

Figure 5.20: Vertical bunch-bunch offset at the IP versus bunch number, with Proportional-Only feedback simulated on rigid bunch trains with a range of initial bunch-bunch offsets. Bunch-1 shows the uncorrected offsets of the train.

A more advanced feedback algorithm could increase the rate of convergence for bunches outside the maximum of the deflection-angle curve. If, after correction, the measured offset of the corrected bunch is larger than for the previous bunch, this could indicate that the offsets have been underestimated and that the correction should be increased correspondingly.

Results of simulating feedback with a range of feedback gains are shown in Fig. 5.21; where a gain of 1 is designed to reduce the offset to zero by the second bunch. When considering BPM resolution effects and bunch-to-bunch jitter, the gain should be reduced to avoid over-correcting. From Fig. 5.21, it can be seen that even with a low gain, the bunches are still brought into alignment within the first $\sim$ 10 bunches. For trains of 1312 bunches this slower convergence would only have a small impact on the luminosity. With gains above 1, 'ringing' was observed, highlighting the risks of over-correcting the beam-beam offsets. For rigid bunch trains, if an integral component is used, the gain should be kept very low as the integral term is only used to remove the offset error.

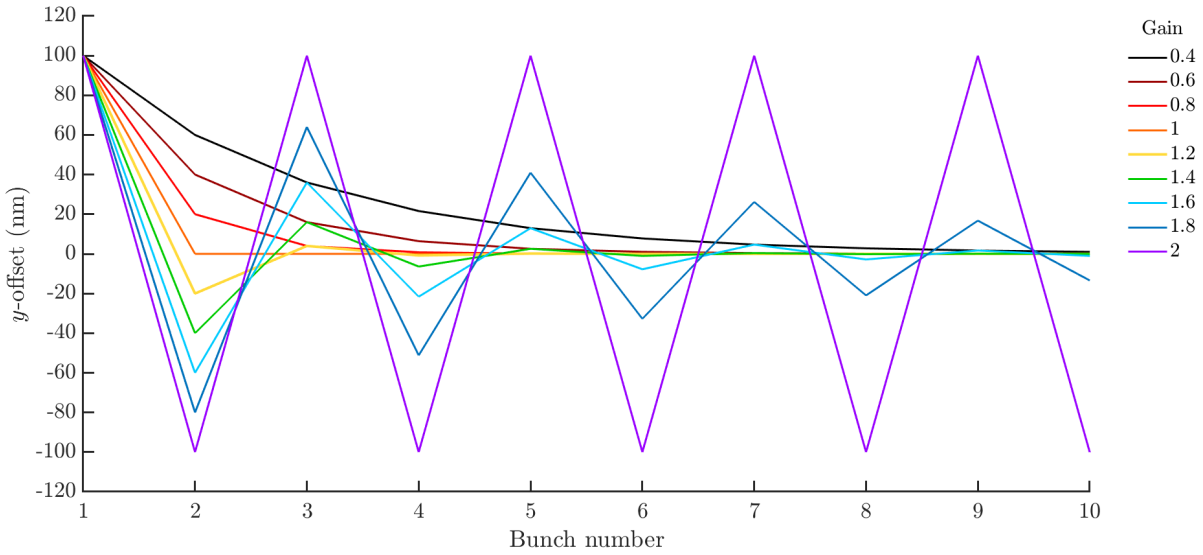

Figure 5.21: Vertical bunch-bunch offset at the IP versus bunch number, with Proportional-Only feedback operating on a rigid bunch train with a 100 nm offset. The feedback gain is denoted by the colour of the line.

5.6.3 Bunch-train structures

Feedback was simulated for bunch trains with a constant bunch-to-bunch drift (as shown in Fig. 5.18(b)). Proportional-Only feedback was modelled for various magnitudes of drift, the results of which are presented in Fig. 5.22. For this study, the BPM resolution and kicker error were modelled as zero. The uncorrected bunch trains had a 50 nm offset for the pilot bunch and 1 nm, 2 nm and 3 nm between consecutive bunches. The uncorrected bunches are

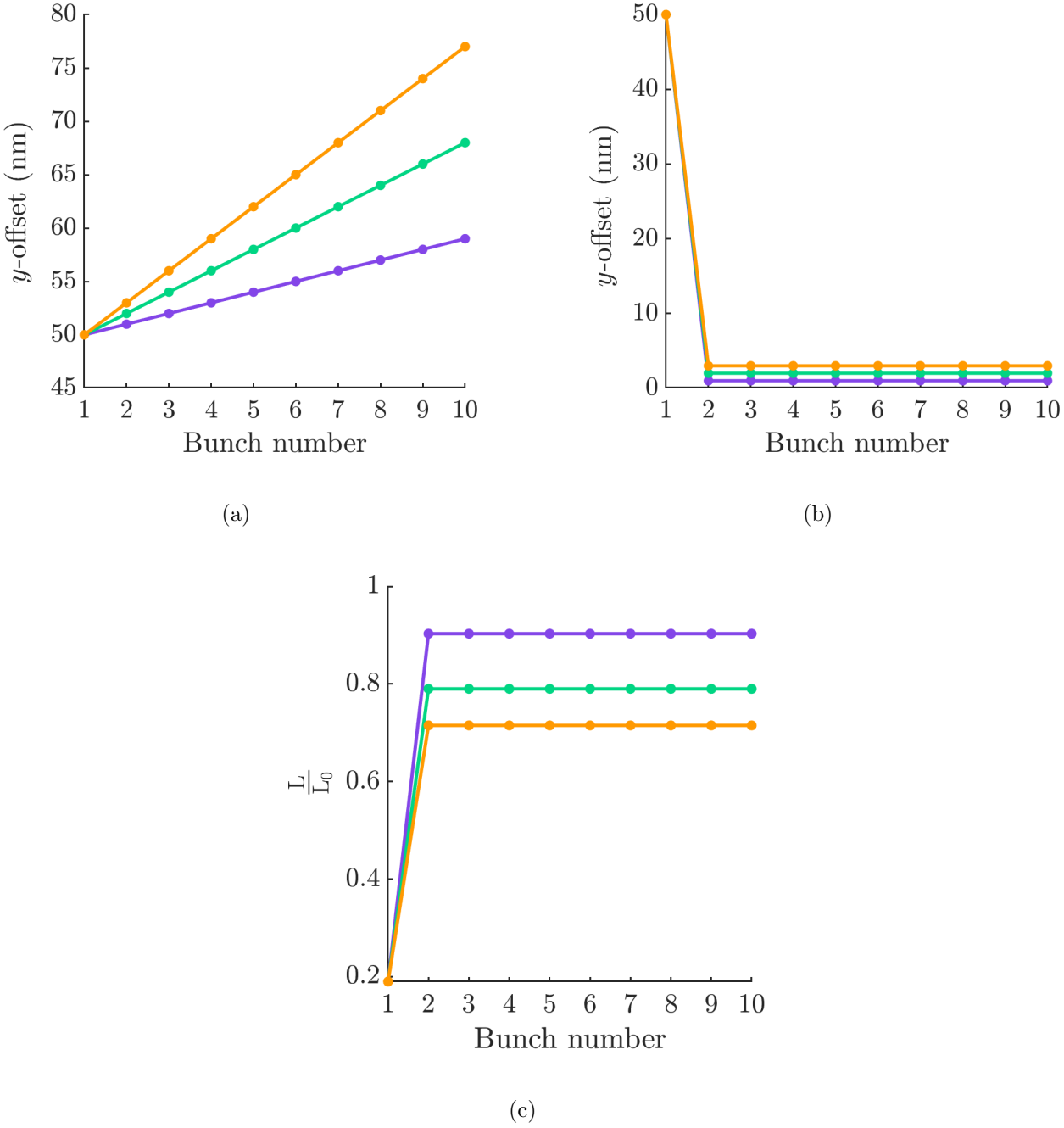

Figure 5.22: (a) Uncorrected bunch offsets, (b) offsets with Proportional-Only feedback operating (gain $G_p = 1$) and (c) the luminosity (with feedback) versus bunch number. Uncorrected bunch trains had an offset of 50 nm for the pilot bunch and a drift across the train with 1 nm (purple), 2 nm (green) and 3 nm (orange) between consecutive bunches.

displayed in Fig. 5.22(a) and the stabilised bunches in Fig. 5.22(b). The larger the offset between consecutive bunches, the lower the luminosity achievable with Proportional-Only feedback; as shown in Fig. 5.22(c). The inability of the feedback to deal with offsets between consecutive bunches means an integral term is required, as the luminosity is significantly reduced with even a small drift term.

Results for a similar simulation with Proportional-Integral feedback are presented in Fig. 5.23; four integral gain settings were simulated. By setting the integral gain to 1, the feedback will bring the bunches to collision by the third bunch. With a lower integral gain, the feedback system converges to 0 nm offset within several bunches. Typically, integral gains are set to values of order 0.1, so as to avoid integrating up noise.

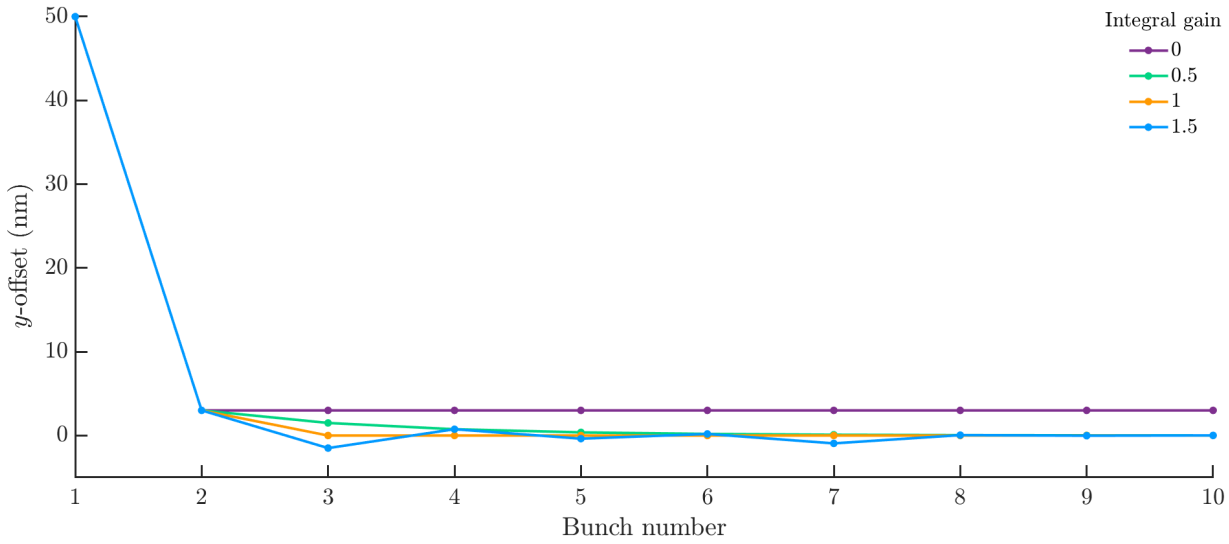

Figure 5.23: Bunch-bunch offset at the IP versus bunch number for trains with a 50 nm pilot bunch offset and with 3 nm offset between consecutive bunches. Proportional-Integral feedback was simulated with a proportional gain of 1; the integral gain is denoted by the colour of the data points.

A further simulation of Proportional-Integral feedback was performed for bunch trains with offsets of 1 nm between consecutive bunches and also random bunch-to-bunch jitter from 0.25 nm to 2 nm, sampled from a Gaussian distribution. Examples of the uncorrected bunch trains are shown in Figs. 5.24(a) and (b). The results with feedback operating are presented in Fig. 5.25, showing an improved performance with an integral gain. A bigger improvement is observed for trains where the drift term is larger compared with the jitter term.

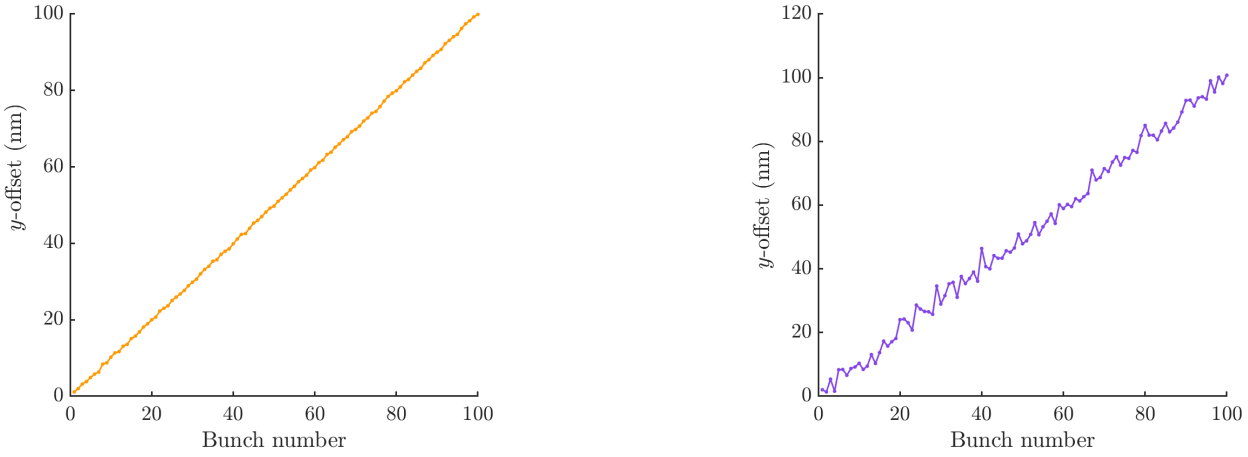

(a) (b)

Figure 5.24: Vertical bunch-bunch offset at the IP versus bunch number for trains with 1 nm bunch-to-bunch drift and (a) 0.25 nm and (b) 2 nm r.m.s jitter.

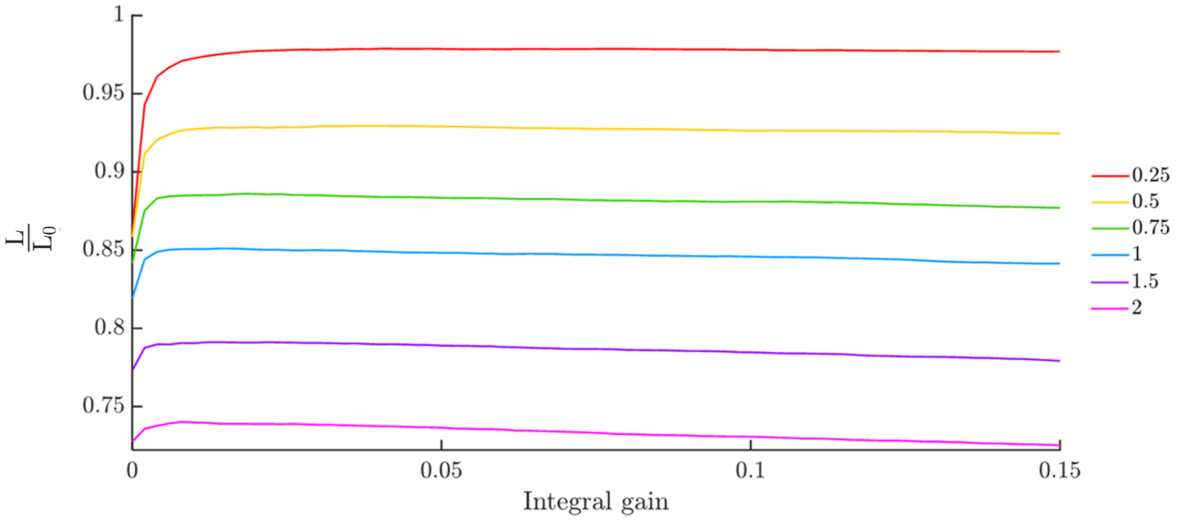

Figure 5.25: Normalised luminosity versus integral gain, for bunch trains with Proportional-Integral feedback applied, with a proportional gain of 1. The uncorrected bunches have 1 nm drift between consecutive bunches and bunch-to-bunch jitter, with the colour of the line denoting the r.m.s jitter in nm. Examples of the uncorrected trains are shown in Fig. 5.24.

5.6.4 Bunch jitter

Filtering and averaging techniques were studied with the aim of making the feedback system more robust with respect to uncorrelated jitter and noise. By simply averaging over the bunch positions of several bunches, the effect of random bunch-to-bunch fluctuations can be smoothed. This was investigated by simulating feedback, where the input was calculated by averaging over multiple consecutive bunches. The resulting improvement to the luminosity is shown in Fig. 5.26. The first bunches should be corrected without averaging so as to avoid having more than one uncorrected bunch. As the IP feedback system cannot remove uncorrelated jitter, feed-forward systems, such as the RTML feed-forward system, are required to mitigate this.

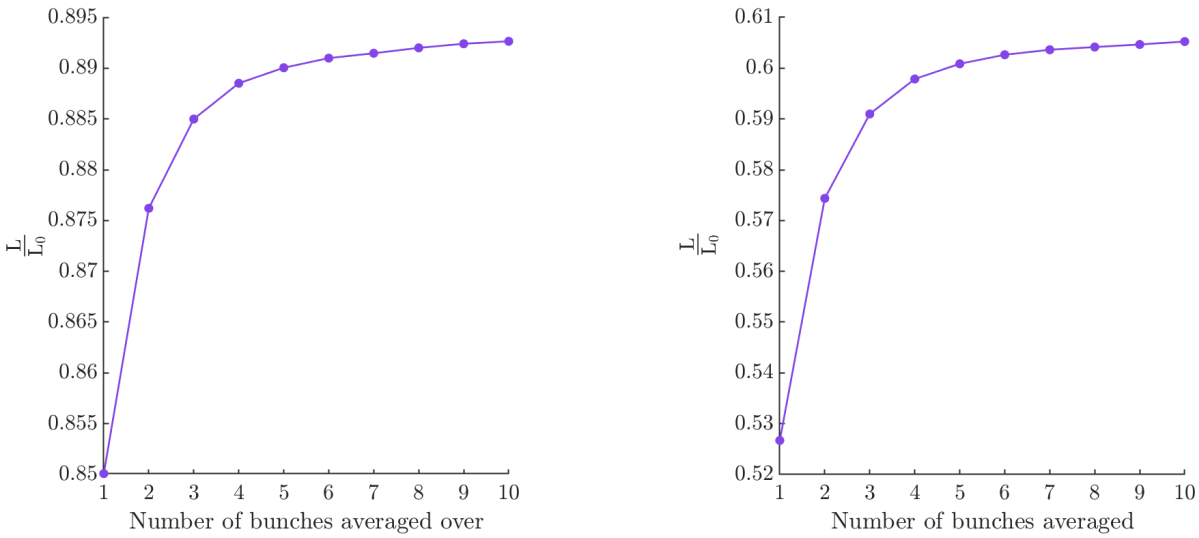

(a) (b)

Figure 5.26: Normalised luminosity versus number of bunches averaged within the feedback calculation. Feedback was simulated on bunch trains with (a) 1 nm and (b) 5 nm of random noise, with a BPM resolution of 0 nm.

The ability of the feedback system to remove offsets due to drifts would be reduced by averaging, as previous bunches become less representative of the current bunch. Consequently, slower drifts and random noise must be considered together to find an optimal solution. A more advanced algorithm would recognise that there would be a higher correlation between bunches $y[n]$ and $y[n-1]$ than between $y[n]$ and $y[n-2]$. Instead of assigning equal weight to all bunches during averaging, the most recent bunch $y[n]$ should receive a larger weighting.

An estimate $\hat{y}$[n] for the offset of bunch n using a weighted average can be written as

$$\hat{y}[n] = (\sum_{m=1}^{m=\mathrm{M}} a_m y[n-m+1]), \tag{5.10}$$

where M represents the number of bunches to be averaged and the coefficients a_m should be optimised based on the bunch-to-bunch position correlation. This type of feedback is called 'recursive', for which a history of the outputs $\hat{y}[n]$ is used alongside measured bunch position.

A commonly used weighting algorithm is the Kalman filter which uses a weighted average of a prediction of the position of bunch, $\hat{y}[n-1]$, and the measured position $y[n]$ to derive a more accurate estimate for the true position as

$$\hat{y}[n] = \hat{y}[n-1] + \mathrm{K}[n](y[n] - \hat{y}[n-1]), \tag{5.11}$$

where K[n] is the Kalman gain factor.

A Kalman filter was incorporated into the feedback algorithm and tested on bunch trains with a 1 nm drift between consecutive bunches and a range of BPM resolutions between 10 nm and 60 nm. The results of the simulation in terms of the luminosity are presented in Fig. 5.27.

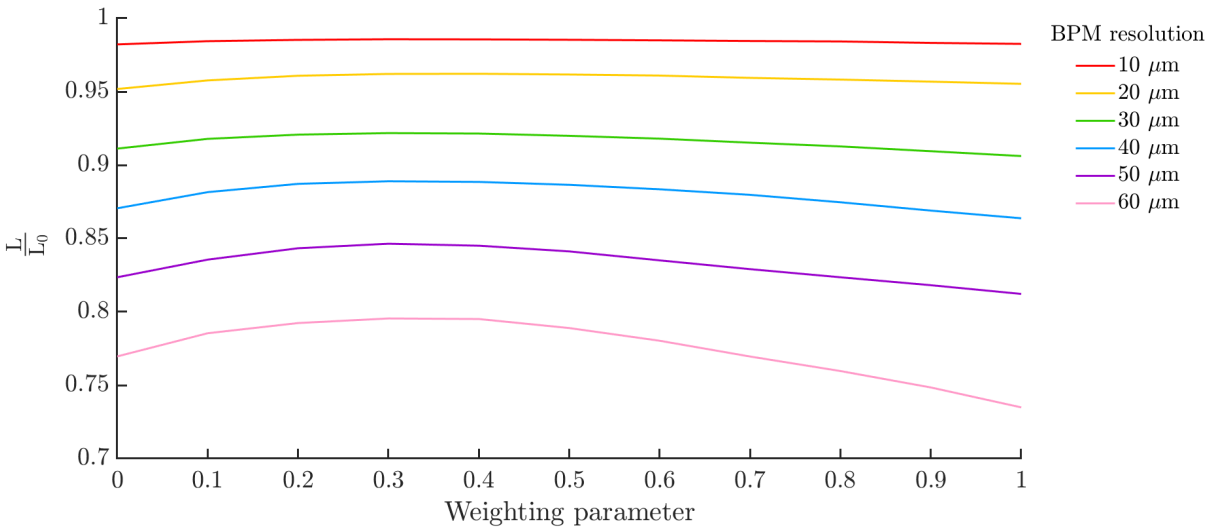

Figure 5.27: Normalised luminosity versus weighting parameter, K (Eq. 5.11) with Proportional-Only feedback operating on a train with a 1 nm offset between consecutive bunches and with the simulated BPM resolution denoted by the colour of the line.

A gain of zero corresponds to feedback without any filtering and a gain of 0.5 corresponds to equal weighting between the two previous bunches. The improvements from the filter are more prominent with poorer BPM resolutions. With 20 µm resolution, the optimum gain is 0.3 and the filter improves the luminosity by only 1%, however with a resolution of 60 µm the application of a Kalman filter with a gain of 0.4 increases the luminosity by 3%.

5.6.5 Overview

These studies have demonstrated the importance of obtaining an accurate measurement of the bunch parameters before running feedback, to ensure the LUT mapping is accurate. Within the capture range of the system, the feedback was shown to perform well, although if further studies suggest the bunch-bunch offset at the IP is likely to exceed 200 nm, then a more advanced algorithm would be required to account for this. Studies of feedback gains suggest the proportional gain should be set slightly lower than 1 as this offers good beam stabilisation but avoids the risk of over-correction and ringing. An integral term was shown to improve the feedback performance when there was bunch-to-bunch drift; the gain for this should be kept much lower than 1 so as to avoid integrating up noise and uncorrelated jitter. Depending on the bunch-to-bunch correlation, a weighted-averaging algorithm may be employed to smooth out the effect of random fluctuations on the feedback calculation.

5.7 ILC simulations

Using the PLACET simulation described in Section 5.3, the effects of ground motion, wakefields and DR extraction kicker jitter were studied with regards to the performance of an IP feedback system.

5.7.1 Ground motion

Ground motion, described in Section 1.3.1, will act to misalign beamline components, causing bunch offsets at the IP and emittance growth. Depending on the frequency of the vibrations, different mitigation methods may be used. For the 'slow' ground motion, beam steering or pulse-by-pulse feedback would be used to correct the offset at the IP, whereas for ground motion above 5 Hz intra-train IP feedback is required.

Ground motion model K (modelled on seismometer measurements at KEK, Japan) has typically been used for ILC ground-motion simulations, as one proposed site for the ILC is in Northen Japan [114]. The effects of ground-motion model C, measured at DESY, have also previously been considered for the ILC [89]. Ground-motion models C and K represent noisy sites and models A and B, corresponding to CERN and Fermilab respectively, are quieter [115].

5.7.2 Mitigation of ground motion

As described in Section 5.1.3, a cascaded feedback system is required to control the beam orbit through the ML and BDS, in order to reduce the impact of wakefields and improve the performance of beam diagnostics. For this simulation, the effect of the cascaded feedback system has been modelled as a 'deadbeat' feedback system, which is designed to reduce the error term to zero in as few steps as possible. The difference equation for deadbeat feedback is

$$Y[n] - Y[n-1] = y[n] - y[n-1] - gY[n-1], \tag{5.12}$$

where $Y[n]$ is the corrected beam position for bunch n and y is the uncorrected beam position. The transfer function $T(\omega)$ for this system is

$$T(\omega) = \frac{1 - e^{\frac{-j\omega}{f_{\text{rep.}}}}}{1 + (g-1)e^{\frac{-j\omega}{f_{\text{rep.}}}}}, \tag{5.13}$$

where ω is the frequency of the input signal, $f_{\text{rep.}}$ is the repetition frequency of the machine and g is the gain. This transfer function was used within PLACET to filter the Power Spectral Density for the ground motion, with a range of gain settings.

5.7.3 Previous studies

Previous studies have determined that with ground motion model K disturbing the BDS, and no pulse-by-pulse or intra-train feedback operating, the luminosity would be reduced to 37% of the nominal value [89]. With the addition of other sources of jitter, including facilities noise, DR extraction jitter and beam-current jitter, the luminosity is further reduced to 17% of the nominal value. Pulse-by-pulse feedback was simulated to recover the luminosity to 84% of the nominal value but to increase the luminosity further, intra-train feedback would be required. The reduction in luminosity from ground motion was found to originate mainly from the BDS. It was concluded that the luminosity losses were within acceptable limits, although, ideally, for the ILC the high-frequency ground motion would be a factor of three quieter than in model K [89].

5.7.4 Current ground-motion study

All four ground-motion models were studied for the ILC ML and BDS and the bunch jitters and the luminosities were calculated. To study pulse-by-pulse effects, 100 random seeds of ground motion were simulated for 0.2 s, corresponding to the separation between consecutive

bunches. The effect of low-frequency ground motion was also investigated, with 30 minutes of ground motion simulated with 100 different seeds. The electron and positron beamlines were each modelled and separately disturbed by a random seed of ground motion. Bunches were then tracked through the ML and BDS to the IP.

The beam jitter and normalised luminosities for four different ground-motion models are presented in Table 5.4. Models A and B cause jitter which is more than an order of magnitude smaller than models C and K. The bunch-bunch offsets at the IP caused by 0.2 s of ground motion happen over too short a timescale to be recovered with 5 Hz feedback and instead must be accounted for with IP feedback. These simulations show that for 0.2 s of ground motion, the bunch offsets at the IP are safely within the capture range of the IP feedback system. If ground-motion model K is left uncorrected for over 30 minutes, nearly all of the luminosity is lost and the offsets at the IP exceed the capture range for IP feedback. The distributions of vertical bunch positions for 100 random seeds of model K are given in Fig. 5.28 for 0.2 s of ground motion and in Fig. 5.29 for 30 minutes.

The 5 Hz feedback system was modelled in PLACET using the transfer function for deadbeat feedback (see Section 5.7.2). This was tested for 0.2 s of ground-motion model K with a range of gains and the results are displayed in Fig. 5.30. From [89], it was found that the jitter should remain less than the bunch size throughout the BDS. Fig. 5.30 suggests that a deadbeat feedback system could achieve this level of stabilisation, with gains above 8 reducing the jitter to less than $\sigma_y = 5.9\,\text{nm}$. More sophisticated simulations of the cascaded feedback system would be recommended, explicitly taking into account the resolution of the BPMs, kicker errors and the phase advance between the coupled feedback loops.

Table 5.4: IP bunch jitter and luminosity with ground motion models A, B, C and K applied to the ML and BDS. The luminosities have been normalised by the peak luminosity for 0 nm offset.

Ground motion model	Time applied (s)	IP jitter (nm)	$\frac{L}{L_0}$
A	0.2	0.15	0.99
B	0.2	0.9	0.94
C	0.2	16.9	0.44
K	0.2	34.9	0.27
A	1800	31.2	0.30
B	1800	57.3	0.19
C	1800	360.0	0.053
K	1800	1029.8	0.036

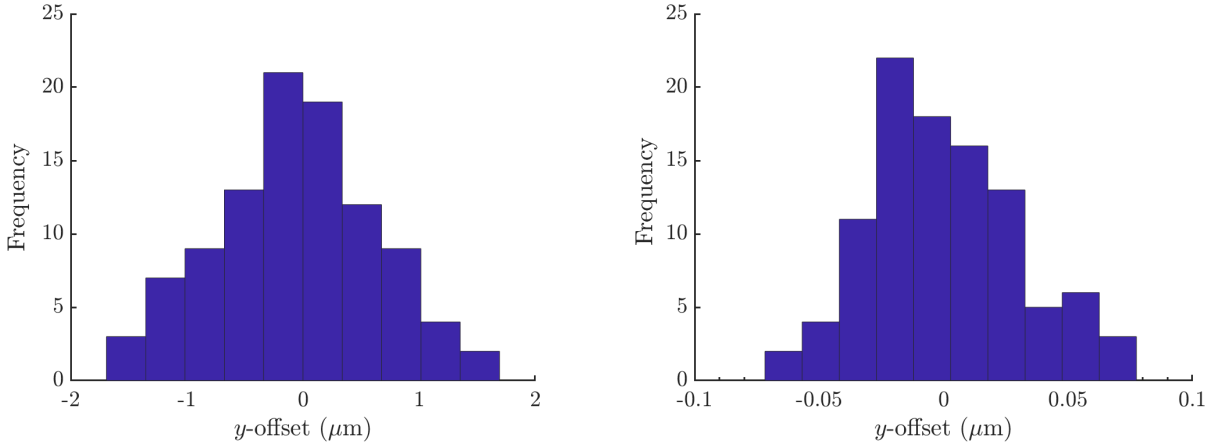

(a) (b)

Figure 5.28: Distribution of vertical bunch positions at (a) the end of the ML and (b) the IP, with 100 seeds of ground motion model K simulated for 0.2 seconds.

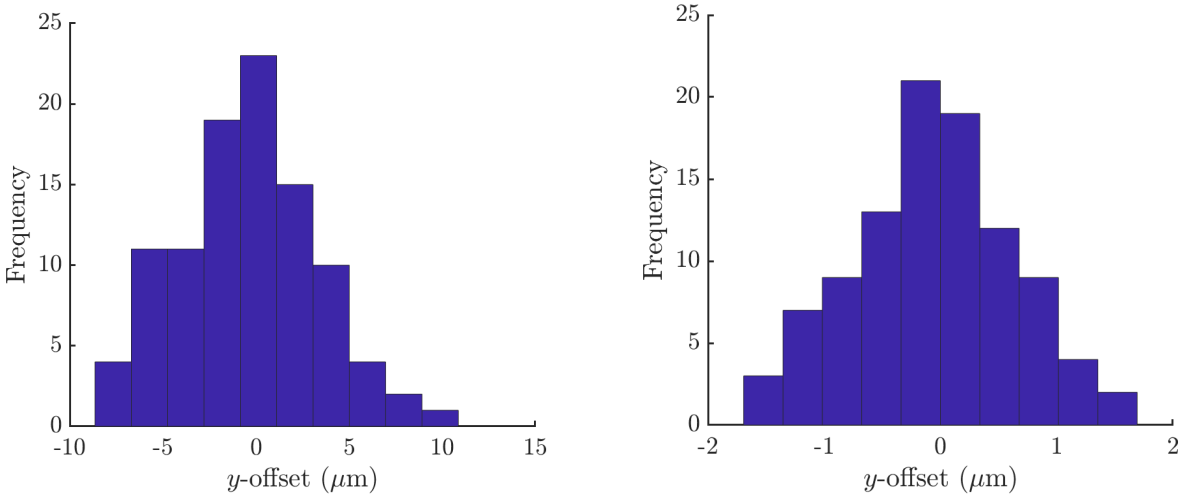

(a) (b)

Figure 5.29: Distribution of vertical bunch positions at (a) the end of the ML and (b) the IP, with 100 seeds of ground motion model K simulated for 30 minutes.

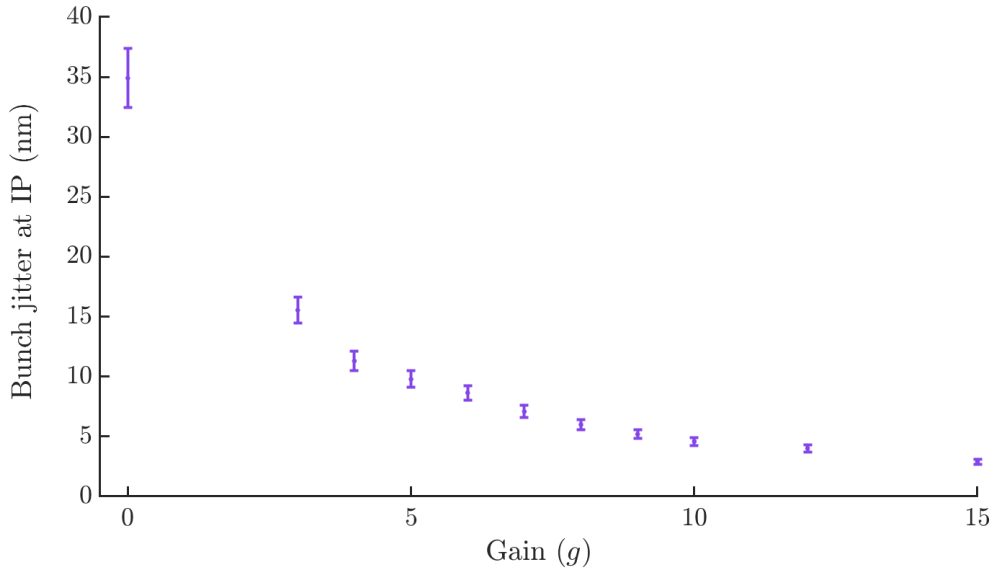

Figure 5.30: Bunch jitter at the IP versus transfer function gain; 100 random seeds of 0.2 seconds of ground motion model K were applied and a 5 Hz deadbeat feedback system was simulated, with gain g. The error bars correspond to the standard error.

5.7.5 Wakefield effects

Short-range wakefields were simulated for the accelerating cavities, cavity BPMs and for resistive walls to determine whether 'banana-bunch' effects could be seen. The macroparticles used to simulate the bunch were plotted, an example of which is shown in Fig. 5.31(a). No significant banana-bunch shapes were observed and the luminosity was maximised for ~ 0 nm bunch-bunch offset. As described in Section 5.1.2, short-range wakefields in the accelerating cavities could also introduce longitudinal energy variation in the bunch, which can be seen by plotting E versus z; an example is presented in Fig. 5.31(b) showing clear E-z correlation.

Long-range wakefields were simulated on trains of 300 bunches to study the impact on beam stability at the IP. Trains with intial offsets of 1 µm and 2 µm were tracked through the ML and BDS with the wakefield modes detailed in Tab. 5.3 simulated. The resulting bunch trains at the end of the ML are presented in Fig. 5.32(a). The long-range wakefields predominantly affect the first few tens of bunches and are considerably damped within the first 100 bunches by a higher-order-mode-damping coupler on the accelerating cavities [116].

The corresponding trains at the IP are shown in Fig. 5.32(b). If uncorrected by the train straightener, the 1 µm offset simulated at the start of the ML propagates to a ~ 0.15 nm offset at the IP. Any long-range wakefield effects not removed by the train straightener could be corrected by the IP feedback system by adding the appropriate constant offsets for individual bunches to the feedback correction.

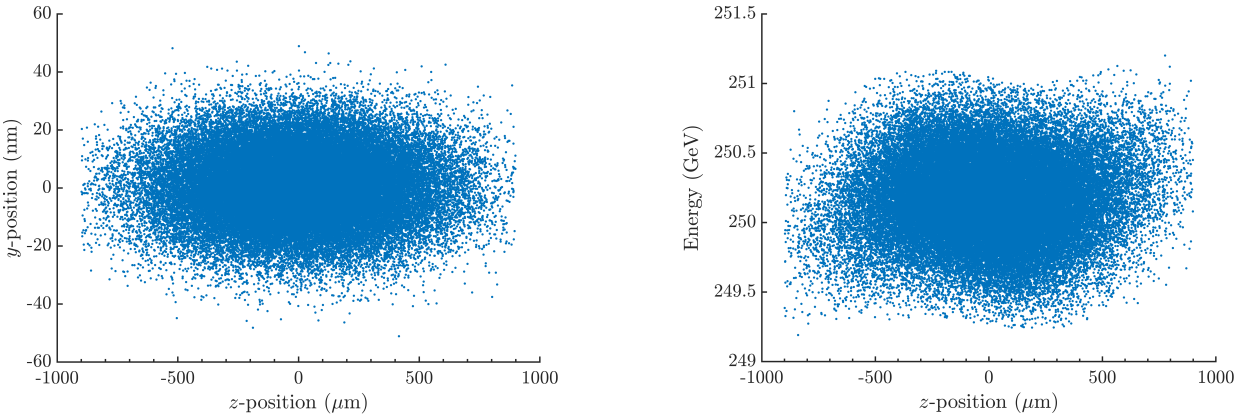

(a) (b)

Figure 5.31: (a) Vertical position versus longitudinal position and (b) energy versus longitudinal position, with short-range wakefield effects modelled. Data points represent the 20,000 macroparticles used for the simulation.

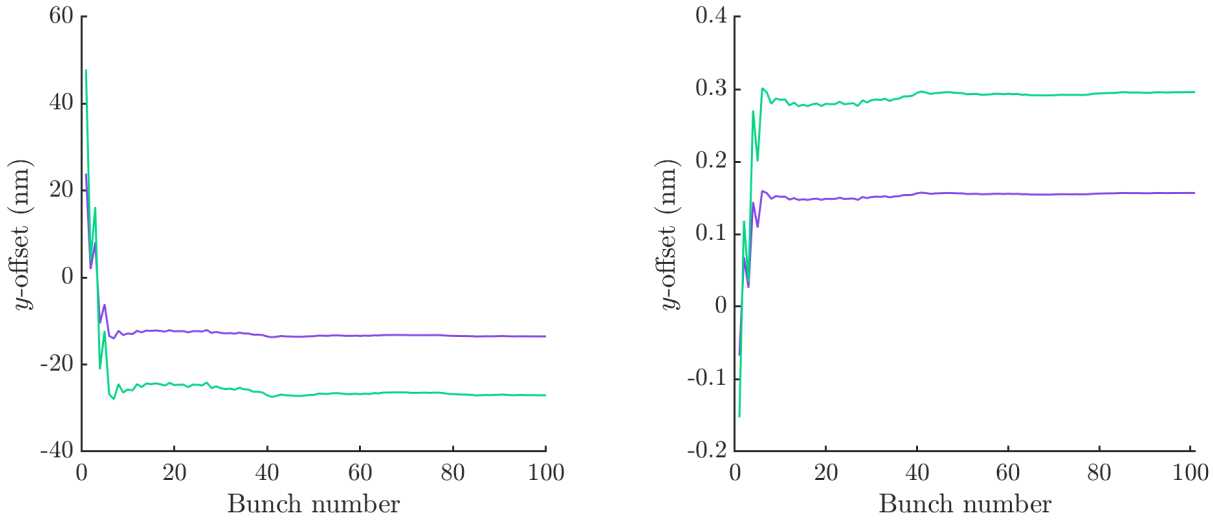

(a) (b)

Figure 5.32: Vertical bunch offsets (a) at the end of the ML and (b) at the IP, with long-range wakefields simulated. Bunch trains had an initial offset of 1 µm (purple) and 2 µm (green) at the start of the ML.

5.7.6 Damping-ring extraction jitter

The RTML feed-forward system is designed to reduce the DR extraction kicker jitter to less than 10% of the beam size when propagated to the IP. The vertical bunch size at the start of the ML is $\sim 5\,\mu m$. Bunch jitter was modelled at the start of the ML from a Gaussian distribution with standard deviation of $0.5\,\mu m$; this propagated to a jitter of $0.09\,nm$ at the IP. In the worst case, if the jitter is fully uncorrelated bunch-to-bunch, and could not be corrected by IP feedback, this would lead to a luminosity loss of $\sim 4\%$ at the IP.

5.7.7 Intra-train IP feedback

Simulations were performed to study the beam stabilisation in the presence of wakefield effects, ground motion and bunch jitter. The corrector was modelled with a 0.1% kick error and the BPM with a $1\,\mu m$ resolution. Jitter was introduced to the ML to represent DR extraction kicker jitter, corresponding to a 10% beam-size increase at the IP, as this was the tolerance suggested in [89]. The electron and positron beamlines were each simulated and separately disturbed by a random seed of ground-motion model K, applied for 0.2 seconds. The relative Final Doublet jitter was simulated to have a standard deviation of $100\,nm$ at frequencies below $5\,Hz$.

For the IP feedback system, Proportional-Only feedback was simulated; the results are presented in Fig. 5.33. With a gain of 1, much of the luminosity was recovered by the second bunch, as all of the bunch trains were within the capture range of the feedback system. The luminosity for the subsequent bunches is limited by the bunch-to-bunch correlation, which is reduced by the BPM resolution and the bunch-to-bunch jitter. If this becomes too large, the gain of the feedback should be reduced correspondingly, although this would reduce the initial rate of convergence. For these simulations, the luminosity showed negligible improvement with a reduced gain, as the dominant effect was the constant offset of the whole bunch train as opposed to bunch-to-bunch variations.

Further simulations with feedback gains of $g = 0.1$ (Fig. 5.33(b)) and $g = 1.9$ (Fig. 5.33(c)) were performed. For a lower gain, the beam takes longer to converge; however, even with a gain of 0.1 the luminosity is almost fully recovered by bunch 40. With a train of 1312 bunches this represents a luminosity loss of only a few percent and for a real system the feedback gain would be set lower than 1, in order to make system more robust to noise and errors. If the gain is set too high, as shown in Fig. 5.33(b), again the system takes longer to converge. However, when the gain is too high, a lower luminosity is achieved, with the over-correction causing 'ringing'. For $g = 1$, the luminosity reaches $\sim 95\%$ of the design

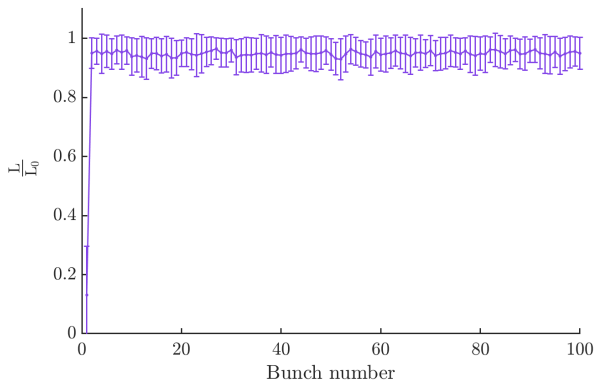

(a) $g = 1$

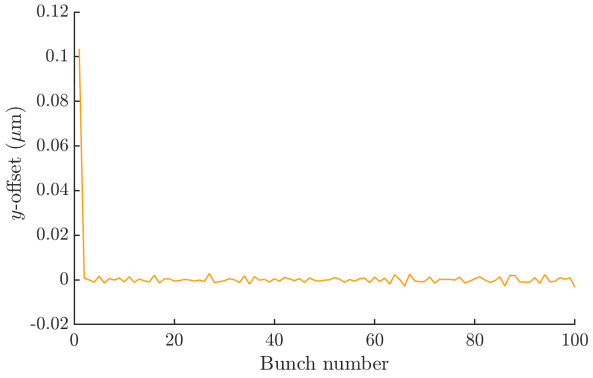

(b) $g = 1$

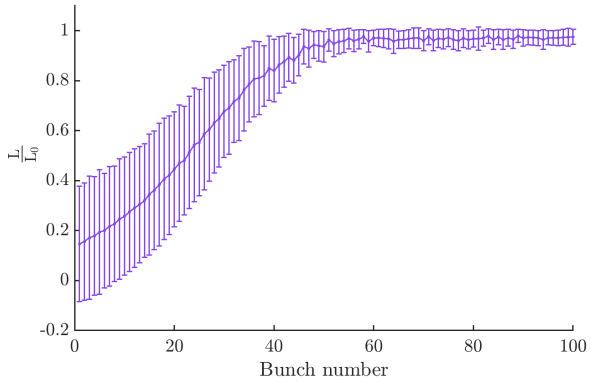

(c) $g = 0.1$

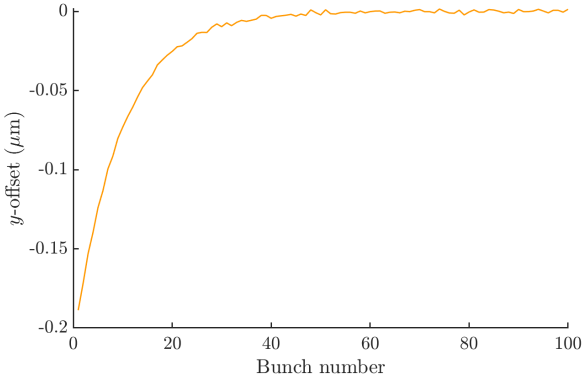

(d) $g = 0.1$

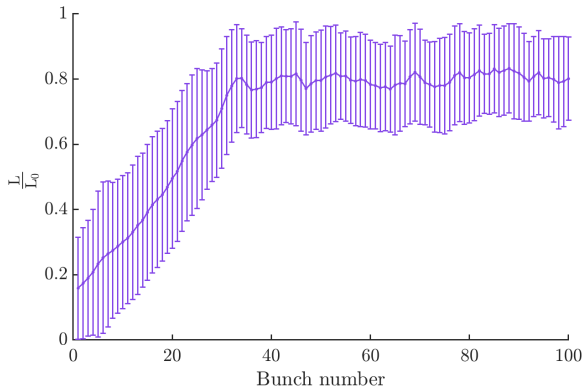

(e) $g = 1.9$

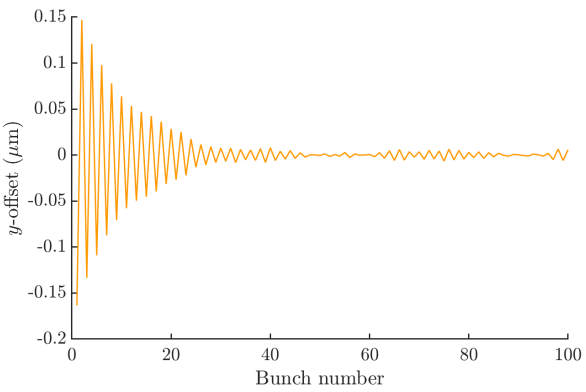

(f) $g = 1.9$

Figure 5.33: (a), (c) and (e) show normalised luminosity versus bunch number, with Proportional-Only feedback and (b), (d), (f) show vertical bunch-bunch offset at the IP versus bunch number for a single seed. The gains used for feedback are given as captions. Simulations were performed for 100 trains with ground motion, bunch-to-bunch jitter and FD jitter. For (a), (c) and (e) the data points show the mean luminosity for 100 trains and the error bars show the standard deviation.

value, but with $g = 1.9$ the luminosity only reaches $\sim 80.0\%$, demonstrating the importance of not over-correcting.

5.8 Summary

This chapter has detailed simulations of the beam transport in the ML and BDS, the beam-beam interaction and the IP feedback system. The ML and BDS were simulated in PLACET in order to study the effect of wakefields, jitter sources and ground motion on beam stability. The beam-beam interactions were modelled in GUINEA-PIG, allowing for the beam-beam deflection and luminosity to be determined. The peak luminosity was simulated to be $1.79 \times 10^{34}\,\mathrm{cm}^{-2}\mathrm{s}^{-1}$ and the maximum deflection angle to be $360\,\mu\mathrm{rad}$. To stabilise the luminosity to within 0.1% of the design value, a BPM resolution of better than $1\,\mu\mathrm{m}$ would be required, with a linear working region of $\sim \pm 1400\,\mu\mathrm{m}$.

The beam deflection and luminosity were studied as a function of the bunch charge and bunch size and were shown to be particularly sensitive to the bunch charge. It was demonstrated that if the horizontal bunch size became too large, the capture range of the feedback system would be reduced; a similar effect was shown for low bunch charges.

The performance of the feedback system was studied for trains with slow drifts and bunch-to-bunch jitter. It was demonstrated that an integral term would significantly improve the performance of the system, even with small integral gains. With higher levels of bunch-to-bunch jitter, an integral term could potentially amplify any random fluctuations and so it is important to optimise this gain to ensure system stability.

The simulations of the beam transport were used to estimate the impact of short-range and long-range wakefields. It was concluded that short-range wakefields had little effect on the x-y bunch profile, so that the luminosity is maximised for a zero bunch-bunch offset. Although short-range wakefields were not observed to distort the y-z profile, they were shown to introduce E-z dependence. Long-range wakefields were also modelled and these were found to affect predominantly the first 100 bunches, introducing static offsets at the IP of less than a nanometre. If these were not fully removed with a train straightener it would be possible to remove them with the IP feedback system.

Four ground-motion models were considered, with two quieter sites (model A and B) and two noisier sites (C and K). Ground motion was considered over short timescales, for which the high-frequency components are important and over longer timescales of 30 minutes for which low-frequency vibrations dominate. Models A and B had little effect on the luminosity

over 0.2 s but model K was simulated to reduce the luminosity to 27% of the nominal value. Over 30 minutes, models C and K both reduced the luminosity to close to zero. A preliminary model for the cascaded 5 Hz feedback system was created using a filter on the ground-motion spectrum, corresponding to a deadbeat feedback algorithm. A range of feedback gains was modelled and the effects on the beam stabilisation and luminosity were considered. The results suggested that with sufficient BPM resolution and kicker dynamic range, a 5 Hz deadbeat feedback system could keep the vertical bunch jitter to less than the bunch size.

Finally, IP feedback was simulated on bunch trains tracked through the ML and BDS with wakefields, ground motion and DR jitter modelled. The beamlines were each disturbed with 100 random seeds of ground-motion model K and bunch trains were tracked to the IP. All of the trains fell within the capture range of the IP feedback system, allowing for the luminosity to be increased to $\sim$ 95% by the second bunch. With IP feedback the luminosity was maintained at $\sim$ 95% of the nominal value for the rest of the train, where the remaining luminosity loss stemmed from the finite BPM resolution and the uncorrelated bunch-to-bunch jitter.

Chapter 6

Conclusions

The International Linear Collider is a future electron-positron collider, designed for further studies of the Higgs boson and for the investigation of physics beyond the Standard Model. To meet the design luminosity, beam stabilisation is required at the IP; this is proposed to be performed with a dedicated bunch-by-bunch feedback system. The feedback system would make use of the beam-beam deflection due to the strong electromagnetic forces between the bunches at collision and would measure a deflected bunch downstream of the IP so as to correct following bunches. The system should be able to correct offsets of up to ± 200 nm with a latency of less than 554 ns.

A prototype system is installed at the IP of the ATF2 and was designed to demonstrate that a nanometre-level resolution could be achieved with low-latency feedback. The system comprises three cavity BPMs and the specifications and calibrations for these were described. The calibration constant was shown to scale as expected with signal level, suggesting good linearity of the system. Work towards optimising the resolution of the system was also presented. A geometric resolution of 20 nm was achieved using sample integration, which was corroborated by the fitted resolutions for the three BPMs of $\sim$ 19 nm. The system resolution scaled as expected with signal attenuation from 50 dB to 20 dB but deviated from the predicted scaling for 10 dB, which may indicate non-linearities in the system for higher signal levels.

The dependence of the resolution on several parameters was analysed, with a particular focus on the effect of the phase jitter introduced by the limiting amplifier. The coupling of angular information into the position measurement was also considered, demonstrating the importance of minimising the tilt of the BPM with respect to the beam. With a 2.1 mrad angular offset, the geometric resolution was reduced to 80 nm and while this could be improved to 30 nm using multi-parameter fitting, this is not possible within the latency limits

specified by intra-train feedback.

The importance of sample integration in improving the resolution was shown and improvements to the feedback firmware which allow for the use of sample integration during intra-train feedback were detailed. The input to the feedback system can be from a single BPM to provide local beam stabilisation, or from two BPMs to stabilise the beam at an intermediate location: the firmware was tested in both modes and an improved feedback performance was achieved. Stabilisation of the beam jitter to 50 ± 5 nm was achieved for 1-BPM feedback and stabilisation to 41 ± 4 nm for 2-BPM feedback. The current version of firmware, with integration of up to fifteen samples, has a latency of 232 ns, which is well within the limit set by the bunch spacing.

Experimental data from the ATF2 extraction-line feedback system has proven that the resolution, latency and kick requirements for the ILC could be met. Further simulations were designed to show that the proposed IP feedback system could help achieve the design luminosity. To demonstrate this, a model of the feedback system was constructed in Octave, and used to test the performance of various feedback algorithms on ILC-like bunch trains. To generate the bunch trains and model the beam transport through the ML and BDS, the simulation tool PLACET was used. PLACET was interfaced with GUINEA-PIG to simulate the beam-beam interaction. The beam stabilisation at the IP was studied as a function of various parameters including variations in the bunch intensity, bunch dimensions and length and the incoming position jitter.

The benefits and drawbacks of Proportional-Only and Proportional-Integral feedback were considered, with studies of the optimum gain settings for each. Filtering and averaging methods were also analysed in order to improve the accuracy of the bunch position measurements. Simulations of the beam-beam interaction were used to study the variations in the beam-beam deflection curve for changes in the bunch parameters. The performance of the feedback system was shown to be particularly sensitive to the bunch charge, with a lower charge reducing the capture range of the feedback system. It was determined that to meet the requirements for luminosity recovery, a BPM with 1 µm resolution and a dynamic range of more than ±1400 µm was needed. Short-range wakefields were modelled and it was concluded that banana-bunch effects were negligible and consequently that the luminosity was maximised for a zero bunch-bunch offset.

Four different ground motion models (A, B, C and K) were simulated, with ground motion model K typically considered for the ILC. By applying 0.2 seconds of ground motion model K and no beam-based feedback, the luminosity was reduced to 27% of the nominal value. A simplified model of the pulse-by-pulse feedback system suggested that it could reduce the

effects of ground motion on the IP beam jitter to less than the bunch size. The performance of an IP feedback system was modelled while including the effects of ground motion, short-range wakefields, DR extraction kicker jitter and FD jitter. The luminosity was simulated to increase from $\sim 15\%$ to $\sim 95\%$ with IP feedback, where the remaining luminosity loss corresponded to the imperfectly measured bunch-to-bunch correlation caused by the DR extraction kicker jitter and BPM resolution.

6.1 Suggestions for further work

The deviation from the expected scaling of the resolution with attenuation could be indicative of non-linearities in the system and, to characterise this, further studies of the scaling of the resolution with dipole attenuation are recommended. A finer scan of attenuations could be used as well as studies at a range of bunch charges, to get a better understanding of the BPMs' linear operating region in terms of input signal amplitude.

Beam stabilisation to 41 nm has been achieved with 2-BPM feedback but the resolution of the system suggests that 25 nm stabilisation would be achievable. To achieve this, effort should be made to minimise the offsets of the BPMs' positions and angles with respect to the beam, requiring an estimation of the zero-offset of the position and angle signals in offline analysis. Furthermore, it was shown that the correlation was not fully removed during feedback, suggesting the gains were not fully optimised. Finer gain scans are therefore recommended to achieve the best stabilisation performance.

Although 2-BPM feedback has been demonstrated to offer better stabilisation, it has so far been restricted to operation with high-beta optics. For future tests of 2-BPM feedback, operation with a nominal β_y^* would best mimic the performance of a feedback system for a future linear collider. Such a configuration would mean larger jitters at IPA and IPC and, consequently, alignment of all three BPMs would be considerably more difficult, possibly requiring extra attenuation on the dipole cavity (position) signal. Further studies are recommended to determine whether this is feasible, and also the effect of changing the optics on the feedback performance.

Preliminary studies of an ILC IP feedback system were presented. To continue these studies, the cascaded 5 Hz feedback system should be fully modelled, along with the train straightener and RTML FF system. Further studies are also required to characterise the high-frequency facilities noise which would be expected to significantly affect the performance of an intra-train feedback system. Regarding future studies of feedback algorithms, a more comprehensive study of Proportional and Integral feedback gains is needed. The addition

of filtering to the position measurements should be considered further, with a Kalman filter or similar method of weighted averaging investigated. These studies focus only on the 500 GeV baseline design and additional studies for the 250 GeV and 350 GeV designs are recommended.

Bibliography

[1] R. Oerter. "The theory of almost everything: The standard model, the unsung triumph of modern physics". Penguin (2006).

[2] D.H. Perkins. "Introduction to high energy physics". Cambridge University Press (2000).

[3] R.J. Blin-Stoyle. "Nuclear and particle physics". Springer Science & Business Media (2013).

[4] D. Griffiths. "Introduction to elementary particles". John Wiley & Sons (2008).

[5] B. Povh, K. Rith & F. Zetsche. "Particles and nuclei", volume 4. Springer (1995).

[6] J. Womersley. "Beyond the Standard Model". *Symmetry Magazine* (2005).

[7] S. Carroll. "Dark Matter, Dark Energy: The Dark Side of the Universe". Teaching Company (2007).

[8] G. Bertone, D. Hooper & J. Silk. "Particle dark matter: Evidence, candidates and constraints". *Physics Reports*, **405** (2005) 279–390.

[9] L.M. Krauss, S. Nasri & M. Trodden. "Model for neutrino masses and dark matter". *Physical Review D*, **67**, 8 (2003) 085002.

[10] G. Aad et al. "Observation of a new particle in the search for the Standard Model Higgs boson with the ATLAS detector at the LHC". *Physics Letters B*, **716**, 1 (2012) 1–29.

[11] P. Higgs. "Broken symmetries and the masses of gauge bosons". *Physical Review Letters*, **13**, 16 (1964) 508.

[12] R. Wolf. "The Higgs Boson in the Standard Model of Particle Physics". In "The Higgs Boson Discovery at the Large Hadron Collider", pages 15–51. Springer (2015).

[13] J. Bernstein. "Spontaneous symmetry breaking, gauge theories, the Higgs mechanism and all that". *Reviews of modern physics*, **46**, 1 (1974) 7.

[14] D. Barducci et al. "Future Electron-Positron Colliders and the 4-Dimensional Composite Higgs Model". *JHEP*, **02** (2014) 005.

[15] T. Horiguchi et al. "Study of top quark pair production near threshold at the ILC". *arXiv:1310.0563*.

[16] S. Marti-Garcia. "Top quark mass measurements in ATLAS". *Journal of Physics: Conference Series*, **556** (2014) 012033.

[17] Y. Chiu-Tien. "The Top Quark as a Window to Beyond the Standard Model Physics". PhD. thesis, University of Winsconsin (2013).

[18] P. Doublet et al. "Determination of Top-quark Asymmetries at the ILC". *arXiv:1202.6659*.

[19] J. Fuster et al. "Study of single top production at high energy electron positron colliders". *Eur. Phys. J.*, **C75** (2015) 223.

[20] ATLAS collaboration. "Measurements of b-jet tagging efficiency with the ATLAS detector using tt events at s= 13 TeV". *Journal of High Energy Physics*, **2018**, 8.

[21] S. Lee. "Accelerator physics". World Scientific Publishing Company (2011).

[22] K. Wille. "The physics of particle accelerators: an introduction". Clarendon Press (2000).

[23] H. Wiedemann. "Particle accelerator physics". Springer (2015).

[24] D. Möhl & A.M. Sessler. "Beam cooling: principles and achievements". *Nuclear Instruments and Methods in Physics Research Section A: Accelerators, Spectrometers, Detectors and Associated Equipment*, **532**, 1-2 (2004) 1–10.

[25] M. Benedikt, J. Wenninger, D. Schulte & F. Zimmermann. "Challenges for highest energy circular colliders". Technical report (2014).

[26] M. Aicheler et al. "A Multi-TeV linear collider based on CLIC technology: CLIC Conceptual Design Report". Technical report, SLAC National Accelerator Lab., Menlo Park, CA (United States) (2014).

[27] G. Weiglein et al. "Physics interplay of the LHC and the ILC". *Physics Reports*, **426**, 2-6 (2006) 47–358.

[28] "Status of Higgs Boson Physics" (2016). `http://pdg.lbl.gov/2016/reviews/rpp2016-rev-higgs-boson.pdf`

[29] T. Behnke et al. "The International Linear Collider: Technical Design Report - Volume 1: Executive Summary" (2013). CERN-ATS-2013-037.

[30] P. Bambade et al. "The International Linear Collider: A Global Project". *arXiv:1903.01629*.

[31] H. Aihara et al. "The International Linear Collider. A Global Project". *arXiv:1901.09829*.

[32] Z. Liu, L-T. Wang & H. Zhang. "Exotic decays of the 125 GeV Higgs boson at future e^+e^- colliders". *Chinese Physics C*, **41**, 6 (2017) 063102.

[33] H. Baer et al. "The International Linear Collider Technical Design Report - Volume 2: Physics" (2013). CERN-ATS-2013-037.

[34] C. Adolphsen et al. "The International Linear Collider: Technical Design Report - Volume 3.II: Accelerator Baseline Design". CERN-ATS-2013-037 (2013).

[35] A. Faus-Golfe & J. Resta-López. "Beam Size and Emittance Reconstruction in the RMTL of Future Linear Colliders". THPME163 (2014).

[36] A. Kalinin et al. "Turnaround feed-forward correction at the ILC". In "Proc. of PAC'07", Albuquerque, New Mexico (2007).

[37] S Seletskiy & N Solyak. "Renovated Two-stage Bunch Compressor for the International Linear Collider". In "Proc. of IPAC '12", volume 1205201, pages 1801–1803 (2012).

[38] E. Wilson & E.J.N Wilson. "An introduction to particle accelerators". Clarendon Press (2001).

[39] R. Amirikas, H. Ehrlichmann, W. Bialowons & A. Bertolini. "Ground motion and comparison of various sites". Technical report (2005).

[40] R.H. Siemann. "Overview of linear collider designs". In "Proceedings of International Conference on Particle Accelerators", pages 532–536. IEEE (1993).

[41] J. Resta-López, P.N. Burrows, A.F. Hartin, A. Latina & D. Schulte. "PLACET based start-to-end simulations of the ILC with intra-train fast feedback system". *EUROTeV-Report-2008-052*.

[42] R.J. Apsimon et al. "Design and operation of a prototype interaction point beam collision feedback system for the International Linear Collider". *Phys. Rev. Accel. Beams*, **21** (2018) 122802.

[43] P.N. Burrows et al. "The FONT4 ILC intra-train beam-based digital feedback system prototype". In "Particle Accelerator Conference '07", pages 416–418 (2007).

[44] G. White et al. "Experimental validation of a novel compact focusing scheme for future energy-frontier linear lepton colliders". *Physical review letters*, **112**, 3 (2014) 034802.

[45] B.I. Grishanov et al. "ATF2 Proposal" (2005), CERN-AB-2005-035.

[46] P. Bambade et al. "Present status and first results of the final focus beam line at the KEK Accelerator Test Facility". *Physical Review Special Topics-Accelerators and Beams*, **13**, 4 (2010) 042801.

[47] A. Seryi et al. "Experimental and theoretical progress of linear collider final focus design and ATF2 facility". *Nuclear Instruments and Methods in Physics Research Section A: Accelerators, Spectrometers, Detectors and Associated Equipment*, **740** (2014) 2–5.

[48] "Achieving tiny beam spot sizes with ATF2" (2008). `www.linearcollider.org/ILC/GDE/Director%27s-Corner/2008/2-October-2008---Achieving-tiny-beam-spot-sizes-with-ATF2`

[49] O. Blanco. "Beam dynamics in the final focus section of the future linear collider". PhD. thesis, Universit paris-sud (2015).

[50] P. Raimondi & A. Seryi. "Novel final focus design for future linear colliders". *Physical review letters*, **86**, 17 (2001) 3779.

[51] ATF collaboration et al. "Aiming for nanobeams: Accelerator Test Facility" (2011). `http://www-atf.kek.jp/atf/files/ATF-E1227.pdf`

[52] T. Naito, S. Araki, H. Hayano, K. Kubo, S. Kuroda, N. Terunuma, T. Okugi & J. Urakawa. "Multibunch beam extraction using the strip-line kicker at the KEK Accelerator Test Facility". *Physical Review Special Topics-Accelerators and Beams*, **14**, 5 (2011) 051002.

[53] N. Blaskovic Kraljevic. "Development of a high-precision low-latency position feedback system for single-pass beamlines using stripline and cavity beam position monitors". D.Phil. thesis, University of Oxford (2015).

[54] S. Walston et al. "Performance of a High Resolution Cavity Beam Position Monitor System". *Nuclear Instruments and Methods*, **A 578**.

[55] Y. Inoue et al. "Development of a high-resolution cavity-beam position monitor". *Physical Review Special Topics-Accelerators and Beams*, **11**, 6 (2008) 062801.

[56] D. Lipka et al. "Cavity BPM designs, related electronics and measured performances". In "Proc. of DIPAC'09", Basel, Switzerland (2009).

[57] R. Lorenz. "Cavity beam position monitors". In "AIP Conference Proceedings", volume 451, pages 53–73. AIP (1998).

[58] S. Jang, E. Kim, Y. Honda, T. Tauchi & N. Terunuma. "Development of a cavity-type beam position monitors with high resolution for ATF2". In "International Particle Accelerator Conference", (2013).

[59] S. Jang. "KNU IP-BPM and reference cavity" (2013). `http://atf.kek.jp/twiki/bin/view/ATFlogbook/IPBPMMeeting20131007`

[60] T. Bromwich. "Development of high-resolution cavity beam position monitors for use in low-latency feedback systems". D.Phil. thesis, University of Oxford (2018).

[61] Arysev A. et al. "ATF2 meeting" (2017). `http://www-atf.kek.jp/atf/files/ATF-E1227.pdf`

[62] Y.I. Kim. "Cavity beam position monitor system for the beam delivery and interaction point of the Accelerator Test Facility 2 and future linear collider". D.Phil. thesis, PhD thesis, Kyungpook National University, Deagu, Korea (2012).

[63] T. Naito, H. Hayano, T. Korhonen, S. Takeda & J. Urakawa. "Timing system of the ATF". No. KEK-97-230. SCAN-9806036.

[64] N. Blaskovic Kraljevic et al. "Development of a low-latency, high-precision, intra-train beam feedback system based on cavity beam position monitors". In "Proc. of IPAC '14", Dresden, Germany (2014).

[65] Y.I. Kim et al. "Cavity beam position monitor system for the Accelerator Test Facility 2". *Phys. Rev. ST Accel. Beams*, **15** (2012) 042801. https://link.aps.org/doi/10.1103/PhysRevSTAB.15.042801

[66] S. Liu. "Development of Diamond Sensors for Beam Halo and Compton Spectrum Diagnostics after the Interaction Point of ATF2". PhD. thesis, Universit paris-sud (2015).

[67] S. Bai et al. "First beam waist measurements in the final focus beam line at the KEK Accelerator Test Facility". *Physical Review Special Topics-Accelerators and Beams*, **13**, 9 (2010) 092804.

[68] Y. Honda. "Bench test of limiter/int detector module" (2006). http://atf.kek.jp/twiki/pub/ATF/IPBPMmeetings2/limiter_module_test_0.pdf

[69] Xilinx. "Virtex-5 Family Overview Data Sheet" (2015). www.xilinx.com/support/documentation/data_sheets/ds100.pdf

[70] B. Constance. "Design and beam testing of a fast, digital intra-train feedback system and its potential for application at the International Linear Collider". D.Phil. thesis, University of Oxford (2011).

[71] G. Christian et al. "Latest performance results from the FONT5 intra-train position and angle feedback system at ATF2" (2011). Proc. of IPAC '11.

[72] D. Bett. "The development of a fast intra-train beam-based feedback system capable of operating on the bunch trains of the International Linear Collider". D.Phil. thesis, University of Oxford (2013).

[73] Xilinx. "7 Series DSP48E1 Slice" (2016). www.xilinx.com/support/documentation/user_guides/ug479_7Series_DSP48E1.pdf

[74] N. Blaskovic Kraljevic et al. "Development of a Low-latency, Micrometre-level Precision, Intra-train Beam Feedback System based on Cavity Beam Position Monitors". In "Proc. of IPAC '16", Busan, Korea (2016). THPOR035.

[75] A Lyapin et al. "Cavity BPM system for ATF2". In "DIPAC2011, Hamburg, Germany", (2011).

[76] TMD Technoligies Limited. http://www.tmd.co.uk/

[77] S. Jolly. "An Intra-pulse Fast Feedback System for a Future Linear Collider". D.Phil. thesis, University of Oxford (2003).

[78] G. Lambertson. "Dynamic devices, pickups and kickers". In "AIP Conference Proceedings", volume 153, pages 1413–1442. AIP (1987).

[79] C. Belver-Aguilar & A. Faus-Golfe. "Stripline design for the extraction kicker of Compact Linear Collider damping rings". *Physical Review Special Topics-Accelerators and Beams*, **17**, 7 (2014) 071003.

[80] T. Naito et al. "Development of a 3 ns rise and fall time strip-line kicker for the International Linear Collider". *Nuclear Instruments and Methods in Physics Research Section A: Accelerators, Spectrometers, Detectors and Associated Equipment*, **571**, 3 (2007) 599–607.

[81] A. Kalinin. "An ILC Turnaround Feed-Forward Prototype at the ATF". In "Third ATF2 Project Meeting, KEK", (2006).

[82] K.L.F Bane et al. "Wakefield Effects in the Beam Delivery System of the ILC". In "Proc. of PAC'07", Albuquerque, New Mexico (2007).

[83] K.L.F Bane & G. Stupakov. "Resistive wall wakefield in the LCLS undulator". In "Proceedings of the 2005 Particle Accelerator Conference", pages 3390–3392 (2005).

[84] G. White, N. Walker & D. Schulte. "Multi-bunch simulations of the ILC for luminosity performance studies". In "Proc' of PAC'05", pages 1368–1370. IEEE (2005).

[85] C. Glasman. "Long Range Wakefields Due to High Gradient Cavity Designs and Beam Dynamics Studies at Future Linear Colliders". PhD. thesis, University of Manchester (2012).

[86] R.M Jones et al. "Higher order mode wakefield simulations and beam dynamics simulations in the ILC main linacs". In "Proc. of LINAC", pages 199–201 (2006).

[87] G. Aarons et al. "International Linear Collider Reference Design Report - Volume 3: Accelerator". *arXiv:0712.2361*.

[88] P.N. Burrows. "The Interaction Point Collision Feedback System at the International Linear Collider and its sensitivity to expected electromagnetic backgrounds". D.Phil. thesis, University of Oxford (2008).

[89] A. Seryi, L. Hendrickson & G. White. "Issues of Stability and Ground Motion in ILC" (2006).

[90] V. Ivanov. "Beam-based feedback system for the International Linear Collider". *International Journal of Modern Physics A*, **24**, 05 (2009) 857–868.

[91] R.E. Kalman. "A New Approach to Linear Filtering and Prediction Problems". *Transactions of the ASME–Journal of Basic Engineering*, **82**, Series D (1960) 35–45.

[92] A. Latina et al. "Comparison of ILC Fast Beam Beam Feedback Performance in the e^-e^- and e^+e- Modes of Operation". In "Proc. of PAC'07", Albuquerque, New Mexico (2007).

[93] D. Schulte. "Beam-Beam Effects in Linear Colliders". CAS-CERN Accelerator School: Intensity Limitations in Particle Beams (2017). CERN-2017-006-SP.

[94] M. Pivi. "Beam-beam effects in particle colliders" (2011). `http://uspas.fnal.gov/materials/11ODU/Beam-Beam.pdf`

[95] K. Nakamura et al. "25. ACCELERATOR PHYSICS OF COLLIDERS". `pdgfloat.lbl.gov/2011/reviews/rpp2011-rev-accel-phys-colliders.pdf`

[96] K. Yokoya & P. Chen. "Beam-beam phenomena in linear colliders". In "Frontiers of Particle Beams: Intensity Limitations", pages 415–445. Springer (1992).

[97] P. Chen. "Disruption, beamstrahlung, and beamstrahlung pair creation". Technical report, Stanford Linear Accelerator Center (1988).

[98] J. Wu et al. "Luminosity Loss due to Beam Distortion and the Beam-Beam Instability". In "Proc' of the 2005 Particle Accelerator Conference", pages 1586–1588 (2005).

[99] C. Sramek, T.O. Raubenheimer, A. Seryi, M. Woods & J. Yu. "Beam-Beam Interaction Simulations with Guinea Pig". (2003).

[100] D. Wang, P. Bambade, Y. Wang, C. Rimbault & J. Gao. "Study of alternative ILC final focus optical configurations". *Nuclear Instruments and Methods in Physics Research Section A: Accelerators, Spectrometers, Detectors and Associated Equipment*, **781** (2015) 14–19.

[101] D. Schulte et al. "The Tracking Code PLACET Version 1.00" (2018). `http://svn.cern.ch/guest/clicsw/trunk/placet/doc/placet.pdf`

[102] J.W. Eaton, D. Bateman, S. Hauberg & R. Wehbring. "GNU Octave. A high-level interactive language for numerical computations. Free Software Foundation". *Inc., Boston, MA*.

[103] J.K. Ousterhout & K. Jones. "Tcl and the Tk toolkit". Pearson Education (2009).

[104] A. Latina, D. Schulte, Y. Levinsen & J. Snuverink. "Evolution of the tracking code PLACET". Technical report (2013).

[105] M. Woodley. `https://bitbucket.org/whitegr/ilc-lattices/`

[106] Toshiyuki Okugi et al. "Achievement of small beam size at atf2 beamline". *Proceedings of LINAC16, MO3A02*, page 93.

[107] M. Fouaidy. "TESLA Design Report". Technical report (2015).

[108] "ATF2 Wakes" (2018). `http://atf.kek.jp/twiki/bin/view/ATF/Atf2Wakes`

[109] D. Schulte. "Study of Electromagnetic and Hadronic Background in the Interaction Region of the TESLA Collider". PhD. thesis, DESY/Universität Hamburg (1997).

[110] G. Le Meur, P. Bambade, C. Rimbault, F. Touze, F. Blampuy & D. Schulte. "Description of guineapig++, the C++ upgraded version of the GUINEA-PIG beam-beam simulation program". EUROTeV-Report-2008-067.

[111] R. Hollebeek. "Disruption limits for linear colliders". *Nuclear Instruments and Methods*, **184**, 2 (1981) 333 – 347.

[112] K. Thompson. "GUINEA PIG Manual (SLAC NLC webpage version)" (2007). `www-sldnt.slac.stanford.edu/snowmass/Software/GuineaPig/gpman.pdf`

[113] A. Chao & W. Chou. "Reviews Of Accelerator Science And Technology - Volume 7: Colliders". World Scientific Publishing (2015).

[114] R. Bodenstein et al. "IP Feedback Ground Motion Simulation Studies for the ILC". In "Proc. of IPAC '17", Copenhagen, Denmark (2017).

[115] A. Seryi. `http://www.slac.stanford.edu/~seryi/gm/model`

[116] D. Kruecker et al. "Simulation Studies on Coupler Wakefield and RF Kicks for the International Linear Collider with MERLIN". In "Proc. 11th European Particle Accelerator Conference", (2008).